

University of Nottingham
School of Mathematical Sciences

New effective descriptions of deformable, adaptively remodelling biological tissue

Elizabeth Holden

A thesis submitted to the University of Nottingham for the degree of
Doctor of Philosophy

July 2018

Gloria in excelsis Deo

Abstract

Biological tissue is distinguished from materials described historically by continuum mechanical theory by its ability to grow and remodel adaptively, driven by a wide range of processes across multiple spatial and temporal scales. In this thesis we derive new mathematical descriptions that capture details from across various scales and their effect on the resulting overall behaviour.

Motivated by tissue engineering, we consider tissue growth on a porous scaffold. Using the multiscale homogenisation method of O'Dea *et al.*, [Mathematical Medicine and Biology, 32(3):345–366, 2014] and Penta *et al.*, [The Quarterly Journal of Mechanics and Applied Mathematics, 67(1):69–91, 2014] we derive a macroscale description from one posed on the microscale. Through use of a multiphase mixture model for the tissue we extend the ideas in the above to incorporate interstitial growth and cell motility. Macroscale models are obtained via two simplifications which facilitate the homogenisation: first, by taking the limit of large interphase drag and second, by linearisation about a uniform steady state. These models consist of Darcy flow and differential equations for the cell volume fraction within the scaffold and concentration of nutrient, required for growth. Effective parameters are obtained via solution of a cell problems, hence providing explicit dependence on the microscale geometry and dynamics. Closure of the model is provided by an expression for the tissue-interstitium boundary velocity, obtained from numerical investigation of the underlying multiphase description, and solutions for a sample geometry are given.

The same multiscale homogenisation technique is then employed in a different context: drug uptake by cancer cells and spheroids. Beginning with a description of drug uptake and binding for a single spheroid, two different macroscale models are derived based on different scaling

assumptions. These are fitted to experimental data to provide insight into uptake behaviour, with a view to revealing underlying dynamics.

Acknowledgements

First I would like to thank my supervisors Reuben O'Dea and Bindi Brook for their guidance and assistance over the past three and a half years. Thank you both for obsessing over brackets, semi colons, word choice, sentence structure and other vitally important mathematical concepts to make this thesis readable. Thanks Reuben for your patience and good sense of humour. Thanks also to Matthew Hubbard for advice on finite volume schemes.

Thanks to my parents for believing in me and to Christopher for always being there, although possibly not always actually listening.

And finally, thank you Ginger the cat, for company and occasional acupuncture.

CONTENTS

1 INTRODUCTION 1

1.1 Statement of originality . . . 3

2 BACKGROUND 5

2.1 Biological tissue . . . 5

2.2 Deformable, adaptively remodelling biological tissue . . . 9

2.2.1 Elastic deformation . . . 9

2.2.2 Collective cell migration . . . 10

2.2.3 Growth . . . 10

2.3 Areas of research into tissue growth . . . 12

2.3.1 Morphogenesis . . . 13

2.3.2 Cancer . . . 13

2.3.3 Wound healing . . . 14

2.3.4 Tissue engineering . . . 14

2.4 Descriptions of deformable, adaptively remodelling biological tissue . . . 19

2.4.1 Discrete sub-cellular models . . . 21

2.4.2 Discrete cell level models . . . 22

2.4.3 Hybrid models . . . 24

2.4.4 Continuous models for tissue . . . 24

2.4.5 Summary of mathematical methods . . . 30

2.5 Summary . . . 30

3 MULTIPHASE TISSUE MODEL 32

3.1 Introduction . . . 32

3.2 The scaffold . . . 33

3.3 The tissue . . . 36

3.4 The interstitium . . . 40
3.5 Nutrient . . . 41
3.6 Boundary conditions . . . 42
3.6.1 Scaffold-tissue boundary, $\partial\Omega_s$ . . . 42
3.6.2 Tissue-interstitium boundary, Γ . . . 43
3.7 Initial conditions . . . 44
3.8 Nondimensionalisation . . . 45
3.9 Summary . . . 46

4 A MULTISCALE MODEL IN THE LARGE DRAG LIMIT 48
4.1 Introduction . . . 48
4.2 In the large drag limit . . . 48
4.3 Multiple scales analysis . . . 52
4.3.1 Rescaling . . . 52
4.3.2 At leading order . . . 54
4.3.3 At $O(\varepsilon)$ . . . 57
4.3.4 Appropriate form for macroscale velocities and microscale pressures . . . 58
4.3.5 Microscale cell problem . . . 59
4.3.6 Averaging over the microscale . . . 60
4.3.7 Three special cases of the macroscale model . . . 63
4.4 Summary . . . 64

5 A LINEARISED MULTISCALE MODEL 66
5.1 Introduction . . . 66
5.2 Linearisation . . . 67
5.2.1 Steady state . . . 67
5.2.2 Perturbation to steady state . . . 69
5.2.3 Stability . . . 71
5.3 Multiple scales analysis . . . 72
5.3.1 Rescaling . . . 72
5.3.2 At leading order . . . 74

5.3.3 At O(ε) . . . 76
5.3.4 Appropriate form for macroscale velocities and microscale pressures . . . 77
5.3.5 Microscale cell problem . . . 78
5.3.6 Averaging over the microscale . . . 79
5.4 Subcases of the model and alternative boundary conditions . 81
5.4.1 Inviscid water . . . 82
5.4.2 Trivial steady state for cell volume fraction . . . 83
5.4.3 Alternative scaffold boundary conditions . . . 83
5.4.4 Alternative nutrient concentration boundary conditions 84
5.5 Summary . . . 89

6 AN ALTERNATIVE ANSATZ FOR THE LINEARISED MULTISCALE MODEL 92
6.1 Introduction . . . 92
6.2 Appropriate form for the macroscale velocities and microscale pressures . . . 92
6.3 Microscale cell problem . . . 93
6.4 Impact on the macroscale description . . . 95
6.5 In the inviscid water subcase . . . 96
6.6 Summary . . . 96

7 MODEL CLOSURE AND NUMERICAL SOLUTIONS 97
7.1 Introduction . . . 97
7.2 Model equations . . . 98
7.3 Reduction . . . 100
7.3.1 Interstitial domain, Ω_I . . . 101
7.3.2 Tissue domain, Ω_T . . . 101
7.3.3 Nutrient concentration . . . 102
7.3.4 Boundary conditions . . . 103
7.4 Finite volume numerical scheme . . . 103
7.4.1 Overview . . . 103

7.4.2 Method . . . 105
7.4.3 Velocity . . . 107
7.4.4 The boundary region . . . 107
7.5 Results . . . 109
7.5.1 Sub case 1: Viscous cells - inviscid water . . . 109
7.5.2 Sub case 2: Viscous cells - viscous water . . . 121
7.6 Numerical experiments . . . 126
7.6.1 Microscopic cell problem . . . 127
7.6.2 Macroscale description . . . 128
7.6.3 Microscale Problem . . . 128
7.6.4 Macroscale Problem . . . 131
7.7 Summary . . . 133

8 DRUG DELIVERY TO TUMOUR SPHEROIDS 138
8.1 Introduction . . . 138
8.2 Experimental setup . . . 140
8.2.1 Uptake experiment . . . 141
8.2.2 Efflux experiment . . . 141
8.3 Binding model for drug uptake . . . 142
8.4 Model setup . . . 145
8.4.1 Steady state . . . 146
8.4.2 Non dimensionalisation . . . 146
8.5 Homogenisation . . . 147
8.5.1 Similar drug diffusivities in both domains . . . 148
8.5.2 Highly contrasting diffusivities, membrane law . . . 152
8.5.3 Model simulations and comparison . . . 155
8.6 Data fitting . . . 160
8.7 Effective Diffusion . . . 164
8.8 Summary . . . 166

9 CONCLUSIONS AND FURTHER WORK 172
9.1 Concluding discussion . . . 172

9.2 Further work 177

A BOUNDARY LAYER ANALYSIS IN THE LARGE DRAG LIMIT 180

A.1 Initial boundary layer analysis 180

A.1.1 Multiple scales analysis 182

A.1.2 Matching to the core flow 183

A.1.3 Matching to the exterior flow 184

A.2 Second boundary layer analysis 185

A.3 Summary 187

Bibliography 188

1

INTRODUCTION

A key feature of biological tissue is its ability to grow and remodel adaptively, processes that involve a wide range of interacting biological and physical factors, spanning multiple spatial and temporal scales, from intracellular gene networks to tissue level patterning and mechanics. Due to its importance in the development of an organism's shape, wound healing, cancer and creation of functional tissues for a wide range of applications, the growth of biological tissue receives much attention.

Motivated by the application to tissue engineering, the focus of this thesis is to derive new effective descriptions of deformable, adaptively remodelling biological tissue. In particular, we seek descriptions that capture detail from across the various scales and their effect on the resulting growth.

O'Dea *et al.* [115] derive a mathematical model of this type, describing the growth of tissue in porous scaffolds that are used within tissue culture systems. By employing the method of multiscale homogenisation, the authors obtain macroscale equations that accommodate explicitly the influence of the microscale structure and dynamics. In this model, cell proliferation, and extracellular matrix deposition, are represented by accretion or surface growth at a rate dependent on the uptake of some generic nutrient. The tissue is considered to be a solid layer on a rigid (indistinguishable) scaffold. In a similar model, [126], multiscale homogenisation is used by Penta *et al.* to incorporate the effects of the

microscale on macroscale growth but the growing media is taken to behave as a linear elastic solid.

Whilst the above are successful in their inclusion of some of the various scales involved in growth of tissue on a porous structure, the description of the tissue itself, and its growth by accretion, is somewhat simplistic. Alternatively, Lemon *et al.* [90] use a mixture model, which permits interstitial growth and motion due to cell-cell interaction. Here, we extend and combine the above studies to obtain, by means of multiscale homogenisation, a more complex representation of macroscale tissue growth that accommodates volumetric growth and active cell motion by utilising this multiphase mixture approach to describe the microscale tissue dynamics.

We begin with an overview of the biology related to tissues and their growth in chapter 2, as well as summarising research in this area, including tissue engineering. We then discuss different mathematical methods which have been used to describe and model the complex behaviour of biological tissues.

In chapter 3, we set up our model, including a detailed description of the multiphase mixture model of Lemon *et al.* [90] which we use to describe the tissue. This allows the accommodation of both cell-cell interactions and volumetric growth, as opposed to accretion (as is the case in [115]). However, this more complex tissue description leads to difficulties in the application of the method of multiple scales, used to derive a macroscale description from the microscale. To overcome this we use two different methods to simplify the problem. First, in chapter 4, we suppose the drag between the phases is large, in which limit we find all phases have a common velocity. We then derive the effective macroscale description and associated 'cell' problem, used to define the scaffold permeability.

As simplification by taking the limit of large interphase drag results in a common phase velocity, it removes the effects of any intraphase forces through which the cells' active motion is accommodated. To derive a model

where these intraphase forces, particularly cell-cell interactions, affect the tissue growth, in chapter 5 we linearise the mixture equations instead. Again the effective macroscale description and the coupled 'cell' problem are derived. An alternative 'cell' problem, derived using an ansatz given in terms of the separate components of the macroscale pressure rather than their sum, which is significantly simpler to solve, is then derived in chapter 6. The macroscale descriptions in both models, however, are not closed.

In chapter 7 we investigate the behaviour of the microscale tissue mixture model, both analytically and numerically, in order to provide insight on the closure of the macroscale models derived in chapters 4 and 5. Additionally, a simple case of the macroscale model, and accompanying microscale 'cell' problem, of chapter 5 is solved numerically.

We employ the techniques of multiscale homogenisation in a different context in chapter 8. Experimental data supplied by collaborators (University of Bradford) highlights differences in the uptake of a drug by cancer cells and spheroids in solution. This study aims to explore drug penetration and distribution, and hence inform the development and optimisation of cancer treatment regimes. We look to derive a mathematical model that captures the difference in drug uptake rate observed between the cells and spheroids, and could be used improve understanding of drug transport. By supposing that diffusion of the drug in the solution is fast, in comparison to the uptake rate, we derive two different models via multiscale analyses and compare them to the available data.

Finally, in chapter 9, we include a review of the main conclusions of the thesis, along with possible direction for future work.

1.1 STATEMENT OF ORIGINALITY

In chapter 4, originality is claimed for analysis but this same analysis was also carried out separately by Joseph Collis (University of Nottingham) and published in [46]. The model of [46] has minor differences given that

the context is of avascular tumour growth, and hence no scaffold or rigid phase is present, and it includes response to chemotherapeutic treatment. Originality is claimed for chapter 5. The alternative ansatz described in chapter 6 was proposed by Jon Chapman. In chapter 7 the numerical investigation and solutions to the 'cell' and macroscale problems are the work of Joseph Collis. The experimental data in chapter 8 was obtained by Jade Spencer and Maria Jove Casulleras (University of Bradford), and the determination of the reaction rates from the experimental data, via parameter fitting analysis, was carried out by Matthew Hubbard (University of Nottingham). Additionally, the underlying microscale model for the drug concentrations is taken from [68].

The results of chapter 5 and some of chapter 7 have been published in [71]. The experiments described in chapter 8 and the accompanying mathematical model are currently in preparation for publication [39].

2

BACKGROUND

As described in chapter 1, motivated by the application to tissue engineering, we wish to derive new effective descriptions of biological tissue, building on the work of O'Dea *et al.* [115] and Penta *et al.*[126]. In particular, we seek to improve the description of tissue growth from that of simple accretion to a more realistic representation.

In this chapter we provide some biological background to tissue, features that could be accommodated in our model, such as its basic structure and properties, as well as the various ways it can deform and remodel. We then give some detail on areas of research, such as cancer and tissue engineering, where tissue growth is studied. A number of popular discrete and continuous mathematical approaches, used to model tissue, are described along with their advantages and disadvantages.

2.1 BIOLOGICAL TISSUE

We begin with a brief summary of biological tissues, their types, structures and properties. Understanding these features is necessary to inform a suitable mathematical representation for our model.

A tissue is defined by [5] to be an aggregation of morphologically similar cells and associated intercellular matter (table 1) acting together to perform specific functions in the body. It is an organisation level between cells and organs, as illustrated by figure 1.

Component of tissue	Description
Cells	Cells make up all living things and consist, at their most basic level, of a quantity of protoplasm and a nucleus contained by a cell membrane. They have the ability to synthesise proteins and replicate themselves. [1]
Interstitial fluid	Formed by filtration through the blood capillaries, it brings nutrients to the cells and removes waste products when it drains away as lymph [2]. It generally contains glucose, salt, fatty acids, minerals and water.
Extra cellular matrix	This is mainly comprises proteins, largely collagen, and carbohydrates which act to hold cells together to form tissues and to allow communication between them [64].

Table 1.: The components of tissue.

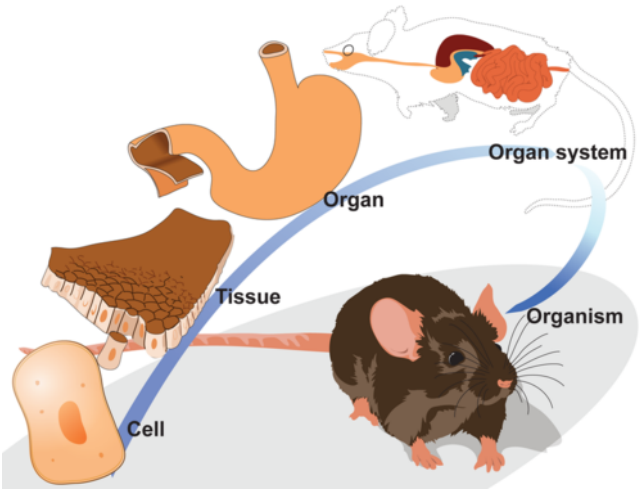


Figure 1: Levels of structural organisation, from cells to organism, [10]

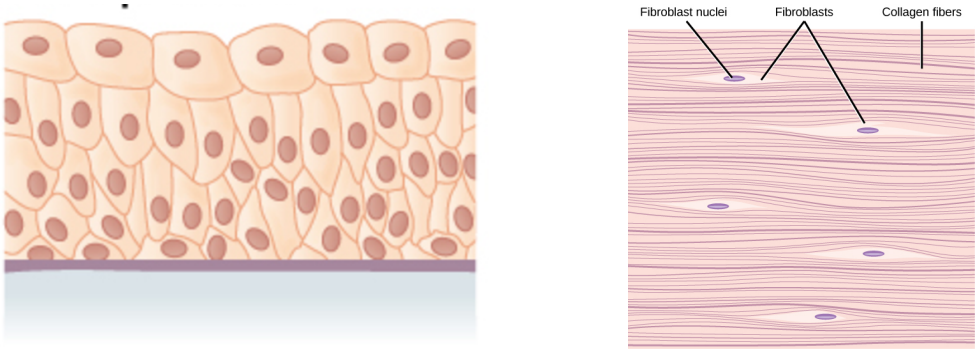
The exact structure and properties of a biological tissue vary according to its function. There are four basic types of tissue in humans: muscle, nerve, epithelial and connective. Their functions and subtypes are described in table 2. For example, epithelial tissue is composed of tightly packed

Tissue type	Function	Subtypes
muscle	to contract	smooth, skeletal cardiac
nerve	for communication using electrical signals	
epithelial	covers outside of organs and structures, lines lumens of organs	squamous, cuboidal columnar, transitional
connective	support and shock absorption for bone and tissue	loose, fibrous, bone cartilage, blood, adipose (fat)

Table 2.: Basic tissue types and their function, [132]. Several types of tissue come together to form an organ.

cells with strong cell-cell attachments. This allows them to form an effective protective layer over the tissues beneath them. In contrast, fibrous connective tissue that forms ligaments and tendons contains very few cells

but large numbers of collagen fibres, which make it very strong. These two tissue types are illustrated in figure 2.



(a) (b)

Figure 2: Different tissue types and their structure. (a) transitional epithelial tissue [9], (b) fibrous connective tissue [8]

The cell-cell and cell-collagen adhesions required to hold a tissue's components together are dependent on the actions of integral membrane proteins or cell adhesion molecules (CAM), illustrated by figure 3. These

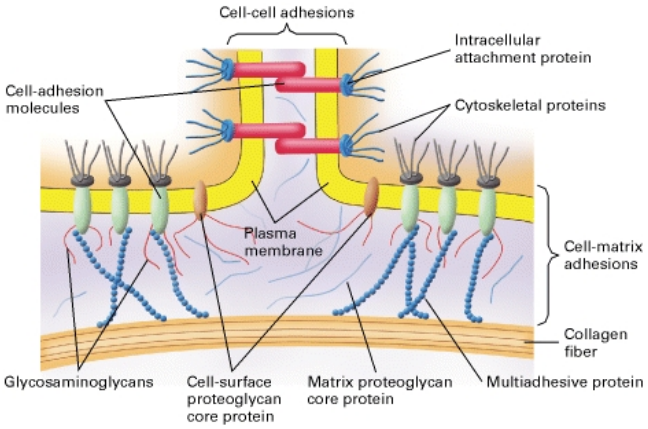


Figure 3: Schematic overview of the types of molecules that bind cells to each other and to the extracellular matrix, [94]

adhesion molecules, as well as holding cells together and having a role in cell-cell communication, play a key part in the metastasis of cancer [57], where cancerous cells leave the main tumour and travel to a new location usually via blood vessels or lymphatics.

SUMMARY Biological tissue is comprised of groups of similar cells along with interstitial fluid and extracellular matrix. Dependent on the specific function of the tissue, the structure and properties differ, from the densely packed cells of epithelial tissue to the sparsely distributed cells and dense collagen fibres of fibrous connective tissue. It is not just these features that are important to consider if a mathematical model is to be representative; tissue is not static, but can deform and adapt, as described in the next section.

2.2 DEFORMABLE, ADAPTIVELY REMODELLING BIOLOGICAL TISSUE

Biological tissue can deform and remodel in response to internal or external factors and events. In this section we explore how tissue may react to applied forces due to its elastic properties and how it can remodel through collective cell migration and growth.

2.2.1 *Elastic deformation*

Tissue, from muscle [40] to bone [49], may be subjected to stretching or compressive forces in order to determine its degree of elasticity. Its elasticity is dependent on the tissue type, in particular to the proteins present in the cells and extracellular matrix (ECM), such as collagen, fibrillin and elastin [13].

In the cytoplasm of a cell there is a network of protein fibres, known as the cytoskeleton, which helps the cell to maintain its shape. Microfilaments, made of actin, provide rigidity and shape but are additionally involved in cell movement so can also reform quickly. Larger fibres, known as microtubules can also dissolve and reform quickly helping the cell to divide, as well as resisting compression of the cell.

Outside the cells, proteins that form the ECM also contribute to the deformability of the tissue. Collagen, that occurs in large quantities in fibrous connective tissue provides strength and structure whilst elastin, as the name suggests, is a highly elastic protein found, for example, in skin where it helps the tissue to return to its previous shape after being stretched or compressed.

The elastic properties of soft tissues can be mapped using a type of medical imaging known as elastography. This technique is used to look for diseased tissue as for example cancerous tumours and diseased liver tissue as these are stiffer than healthy tissue [136].

2.2.2 *Collective cell migration*

Tissue remodelling may occur through collective cell migration. Sheets, strands or clusters of cells move together, using motor proteins, in response to chemical or mechanical stimulus [60]. This behaviour occurs in embryogenesis, wound repair and in invasive tumours with the cells migrating across or through other tissues or ECM. An example of this can be seen in [53], which describes the migration of the zebra fish lateral line primordium, a collection of around 100 cells, along the main body axis in response to a stripe of chemokine.

2.2.3 *Growth*

Another way that biological tissue can remodel is through growth (or death) of the cells that make it up. Cells divide to produce new cells for the purpose of growth and to repair/regenerate tissues. Some cells such as mature cardiac muscles rarely divide, whilst others such as blood and skin cells are constantly being produced. The process of cell division occurs in

a number of tightly regulated phases. First is the interphase which is split into three phases.

- G1 – First gap – the cell grows and accumulates the building blocks required for DNA.
- S – Synthesis of DNA – DNA is duplicated.
- G2 – Second gap – additional growth occurs, energy is replenished, new proteins synthesised, cytoskeleton is dismantled.

The cell then enters the mitotic phase (M) where the nucleus divides (karyokinesis) and then the daughter cells separate (cytokinesis). The cells may then start the process again or stop temporarily (or permanently for some cells) at the inactive phase, G0 [17].

This cell cycle can be affected by a number of internal and external factors. The death of nearby cells or the presence of growth promoting hormones encourages cell division, whilst, conversely, cell crowding can stop it. Cells also divide if their surface to volume ratio has decreased due to growth in size, as transport of oxygen and nutrients across the cell membrane is reduced per unit volume.

Internally there is significant regulation of growth, with various checkpoints where progression to the next stage can be stopped if conditions such as energy and protein requirements are not met. It can also be halted if there has been some damage to the DNA or the chromosomes have not replicated correctly. This is important because if the cell cycle were allowed to continue it would lead to mutations which may then cause cancers to form. Some typical lengths of the cell cycle are shown in 4, assuming that the growth conditions are favourable.

SUMMARY In response to internal and external factors, biological tissue can deform, move and grow. Tensile or compressive forces cause deformation, as permitted by the proteins within the cells and that form the

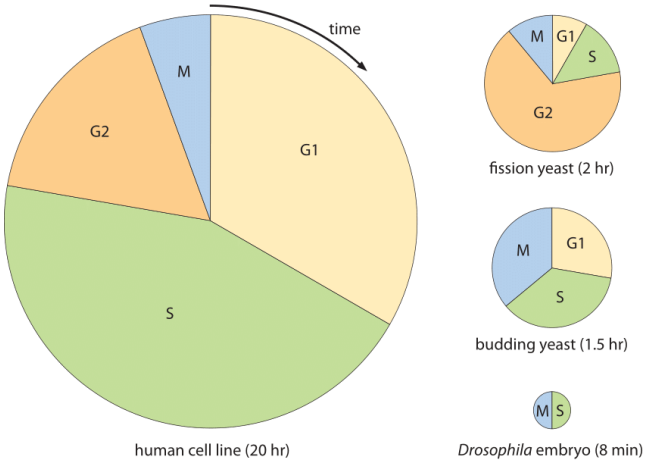


Figure 4: Cell cycle times for different cell types. Each pie chart shows the fraction of the cell cycle devoted to each of the primary stages of the cell cycle. The area of each chart is proportional to the overall cell cycle duration. Cell cycle durations reflect minimal doubling times under ideal conditions. (Adapted from *The Cell Cycle - Principles of Control* by David Morgan.), [4]

extracellular matrix. Groups of cells can also move in response to chemical or mechanical stimuli. Growth of tissue occurs as a number of complex stages within the individual cells. These processes are important features of biological tissue, forming the basis of many important areas of research, some of which are described in the following section.

2.3 AREAS OF RESEARCH INTO TISSUE GROWTH

There are many important areas of research in which tissue, in particular its growth, is studied, from personalising medicine with replacement organs grown *in vitro* from patients' own cells, to halting the spread of a cancerous tumour. Some examples are briefly described below.

2.3.1 *Morphogenesis*

Morphogenesis is the carefully orchestrated process by which the shapes and structures of organs and organisms form, such that they can reliably fulfil their function [144]. Popular subjects for these studies are the fruit fly drosophila, zebra fish and chickens. Changes in geometry of the tissue, for example the bending of epithelial sheets to form the 3D structures, are driven by changes to the geometry of the cells, caused by protein filaments present in the cytoskeleton. As well as providing information on the early stages of development, morphogenesis can also provide insight into the problems associated with aging and disease.

2.3.2 *Cancer*

With current statistics estimating that 1 in 2 people in the UK will get cancer in their lifetime [12], there is a lot of interest in cancer research. Cancer is caused by changes to a cell's genetic material, resulting in uncontrolled division and growth.

Initially, composed of a relatively small number of cells, growth of the tumour is driven by nutrient acquired from its surroundings, during which phase it may grow exponentially. As the tumour grows in this 'avascular' stage, hypoxic and possibly necrotic regions develop towards the centre as the supply of oxygen and nutrients is limited by their diffusion.

During later stages angiogenesis occurs, whereby the tumour releases a tumor angiogenic factor (TAF) to encourage the growth of new blood vessels in order to better supply itself with nutrients [11]. Once the cancerous tissue is vascularised, tumour cells can escape via the circulatory system, setting up secondary tumours else where in the body. This is known as metastasis [95]. Understanding how the disease progresses and spreads can be used to

provide insights on how to improve the delivery and effectiveness of drugs [77], and therefore the survival rate.

2.3.3 *Wound healing*

As well as for growth, cells may also divide to repair damaged tissues. The healing of wounds is a complex process where events at the cell and tissue levels contribute to reduction in wound size [26, 119]. Healing can be much slower in diabetic and older patients [130], motivating study in this area.

2.3.4 *Tissue engineering*

Tissue engineering is defined by [7] to be the practice of combining scaffolds, cells and biologically active molecules into functional tissues. Motivations for this vary and include:

- **Organ replacement** With over 7000 people in the UK alone waiting for an organ transplant [6] being able to grow replacement tissues and organs in the lab could dramatically reduce waiting times. In 2014-2015, of those waiting, 30% of people had been waiting for over 2 years and more than 10% died before receiving the transplant they needed. Moreover, if grown from the recipient's own cells, complications related to rejection and immunosuppression could be avoided. In the laboratory there has been success in creating a new heart, lung, liver and most recently a functioning kidney [142] by stripping existing organs of cells leaving the collagen on which to grow the new tissue. Simpler structures such as supplemental bladders, small arteries, skin grafts and cartilage have been produced and implanted into patients.

- **Toxicological research** Alternatively tissue can be grown for use in toxicological research and drug screening. With increasing regulation of animal testing, and animal experiments not always able to predict

the human response to drugs [27, 138], growing the relevant tissues required for research could lead to cheaper and more accurate results. Cell monolayers can be used for this purpose but 3D cultures provide a better representation of the response from living organisms [123].

- **Cultured meat** As the world population increases so does the demand for meat products. One method proposed for improving production is that of *in vitro* or cultured meat, which has lower greenhouse emissions and requirements for land, water and energy [147]. As shown by the prototype burger created in 2013 [3], meat can be produced *in vitro* using tissue engineering techniques to grow cow muscle tissue from stem cells.

Whilst tissue engineering may reach back to the creation of Eve from Adam's rib [102] most of the work in this area is highly experimental and expensive. To grow tissue successfully for the applications above, the materials used, and the experimental setup must be just right for the particular type of tissue. First one needs the correct choice of cells for the desired result together with suitable biomolecules such as growth factors.

Secondly, the optimum environment should be provided, often mimicking *in vivo* conditions. This includes basic conditions such as temperature, pH and availability of oxygen, but may also include the application of external forces. For example, some tissues, such as bone, additionally require the application of flow and strain in order to be conditioned according to the implantation environment [38].

Another important consideration is how to create the structure of the tissue. Whilst monolayers or small spheroids are easy to grow, a three dimensional functional tissue is more challenging. Once a tissue reaches a size of approximately $100 - 200\mu m$ thick, diffusion is no longer a sufficient process to deliver enough oxygen and nutrients to all cells [78], resulting in the development of hypoxic or necrotic regions at the centre. To overcome this, a wide range of scaffolds and bioreactors have been created,



Figure 5: Examples of carbohydrate glass that can be fabricated and used to create channels through an ECM polymer gel. Scale bar = 1mm. [103]

in order to provide a form of artificial vasculature – a network of pipes or interconnected gaps to bring the cells requirements to within diffusible distance throughout the tissue.

In [103], a printed network of carbohydrate glass (see figure 5) is used as a sacrificial template to create channels through an ECM polymer gel, so that blood can be perfused through the tissue, whilst decellularized animal and plant material is used in [66, 121], with its pre-existing vasculature (see figure 6). Hollow fibre membrane bioreactors [124] follow a similar approach. Here the culture medium is driven through a porous hollow fibre, mimicking a capillary, around which, in the extracapillary space (ECS), the cell seeded scaffold is located (see figure 7). ECS ports can be opened to improve flow through the membrane and allow flow out of the ECS.

Other methods rely on the construction of porous scaffolds, with interconnected gaps through which a nutrient rich fluid can be transported. Some examples include woven fibres [106], electrospun 3D matrix [105] and 3D printed lattice structures [79] (see figure 10). These can be combined with a perfusion bioreactor, to improve the supply of nutrients and removal of waste products, and hence result in a viable 3D tissue. In this system, a porous scaffold, seeded with cells, is placed in a cylinder filled with a culture medium which is pumped through it (figure 7). There are many

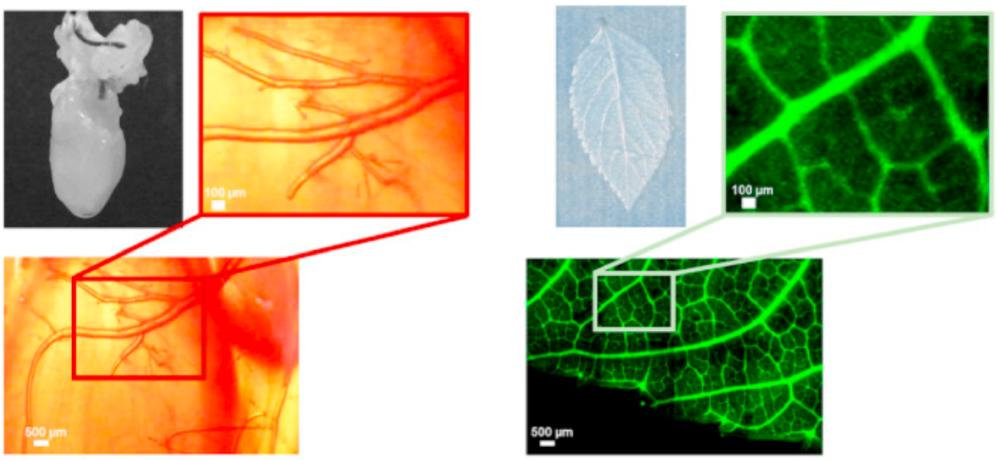


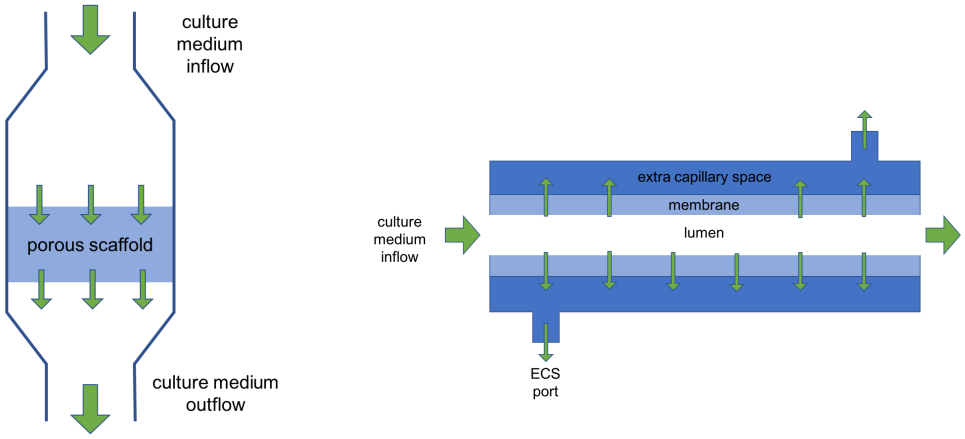
Figure 6: A decellularised rat heart and *Buddleja davidii* leaf including vasculature detail. [66]

other types of bioreactor for tissue engineering, for example those described in [41], aiming to provide the best conditions for the growth of a particular type of tissue.

As well as the choice of bioreactor, there are other key considerations when contemplating the choice of scaffold in addition to its architecture, i.e. the porosity and the pathways for cells and nutrients to travel through the structure. These include [111]:

- biocompatibility - Will the cells grow on the material? If implanted, will the body reject it?
- biodegradability - Will it degrade over an appropriate time scale into non toxic products?
- mechanical properties - Is it strong enough? This is particularly important for bone and cartilage transplants which are subject to loading in the body.
- manufacturing technology - Is it cost effective?

Tissue engineering has not yet delivered on its potential, as methods need refining in order to provide 3D tissues that are viable and functional. To improve the process there are many areas to investigate, experimentally



(a) (b)

Figure 7: Cross sections of (a) a perfusion bioreactor and (b) a hollow fibre membrane bioreactor.

and with mathematical models, for example: the influence of the bioreactor on the tissue morphology [152], cell behaviour under different bioreactor flow rates [124] and scaffold design [92]. The research in this thesis, into new descriptions of deformable, adaptively remodelling biological tissue, is particularly motivated by tissue engineering.

SUMMARY From early stages of development to the healing of wounds, tissue growth is studied across a wide range of important areas of research. Our focus is on tissue engineering, the creation of functional tissues, for transplant, use in toxicological research or the production of cultured meat. A number of factors contribute to the successful growth of tissue, including provision of the optimal environment and requirements for growth, in particular a process to deliver oxygen and nutrient to all cells. To achieve this, a number of scaffolds and bioreactors have been created, but the methods need refining to deliver improved results.

Having provided motivation for the modelling of tissue growth, in the next section we discuss how this complex biological process can be described using mathematics.

2.4 DESCRIPTIONS OF DEFORMABLE, ADAPTIVELY REMODELLING BIOLOGICAL TISSUE

As tissue growth consists of contributions across multiple spatial and temporal scales, and non-linear mechanical properties, the mathematical methods used to describe and model them are wide and varied. The two main classes of model are discrete, typically considering individual cells and their interactions, and continuous, describing, in some sense, overall trends and behaviour of entire cell populations. The decision of which type of model to use depends on the level of detail that is important to incorporate and the accompanying computational cost. For example, if cell shape and volume is an essential feature under consideration then a discrete model would be most appropriate. For a large number of cells, however, continuous models are preferable due to the reduced computational expense and improved potential for analysis.

Models for the same biological behaviour or event can be constructed via both of the two approaches for mutual validation or to provide different insights. For example, in [107], a discrete (vertex) model and a continuous model for deformations in epithelial sheets are derived, showing good agreement despite the simplifications of the continuous model. In [108] a discrete model for cell dynamics in an intestinal crypt, a continuum model and experimental data all show good agreement. The continuum model shows that biologically realistic solutions are only provided by a limited region of parameter space hence informing the discrete model and removing the need for many numerical simulations.

We begin by looking at some of the popular discrete methods used for modelling tissue, as illustrated by Figure 8.

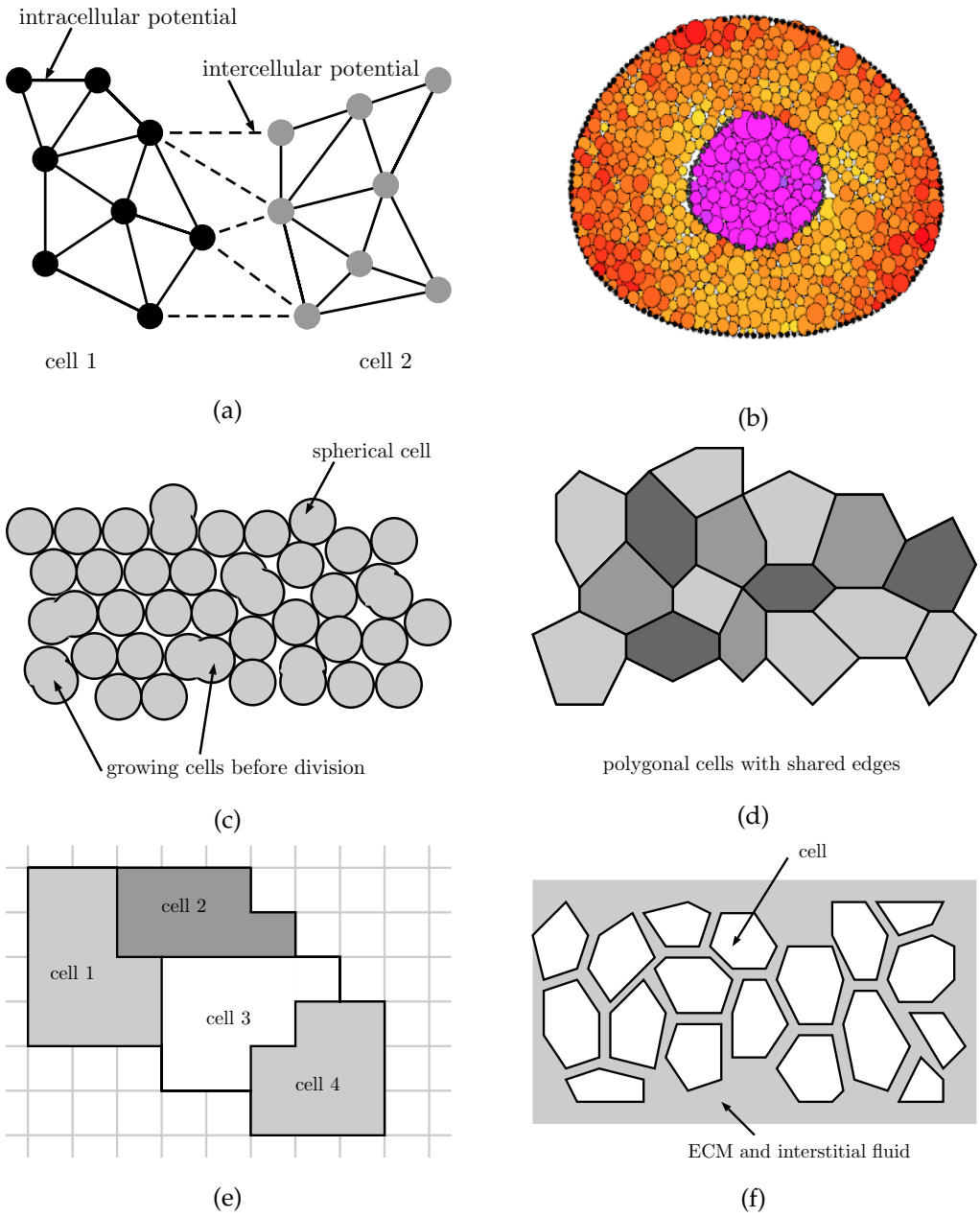


Figure 8: Illustrations of some different discrete tissue models. (a) Sub-cellular element model: Two cells constructed from elements with intra- and inter-cellular potentials. (b) A single cell composed of sub-cellular particles with different properties, from [62]. (c) Spheroid model: cells as spheres/ellipsoids. (d) Vertex model: cells as polygons with shared edges. (e) Cellular Potts: cells represented as a series of square lattice sites. (f) Immersed boundary: cells as fluid filled polygons surrounded by fluid representing ECM and interstitial fluid.

2.4.1 *Discrete sub-cellular models*

Sub-cellular element model

In these models, small volume elements of intracellular cytoskeleton are used to make up cells, to capture their mechanical and dynamical properties [109]. Each subcellular element is represented by a node at its centre of mass. These nodes move and interact with each other in response to intra- and inter-cellular forces, derived from the potential assigned to the type of interaction. A simple example of two cells, with element interactions represented by lines, is shown in figure 8(a), but the model can be extended to 3D and cells composed of many more volume elements and interactions. This model has been extended by Sandersius *et al.* [135] to include active biomechanical subcellular processes. Subcellular interactions were 'faded in or out', i.e. created or destroyed over a time period, to include the assembly and disassembly of the cytoskeletal network in response to an external mechanical force.

In a similar vein, Gardiner *et al.* [62] present a discrete modelling framework, whereby all components of the tissue are represented by collections of particles. As illustrated in figure 8(b), an individual cell is composed of different particles, representing the membrane, cytoplasm etc whilst further particles represent the ECM. The particles' properties and behaviour vary by type and in response to their local environment. They can grow and divide and interact with other particles, with inter-particle forces modelled as non-linear springs. Examples are shown of the deformation of individual cells as well as of epithelial sheets under compression.

Models that consider sub-cellular volumes or particles provide a high simulation resolution, allowing the inclusion of intracellular biology and adaptive cell shape dynamics, but, unsurprisingly, they can be computationally expensive.

2.4.2 *Discrete cell level models*

Spheroid model

The spheroid model for tissue is conceptually analogous to a model for colloidal particles [54], small particles floating in some medium, with individual cells modelled as single spheres or as ellipsoids (see figure 8(c)). Depending on the cell division algorithm, spheres may grow and deform simultaneously before division, or double in size whilst remaining spherical and then deform. Cells can move randomly or in response to chemoattractant as well as interacting with other cells. Interactions between spheres, such as cell-cell adhesion, can be described by choice of interaction potentials. Palsson *et al.* [122], use the spheroid model to reproduce the movement observed for cells and aggregates of the cellular slime mold *Dictyostelium discoideum* in [25].

Vertex model

In this approach cells are generally modelled as 2D polygons (see figure 8(d)), although 3D representation is also possible. The edges of the polygon are shared with neighbouring cells, so no overlaps or interstitial space are included, and the vertices move in response to forces arising from the growth, interfacial tension and pressure in each cell. As a result, this method is particularly suited to modelling epithelial tissue, that covers most surfaces of the body and organs, as the interstitial space that is present in other tissue types cannot easily be represented. An example of the vertex model can be found in [74], where Drosophila wing disc growth is explored. The vertex model is used to demonstrate a proposed mechanism for wing size determination.

Cellular Potts model

Unlike the other discrete models mentioned, the cellular Potts model is a lattice based method. In some cellular automata, a discrete particle (or cell) is represented by one lattice site. The Cellular Potts Model is more complex, allowing a single cell to be composed of a number of connected lattice sites hence describing cell volume and shape more realistically [70] (figure 8(e)). Connections between neighbouring cells are assigned an energy, determining the strength of their adhesion to each other. Additional energy can also be defined based on a cell's shape. This model is used by Osborne [120] to model colorectal cancer, with cell shapes evolved by minimising the energy of the system. Mutant cells are modelled and their influence on the shape of cells in the crypt determined. Using an extension of the Potts model, Turner and Sherratt [148] demonstrate the influence of changes in cell-cell adhesion on the cancer invasion process.

Immersed boundary

Similarly to the vertex model, cells (or clusters of cells) are modelled as polygons, here containing a viscous fluid representing the cytoplasm. In the immersed boundary model, however, the polygons do not share edges but are surrounded by a further viscous fluid representing the ECM and interstitial fluid (figure 8(f)). The fluid is described by Navier-Stokes equations, whilst forces on the cell boundary can be represented, for example, by springs. This model is used by Rejniak [129] to simulate early tumour development in various geometrical configurations whilst explicitly allowing cell interactions to be modelled on the level of cell membrane receptors.

2.4.3 *Hybrid models*

All the methods that we have considered so far give a great deal of cell scale information, from cell-cell interactions to changes in shape of individual cells, but all this comes at a computational cost. Hybrid models, such as [16], retain much of this information by using a mixture of discrete and continuous approaches. In the example, individual tumour cells are modelled as discrete but the host tissue, enzymes and oxygen are described by spatially continuous variables, as detailed in the next subsection.

2.4.4 *Continuous models for tissue*

Continuous models allow the tissue dynamics to be described using PDEs, for which there is a wide range of well understood analytical and numerical solution methods. Typically the tissue constituents are described by mass balance equations, and any solutes (such as nutrients or drugs) by reaction-diffusion equations. The model is then closed by either equations for the conservation of momentum or other assumptions about the movement of cells, ECM etc.

One simplistic approach is to model the tissue as a radially symmetric rigid solid undergoing exponential growth, although solid tissue models can be made increasingly complex by introducing nutrient dependent growth or elasticity. Choosing to model the tissue as a fluid, an approach taken in the tumour model of Lubkin and Jackson [96], allows one to use the well known Navier-Stokes equations to describe the momentum. If the fluids are slow moving, of large viscosity, or the length scales under consideration are small, Stokes flow may be used. This choice also provides significant simplification in comparison with tissue growth models involving elastic effects [90].

For complicated phenomena, such as tissue growth, the models can be complex and difficult to analyse. It may be preferable to obtain simplified descriptions that capture the important features of the model or the averaged or overall behaviour, whilst removing unnecessary detail. For example, the authors of [20, 114, 118] systematically derive continuum models from discrete models, simplifying them whilst retaining the essential biology. Band and King [20] derive a tissue scale model, describing the transport of the hormone auxin in a plant root, consisting of a few partial differential equations from hundreds of ordinary differential equations governing the underlying discrete cell-based model. A discrete protein signalling model (Delta-Notch), used to describe pattern formation, is used to derive one and two dimensional continuum models in [114, 118]. These new models are shown to provide good quantitative agreement with the discrete system.

Continuum models can also be simplified to give effective descriptions or homogenised equations such as Darcy's law [51]. This describes the flow of viscous fluid through porous media, relating the flow velocity to the pressure gradient via the permeability of the media. A much less complicated description than the Navier-Stokes equations, it was originally formulated based on experiments of water flowing through beds of sand. Later, Darcy's law was derived theoretically from the Navier-Stokes equations using an averaging technique [82]. This took advantage of the presence of well-separated space scales, for example small pores in a much larger piece of material. We shall refer to these as the micro- and macro-scales. Properties may vary rapidly relative to the macroscale but these variations are 'filtered out' resulting in a macroscale description, with 'effective' parameters, that describes the impact of the microstructure and dynamics on the macroscale.

There are a number of methods, designed to reduce the complexity of models by deriving effective macroscale equations from information on the microscale. These include multiscale asymptotics, volume averaging,

mixture theory, moment methods, central limit methods and stochastic-convective approaches [50], some of which are described below.

Volume averaging

The first upscaling approach we consider is volume averaging. Here an average is defined, along with its interaction with differential operators, and then used to average the model equations. Next, variables are decomposed into an average, which varies slowly in space, and a perturbation, which varies more quickly. Approximate forms of the perturbations are determined through making simplifying assumptions on their periodicity and time and length scales. These can then be used to obtain macroscale equations in closed form, containing only the average part of the variables.

Mixture theory

Using averaging, one can derive equations for the interacting continua of multicomponent materials or mixtures [55]. Gas or fluid mixtures, alloys, suspensions, porous media or other materials of more than one component, each with different properties or behaviours, can be described using mixture theory. Each component is treated as a continuum that occupies the same region of space but is described with separate equations for their conservation of mass and momentum [146]. These equations incorporate terms to account for the interchange of mass and momentum between components [47]. Mixture theory therefore provides a natural framework to accommodate the complexity associated with tissue growth dynamics and, consequently, has therefore been widely used in the context of tumour growth [36, 48, 72, 96] and tissue engineering [88–90, 117].

Whilst the original tumour growth models used two phases [29], the mixture approach allows the tissue to be comprised of multiple components, such as the four distinct phases of tumour cells, healthy cells, blood vessels and extracellular matrix that make up the model for a vascularised tumour in [72] where each phase behaves like a viscous fluid. Numerical

simulations reproduced the characteristic pattern of tumour growth; a proliferating rim and necrotic core.

Of particular relevance to this thesis is the study of Lemon *et al.* [90] in which tissue growth within a tissue engineering scaffold is described using a porous flow mixture theory model. The growing cell population is represented by a viscous fluid as in [96] but additionally accommodates cell-cell interactions via the specification of extra pressure, an approach first introduced by Breward *et al.* [29]. Later, in [88], this model is used to investigate the effect of the choice of scaffold seeding on growth and the effect of nutrient depletion, in order to suggest how cell distribution at large time could be improved. Equation level detail can be found in section 3.

Within mixture theory one method of simplifying the model setup is to suppose that the interphase drag is large, resulting in all the phases being subject to the same velocity. This is known as the constrained mixture assumption [15] as used in [151] and is utilised in chapter 4.

Multiscale asymptotics

Early work in this area was carried out in the 1970s by Babuska [19], Larsen [86, 87], Sanchez-Palencia [133, 134] and Keller, whose work includes deriving Darcy's law [82] and the equations of linear poroelasticity (Burridge and Keller [34]) from the Navier-Stokes equations and the linearised equations of elasticity. Formal approaches and convergence proofs, which are not discussed here, can be found in [22].

First, assumptions are made on the spatial periodicity of the problem; that it is, or can be approximated as, periodic. The periodic unit is known as the unit cell, and variables are assumed to be periodic in the microscale variable. A choice of scalings must then be made, choosing the timescale of interest and dependence on micro and macro length scales. This is of fundamental importance as alternative choices lead to different macroscale equations [52]. Variables and derivatives are then expanded and by equating the coefficients at each order, a number of subproblems are then created. Using an average

defined over the unit cell, periodicity and by solving local cell problems, macroscale equations can be derived.

Over the past decade, homogenisation by multiscale asymptotics has been used in a number of biological models [92, 98, 115, 126, 140, 141]. In [139, 140] homogenization is used to develop a multiscale model that describes fluid and drug transport in a vascularised tumour. At the microscale, characterised by the inter-capillary distance, the tumour consists of distinct vascular and interstitial phases, that are assumed to be periodic. A multiple scales analysis is then used obtain the effective transport equations on the tumour scale; this consists of Darcy flow for the fluid and advection-reaction equations for the drug. The transport coefficients, occurring in the effective equations, are determined by solving problems on the unit cell, imparting explicit dependence on the microscale geometry of the vasculature to the macroscale description.

Another macroscale model is derived in [141], describing the effective flow and transport properties of a printed tissue engineering scaffold. The flow and transport are affected by the choice of scaffold microstructure, so using the macroscale description the scaffold design can be optimised by considering the model predictions on nutrient and waste product distribution. Cells are present, and remain, within the hydrogel scaffold, taking up nutrients and releasing waste products. For simplicity, the cells are assumed to remain at a constant cell density within the scaffold.

More recently, these techniques have begun to be employed in the context of growing materials. O'Dea *et al.* [115] develop a simple model of tissue growth within a porous scaffold, represented by nutrient-limited microscale accretion of a rigid solid structure. A macroscale description of growth and transport was obtained using the multiple-scales technique, with effective permeability determined by a cell problem and hence accommodating explicit dependence on microscale dynamics and structure. In this work, scalings are chosen such growth is slow and the microscale domains are therefore quasi-static. A significant advantage of this assumption is that

the Stokes flow problem on the periodic cell, from which the effective permeability is determined, only requires solving once. Despite this, growth does appear in the macroscopic equation for pressure, as well as in the nutrient equation through uptake due to growth. The appearance of microscale growth in the macroscale description is of a similar structure to the equation for macroscale pressure in [140], where a contribution from microscale continuity of mass flux on capillary wall, also not at leading order, is present.

Many soft biological tissues behave as complex non-linear elastic materials motivating modelling approaches such as that in [126]. Following a similar analysis to [115] they described accretion in a poroelastic setting. Here the tissue is modelled as a porous linear elastic solid saturated with a slow flowing viscous fluid, and growth occurs at the interface between the solid and fluid through mass exchange at a prescribed rate. Via a two-scale asymptotic expansion a new poroelastic model for macroscale fluid flow, fluid pressure and solid displacement is derived. This is accompanied by problems to be solved on a representative cell to determine the relative fluid-solid velocity, microscale pressure and displacement of the solid compartment. Additionally, the evolution of the microstructure, governed by a level set equation, must be updated as mass exchange on the fluid-solid boundary occurs.

To permit analysis, the authors of [115, 126] (and other similar studies) exploit asymptotic restrictions on the underlying model, considering slow (quasi-static) growth and linearised deformation. In Collis *et al.* [44], such assumptions are relaxed to consider a macroscale representation of finite volumetric nutrient-limited growth of a hyperelastic solid, employing the Arbitrary-Lagrangian-Eulerian approach [31] to ameliorate the challenges involved in applying two-scale asymptotics to such a system.

As noted in chapter 1, the underlying description of growth, and tissue dynamics in these models [44, 115, 126] is highly idealised, being restricted to accretion [115, 126] or simple volumetric growth of a solid

body [44]. We seek, therefore, to extend these studies to allow a more complex representation of tissue growth, in particular volumetric growth and active cell motion, whilst retaining the simplicity provided by quasi-static assumptions.

2.4.5 *Summary of mathematical methods*

Discrete sub-cellular and cell level models allow a high level of detail, such as individual cells' shape and volume, allowing the incorporation of many biological features. However, as the number of cells included increases, so does the computational cost causing continuous models to become preferable. This is despite the reduced detail since many cellular processes are not amenable to a continuous formulation in a straightforward way [144]. Complex continuous models can themselves be simplified via upscaling techniques, such as volume averaging and multiscale asymptotics, where there are well-separated scales. This process, used in recent work on models of tissue growth and dynamics, removes unnecessary detail and results in 'effective' descriptions.

2.5 SUMMARY

In this chapter we have provided an overview of the biology related to tissues and their growth, along with a summary of research in this area, with a particular focus on tissue engineering. Different mathematical methods, used to describe and model the complex behaviour of biological tissues, were then discussed along with the advantages and disadvantages of the alternative approaches.

In the next chapter, we set up our model for tissue growth on a porous scaffold, using the multiphase mixture description of Lemon *et al.* [90] for

the tissue. This is in preparation for the multiscale asymptotic analysis that follows.

3

MULTIPHASE TISSUE MODEL

3.1 INTRODUCTION

In this chapter we describe in some detail the multiphase model of Lemon *et al.* [90] which we will utilise in the following chapters, in a tissue engineering context. Multiphase models have been popularly used to describe tissues [46, 72, 90, 117, 124], and are able to accommodate cell-cell interactions via the specification of extra pressure, as first introduced by Breward *et al.* [29]. Allowing cells to move in response to their local volume fraction gives a more realistic description of tissue dynamics and growth than the simplistic solid tissue undergoing accretion of [115].

In contrast to Lemon *et al.* [90], where the mixture model is used as a scaffold-scale description, with the scaffold represented as another phase, here we assemble a model on the pore scale, i.e. the scale of the holes and gaps within the scaffold. We consider a rigid scaffold, on the surface of which the multiphase tissue, comprising cells and extracellular fluid, grows. A culture medium, containing nutrients for the cells, surrounds the tissue, filling the remaining interstitial space. See figure 9 for a 2D schematic at the pore scale. By looking at a smaller scale we can include additional information, such as the microscale geometry of the scaffold, which may have an impact on macroscale behaviour.

Here we describe the three components: scaffold, tissue and culture medium, as well as the nutrient concentration. Suitable boundary

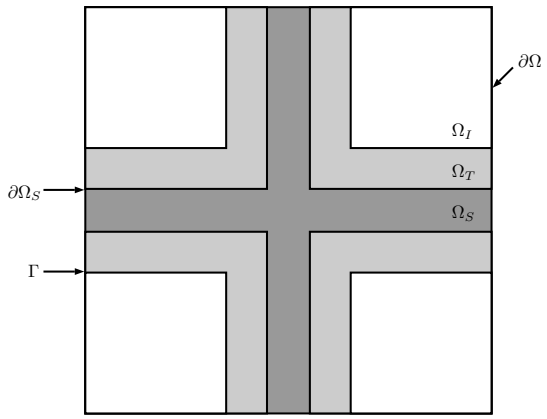
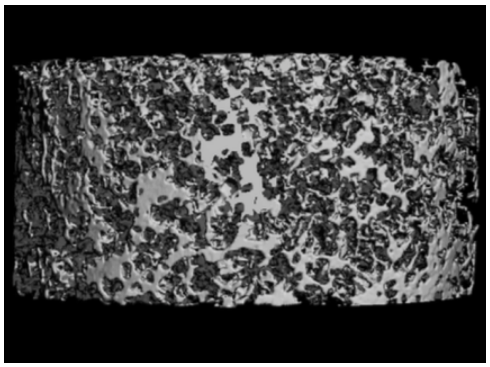


Figure 9: 2D representation of the periodic cell Ω, boundary $\partial\Omega$, showing the scaffold domain Ω_S, tissue domain Ω_T and interstitial domain Ω_I. The scaffold-tissue boundary is denoted $\partial\Omega_S$, and tissue-interstitium boundary by Γ.

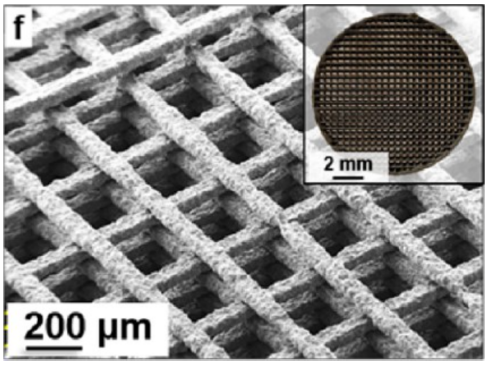
conditions are discussed for the tissue-scaffold and tissue-interstitium interfaces. The equations are then nondimensionalised, in preparation for the analysis of the following chapters.

3.2 THE SCAFFOLD

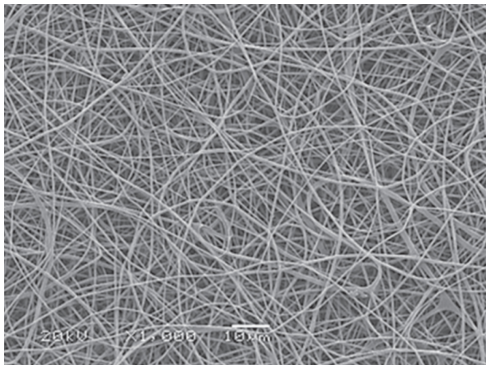
Scaffolds for tissue engineering have been created from a range of materials, from polymers [153] to graphene [79], using a number of methods that reflect the different requirements for successfully producing tissues for diverse purposes. In [18], a poly(L-lactide) (PLLA) scaffold is used specifically for growing bone tissue. This has a swiss cheese like form (see figure 10a) with a highly interconnected, irregular structure. Other scaffolds have been created using a technique known as electrospinning [23, 105], where nanoscale fibres are created by the application of a strong electric field to a polymer solution or melt. More structured scaffolds have been achieved using 3D printing which allows a great deal of control over the size of the lattice and the overall shape. Figure 10b shows an example of what can be created.



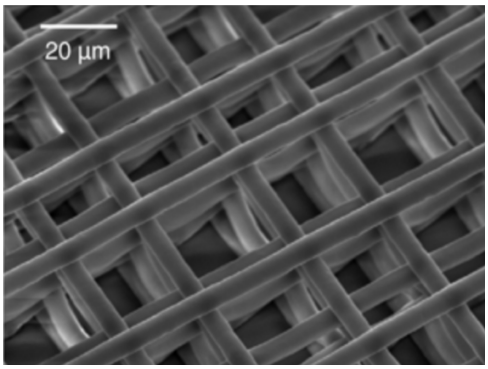
(a) A PLLA scaffold. 9 mm (diameter), 4 mm (height) [18]



(b) A high content graphene scaffold produced using 3D printing. [79]



(c) An electrospun PET scaffold. [105]



(d) A polymeric scaffold produced using electrohydrodynamic hot jet plotting. [153]

Figure 10: Various scaffolds

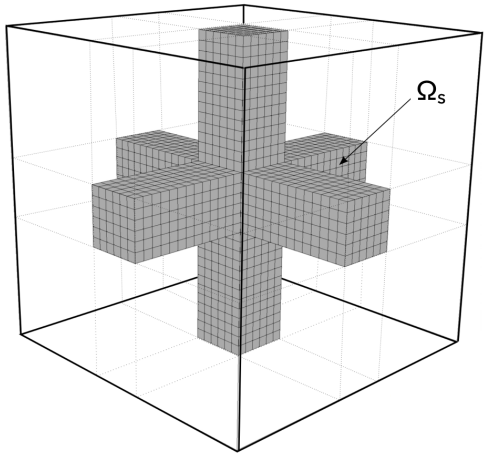


Figure 11: Periodic cell showing the scaffold domain, Ω_s

As discussed in the previous chapter the two major assumptions required for the use of multiscale homogenisation methods are that of a periodic microstructure and well-separated length scales. For this reason we choose to consider the growth of tissue on a scaffold, with a periodic lattice structure as shown in figure 11. Note that the analysis of the following chapters is not restricted to such a choice of scaffold, any structure which is locally-periodic is acceptable. We consider two length scales, the characteristic macroscale length scale (L) taken to be that of the scaffold, typically 4–10mm, and that of the microscale to be the pore size (characteristic length l). The pore size can be controlled by the settings used in the creation of the scaffold, with values in the range 20–200μm (see figure 10). We consider the two scales to be sufficiently well separated if the smaller pore size is chosen.

We model the scaffold as a rigid solid, occupying a fixed domain, Ω_s, and taken to be stationary, $v_s = \mathbf{0}$. The material used to produce the scaffold is often degradable. Over time it breaks down whilst being replaced by extracellular material such as collagen and proteoglycans laid down by the cells [85]. Although other models such as [116] include the interplay between tissue growth and scaffold degradation; for simplicity, we choose

to consider a non-degradable scaffold, or one which does not start to break down on the timescale under investigation.

3.3 THE TISSUE

Cells are seeded onto porous scaffolds, such as our lattice structure described in section 3.2, by a variety of methods [33]. These include:

- static seeding, where cells are injected into or onto the scaffold,
- dynamic seeding, where cells are shaken/spun/stirred throughout the scaffold,
- inclusion within the material used for creating the scaffold.

Static seeding results in the initial cell distribution being concentrated at the point of injection. Recalling that the focus of this thesis is the derivation of an effective macroscale description via asymptotic homogenisation, such a seeding is inconsistent with the requirement for periodicity. The work here is therefore more suited to dynamic seeding and inclusion in the scaffold manufacture, as these provide a better distribution of cells, more suited to our analysis. We suppose that we have an idealised set up where the scaffold structure under consideration is coated with a layer of tissue, Ω_T, as shown in figure 9.

The tissue domain comprises a two phase mixture, of cells and water, of volume fractions θ_n and θ_w respectively. Multiphase mixtures, where each component is treated as a continuum that occupies the same region of space [146], (a description obtained, for example, via a volume averaging process [55]) are popularly used for describing tissues, see [46, 72, 90, 117, 124] for some examples. In particular, note that the tissue description used here is an adaptation of the model of Lemon *et al.* [90].

As first proposed in [96], we model both phases as viscous fluids described by the Stokes equations. Studies of embryonic tissues [58] have

shown that their properties can be explained by considering them to be fluids. In this study, where spherical cell aggregates are mechanically compressed and their viscoelastic response measured, it is shown that the tissue behaves as an elastic material on short timescales but as a viscous fluid on longer timescales. Properties of other tissues, such as liver [93], connective [56] and muscle [63], as well as cellular components like cytoskeletal polymers [80], are also observed to be viscoelastic during stress relaxation experiments, with viscosity arising from cytoskeletal resistance to cell motion [90]. In addition to providing a good description for the observed biological behaviour, unlike solid tissue models such as [115], fluid models allow a convenient description of cell motion. Stokes equations are used in [36, 72] for example, where it is noted that the motion of cells and of intercellular fluid is very slow so inertial terms can be neglected when compared to the stress terms. We could alternatively begin with the Navier-Stokes equations but we later find, in the multiscale analysis, that the inertial terms are much smaller and so following [46] we ignore them from the start. The momentum equations for each phase are therefore given by

$$\boldsymbol{\nabla} \cdot (\theta_n \boldsymbol{\sigma}_n) + f_{nw} = 0 \text{ and } \boldsymbol{\nabla} \cdot (\theta_w \boldsymbol{\sigma}_w) + f_{wn} = 0 \tag{3.3.1}$$

where the phase stress tensor and interphase forces are given by

$$\boldsymbol{\sigma}_i = -p_i \boldsymbol{I} + \mu_i \left(\boldsymbol{\nabla} \boldsymbol{v}_i + \boldsymbol{\nabla} \boldsymbol{v}_i^{\mathsf{T}} - \frac{2}{3} (\boldsymbol{\nabla} \cdot \boldsymbol{v}_i) \boldsymbol{I} \right) \tag{3.3.2}$$

$$f_{nw} = p \boldsymbol{\nabla} \theta_n + \beta_{nw} \theta_n \theta_w (\boldsymbol{v}_w - \boldsymbol{v}_n), \tag{3.3.3}$$

$$f_{wn} = p \boldsymbol{\nabla} \theta_w + \beta_{wn} \theta_w \theta_n (\boldsymbol{v}_n - \boldsymbol{v}_w). \tag{3.3.4}$$

for $i = n, w$, and where the phase pressures, viscosities, velocities, and interphase viscous drag coefficient are denoted by p_i, μ_i, $\boldsymbol{v}_i$ and β_{ij} respectively. Note that we have expressed the bulk viscosity coefficient in terms of the shear viscosity coefficient, i.e. $\lambda_i = -\frac{2}{3}\mu_i$. (Stokes introduced the hypothesis that $\lambda + \frac{2}{3}\mu = 0$ [143], and with the exception of extremely

high temperatures or pressures there is no experimental evidence that it does not hold [24, 61].) The pressure for each phase is given by

$$p_w = p, \text{ and } p_n = p + \phi_n, \tag{3.3.5}$$

where p is the common mixture pressure and ϕ_n is the extra pressure due to the natural tendency of cells to aggregate. We assume that the w-phase experiences no intraphase pressure. The cell aggregation term can be modelled at its simplest by a constant but in [29, 37] it has been defined to be

$$\phi_n = n\left(-\nu + \frac{\kappa\theta_n^a}{(1-\theta_n)^a}\right), \tag{3.3.6}$$

where the parameter ν is a measure of aggregation and κ is the tendency to repel at close range, $\kappa > 0$. a is some constant greater than zero, which for simplicity we set $a = 1$ as used in [90]. From figure 12, one can see that at low volume fractions the cells tendency to aggregate dominates. Then there is an optimum non-zero cell volume fraction at which the tendency to aggregate is balanced by repulsion at close range (as long as $\nu > 0$). As the cell volume fraction tends to 1, the pressure asymptotes to infinity because the cells become too tightly packed and repel each other.

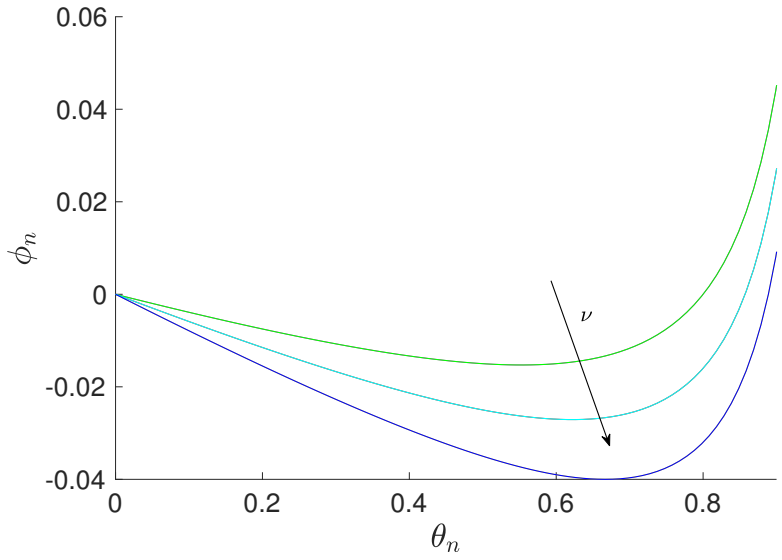


Figure 12: Extra pressure (due to cell aggregation) as a function of cell volume fraction θ_n. Arrow shows direction of increasing tendency of cells to aggregate.

We simplify the setup further by setting the interphase drag coefficients to be equal, $\beta_{nw} = \beta_{wn} = \beta$ and satisfy Newton's third law by setting the interphase forces f_{ij} to be equal and opposite. Using this information the momentum equations for the two phases are:

$$\theta_n \boldsymbol{\nabla} p_w + \boldsymbol{\nabla}(\theta_n \phi_n) + \beta \theta_n \theta_w (\boldsymbol{v}_n - \boldsymbol{v}_w) - \boldsymbol{\nabla} \cdot \left(\mu_n \theta_n \left(\boldsymbol{\nabla} \boldsymbol{v}_n + \boldsymbol{\nabla} \boldsymbol{v}_n^{\mathsf{T}} - \frac{2}{3} (\boldsymbol{\nabla} \cdot \boldsymbol{v}_n) \boldsymbol{I} \right) \right) = \mathbf{0}, \quad (3.3.7)$$

$$\theta_w \boldsymbol{\nabla} p_w + \beta \theta_n \theta_w (\boldsymbol{v}_w - \boldsymbol{v}_n) - \boldsymbol{\nabla} \cdot \left(\mu_w \theta_w \left(\boldsymbol{\nabla} \boldsymbol{v}_w + \boldsymbol{\nabla} \boldsymbol{v}_w^{\mathsf{T}} - \frac{2}{3} (\boldsymbol{\nabla} \cdot \boldsymbol{v}_w) \boldsymbol{I} \right) \right) = \mathbf{0}. \quad (3.3.8)$$

The evolution of volume fraction for each phase, θ_n and θ_w, is described by

$$\rho_n \left(\frac{\partial \theta_n}{\partial t} + \boldsymbol{\nabla} \cdot (\theta_n \boldsymbol{v}_n) \right) = S_n, \quad (3.3.9)$$

$$\rho_w \left(\frac{\partial \theta_w}{\partial t} + \boldsymbol{\nabla} \cdot (\theta_w \boldsymbol{v}_w) \right) = S_w, \quad (3.3.10)$$

where ρ_n and ρ_w denote the phase densities and S_n and S_w are mass transfer between phases due to growth or death. To model tissue growth, given the chain of events that form the cell cycle (see 2.2.3), we suppose that water is taken up by cells to increase their size and that given sufficient concentration of a generic nutrient, the cells divide at rate k_m. As cells die at rate k_n, due to natural apoptosis or lack of nutrient, for simplicity we take the only product of cell death to be water. Therefore, the processes of tissue growth and atrophy are represented by mass transfer between the two phases, as some function of phase volume fractions, θ_i and nutrient concentration, c, for example

$$S_n = \rho_w k_m(c) \theta_n (1 - \theta_n) - \rho_n k_n(c) \theta_n, \quad (3.3.11)$$

$$S_w = -\rho_w k_m(c) \theta_n (1 - \theta_n) + \rho_n k_n(c) \theta_n, \quad (3.3.12)$$

where $k_m(c)$ and $k_n(c)$ are increasing and decreasing functions respectively (see, for example, [88, 151]). For the sake of generality in our model, we retain different water and cell densities in our calculations although many authors, including [72, 90], set them to be equal. They justify this by arguing that although cell density varies with type and during different processes [32, 69], as cells consist largely of water, approximately 80% [14], it is reasonable to take $\rho_n = \rho_w$.

As the two phases make up the entire tissue domain, they fulfil the no voids condition, i.e. the two volume fractions sum to one,

$$\theta_n + \theta_w = 1. \tag{3.3.13}$$

Combining (3.3.9), (3.3.10) and (3.3.13) we have

$$\boldsymbol{\nabla} \cdot (\theta_n \boldsymbol{v}_n + \theta_w \boldsymbol{v}_w) = \frac{1}{\rho_n} S_n + \frac{1}{\rho_w} S_w. \tag{3.3.14}$$

(If $\rho_n = \rho_w$, and $S_n = -S_w$, equation 3.3.14 implies that the cell/water mixture is incompressible. This is a reasonable assumption given that cells are composed mainly of water and contain a cytoskeleton which helps maintain shape and resists compression.)

3.4 THE INTERSTITIUM

The interstitial space, Ω_I, (see figure 9) is filled entirely with water, so here our equations are given by

$$\theta_w = 1, \tag{3.4.1}$$

$$\boldsymbol{\nabla} \cdot \boldsymbol{v}_I = 0, \tag{3.4.2}$$

$$\boldsymbol{\nabla} p_I - \boldsymbol{\nabla} \cdot \left(\mu_w \left(\boldsymbol{\nabla} \boldsymbol{v}_I + \boldsymbol{\nabla} \boldsymbol{v}_I^{\mathsf{T}} \right) \right) = \mathbf{0}. \tag{3.4.3}$$

This represents the culture medium which surrounds the tissue construct in an engineering context. The purpose of this is to supply the cells with their requirements for growth, such as oxygen and glucose, and remove waste products. The culture medium may be static but if a perfusion bioreactor is used then it is forced through the seeded scaffold at a prescribed flow rate.

3.5 NUTRIENT

The culture medium, which can be perfused through the scaffold, supplies the tissue with the essentials for growth. Hence, we include in our model the presence of some generic dissolved nutrient, of concentration c. In the interstitial domain the nutrient is advected by the flow and diffuses, with diffusivity D_I, as described by

$$\frac{\partial c_I}{\partial t} + \boldsymbol{\nabla} \cdot (c_I \boldsymbol{v}_I) = \boldsymbol{\nabla} \cdot (D_I \boldsymbol{\nabla} c_I) \,. \tag{3.5.1}$$

In the tissue domain, following [88], we assume that the concentration of nutrient in the cell and water phases is equal, due to permeablity of cell membranes leading to equilibrium of the mixture being rapidly achieved on the microscale. Summing the nutrient transport equation for each phase results in

$$\frac{\partial c_T}{\partial t} + \boldsymbol{\nabla} \cdot (c_T \left(\theta_n \boldsymbol{v}_n + \theta_w \boldsymbol{v}_w\right)) = \boldsymbol{\nabla} \cdot (D_T \boldsymbol{\nabla} c_T) - \Lambda, \tag{3.5.2}$$

where the nutrient is advected by the composite mixture velocity and the additional term, Λ, describes uptake by cells during growth. In general, diffusivity D_T varies with the volume fraction of cells, and hence $D_T(\theta_n)$.

In this kind of problem, the typical diffusion timescale of minutes is much shorter than the days for tissue growth, [35], so the transport of nutrient is diffusion-dominated and advection is usually neglected [28, 72]. Here, for generality, and as macroscale advection may be enforced in a perfusion bioreactor, we retain the entire transport description.

The nutrient uptake term can be made up of two parts, the consumption of nutrient by mitotic and non-mitotic processes, as in, for example, [151], although later in [151] the contribution from non-mitotic processes is neglected based on experimental data. At this stage, for the sake of simplicity and generality we simply assume that uptake is a function of cell volume fraction and nutrient concentration.

Nutrient sources, such as that delivered to the tissue via a perfusion bioreactor, are represented by specifying suitable boundary conditions

on the macroscale. Boundary conditions appropriate for the microscale description (3.5.1–3.5.2) are considered in the following subsection.

3.6 BOUNDARY CONDITIONS

We now consider the appropriate boundary conditions for the scaffold-tissue and tissue-interstitium interfaces.

3.6.1 *Scaffold-tissue boundary, $\partial\Omega_s$*

In [90] cells are modelled as having an affinity for the scaffold described by a function of similar form to ϕ_n, the cell-cell attraction, because the scaffold is modelled as a component of a multiphase mixture along with the cells and water. In our model, where in the periodic cell the scaffold is in a separate domain to cell-water mixture, the interaction between cells and the scaffold is described by boundary conditions specified on the scaffold-tissue boundary $\partial\Omega_s$.

The simplest option, and consistent with the fluid model of the cell phase, is that of no slip;

$$\boldsymbol{v}_n \cdot \boldsymbol{t} = 0, \quad \boldsymbol{v}_w \cdot \boldsymbol{t} = 0, \tag{3.6.1}$$

which we use in chapter 4 and 5; however, more complicated scenarios can easily be accommodated. For example cells crawling along the scaffold surface due to the presence of other cells, the presence of a chemoattractant, or local pressure gradients in the surrounding mixture can be represented by a slip condition. Choices of boundary condition include the slip condition

$$\boldsymbol{v}_n = b\frac{\partial \boldsymbol{v}}{\partial n}, \tag{3.6.2}$$

where b is a constant of proportionality and $\partial/\partial n$ denotes the normal derivative, or free slip, given by

$$\frac{\partial \boldsymbol{v}_n}{\partial n} = 0. \tag{3.6.3}$$

These alternative boundary conditions are considered in section 5.4.3.

Finally we specify

$$\boldsymbol{v}_n \cdot \boldsymbol{n} = 0, \quad \boldsymbol{v}_w \cdot \boldsymbol{n} = 0, \tag{3.6.4}$$

$$(-D_T \boldsymbol{\nabla} c_T) \cdot \boldsymbol{n} = 0, \tag{3.6.5}$$

on $\partial\Omega_s$ as material and nutrient can not enter the rigid scaffold.

3.6.2 *Tissue-interstitium boundary,* Γ

On the tissue-interstitium interface, Γ, which exists along the surface where cells are present on one side but absent on the other, we apply a number of boundary conditions. We allow a flux of water (w-phase) across the boundary but restrict the cells to staying in Ω_T. We therefore impose the condition that the cells (n-phase) on the boundary must move with the same velocity as the boundary in order for it to be well defined. The position of the boundary is described by

$$\frac{\partial F}{\partial t} + \boldsymbol{\nabla} F \cdot \boldsymbol{v}_\Gamma = 0 \tag{3.6.6}$$

where $\boldsymbol{v}_\Gamma$ is its velocity and the level set equation $F(\boldsymbol{x}, t) = 0$ describes the position of moving interface. The mass flux conditions are given by

$$\rho_n \theta_n \left(\boldsymbol{v}_n - \boldsymbol{v}_\Gamma\right) \cdot \boldsymbol{n} = 0, \tag{3.6.7}$$

$$\rho_w \theta_w \left(\boldsymbol{v}_w - \boldsymbol{v}_\Gamma\right) \cdot \boldsymbol{n} = \rho_w \left(\boldsymbol{v}_I - \boldsymbol{v}_\Gamma\right) \cdot \boldsymbol{n}, \tag{3.6.8}$$

and we also impose continuity of tangential velocity,

$$\left(\theta_n \boldsymbol{v}_n + \theta_w \boldsymbol{v}_w\right) \cdot \boldsymbol{t} = \boldsymbol{v}_I \cdot \boldsymbol{t}. \tag{3.6.9}$$

Continuity of stress on the boundary is given by [104] as

$$\left(\boldsymbol{\sigma}_T - \rho_w \theta_w \boldsymbol{v}_w \left(\boldsymbol{v}_w - \boldsymbol{v}_\Gamma\right)\right) \cdot \boldsymbol{n} = \left(\boldsymbol{\sigma}_I - \rho_w \boldsymbol{v}_I \left(\boldsymbol{v}_I - \boldsymbol{v}_\Gamma\right)\right) \cdot \boldsymbol{n}. \tag{3.6.10}$$

where the weighted mixture stress $\boldsymbol{\sigma}_T$ is given by $\theta_n \boldsymbol{\sigma}_n + \theta_w \boldsymbol{\sigma}_w$. After the rescaling for the multiscale analysis of chapters 4 and 5, the contributions

to stress from the product of mass flux and phase velocity are very small and so are ignored along with inertial terms. We therefore reduce (3.6.10) to

$$\boldsymbol{\sigma}_T \cdot \boldsymbol{n} = \boldsymbol{\sigma}_I \cdot \boldsymbol{n}. \tag{3.6.11}$$

Finally, continuity of flux of nutrient concentration requires

$$c_T \left(\theta_n \boldsymbol{v}_n + \theta_w \boldsymbol{v}_w - \boldsymbol{v}_\Gamma\right) \cdot \boldsymbol{n} - D_T \boldsymbol{\nabla} c_T \cdot \boldsymbol{n} = c_I \left(\boldsymbol{v}_I - \boldsymbol{v}_\Gamma\right) \cdot \boldsymbol{n} - D_I \boldsymbol{\nabla} c_I \cdot \boldsymbol{n}. \tag{3.6.12}$$

As the descriptions of nutrient concentration (3.5.1) and (3.5.2) are second order differential equations, we are required to specify a further condition on c. Some common choices [139] are:

- continuity of concentration, $c_T = c_I$,
- a concentration jump proportional to the nutrient flux, $r\left(c_T - c_I\right) =$ nutrient flux, for some constant r,
- a concentration jump as a consequence of species solubility, $c_T = \alpha c_I$, for some constant α.

For simplicity we choose continuity of concentration in the model of chapter 4, but we do investigate the effect of the alternatives on the model of chapter 5 in section 5.4.4.

3.7 INITIAL CONDITIONS

The model additionally requires appropriate initial conditions (and later, boundary conditions on the macroscale boundaries) but these are not specified here. In the numerical experiments of chapter 7 section 7.6.4 these are specified in order to obtain solutions to the macroscale problem.

3.8 NONDIMENSIONALISATION

We non-dimensionalise our model equations by using the following scalings:

$$\begin{aligned} &\boldsymbol{x} = l\hat{\boldsymbol{x}}, \quad \boldsymbol{v} = V\hat{\boldsymbol{v}}, \quad c = C\hat{c}, \quad p = \frac{\mu_n V}{l}\hat{p}, \quad t = \frac{l}{V}\hat{t}, \\ &S_i = \frac{\rho_n V}{l}\hat{S}_i, \quad \beta = \frac{\mu_n}{l^2}\hat{\beta}, \quad \mu = \frac{\mu_w}{\mu_n}, \quad \frac{D_I}{Vl} = \frac{1}{Pe_I}, \quad \frac{D_T^*}{Vl} = \frac{1}{Pe_T} \\ &\Lambda = \frac{V}{l}\hat{\Lambda}, \quad \bar{\rho} = \frac{\rho_n}{\rho_w}. \end{aligned} \tag{3.8.1}$$

in which circumflexes denote dimensionless variables and l, V, and C are a characteristic microscale length, and macroscale velocity and nutrient concentration respectively. These characteristic quantities are to be determined by the specific application, depending, for example, on the imposed fluid pressure drop in the bioreactor and the choice of nutrient. In the interest of generality we do not specify them here. D_T^* is a reference diffusion in the tissue such that $D_T(\theta_n) = D_T^*\hat{D}(\theta_n)$. We have defined the Péclet numbers, Pe_T and Pe_I, as the dimensionless parameters representing the ratio of diffusive to advective timescales within Ω_T and Ω_I respectively. As we work exclusively in dimensionless variables in the following sections, we drop the circumflex notation for convenience.

The dimensionless equations are summarised below. In the tissue, Ω_T,

$$\frac{\partial \theta_n}{\partial t} + \boldsymbol{\nabla} \cdot (\theta_n \boldsymbol{v}_n) = S_n, \tag{3.8.2}$$

$$\frac{\partial \theta_w}{\partial t} + \boldsymbol{\nabla} \cdot (\theta_w \boldsymbol{v}_w) = \bar{\rho} S_w, \tag{3.8.3}$$

$$\theta_n + \theta_w = 1, \tag{3.8.4}$$

$$\boldsymbol{\nabla} \cdot (\theta_n \boldsymbol{v}_n + \theta_w \boldsymbol{v}_w) = S_n - \bar{\rho} S_w, \tag{3.8.5}$$

$$\begin{aligned} &\theta_n \boldsymbol{\nabla} p_w + \boldsymbol{\nabla}(\theta_n \phi_n) + \beta \theta_n \theta_w (\boldsymbol{v}_n - \boldsymbol{v}_w) \\ &\qquad - \boldsymbol{\nabla} \cdot \left(\theta_n \left(\boldsymbol{\nabla} \boldsymbol{v}_n + \boldsymbol{\nabla} \boldsymbol{v}_n^{\mathsf{T}} - \frac{2}{3} (\boldsymbol{\nabla} \cdot \boldsymbol{v}_n) \boldsymbol{I} \right) \right) = \boldsymbol{0}, \end{aligned} \tag{3.8.6}$$

$$\theta_w \boldsymbol{\nabla} p_w + \beta \theta_n \theta_w \left(\boldsymbol{v}_w - \boldsymbol{v}_n\right) - \boldsymbol{\nabla} \cdot \left(\mu \theta_w \left(\boldsymbol{\nabla} \boldsymbol{v}_w + \boldsymbol{\nabla} \boldsymbol{v}_w^{\mathsf{T}} - \frac{2}{3} \left(\boldsymbol{\nabla} \cdot \boldsymbol{v}_w\right) \boldsymbol{I}\right)\right) = \boldsymbol{0}, \quad (3.8.7)$$

$$\frac{\partial c_T}{\partial t} + \boldsymbol{\nabla} \cdot \left(c_T \left(\theta_n \boldsymbol{v}_n + \theta_w \boldsymbol{v}_w\right)\right) = \boldsymbol{\nabla} \cdot \left(\frac{D_T}{Pe_T} \boldsymbol{\nabla} c_T\right) - \Lambda. \quad (3.8.8)$$

In the interstitium, Ω_I,

$$\theta_w = 1, \quad (3.8.9)$$

$$\boldsymbol{\nabla} \cdot \boldsymbol{v}_I = 0, \quad (3.8.10)$$

$$\boldsymbol{\nabla} p_I - \boldsymbol{\nabla} \cdot \left(\mu \left(\boldsymbol{\nabla} \boldsymbol{v}_I + \boldsymbol{\nabla} \boldsymbol{v}_I^{\mathsf{T}}\right)\right) = \boldsymbol{0}, \quad (3.8.11)$$

$$\frac{\partial c_I}{\partial t} + \boldsymbol{\nabla} \cdot \left(c_I \boldsymbol{v}_I\right) = \boldsymbol{\nabla} \cdot \left(\frac{1}{Pe_I} \boldsymbol{\nabla} c_I\right). \quad (3.8.12)$$

On the scaffold-tissue boundary, $\partial\Omega_s$,

$$\boldsymbol{v}_n \cdot \boldsymbol{n} = 0, \quad \boldsymbol{v}_w \cdot \boldsymbol{n} = 0, \quad (3.8.13)$$

$$\boldsymbol{v}_n \cdot \boldsymbol{t} = 0, \quad \boldsymbol{v}_w \cdot \boldsymbol{t} = 0, \quad (3.8.14)$$

$$\boldsymbol{\nabla} c_T \cdot \boldsymbol{n} = 0. \quad (3.8.15)$$

On the tissue-interstitium boundary, Γ,

$$\frac{\partial F}{\partial t} + \boldsymbol{\nabla} F \cdot \boldsymbol{v}_\Gamma = 0, \quad (3.8.16)$$

$$\theta_n \left(\boldsymbol{v}_n - \boldsymbol{v}_\Gamma\right) \cdot \boldsymbol{n} = 0, \quad (3.8.17)$$

$$\theta_w \left(\boldsymbol{v}_w - \boldsymbol{v}_\Gamma\right) \cdot \boldsymbol{n} = \left(\boldsymbol{v}_I - \boldsymbol{v}_\Gamma\right) \cdot \boldsymbol{n}, \quad (3.8.18)$$

$$\left(\theta_n \boldsymbol{v}_n + \theta_w \boldsymbol{v}_w\right) \cdot \boldsymbol{t} = \boldsymbol{v}_I \cdot \boldsymbol{t}, \quad (3.8.19)$$

$$\boldsymbol{\sigma}_T \cdot \boldsymbol{n} = \boldsymbol{\sigma}_I \cdot \boldsymbol{n}, \quad (3.8.20)$$

$$c_T \left(\theta_n \boldsymbol{v}_n + \theta_w \boldsymbol{v}_w - \boldsymbol{v}_\Gamma\right) \cdot \boldsymbol{n} - \frac{D_T}{Pe_T} \boldsymbol{\nabla} c_T \cdot \boldsymbol{n} = c_I \left(\boldsymbol{v}_I - \boldsymbol{v}_\Gamma\right) \cdot \boldsymbol{n} - \frac{1}{Pe_I} \boldsymbol{\nabla} c_I \cdot \boldsymbol{n}, \quad (3.8.21)$$

$$c_I = c_T. \quad (3.8.22)$$

3.9 SUMMARY

We have described our model setup of tissue growing on scaffold with, for example, a periodic lattice structure, as can be manufactured by 3D

printing. We formulated the model equations for the three domains: the scaffold, the tissue and the interstitium. The scaffold is modelled as a rigid solid with periodic microstructure, on the surface of which the tissue grows. To describe the tissue we use an adaptation of the mixture model of Lemon *et al.* [90], which built on the work in [29, 36]. The tissue is composed of two phases, cells and water, both modelled as viscous fluids, with the cellular phase subject to intraphase pressure. This type of tissue model allows cells to move in response to their properties and local cell volume fraction, and accommodates volumetric growth, resulting in a more complex description than of [115] where the tissue is considered to be a solid undergoing accretion. The interstitium is entirely filled with culture medium, modelled by Stokes flow, which is used to deliver nutrients to the growing tissue. The nutrient is both advected by the fluid flow and diffuses, within the tissue and interstitial domain, and is taken up by cells to allow growth. Suitable boundary conditions are discussed for the scaffold-tissue and tissue-interstitium interfaces.

In the next chapter we will use the microscale model proposed here to derive an effective macroscale description for tissue growth on a scaffold, using multiscale homogenisation. A macroscale description obtained in this way is much simpler to use than applying the microscale model across the entire scaffold, but still allows dependence on the microscale dynamics and structure.

4

A MULTISCALE MODEL IN THE LARGE DRAG LIMIT

4.1 INTRODUCTION

In this chapter we derive an effective macroscale description of tissue growth from the microscale model proposed in the previous chapter. The tissue, a two phase mixture, growing on a rigid scaffold and surrounded by a fluid, is assumed to have a periodic microstructure, which enables the application of the multiscale homogenisation technique. Here, we make the assumption that the drag between the two phases which constitute the tissue is very large, and hence simplify the analysis that follows.

In section 4.2, we consider the limit of the model equations, described in chapter 3, in which the interphase drag is large and find that at leading order the two phases of the tissue have a common velocity. A two scale asymptotic analysis is carried out in section 4.3, resulting in an effective macroscale description and a coupled problem on the periodic cell. We discuss these results, and their limitations in section 4.4.

4.2 IN THE LARGE DRAG LIMIT

In order to simplify the multiphase tissue description (see chapter 3) we consider the limit in which the interphase drag is large, i.e. $\beta \gg 1$. This

leads us to take an expansion of the dependent variables of the following form:

$$\psi\left(\boldsymbol{x},t\right)=\psi^{(0)}\left(\boldsymbol{x},t\right)+\frac{1}{\sqrt{\beta}}\psi^{(1)}\left(\boldsymbol{x},t\right)+\frac{1}{\beta}\psi^{(2)}\left(\boldsymbol{x},t\right)+... \tag{4.2.1}$$

Note the expansion is in terms of $1/\sqrt{\beta}$, as opposed to $1/\beta$, as within a boundary layer of thickness $O(1/\sqrt{\beta})$ drag no longer dominates the other terms of the momentum equations for the tissue (3.8.6,3.8.7). For more information see Appendix A. At leading order, from equation (3.8.6), we find that

$$\boldsymbol{v}_n^{(0)}=\boldsymbol{v}_w^{(0)}, \tag{4.2.2}$$

so the two phases that make up the tissue have the same velocity, which we denote $\boldsymbol{u}_T^{(0)}$. Equations (3.8.2, 3.8.4, 3.8.5) become:

$$\frac{\partial\theta_n^{(0)}}{\partial t}+\boldsymbol{\nabla}\cdot\left(\theta_n^{(0)}\boldsymbol{u}_T^{(0)}\right)=S_n^{(0)}, \tag{4.2.3}$$

$$\theta_n^{(0)}+\theta_w^{(0)}=1, \tag{4.2.4}$$

$$\boldsymbol{\nabla}\cdot\boldsymbol{u}_T^{(0)}=S_n^{(0)}+\bar{\rho}S_w^{(0)}. \tag{4.2.5}$$

By setting $\mu=1$, i.e. assigning the two tissue phases the same viscosity, and combining (3.8.6) and (3.8.7) with (4.2.2) we obtain

$$-\boldsymbol{\nabla}p_T^{(0)}+\nabla^2\boldsymbol{u}_T^{(0)}+\frac{1}{3}\boldsymbol{\nabla}\left(\boldsymbol{\nabla}\cdot\boldsymbol{u}_T^{(0)}\right)=0, \tag{4.2.6}$$

where $p_T^{(0)}$ is a lumped pressure field defined by $p_T^{(0)}=p_w^{(0)}+\theta_n^{(0)}\phi_n^{(0)}$. Taking the divergence of (4.2.6) and substituting from (4.2.5) gives

$$\nabla^2p_T^{(0)}=\frac{4}{3}\nabla^2\left(S_n^{(0)}+\bar{\rho}S_w^{(0)}\right), \tag{4.2.7}$$

and substituting from (4.2.5) into (4.2.6), and rearranging provides

$$\nabla^2\boldsymbol{u}_T^{(0)}=\boldsymbol{\nabla}p_T^{(0)}-\frac{1}{3}\boldsymbol{\nabla}\left(S_n^{(0)}+\bar{\rho}S_w^{(0)}\right). \tag{4.2.8}$$

The nutrient transport equation for the tissue domain becomes

$$\frac{\partial c_T^{(0)}}{\partial t}+\boldsymbol{\nabla}\cdot\left(c_T^{(0)}\boldsymbol{u}_T^{(0)}\right)=\boldsymbol{\nabla}\cdot\left(\frac{D_T^{(0)}}{Pe_T}\boldsymbol{\nabla}c_T^{(0)}\right)-\Lambda^{(0)}. \tag{4.2.9}$$

The equations valid in the interstitial domain, Ω_I, along with (3.8.15,3.8.16,3.8.20,3.8.22) remain unchanged, whilst the other boundary conditions simplify as below. On the scaffold-tissue boundary, $\partial\Omega_S$,

$$\boldsymbol{u}_T^{(0)} \cdot \boldsymbol{n} = 0, \quad \boldsymbol{u}_T^{(0)} \cdot \boldsymbol{t} = 0. \tag{4.2.10}$$

On the tissue-interstitium boundary, Γ,

$$\theta_n^{(0)} \left(\boldsymbol{u}_T^{(0)} - \boldsymbol{v}_\Gamma^{(0)} \right) \cdot \boldsymbol{n} = 0, \tag{4.2.11}$$

$$\theta_w^{(0)} \left(\boldsymbol{u}_T^{(0)} - \boldsymbol{v}_\Gamma^{(0)} \right) \cdot \boldsymbol{n} = \left(\boldsymbol{v}_I^{(0)} - \boldsymbol{v}_\Gamma^{(0)} \right) \cdot \boldsymbol{n}, \tag{4.2.12}$$

$$\boldsymbol{u}_T^{(0)} \cdot \boldsymbol{t} = \boldsymbol{v}_I^{(0)} \cdot \boldsymbol{t}, \tag{4.2.13}$$

$$c_T^{(0)} \left(\boldsymbol{u}_T^{(0)} - \boldsymbol{v}_\Gamma^{(0)} \right) \cdot \boldsymbol{n} - \frac{D_T}{Pe_T} \boldsymbol{\nabla} c_T^{(0)} \cdot \boldsymbol{n} = c_I^{(0)} \left(\boldsymbol{v}_I^{(0)} - \boldsymbol{v}_\Gamma^{(0)} \right) \cdot \boldsymbol{n} - \frac{1}{Pe_I} \boldsymbol{\nabla} c_I^{(0)} \cdot \boldsymbol{n}. \tag{4.2.14}$$

As a consequence of taking the large drag limit, we find that at leading order on the tissue-interstitium boundary, Γ, equations (4.2.11) and (4.2.12) give that

$$\boldsymbol{u}_T^{(0)} \cdot \boldsymbol{n} = \boldsymbol{v}_\Gamma^{(0)} \cdot \boldsymbol{n} = \boldsymbol{v}_I^{(0)} \cdot \boldsymbol{n}. \tag{4.2.15}$$

Hence, no material can cross Γ to supply the growth of the tissue via phase transfer. The tissue may grow:

- by phase transfer within the tissue until the water phase is exhausted
- by instantaneous mass creation within the tissue
- by phase transfer occurring on the boundary, i.e. a proportion of water on the Ω_I side of Γ transfers to cell phase, which is effectively accretion type behaviour [46, 115]. This does mean that cells on the boundary do not stay on the boundary, but are replaced by the newly created cells.

The inclusion of the last possibility requires modified boundary conditions, as the same cells do not remain on the boundary for all time. These are given, in dimensional form, by

$$\rho_n \theta_n \left(\boldsymbol{u}_T - \boldsymbol{v}_\Gamma\right) \cdot \boldsymbol{n} = M, \tag{4.2.16}$$

$$\rho_w \theta_w \left(\boldsymbol{u}_T - \boldsymbol{v}_\Gamma\right) \cdot \boldsymbol{n} - \rho_w \left(\boldsymbol{v}_I - \boldsymbol{v}_\Gamma\right) \cdot \boldsymbol{n} = -M, \tag{4.2.17}$$

where M is a surface production term and we have assumed that no mass is instantaneously created or destroyed at the boundary, only transferred from one phase to the other. If $M = 0$, we recover the previous boundary conditions. Alternatively, combining these two boundary conditions

$$\rho_T \left(\boldsymbol{u}_T - \boldsymbol{v}_\Gamma\right) \cdot \boldsymbol{n} = \rho_I \left(\boldsymbol{v}_I - \boldsymbol{v}_\Gamma\right) \cdot \boldsymbol{n} = G, \tag{4.2.18}$$

as used in [46], where G is termed the phase transition rate on Γ,

$$G = M \left(1 + \frac{\rho_w \theta_w}{\rho_n \theta_n}\right), \tag{4.2.19}$$

and

$$\rho_T = \theta_n \rho_n + \theta_w \rho_w, \tag{4.2.20}$$

is the mixture density.

Note that the above applies only in the large drag limit and at leading order. There exists a boundary layer, of thickness $O(1/\sqrt{\beta})$, where the large drag model breaks down and distinct phase velocities are permitted, allowing a flux of water into the tissue. As the boundary layer is very narrow this would appear to be some form of accretion type growth. See Appendix A for boundary layer analyses for this model.

In the analysis which follows, we use boundary condition (4.2.18) in its non-dimensional form

$$\bar{\rho}_T \left(\hat{\boldsymbol{u}}_T - \hat{\boldsymbol{v}}_\Gamma\right) \cdot \boldsymbol{n} = \left(\hat{\boldsymbol{v}}_I - \hat{\boldsymbol{v}}_\Gamma\right) \cdot \boldsymbol{n} = Q, \tag{4.2.21}$$

where

$$\bar{\rho}_T = \frac{\rho_T}{\rho_w}, \quad G = \rho_w Q, \tag{4.2.22}$$

and henceforth circumflexes are dropped. To remove the surface production of cells, one can set $Q = 0$.

4.3 MULTIPLE SCALES ANALYSIS

We now work with the model in the limit of large drag and so drop the associated superscripts for clarity. To derive a suitable macroscale description incorporating the previously described microscale growth, dynamics and structure, we follow [34, 46, 115, 126, 140] in using the method of multiple scales. This method of homogenisation has been used in the study of porous media such as damaged masonry structures [97] as well as in biological applications [115, 125, 126, 139], and works on the assumption that there is microscale periodicity and suitable separation between the length scales. These conditions have been satisfied by the careful model setup described in chapter 3.

4.3.1 *Rescaling*

First we rescale the model equations such that the timescale (that of macroscale advection) and pressure scaling under consideration results in the appropriate leading order problem:

$$t = \frac{1}{\varepsilon}\tilde{t}, \quad p = \frac{1}{\varepsilon}\tilde{p}, \tag{4.3.1}$$

in which tildes denote the rescaled variables. The small parameter $\varepsilon \ll 1$ is given by the ratio of micro (l) and macro (L) characteristic length scales, i.e. $\varepsilon = l/L$. This choice of time rescaling reduces the problem to a quasi-steady one at leading order, as growth, and hence changes to domains, is slower than macroscale advection, The pressure rescaling is required to obtain the proper leading order problem in the multiscale analysis. (Note that had we used Navier-Stokes equations to describe the fluid, we find that here, as a consequence of the rescaling, the additional terms are of $O(\varepsilon^2)$ and hence are not relevant in the analysis that follows.) We drop the tilde notation for convenience as we work exclusively with the rescaled variables in subsequent sections.

The rescaled equations are given by:

In Ω_T:

$$\varepsilon\frac{\partial\theta_n}{\partial t} + \boldsymbol{\nabla}\cdot(\theta_n\boldsymbol{u}_T) = S_n, \tag{4.3.2}$$

$$\boldsymbol{\nabla}\cdot\boldsymbol{u}_T = S_n + \bar{\rho}S_w, \tag{4.3.3}$$

$$\nabla^2 p_T = \frac{4}{3}\varepsilon\nabla^2\left(S_n + \bar{\rho}S_w\right), \tag{4.3.4}$$

$$\varepsilon\nabla^2\boldsymbol{u}_T = \boldsymbol{\nabla}p_T - \frac{1}{3}\varepsilon\boldsymbol{\nabla}\left(S_n + \bar{\rho}S_w\right), \tag{4.3.5}$$

$$\varepsilon\frac{\partial c_T}{\partial t} + \boldsymbol{\nabla}\cdot(c_T\boldsymbol{u}_T) = \boldsymbol{\nabla}\cdot\frac{D_T}{Pe_T}\boldsymbol{\nabla}c_T - \Lambda. \tag{4.3.6}$$

In Ω_I:

$$\boldsymbol{\nabla}\cdot\boldsymbol{v}_I = 0, \tag{4.3.7}$$

$$\boldsymbol{\nabla}p_I - \varepsilon\nabla^2\boldsymbol{v}_I = \mathbf{0}, \tag{4.3.8}$$

$$\varepsilon\frac{\partial c_I}{\partial t} + \boldsymbol{v}_I\cdot\boldsymbol{\nabla}c_I = \frac{1}{Pe_I}\nabla^2 c_I. \tag{4.3.9}$$

On the scaffold-tissue boundary, $\partial\Omega_S$,

$$\boldsymbol{u}_T\cdot\boldsymbol{n} = 0, \quad \boldsymbol{u}_T\cdot\boldsymbol{t} = 0, \quad \boldsymbol{\nabla}c_T\cdot\boldsymbol{n} = 0. \tag{4.3.10}$$

On the tissue-interstitium boundary, Γ,

$$\varepsilon\frac{\partial F}{\partial t} + \boldsymbol{\nabla}F\cdot\boldsymbol{v}_\Gamma = 0, \tag{4.3.11}$$

$$\bar{\rho}_T\left(\boldsymbol{u}_T - \boldsymbol{v}_\Gamma\right)\cdot\boldsymbol{n} = \left(\boldsymbol{v}_I - \boldsymbol{v}_\Gamma\right)\cdot\boldsymbol{n} = Q, \tag{4.3.12}$$

$$\boldsymbol{u}_T\cdot\boldsymbol{t} = \boldsymbol{v}_I\cdot\boldsymbol{t}, \tag{4.3.13}$$

$$\boldsymbol{\sigma}_T\cdot\boldsymbol{n} = \boldsymbol{\sigma}_I\cdot\boldsymbol{n}, \tag{4.3.14}$$

$$c_T\left(\boldsymbol{u}_T - \boldsymbol{v}_\Gamma\right)\cdot\boldsymbol{n} - \frac{D_T}{Pe_T}\boldsymbol{\nabla}c_T\cdot\boldsymbol{n} = c_I\left(\boldsymbol{v}_I - \boldsymbol{v}_\Gamma\right)\cdot\boldsymbol{n} - \frac{1}{Pe_I}\boldsymbol{\nabla}c_I\cdot\boldsymbol{n}, \tag{4.3.15}$$

$$c_I = c_T, \tag{4.3.16}$$

where

$$\boldsymbol{\sigma}_i = -p_i\mathbf{I} + \varepsilon\left(\boldsymbol{\nabla}\boldsymbol{u}_i + \boldsymbol{\nabla}\boldsymbol{u}_i^{\mathsf{T}} - \frac{2}{3}\left(\boldsymbol{\nabla}\boldsymbol{u}_i\right)\mathbf{I}\right). \tag{4.3.17}$$

Next we introduce a macroscale coordinate $\boldsymbol{X}$ where $\boldsymbol{X} = \varepsilon\boldsymbol{x}$ ($\boldsymbol{x}$ being the microscale coordinate). Since the two length scales are well-separated

we treat $\boldsymbol{x}$ and $\boldsymbol{X}$ as independent and expand dependent variables and differential operators in multiple-scales form as follows:

$$\psi\left(\boldsymbol{x}, \boldsymbol{X}, t; \varepsilon\right) = \psi^{(0)}\left(\boldsymbol{x}, \boldsymbol{X}, t\right) + \varepsilon\psi^{(1)}\left(\boldsymbol{x}, \boldsymbol{X}, t\right) + ... \tag{4.3.18}$$

$$\boldsymbol{\nabla} = \boldsymbol{\nabla}_{\boldsymbol{x}} + \varepsilon\boldsymbol{\nabla}_{\boldsymbol{X}}, \quad \nabla^2 = \nabla^2_{\boldsymbol{x}} + 2\varepsilon\boldsymbol{\nabla}_{\boldsymbol{x}} \cdot \boldsymbol{\nabla}_{\boldsymbol{X}} + \varepsilon^2\nabla^2_{\boldsymbol{X}}. \tag{4.3.19}$$

Moreover, in addition to the boundary conditions (4.3.10–4.3.16) we assume that $\psi^{(i)}$ for $i = 0, 1, ...$ are periodic in $\boldsymbol{x}$. We now analyse the equations at each order in ε, with the aim of obtaining a description of the macroscale growth and transport.

4.3.2 *At leading order*

The equations and boundary conditions at leading order are given below.

In Ω_T:

$$\boldsymbol{\nabla}_{\boldsymbol{x}} \cdot \left(\theta_n^{(0)} \boldsymbol{u}_T^{(0)}\right) = S_n^{(0)}, \tag{4.3.20}$$

$$\boldsymbol{\nabla}_{\boldsymbol{x}} \cdot \boldsymbol{u}_T^{(0)} = S_n^{(0)} + \bar{\rho} S_w^{(0)}, \tag{4.3.21}$$

$$\nabla^2_{\boldsymbol{x}} p_T^{(0)} = 0, \tag{4.3.22}$$

$$\boldsymbol{0} = \boldsymbol{\nabla}_{\boldsymbol{x}} p_T^{(0)}, \tag{4.3.23}$$

$$\boldsymbol{\nabla}_{\boldsymbol{x}} \cdot \left(c_T^{(0)} \boldsymbol{u}_T^{(0)}\right) = \boldsymbol{\nabla}_{\boldsymbol{x}} \cdot \left(\frac{D_T^{(0)}}{Pe_T} \boldsymbol{\nabla}_{\boldsymbol{x}} c_T^{(0)}\right) - \Lambda^{(0)}, \tag{4.3.24}$$

where $S_i^{(0)}$ and $\Lambda^{(0)}$ are functions of $\theta_n^{(0)}$ and $c_T^{(0)}$.

In Ω_I:

$$\boldsymbol{\nabla}_{\boldsymbol{x}} \cdot \boldsymbol{v}_I^{(0)} = 0, \tag{4.3.25}$$

$$\boldsymbol{\nabla}_{\boldsymbol{x}} p_I^{(0)} = \boldsymbol{0}, \tag{4.3.26}$$

$$\boldsymbol{v}_I^{(0)} \cdot \boldsymbol{\nabla}_{\boldsymbol{x}} c_I^{(0)} = \frac{1}{Pe_I} \nabla^2_{\boldsymbol{x}} c_I^{(0)}. \tag{4.3.27}$$

On the scaffold-tissue boundary, $\partial\Omega_s$,

$$\boldsymbol{u}_T^{(0)} \cdot \boldsymbol{n} = 0, \quad \boldsymbol{u}_T^{(0)} \cdot \boldsymbol{t} = 0, \quad \boldsymbol{\nabla}_{\boldsymbol{x}} c_T^{(0)} \cdot \boldsymbol{n} = 0. \tag{4.3.28}$$

On the tissue-interstitium boundary, Γ,

$$\boldsymbol{\nabla} F^{(0)} \cdot \boldsymbol{v}_{\Gamma}^{(0)} = 0, \tag{4.3.29}$$

$$\bar{\rho}_T \left(\boldsymbol{u}_T^{(0)} - \boldsymbol{v}_{\Gamma}^{(0)} \right) \cdot \boldsymbol{n} = \left(\boldsymbol{v}_I^{(0)} - \boldsymbol{v}_{\Gamma}^{(0)} \right) \cdot \boldsymbol{n} = Q^{(0)}, \tag{4.3.30}$$

$$\boldsymbol{u}_T^{(0)} \cdot \boldsymbol{t} = \boldsymbol{v}_I^{(0)} \cdot \boldsymbol{t}, \tag{4.3.31}$$

$$\boldsymbol{\sigma}_T^{(0)} \cdot \boldsymbol{n} = \boldsymbol{\sigma}_I^{(0)} \cdot \boldsymbol{n}, \tag{4.3.32}$$

$$c_T^{(0)} \left(\boldsymbol{u}_T^{(0)} - \boldsymbol{v}_{\Gamma}^{(0)} \right) \cdot \boldsymbol{n} - \frac{D_T^{(0)}}{Pe_T} \boldsymbol{\nabla} c_T^{(0)} \cdot \boldsymbol{n} = c_I^{(0)} \left(\boldsymbol{v}_I^{(0)} - \boldsymbol{v}_{\Gamma}^{(0)} \right) \cdot \boldsymbol{n} - \frac{1}{Pe_I} \boldsymbol{\nabla} c_I^{(0)} \cdot \boldsymbol{n}, \tag{4.3.33}$$

$$c_I^{(0)} = c_T^{(0)}, \tag{4.3.34}$$

where

$$\boldsymbol{\sigma}_i^{(0)} = -p_i^{(0)} \mathbf{I}. \tag{4.3.35}$$

From equations (4.3.23) and (4.3.26) we see that the pressure in each domain is independent of the microscale variable $\boldsymbol{x}$, and with boundary condition (4.3.32), we obtain

$$p_T^{(0)} (\boldsymbol{X}, t) = p_I^{(0)} (\boldsymbol{X}, t) = p^{(0)} (\boldsymbol{X}, t) . \tag{4.3.36}$$

By (4.3.29) we have $\boldsymbol{v}_{\Gamma}^{(0)} = \mathbf{0}$. We therefore conclude that there is no growth, surface production on the boundary or nutrient uptake, i.e. $S_i^{(0)}$, $Q^{(0)}$, $\Lambda^{(0)} = 0$. If growth occurred within the tissue it would move the boundary and cause microscale pressure variations, neither of which are permitted at leading order. This forces us to rescale the growth terms $S_n^{(0)}$ and $S_w^{(0)}$ to $O(\varepsilon)$, along with $Q^{(0)} = 0$ and $\Lambda^{(0)} = 0$. (Alternatively, one could set $S_n^{(0)} = -\bar{\rho} S_w^{(0)}$, permitting phase transfer without motion of the tissue boundary, but for the sake of generality we do not.) This occurs as a consequence of the choice of rescaling, (4.3.1), resulting in a quasi-steady problem with a stationary domain at leading order.

On comparing (4.3.20) and (4.3.21), with the right hand sides now set to zero, we find that

$$\boldsymbol{u}^{(0)} \cdot \boldsymbol{\nabla}_{\boldsymbol{x}} \theta_n^{(0)} = 0. \tag{4.3.37}$$

As, in general, $\boldsymbol{u}^{(0)} \neq \mathbf{0}$ over the whole tissue domain then we must take $\boldsymbol{\nabla}_{\boldsymbol{x}}\theta_n^{(0)} = \mathbf{0}$, which means that the cell volume fraction is independent of the microscale at leading order, i.e. $\theta_n^{(0)} = \theta_n^{(0)}(\boldsymbol{X}, t)$.

At leading order $D^{(0)}$ is a function of $\theta_n^{(0)}$, as diffusion is in general dependent on the volume fraction of cells (see section 3.5), so is also a function of $\boldsymbol{X}$ and t only. Additionally, the nutrient concentration is independent of $\boldsymbol{x}$ at leading order. This can be shown, using the method from [139], as follows. Begin with $c_T^{(0)}\times$ (4.3.24) and $c_I^{(0)}\times$(4.3.27) and integrate over the periodic cell,

$$\int_\Omega c_i^{(0)}\boldsymbol{\nabla}_{\boldsymbol{x}}\cdot\left(c_i^{(0)}\boldsymbol{u}_i^{(0)}\right) - \frac{1}{Pe_i}c_i^{(0)}\nabla_{\boldsymbol{x}}^2 c_i^{(0)}\,\mathrm{d}V = 0, \tag{4.3.38}$$

where $i = T$ or I depending on the domain. We can rewrite the first term of (4.3.38) as

$$\int_\Omega c_i^{(0)}\boldsymbol{\nabla}_{\boldsymbol{x}}\cdot\left(c_i^{(0)}\boldsymbol{u}_i^{(0)}\right)\,\mathrm{d}V = \int_\Omega \boldsymbol{\nabla}_{\boldsymbol{x}}\cdot\left(\left(c_i^{(0)}\right)^2\boldsymbol{u}_i^{(0)}\right)\,\mathrm{d}V - \int_\Omega c_i^{(0)}\boldsymbol{\nabla}_{\boldsymbol{x}}\cdot\left(c_i^{(0)}\boldsymbol{u}_i^{(0)}\right)\,\mathrm{d}V. \tag{4.3.39}$$

Application of the divergence theorem to the first integral on the right hand side gives

$$\int_\Omega c_i^{(0)}\boldsymbol{\nabla}_{\boldsymbol{x}}\cdot\left(c_i^{(0)}\boldsymbol{u}_i^{(0)}\right)\,\mathrm{d}V = \int_{\partial\Omega}\left(c_i^{(0)}\right)^2\boldsymbol{u}_i^{(0)}\cdot\boldsymbol{n}\,\mathrm{d}S - \int_\Omega c_i^{(0)}\boldsymbol{\nabla}_{\boldsymbol{x}}\cdot\left(c_i^{(0)}\boldsymbol{u}_i^{(0)}\right)\,\mathrm{d}V. \tag{4.3.40}$$

Boundary conditions (4.3.28,4.3.30) state that leading order velocities normal to the tissue-interstitial boundary and tissue-scaffold boundary are zero. Along with periodicity, this results in the surface integral vanishing and hence we obtain

$$\int_\Omega c_i^{(0)}\boldsymbol{\nabla}_{\boldsymbol{x}}\cdot\left(c_i^{(0)}\boldsymbol{u}_i^{(0)}\right)\,\mathrm{d}V = -\int_\Omega c_i^{(0)}\boldsymbol{\nabla}_{\boldsymbol{x}}\cdot\left(c_i^{(0)}\boldsymbol{u}_i^{(0)}\right)\,\mathrm{d}V, \tag{4.3.41}$$

and so this integral must also make no contribution. The second term of (4.3.38) can also be rewritten, giving

$$\begin{aligned}\int_\Omega \frac{1}{Pe_i}c_i^{(0)}\nabla_{\boldsymbol{x}}^2 c_i^{(0)}\,\mathrm{d}V &= \frac{1}{Pe_i}\int_\Omega \boldsymbol{\nabla}_{\boldsymbol{x}}\cdot\left(c_i^{(0)}\boldsymbol{\nabla}_{\boldsymbol{x}}c_i^{(0)}\right)\,\mathrm{d}V - \frac{1}{Pe_i}\int_\Omega |\nabla_{\boldsymbol{x}}c_i^{(0)}|^2\,\mathrm{d}V,\\ &= 0 - \frac{1}{Pe_i}\int_\Omega |\nabla_{\boldsymbol{x}}c_i^{(0)}|^2\,\mathrm{d}V,\end{aligned}$$

after application of the divergence theorem, boundary conditions (4.3.28,4.3.33) and periodicity. In summary, (4.3.38) is now given by

$$\frac{1}{Pe_i}\int_\Omega |\nabla_{\boldsymbol{x}} c_i^{(0)}|^2 \,\mathrm{d}V = 0, \tag{4.3.42}$$

which is only the case if nutrient concentration is independent of the microscale variable at leading order in both domains. Finally, using continuity of concentration, (4.3.34), we have

$$c_T^{(0)}\left(\boldsymbol{X},t\right) = c_I^{(0)}\left(\boldsymbol{X},t\right) = c^{(0)}\left(\boldsymbol{X},t\right). \tag{4.3.43}$$

The growth and nutrient uptake functions, $S_i^{(0)}$ and $\Lambda^{(0)}$, as functions of $\theta_n^{(0)}$ and $c_T^{(0)}$, are therefore also independent of $\boldsymbol{x}$.

4.3.3 *At $O(\varepsilon)$*

The equations and boundary conditions at $O(\varepsilon)$ are given below.

In Ω_T:

$$\frac{\partial \theta_n^{(0)}}{\partial t} + \boldsymbol{\nabla}_{\boldsymbol{x}}\cdot\left(\theta_n^{(0)}\boldsymbol{u}_T^{(1)} + \theta_n^{(1)}\boldsymbol{u}_T^{(0)}\right) + \boldsymbol{\nabla}_{\boldsymbol{X}}\cdot\left(\theta_n^{(0)}\boldsymbol{u}_T^{(0)}\right) = S_n^{(0)}, \tag{4.3.44}$$

$$\boldsymbol{\nabla}_{\boldsymbol{X}}\cdot\boldsymbol{u}_T^{(0)} + \boldsymbol{\nabla}_{\boldsymbol{x}}\cdot\boldsymbol{u}_T^{(1)} = S_n^{(0)} + \bar{\rho}S_w^{(0)}, \tag{4.3.45}$$

$$\nabla_{\boldsymbol{x}}^2 p_T^{(1)} = 0, \tag{4.3.46}$$

$$\nabla_{\boldsymbol{x}}^2 \boldsymbol{u}_T^{(0)} = \boldsymbol{\nabla}_{\boldsymbol{X}} p^{(0)} + \boldsymbol{\nabla}_{\boldsymbol{x}} p_T^{(1)} \tag{4.3.47}$$

$$\frac{\partial c^{(0)}}{\partial t} + \boldsymbol{\nabla}_{\boldsymbol{x}}\cdot\left(c^{(0)}\boldsymbol{u}_T^{(1)} + c_T^{(1)}\boldsymbol{u}_T^{(0)}\right) + \boldsymbol{\nabla}_{\boldsymbol{X}}\cdot\left(c^{(0)}\boldsymbol{u}_T^{(0)}\right) = \frac{D_T^{(0)}}{Pe_T}\nabla_{\boldsymbol{x}}^2 c_T^{(1)} - \Lambda^{(0)}. \tag{4.3.48}$$

In Ω_I:

$$\boldsymbol{\nabla}_{\boldsymbol{X}}\cdot\boldsymbol{v}_I^{(0)} + \boldsymbol{\nabla}_{\boldsymbol{x}}\cdot\boldsymbol{v}_I^{(1)} = 0, \tag{4.3.49}$$

$$\nabla_{\boldsymbol{x}}^2 \boldsymbol{v}_I^{(0)} = \boldsymbol{\nabla}_{\boldsymbol{X}} p^{(0)} + \boldsymbol{\nabla}_{\boldsymbol{x}} p_I^{(1)}, \tag{4.3.50}$$

$$\frac{\partial c^{(0)}}{\partial t} + \boldsymbol{v}_I^{(0)}\cdot\left(\boldsymbol{\nabla}_{\boldsymbol{X}} c^{(0)} + \boldsymbol{\nabla}_{\boldsymbol{x}} c_I^{(1)}\right) = \frac{1}{Pe_I}\nabla_{\boldsymbol{x}}^2 c_I^{(1)}. \tag{4.3.51}$$

On the scaffold-tissue boundary, $\partial\Omega_s$,

$$\boldsymbol{u}_T^{(1)}\cdot\boldsymbol{n} = 0, \quad \boldsymbol{u}_T^{(1)}\cdot\boldsymbol{t} = 0, \quad \left(\boldsymbol{\nabla}_{\boldsymbol{x}} c_T^{(1)} + \boldsymbol{\nabla}_{\boldsymbol{X}} c^{(0)}\right)\cdot\boldsymbol{n} = 0. \tag{4.3.52}$$

On Γ:

$$\frac{\partial F^{(0)}}{\partial t} + \boldsymbol{\nabla}_{\boldsymbol{x}} F^{(0)} \cdot \boldsymbol{v}_{\Gamma}^{(1)} = 0, \tag{4.3.53}$$

$$\bar{\rho}_T \left(\boldsymbol{u}_T^{(1)} - \boldsymbol{v}_{\Gamma}^{(1)} \right) \cdot \boldsymbol{n} = \left(\boldsymbol{v}_I^{(1)} - \boldsymbol{v}_{\Gamma}^{(1)} \right) \cdot \boldsymbol{n} = Q^{(0)}, \tag{4.3.54}$$

$$\boldsymbol{u}_T^{(1)} \cdot \boldsymbol{t} = \boldsymbol{v}_I^{(1)} \cdot \boldsymbol{t}, \tag{4.3.55}$$

$$\left[\boldsymbol{\sigma}_i^{(1)} \cdot \boldsymbol{n} \right]_-^+ = 0, \tag{4.3.56}$$

$$\left[c^{(0)} \left(\boldsymbol{v}_i^{(1)} - \boldsymbol{v}_{\Gamma}^{(1)} \right) \cdot \boldsymbol{n} - \frac{1}{Pe_i} \left(\boldsymbol{\nabla}_{\boldsymbol{x}} c_i^{(1)} + \boldsymbol{\nabla}_{\boldsymbol{X}} c^{(0)} \right) \cdot \boldsymbol{n} \right]_-^+ = 0, \tag{4.3.57}$$

$$c_T^{(1)} = c_I^{(1)}, \tag{4.3.58}$$

where

$$\boldsymbol{\sigma}_i^{(1)} = -p_i^{(1)} \mathbf{I} + \left(\boldsymbol{\nabla}_{\boldsymbol{x}} \boldsymbol{u}_i^{(0)} + \boldsymbol{\nabla}_{\boldsymbol{x}} \boldsymbol{u}_i^{(0)T} \right) - \frac{2}{3} \left(\boldsymbol{\nabla}_{\boldsymbol{x}} \cdot \boldsymbol{u}_i^{(0)} \right) \mathbf{I}. \tag{4.3.59}$$

4.3.4 *Appropriate form for macroscale velocities and microscale pressures*

In what follows we require a method of averaging variables across the various domains of the periodic cell. We therefore define the following integral average for some variable, g, over domain Ω_i, by

$$\langle g \rangle_i = \frac{1}{|\Omega|} \int_{\Omega_i} g \, \mathrm{d}V, \tag{4.3.60}$$

where $\Omega = \Omega_I \cup \Omega_T \cup \Omega_S$.

Due to the linearity of the momentum equations (4.3.47,4.3.50), we take an appropriate form for the macroscale velocities and microscale pressures to be given by

$$\boldsymbol{v}_i^{(0)} = -\boldsymbol{K}_i \boldsymbol{\nabla}_{\boldsymbol{X}} p^{(0)} \text{ and } p_i^{(1)} = -\boldsymbol{a}_i \boldsymbol{\nabla}_{\boldsymbol{X}} p^{(0)} - \bar{p}_i \text{ for } i = T, \, I, \tag{4.3.61}$$

where $\boldsymbol{K}_i$ are tensors describing the permeability, $\boldsymbol{a}_i$ are first order tensors imparting microscale variation, and $\bar{p}_i$ are the mean values of the first order pressures in Ω_i, hence microscale invariant; see, for example, [52, 100, 115, 140].

4.3.5 *Microscale cell problem*

As mentioned in section 4.3.2, at leading order we have a quasi-steady problem with stationary domains within the periodic cell. Therefore the tissue and interstitial problems only need to be solved once for a given geometry.

Substituting (4.3.61) into the mass and momentum conservation equations and boundary conditions, provides the 'cell problems' below that determine $\boldsymbol{K}_i$ and $\boldsymbol{a}_i$ in each domain. A 'cell problem' is one posed on the microscale periodic unit or 'cell' that makes up the macroscale domain, from which one establishes the microscale variation of certain quantities (here, the permeability) in order to specify effective coefficients in the macroscale description. So called 'effective' coefficients occur in the study of porous media and provide suitable values for macroscale level descriptions based on the microscale values averaged in some way over the entire periodic cell. Using these in equations (4.3.21), (4.3.47) gives for Ω_T,

$$\boldsymbol{\nabla}_{\boldsymbol{x}} \cdot \boldsymbol{K}_T^{\mathsf{T}} = \boldsymbol{0} \tag{4.3.62}$$

$$\boldsymbol{\nabla}_{\boldsymbol{x}} \boldsymbol{a}_T - \boldsymbol{I} - \boldsymbol{\nabla}_{\boldsymbol{x}}^2 \boldsymbol{K}_T^{\mathsf{T}} = \boldsymbol{0}. \tag{4.3.63}$$

Similarly (4.3.25) and (4.3.50) give for Ω_I,

$$\boldsymbol{\nabla}_{\boldsymbol{x}} \cdot \boldsymbol{K}_I^{\mathsf{T}} = \boldsymbol{0}, \tag{4.3.64}$$

$$\boldsymbol{\nabla}_{\boldsymbol{x}} \boldsymbol{a}_I - \boldsymbol{I} - \boldsymbol{\nabla}_{\boldsymbol{x}}^2 \boldsymbol{K}_I^{\mathsf{T}} = \boldsymbol{0}, \tag{4.3.65}$$

and from (4.3.30,) the following hold on Γ,

$$\boldsymbol{K}_I^{\mathsf{T}} \cdot \boldsymbol{n} = \boldsymbol{0}, \quad \boldsymbol{K}_T^{\mathsf{T}} \cdot \boldsymbol{n} = \boldsymbol{0}, \tag{4.3.66}$$

$$-\boldsymbol{a}_I \otimes \boldsymbol{n} + \left(\boldsymbol{\nabla} \boldsymbol{K}_I + (\boldsymbol{\nabla} \boldsymbol{K}_I)^{\mathsf{T}} \right) = -\boldsymbol{a}_T \otimes \boldsymbol{n} + \left(\boldsymbol{\nabla} \boldsymbol{K}_T + (\boldsymbol{\nabla} \boldsymbol{K}_T)^{\mathsf{T}} \right), \tag{4.3.67}$$

where $\otimes$ denotes tensor product. Finally, on $\partial\Omega_s$, from (4.3.28),

$$\boldsymbol{K}_T^{\mathsf{T}} \cdot \boldsymbol{n} = 0, \quad \boldsymbol{K}_T^{\mathsf{T}} \cdot \boldsymbol{t} = 0. \tag{4.3.68}$$

The 'cell problems' given by (4.3.62)–(4.3.68) do not provide unique solutions, so we use a standard approach [101, 115, 126, 140] and impose that in the relevant domain

$$\langle \boldsymbol{a}_i \rangle = \mathbf{0}, \tag{4.3.69}$$

i.e. that the average microscale pressure variation over the volume of the periodic cell is zero.

This pair of coupled steady cell problems can be solved numerically to determined the permeabilities $\boldsymbol{K}_i$, which have dependence on the microscale geometry.

4.3.6 *Averaging over the microscale*

Using the volume average as defined in (4.3.60) we simplify the problem by using the average values of microscale variables over the domain. Applying this to average our equations (4.3.45) and (4.3.49), and using the divergence theorem, we obtain

$$\boldsymbol{\nabla}_{\boldsymbol{X}} \cdot \langle \boldsymbol{u}_T^{(0)} \rangle_T = -\frac{1}{|\Omega|} \int_\Gamma \boldsymbol{u}_T^{(1)} \cdot \boldsymbol{n} \, \mathrm{d}S + \frac{1}{\Omega} \int_{\Omega_T} S_n^{(0)} + \bar{\rho} S_w^{(0)} \, \mathrm{d}V, \tag{4.3.70}$$

$$\boldsymbol{\nabla}_{\boldsymbol{X}} \cdot \langle \boldsymbol{v}_I^{(0)} \rangle_I = \frac{1}{|\Omega|} \int_\Gamma \boldsymbol{v}_I^{(1)} \cdot \boldsymbol{n} \, \mathrm{d}S, \tag{4.3.71}$$

where the normal, $\boldsymbol{n}$, is directed away from Ω_T, and the contribution from the scaffold-tissue boundary is zero by (4.3.52). Rearranging the boundary conditions (4.3.54) gives

$$\boldsymbol{u}_T^{(1)} \cdot \boldsymbol{n} = \frac{1}{\bar{\rho}_T} Q^{(0)} + \boldsymbol{v}_\Gamma^{(1)} \cdot \boldsymbol{n} \quad \text{and} \quad \boldsymbol{v}_I^{(1)} \cdot \boldsymbol{n} = Q^{(0)} + \boldsymbol{v}_\Gamma^{(1)} \cdot \boldsymbol{n}. \tag{4.3.72}$$

Applying this in equations (4.3.70,) then yields

$$\boldsymbol{\nabla}_{\boldsymbol{X}} \cdot \langle \boldsymbol{u}_T^{(0)} \rangle_T = -\frac{1}{\bar{\rho}_T} \langle Q^{(0)} \rangle_\Gamma - \langle \boldsymbol{v}_\Gamma^{(1)} \cdot \boldsymbol{n} \rangle_\Gamma + \langle S_n^{(0)} + \bar{\rho} S_w^{(0)} \rangle_T, \tag{4.3.73}$$

$$\boldsymbol{\nabla}_{\boldsymbol{X}} \cdot \langle \boldsymbol{v}_I^{(0)} \rangle_I = \langle Q^{(0)} \rangle_\Gamma + \langle \boldsymbol{v}_\Gamma^{(1)} \cdot \boldsymbol{n} \rangle_\Gamma. \tag{4.3.74}$$

Combining equations (4.3.73,4.3.74) allows us to eliminate $\boldsymbol{v}_\Gamma$, yielding

$$\boldsymbol{\nabla}_{\boldsymbol{X}} \cdot \bar{\boldsymbol{v}}^{(0)} = \left(1 - \frac{1}{\bar{\rho}_T}\right) \langle Q^{(0)} \rangle_\Gamma + \langle S_n^{(0)} + \bar{\rho} S_w^{(0)} \rangle_T, \tag{4.3.75}$$

$$\text{where } \bar{\boldsymbol{v}} = \langle \boldsymbol{u}_T^{(0)} \rangle_T + \langle \boldsymbol{v}_I^{(0)} \rangle_I. \tag{4.3.76}$$

We see that the right hand side consists of mass transfer on the boundary, Γ, and growth within the tissue. If the phase densities are equal and growth occurs only through mass transfer (no instantaneous mass creation, i.e. $S_n = -S_w$) then the right hand side is equal to zero and the flow is incompressible.

Using the volume average of (4.3.61),

$$\langle \boldsymbol{v}_i^{(0)} \rangle_i = -\langle \boldsymbol{K}_i \rangle_i \boldsymbol{\nabla}_X p^{(0)}, \tag{4.3.77}$$

and substituting into (4.3.75) gives

$$\boldsymbol{\nabla}_X \cdot \left(\bar{\boldsymbol{K}} \boldsymbol{\nabla}_X p^{(0)} \right) = -\left(1 - \frac{1}{\bar{\rho}_T} \right) \langle Q^{(0)} \rangle_\Gamma - \langle S_n^{(0)} + \bar{\rho} S_w^{(0)} \rangle_T, \tag{4.3.78}$$

$$\text{where } \bar{\boldsymbol{K}} = \langle \boldsymbol{K}_T \rangle_T + \langle \boldsymbol{K}_I \rangle_I. \tag{4.3.79}$$

Next we consider the average of the nutrient concentration equation, (4.3.51), in Ω_I. Applying the divergence theorem, boundary condition (4.3.30) and periodicity, we obtain

$$\Phi_I \frac{\partial c^{(0)}}{\partial t} + \langle \boldsymbol{v}_I^{(0)} \rangle_I \cdot \boldsymbol{\nabla}_X c^{(0)} = -\langle \frac{1}{Pe_I} \boldsymbol{\nabla}_{\boldsymbol{x}} c_I^{(1)} \cdot \boldsymbol{n} \rangle_\Gamma, \tag{4.3.80}$$

where the normal $\boldsymbol{n}$ is directed away from Ω_T and

$$\Phi_i = \frac{|\Omega_i|}{|\Omega|}. \tag{4.3.81}$$

Similarly for (4.3.48) in Ω_T, on averaging, applying the divergence theorem and boundary conditions (4.3.52,4.3.30) and (4.3.45), we obtain

$$\Phi_T \frac{\partial c^{(0)}}{\partial t} + \langle \boldsymbol{u}_T^{(0)} \rangle_T \cdot \boldsymbol{\nabla}_X c^{(0)} + c^{(0)} \langle S_n^{(0)} + \bar{\rho} S_w^{(0)} \rangle_T = \langle \frac{D_T^{(0)}}{Pe_T} \boldsymbol{\nabla}_{\boldsymbol{x}} c_T^{(1)} \cdot \boldsymbol{n} \rangle_\Gamma - \langle \Lambda^{(0)} \rangle_T. \tag{4.3.82}$$

Summing the two equations for c, (4.3.80,4.3.82), and using (4.3.72), we can eliminate the $c_i^{(1)}$ terms, such that

$$\Phi_{T \cup I} \frac{\partial c^{(0)}}{\partial t} + \bar{\boldsymbol{v}} \cdot \boldsymbol{\nabla}_X c^{(0)} = -\langle \Lambda^{(0)} \rangle_T + c^{(0)} \left(\left(\frac{1}{\bar{\rho}_T} - 1 \right) \langle Q^{(0)} \rangle_\Gamma - \langle S_n^{(0)} + \bar{\rho} S_w^{(0)} \rangle_T \right), \tag{4.3.83}$$

where $\Phi_{T\cup I} = \Phi_T \cup \Phi_I$. Notice the nutrient source/sink terms on the right hand side of the above equation (cf. [115]). This is due to change in density associated with phase transfer on the boundary and within the tissue. If $\rho_T > \rho_I$ then the material transferring from water to cell phase must decrease in volume in order to become more dense. In doing this the concentration of nutrient in the material reducing in volume becomes too high in comparison with its surroundings and so gives up nutrient, appearing as a source term in (4.3.83). Conversely, if $\rho_T < \rho_I$, the material must increase in volume and so has a nutrient deficit, giving rise to a sink term. If the phase densities are equal and there is no instantaneous mass creation, i.e. $S_n = -S_w$, the nutrient source/sink terms are zero.

Finally, we consider (4.3.44), the equation describing the cell volume fraction. Averaging and applying boundary conditions (4.3.28,4.3.30) gives

$$\Phi_T \frac{\partial \theta_n^{(0)}}{\partial t} + \langle \boldsymbol{u}_T^{(0)} \rangle_T \cdot \boldsymbol{\nabla}_X \theta_n^{(0)} + \theta_n^{(0)} \langle \boldsymbol{\nabla}_X \cdot \boldsymbol{u}_T^{(0)} + \boldsymbol{\nabla}_x \cdot \boldsymbol{u}_T^{(1)} \rangle_T = \langle S_n^{(0)} \rangle_T, \quad (4.3.84)$$

or substituting from (4.3.45),

$$\Phi_T \frac{\partial \theta_n^{(0)}}{\partial t} + \langle \boldsymbol{u}_T^{(0)} \rangle_T \cdot \boldsymbol{\nabla}_X \theta_n^{(0)} = \langle S_n^{(0)} \rangle_T - \theta_n^{(0)} \langle S_n^{(0)} + \bar{\rho} S_w^{(0)} \rangle_T. \quad (4.3.85)$$

The last term on the right occurs due to differences in phase density or instantaneous growth. When $\rho_n = \rho_w$ and there is no instantaneous mass creation, i.e. $S_n = -S_w$, it makes no contribution. When phase densities are not equal, or when mass is created instantaneously, in addition to the volume fraction of cells increasing due to the creation or transfer of material there is also a contribution due to the associated change in overall volume. For example, when growth is by phase transfer and $\rho_n > \rho_w$, an increase in cell phase increases the overall volume of cells by less than the decrease in the volume of water. Hence we have an additional increase in cell volume fraction due to overall decrease in volume of cells and water. (Note that here there is no term due to phase transfer occurring on the boundary.)

We now consider three particular cases of the model.

4.3.7 *Three special cases of the macroscale model*

Here we highlight three cases of the general macroscale equations described in section 4.3.6. The cell problem, for determination of permeabilities $\boldsymbol{K}$ and hence velocities in terms of macroscale pressure gradients, is given by (4.3.61 –4.3.69) for each case.

Equal phase densities, growth via phase transfer

If $\rho_n = \rho_w$ and $S_n = -S_w$, the macroscale equations are given by:

$$\boldsymbol{\nabla}_{\boldsymbol{X}} \cdot \bar{\boldsymbol{v}}^{(0)} = 0, \tag{4.3.86}$$

$$\boldsymbol{\nabla}_{\boldsymbol{X}} \cdot \left(\bar{\boldsymbol{K}} \boldsymbol{\nabla}_{\boldsymbol{X}} p^{(0)} \right) = 0, \tag{4.3.87}$$

$$\Phi_{T \cup I} \frac{\partial c^{(0)}}{\partial t} + \bar{\boldsymbol{v}} \cdot \boldsymbol{\nabla}_{\boldsymbol{X}} c^{(0)} = -\langle \Lambda^{(0)} \rangle_T, \tag{4.3.88}$$

$$\Phi_T \frac{\partial \theta_n^{(0)}}{\partial t} + \langle \boldsymbol{u}_T^{(0)} \rangle_T \cdot \boldsymbol{\nabla}_{\boldsymbol{X}} \theta_n^{(0)} = \langle S_n^{(0)} \rangle_T. \tag{4.3.89}$$

As one can see above, in this case the macroscale description is much simpler. We have incompressible Darcy flow, an advection-uptake equation for the concentration of nutrient, and a conservation of mass equation for the volume fraction of cells. The equations remain the same whether or not there is surface production on the boundary.

No surface production on the boundary

If $Q = 0$, growth of the tissue must occur via different phase densities or from instantaneous mass creation, i.e. we must have $S_n^{(0)} + \bar{\rho} S_w^{(0)} \neq 0$. The macroscale equations are given by:

$$\boldsymbol{\nabla}_{\boldsymbol{X}} \cdot \bar{\boldsymbol{v}}^{(0)} = \langle S_n^{(0)} + \bar{\rho} S_w^{(0)} \rangle_T, \tag{4.3.90}$$

$$\boldsymbol{\nabla}_{\boldsymbol{X}} \cdot \left(\bar{\boldsymbol{K}} \boldsymbol{\nabla}_{\boldsymbol{X}} p^{(0)} \right) = -\langle S_n^{(0)} + \bar{\rho} S_w^{(0)} \rangle_T, \tag{4.3.91}$$

$$\Phi_{T \cup I} \frac{\partial c^{(0)}}{\partial t} + \bar{\boldsymbol{v}} \cdot \boldsymbol{\nabla}_{\boldsymbol{X}} c^{(0)} = -\langle \Lambda^{(0)} \rangle_T + c^{(0)} \langle S_n^{(0)} + \bar{\rho} S_w^{(0)} \rangle_T, \tag{4.3.92}$$

$$\Phi_T \frac{\partial \theta_n^{(0)}}{\partial t} + \langle \boldsymbol{u}_T^{(0)} \rangle_T \cdot \boldsymbol{\nabla}_{\boldsymbol{X}} \theta_n^{(0)} = \langle S_n^{(0)} \rangle_T - \theta_n^{(0)} \langle S_n^{(0)} + \bar{\rho} S_w^{(0)} \rangle_T. \tag{4.3.93}$$

The additional terms accommodate the changes in volume and/or mass within the system.

Surface production on the boundary, growth via phase transfer

If $Q \neq 0$ and $S_n = -S_w$, the macroscale equations are given by:

$$\boldsymbol{\nabla}_X \cdot \bar{\boldsymbol{v}}^{(0)} = \left(1 - \frac{1}{\bar{\rho}_T}\right) \langle Q^{(0)} \rangle_\Gamma + \langle (1-\bar{\rho})\, S_n^{(0)} \rangle_T, \tag{4.3.94}$$

$$\boldsymbol{\nabla}_X \cdot \left(\bar{\boldsymbol{K}} \boldsymbol{\nabla}_X p^{(0)}\right) = -\left(1 - \frac{1}{\bar{\rho}_T}\right) \langle Q^{(0)} \rangle_\Gamma - \langle (1-\bar{\rho})\, S_n^{(0)} \rangle_T, \tag{4.3.95}$$

$$\Phi_{T\cup I} \frac{\partial c^{(0)}}{\partial t} + \bar{\boldsymbol{v}} \cdot \boldsymbol{\nabla}_X c^{(0)} = -\langle \Lambda^{(0)} \rangle_T + c^{(0)} \left(\left(\frac{1}{\bar{\rho}_T} - 1 \right) \langle Q^{(0)} \rangle_\Gamma - \langle (1-\bar{\rho})\, S_n^{(0)} \rangle_T \right), \tag{4.3.96}$$

$$\Phi_T \frac{\partial \theta_n^{(0)}}{\partial t} + \langle \boldsymbol{u}_T^{(0)} \rangle_T \cdot \boldsymbol{\nabla}_X \theta_n^{(0)} = \langle S_n^{(0)} \rangle_T - \theta_n^{(0)} \langle (1-\bar{\rho})\, S_n^{(0)} \rangle_T. \tag{4.3.97}$$

In this case we require the surface production to be defined or prescribed. This is likely to be some function of cell volume fraction and nutrient concentration on the boundary, Γ. As in [46], it may be some function which acts to maintain an equilibrium cell or water volume fraction.

4.4 SUMMARY

In this chapter we have derived an effective macroscale description of tissue growth, using the multiphase model of the previous chapter. We began by supposing that the drag between the cell and water phases is large, taking the limit and simplifying the tissue description, making it more amenable to a multiscale analysis. As a result of this we find that the velocity of the two phases of the tissue are, at leading order, equal. This constrained mixture assumption leads to complications with the boundary conditions on the tissue-interstitium interface, as water is unable to cross into the tissue. To allow tissue growth to occur in the model we instead propose that one permits instantaneous growth within the tissue and/or introduce the production of cells on the boundary.

A two scale analysis is used to obtain an effective macroscale description. By the choice of scalings, this consists of a Stokes problem on the periodic cell, used to determine the permeabilities based on the geometry, and a set of differential equations on the macroscale. These are Darcy flow, and differential equations for the volume fraction of cells within the scaffold and the concentration of nutrient, required for growth.

There are two important features to this model. Firstly, although microscale growth occurs at $O(\varepsilon)$, due to its cumulative effect, it appears in the leading order macroscale description. Secondly, the flow depends on the microstructure or geometry of the scaffold and tissue, incorporated via the 'cell problem' solved on a periodic cell.

The same analysis, but for avascular tumour growth and response to chemotherapeutic treatment, was carried out separately by Collis *et al.* [46] with accompanying computational modelling in [45]. This model consists of two microscale domains, multiphase tumour and interstitial fluid, and includes the transport and uptake of both nutrient and drug. Due to the effects of taking the large drag limit, growth is driven by density differences between tumour phases and/or by a defined phase transition rate on the tumour-interstitium interface, with both options illustrated by numerical experiments.

In contrast to solid accretion models, the model presented in this chapter allows the cell volume fraction to vary within the tissue. However, the constraint on the phases velocities, due to taking the large drag limit, does not permit cell motility via cell-cell interaction. In the next chapter we use linearisation to simplify the model and retain the effects cell-cell interaction, specified by the extra pressure term (3.3.6) due to the cells tendency to aggregate.

5

A LINEARISED MULTISCALE MODEL

5.1 INTRODUCTION

In the preceding chapter, we considered the limit of large interphase drag, $\beta \gg 1$. This assumption in mixture theory permitted the multiscale analysis that followed, as it effectively linearises the continuity equation and the total momentum equation. However, this resulted in the two phases being of equal velocity at leading order.

In this chapter we investigate an alternative model simplification to that of the constrained mixture assumption. Here we wish to allow the phases to retain their distinct velocities, in particular, in order to allow active cell motion, driven by the cells tendency to aggregate or repel, dependent on their volume fraction. A fully nonlinear analysis of the type considered in [44] is complicated by the interphase mass transfer that we accommodate so, since we seek a tractable description, we consider a linearisation of the model. This permits a more straightforward multiscale analysis, allowing the derivation of macroscale equations that depend explicitly on the microscale structure and dynamics following the method of the previous chapter.

We begin with a discussion of the existence and stability of a steady state, about which we linearise about it in section 5.2, before using a multiscale analysis to obtain the macroscale description in section 5.3. In section 5.4 we look at the model for different subcases including when the water phase

is inviscid and when alternative boundary conditions are used. Finally, our conclusions can be found in section 5.5.

5.2 LINEARISATION

Before the multiscale analysis in section 5.3 we remove the nonlinearities from the continuity and momentum equations. In the previous chapter this was achieved through imposing large interphase drag and so forcing the phase velocities within the tissue to be equal. Here, we linearise the equations about a uniform steady state.

Let

$$\theta_n = \theta_n^* + \delta\theta_{n1} + \dots \tag{5.2.1}$$

$$\boldsymbol{v}_i = \delta\boldsymbol{v}_{i1} + \dots \qquad \text{for } i = n,\, w,\, f \tag{5.2.2}$$

$$p_i = p_i^* + \delta p_{i1} + \dots \qquad \text{for } i = w,\, f \tag{5.2.3}$$

$$c = c^* + \delta c_1 + \dots \tag{5.2.4}$$

$$F = F^* + \delta F_1 + \dots \tag{5.2.5}$$

where $\delta \ll 1$ and $*$ denotes steady state values. Note that the steady state velocities are $\boldsymbol{v}_i^* = \boldsymbol{0}$ for the uniform steady state. Whilst in some models, for example in the infinite drag case in [88], it is possible to have a non-uniform steady state (with $\boldsymbol{v}_i^* = \boldsymbol{0}$), here the only steady state consistent with $\boldsymbol{v}_i^* = \boldsymbol{0}$ is uniform. This is shown below, where we start by assuming that our steady state values are only independent of time but are forced to conclude that they are also independent of space.

5.2.1 *Steady state*

Substituting the expansions (5.2.1)–(5.2.5) in to our model (see chapter 3) and looking at the leading order equations tells us about the steady state

values. Looking first to our momentum equations, (3.8.6), (3.8.7), (3.8.11), we see that at the steady state

$$\theta_n^* \boldsymbol{\nabla} p_w^* + \boldsymbol{\nabla} (\theta_n^* \phi_n^*) = \mathbf{0}, \quad \theta_w^* \boldsymbol{\nabla} p_w^* = \mathbf{0}, \quad \boldsymbol{\nabla} p_\imath^* = \mathbf{0}, \tag{5.2.6}$$

where

$$\phi_n^* = \theta_n^* \left(-\nu + \frac{\kappa \theta_n^*}{1 - \theta_n^*} \right). \tag{5.2.7}$$

From this we conclude that the various pressures are all uniform across their relevant domains. Since $\boldsymbol{\nabla} (\theta_n^* \phi_n^*) = \mathbf{0}$ then

$$\left(2\nu\theta_n^* - (3 - 2\theta_n^*) \frac{\kappa \theta_n^{*2}}{(1 - \theta_n^*)^2} \right) \boldsymbol{\nabla} \theta_n^* = \mathbf{0}, \tag{5.2.8}$$

which implies that either θ_n^* satisfies the bracket equal to zero or $\boldsymbol{\nabla} \theta_n^* = \mathbf{0}$. We set the cell volume fraction across the tissue domain at steady state to be uniform. This is indeed what one would expect as gradients in the cell volume fraction would induce gradients in the pressure and therefore cause the fluids to flow. From (3.8.4), θ_w^* is also uniform across the tissue domain at the steady state.

The mass conservation equation (3.8.2) reduces to $S_n^* = 0$ at the steady state, and we choose to take $\Lambda^* = 0$. We set the nutrient concentration c^* to be uniform across the periodic cell (both tissue and interstitial domains), as variation in nutrient would result in variation in uptake, growth and cell volume fraction.

While a non-uniform steady state may exist and with non-zero velocities within the domains (but with the tissue-interstitial boundary, Γ, fixed) this does not provide sufficient simplification of our equations for the multiscale analysis. We remark that the linearised equations (and subsequent effective macroscale description) that we obtain are only valid for small perturbations to the steady state, but the analysis will still provide an insight into the macroscale behaviour for distinct phase velocities.

In summary, our steady state consists of uniform cell volume fraction, pressures and nutrient concentration as a result of choosing the velocities to be zero. The cell volume fraction must be chosen such that functions S_n^* and

Λ^* are zero, with the extra and common pressures then determined from this.

5.2.2 *Perturbation to steady state*

Having determined the steady state values from the equations at leading order we now obtain our linearised model equations by considering the $O(\delta)$ perturbations. In Ω_T:

$$\frac{\partial \theta_{n,1}}{\partial t} + \theta_n^* \boldsymbol{\nabla} \cdot \boldsymbol{v}_{n,1} = S_{n,1}, \tag{5.2.9}$$

$$\frac{\partial \theta_{w,1}}{\partial t} + \theta_w^* \boldsymbol{\nabla} \cdot \boldsymbol{v}_{w,1} = -\bar{\rho} S_{n,1}, \tag{5.2.10}$$

$$\theta_{n,1} + \theta_{w,1} = 0, \tag{5.2.11}$$

$$\boldsymbol{\nabla} \cdot \left(\theta_n^* \boldsymbol{v}_{n,1} + \theta_w^* \boldsymbol{v}_{w,1}\right) = \left(1 - \bar{\rho}\right) S_{n,1}, \tag{5.2.12}$$

$$\theta_n^* \left[\boldsymbol{\nabla} \left(p_{w,1} + \phi_{n,1}\right) + \beta \theta_w^* \left(\boldsymbol{v}_{n,1} - \boldsymbol{v}_{w,1}\right) - \nabla^2 \boldsymbol{v}_{n,1} - \frac{1}{3} \boldsymbol{\nabla} \left(\boldsymbol{\nabla} \cdot \boldsymbol{v}_{n,1}\right) \right] = \mathbf{0}, \tag{5.2.13}$$

$$\theta_w^* \left[\boldsymbol{\nabla} p_{w,1} + \beta \theta_n^* \left(\boldsymbol{v}_{w,1} - \boldsymbol{v}_{n,1}\right) - \mu \left(\nabla^2 \boldsymbol{v}_{w,1} + \frac{1}{3} \boldsymbol{\nabla} \left(\boldsymbol{\nabla} \cdot \boldsymbol{v}_{w,1}\right) \right) \right] = \mathbf{0}, \tag{5.2.14}$$

$$\frac{\partial c_{T,1}}{\partial t} + \boldsymbol{\nabla} \cdot \left(c^* \left(\theta_n^* \boldsymbol{v}_{n,1} + \theta_w^* \boldsymbol{v}_{w,1}\right)\right) = \frac{1}{Pe_T} \nabla^2 c_{T,1} - \Lambda_1. \tag{5.2.15}$$

where

$$\begin{aligned} S_{n,1} &= \frac{\partial S_n}{\partial \theta_n} \left(\theta_n^*, c^*\right) \theta_{n,1} + \frac{\partial S_n}{\partial c} \left(\theta_n^*, c^*\right) c_{T,1}, \qquad \phi_{n,1} = \frac{1}{\theta_n^*} \frac{\partial \left(\theta_n \phi_n\right)}{\partial \theta_n} \left(\theta_n^*\right) \theta_{n,1}, \\ \Lambda_1 &= \frac{\partial \Lambda}{\partial \theta_n} \left(\theta_n^*, c^*\right) \theta_{n,1} + \frac{\partial \Lambda}{\partial c} \left(\theta_n^*, c^*\right) c_{T,1}, \end{aligned} \tag{5.2.16}$$

are the linearised growth, uptake and intraphase pressure functions, respectively. Note that due to the linearisation, $D_T(\theta_n)$ in (3.8.8) is now a function of the steady state cell volume fraction θ_n^*, and hence takes a constant value. By choosing the reference diffusion D_T^* used in the nondimensionalisation (section 3.8) to be $D_T(\theta^*)$ that constant is 1.

In Ω_I the flow is governed by:

$$\boldsymbol{\nabla} \cdot \boldsymbol{v}_{I,1} = 0, \tag{5.2.17}$$

$$\boldsymbol{\nabla} p_{I,1} - \mu \nabla^2 \boldsymbol{v}_{I,1} = \boldsymbol{0}, \tag{5.2.18}$$

$$\frac{\partial c_{I,1}}{\partial t} + \boldsymbol{\nabla} \cdot (c^* \boldsymbol{v}_{I,1}) = \frac{1}{Pe_I} \boldsymbol{\nabla}^2 c_{I,1}. \tag{5.2.19}$$

Boundary conditions are obtained by linearising (3.8.13–3.8.15) on the scaffold surface, $\partial\Omega_S$:

$$\boldsymbol{v}_{n,1} = \boldsymbol{v}_{w,1} = \boldsymbol{0}, \quad \boldsymbol{\nabla} c_{T,1} \cdot \boldsymbol{n}_S = 0, \tag{5.2.20}$$

while on the tissue boundary Γ:

$$\frac{\partial F_1}{\partial t} + \boldsymbol{\nabla} F^* \cdot \boldsymbol{v}_{\Gamma,1} = 0, \tag{5.2.21}$$

$$\theta_n^* (\boldsymbol{v}_{n,1} - \boldsymbol{v}_{\Gamma,1}) \cdot \boldsymbol{n} = 0, \tag{5.2.22}$$

$$\theta_w^* (\boldsymbol{v}_{w,1} - \boldsymbol{v}_{\Gamma,1}) \cdot \boldsymbol{n} = (\boldsymbol{v}_{I,1} - \boldsymbol{v}_{\Gamma,1}) \cdot \boldsymbol{n}, \tag{5.2.23}$$

$$\begin{aligned} -(p_{w,1} + \theta_n^* \phi_{n,1}) \boldsymbol{I} + \theta_n^* \left(\boldsymbol{\nabla} \boldsymbol{v}_{n,1} + (\boldsymbol{\nabla} \boldsymbol{v}_{n,1})^\mathsf{T} - \frac{2}{3} (\boldsymbol{\nabla} \cdot \boldsymbol{v}_{n,1}) \boldsymbol{I} \right) \\ + \mu \theta_w^* \left(\boldsymbol{\nabla} \boldsymbol{v}_{w,1} + (\boldsymbol{\nabla} \boldsymbol{v}_{w,1})^\mathsf{T} - \frac{2}{3} (\boldsymbol{\nabla} \cdot \boldsymbol{v}_{w,1}) \boldsymbol{I} \right) \\ = -p_{I,1} \boldsymbol{I} + \mu \left(\boldsymbol{\nabla} \boldsymbol{v}_{I,1} + \boldsymbol{\nabla} \boldsymbol{v}_{I,1}^\mathsf{T} \right), \end{aligned} \tag{5.2.24}$$

$$\left[\boldsymbol{v}_{i,1} \cdot \boldsymbol{t} \right]_-^+ = 0, \tag{5.2.25}$$

$$\left[c^* \left(\boldsymbol{v}_{i,1} - \boldsymbol{v}_{\Gamma,1} \right) \cdot \boldsymbol{n} - \frac{1}{Pe_i} \boldsymbol{\nabla} c_{i,1} \cdot \boldsymbol{n} \right]_-^+ = 0, \tag{5.2.26}$$

$$\left[c_{i,1} \right]_-^+ = 0, \tag{5.2.27}$$

where $i = T,\ I$, and the linearised weighted mixture velocity is given by

$$\boldsymbol{v}_{T,1} = \theta_n^* \boldsymbol{v}_{n,1} + \theta_w^* \boldsymbol{v}_{w,1}. \tag{5.2.28}$$

Having determined the steady state and linearised about it we now have simplified equations for the multiscale analysis which follows. Before this we consider the stability of the steady state, of importance in chapter 7, where the tissue dynamics are investigated .

5.2.3 *Stability*

In chapter 7, we investigate the travelling wave behaviour of the above model, to rationalise a constitutive statement for the velocity of the free boundary Γ, as required to close the macroscale description derived in section 5.3. For general interest and because of its relevance to chapter 7, we next consider the stability of the steady state using the linearised equations in one dimension. By assuming that the phase densities are equal, and by elimination of θ_w^*, $v_{w,1}$ and $p_{w,1}$, the equations in the tissue domain, Ω_T, are reduced to

$$\frac{\partial \theta_{n,1}}{\partial t} + \theta_n^* \frac{\partial v_{n,1}}{\partial x} = \frac{\partial S_n}{\partial \theta_n}(\theta_n^*, c^*)\theta_{n,1} + \frac{\partial S_n}{\partial c}(\theta_n^*, c^*)c_{T,1}, \tag{5.2.29}$$

$$J(\theta_n^*)\frac{\partial \theta_{n,1}}{\partial x} + \beta \frac{1}{1-\theta_n^*} v_{n,1} - \frac{4}{3}\left(1 + \mu \frac{\theta_n^*}{1-\theta_n^*}\right)\frac{\partial^2 v_{n,1}}{\partial x^2} = 0, \tag{5.2.30}$$

$$\frac{\partial c_{T,1}}{\partial t} = \frac{1}{Pe_T}\frac{\partial^2 c_{T,1}}{\partial x^2} - \frac{\partial \Lambda}{\partial \theta_n}(\theta_n^*, c^*)\theta_{n,1} - \frac{\partial \Lambda}{\partial c}(\theta_n^*, c^*)c_{T,1}, \tag{5.2.31}$$

where

$$J(\theta_n^*) = -2\nu + \frac{\kappa \theta_n^*(3 - 2\theta_n^*)}{(1-\theta_n^*)^2}. \tag{5.2.32}$$

We remark that the formulation (5.2.29–5.2.31) is of similar form to that considered in Lemon and King [89] (with additional terms reflecting the viscosity of the water phase and dependence on nutrient concentration). The below calculation therefore follows that presented therein and so we omit much of the detail. We seek solutions of the form

$$\theta_{n,1} = Ne^{\lambda t + i\gamma x},\ v_{n,1} = Ve^{\lambda t + i\gamma x},\ c_{T,1} = Ce^{\lambda t + i\gamma x}, \tag{5.2.33}$$

where N, V, C are constants, γ is the wavenumber and λ the growth rate of the perturbation. We find that the growth rate is given by

$$\lambda = \frac{1}{2}\left[G(\gamma) - H(\gamma) \pm \sqrt{(H(\gamma) - G(\gamma))^2 - 4(K - H(\gamma)G(\gamma))}\right], \tag{5.2.34}$$

where

$$E(\gamma) = \frac{\beta}{1-\theta_n^*} + \frac{4}{3}\gamma^2\left(1+\mu\frac{\theta_n^*}{1-\theta_n^*}\right) \tag{5.2.35}$$
$$G(\gamma) = \frac{\partial S_n}{\partial \theta_n}(\theta_n^*, c^*) - \theta_n^*\gamma^2 J(\theta_n^*)\frac{1}{E(\gamma)}$$
$$H(\gamma) = \frac{1}{Pe_T}\gamma^2 + \frac{\partial \Lambda}{\partial c}(\theta_n^*, c^*)$$
$$K = \frac{\partial \Lambda}{\partial \theta_n}(\theta_n^*, c^*)\frac{\partial S_n}{\partial c}(\theta_n^*, c^*).$$

Determination of the stability of the steady state requires values of the various model parameters as well as functions for growth S_n and nutrient uptake Λ. We return to the stability in chapter 7, where we seek illustrative numerical solutions, for given parameters and functions, as the stability of the non-trivial steady state plays an important role in the determination of the tissue growth behaviour.

5.3 MULTIPLE SCALES ANALYSIS

As in chapter 4, in order to derive effective macro- or scaffold-scale equations from those at the micro- or pore-scale, we use a multiple scales analysis. Deriving the macroscale description using the method of multiple scales captures the effects of the influence of the microscale structure and dynamics.

5.3.1 *Rescaling*

As previously, we rescale the model equations such that the timescale (that of macroscale advection) and pressure scalingunder consideration results in the appropriate leading order problem:

$$t = \frac{1}{\varepsilon}\tilde{t}, \quad p = \frac{1}{\varepsilon}\tilde{p}, \tag{5.3.1}$$

in which tildes denote the rescaled variables and $\varepsilon = l/L \ll 1$. We drop the tilde notation for convenience as we work exclusively with the

rescaled variables in subsequent sections. Additionally, from here we drop the subscripts associated with the linearisation around the steady state to simplify the notation in the expansions which follow. Our rescaled equations are given below. In Ω_T:

$$\varepsilon\frac{\partial\theta_n}{\partial t}+\theta_n^*\boldsymbol{\nabla}\cdot\boldsymbol{v}_n=S_n, \tag{5.3.2}$$

$$\varepsilon\frac{\partial\theta_w}{\partial t}+\theta_w^*\boldsymbol{\nabla}\cdot\boldsymbol{v}_w=-\bar{\rho}S_n, \tag{5.3.3}$$

$$\theta_n+\theta_w=0, \tag{5.3.4}$$

$$\boldsymbol{\nabla}\cdot\left(\theta_n^*\boldsymbol{v}_n+\theta_w^*\boldsymbol{v}_w\right)=\left(1-\bar{\rho}\right)S_n, \tag{5.3.5}$$

$$\theta_n^*\left[\boldsymbol{\nabla}\left(p_w+\phi_n\right)+\beta\theta_w^*\left(\boldsymbol{v}_n-\boldsymbol{v}_w\right)-\varepsilon\left(\nabla^2\boldsymbol{v}_n+\frac{1}{3}\boldsymbol{\nabla}\left(\boldsymbol{\nabla}\cdot\boldsymbol{v}_n\right)\right)\right]=\mathbf{0}, \tag{5.3.6}$$

$$\theta_w^*\left[\boldsymbol{\nabla}p_w+\beta\theta_n^*\left(\boldsymbol{v}_w-\boldsymbol{v}_n\right)-\varepsilon\mu\left(\nabla^2\boldsymbol{v}_w+\frac{1}{3}\boldsymbol{\nabla}\left(\boldsymbol{\nabla}\cdot\boldsymbol{v}_w\right)\right)\right]=\mathbf{0}, \tag{5.3.7}$$

$$\varepsilon\frac{\partial c_T}{\partial t}+\boldsymbol{\nabla}\cdot\left(c^*\left(\theta_n^*\boldsymbol{v}_n+\theta_w^*\boldsymbol{v}_w\right)\right)=\frac{1}{Pe_T}\nabla^2c_T-\Lambda. \tag{5.3.8}$$

where

$$\begin{aligned}S_n&=\frac{\partial S_n}{\partial\theta_n}\left(\theta_n^*,c^*\right)\theta_n+\frac{\partial S_n}{\partial c}\left(\theta_n^*,c^*\right)c_T, \qquad \phi_n=\frac{1}{\theta_n^*}\frac{\partial\left(\theta_n\phi_n\right)}{\partial\theta_n}\left(\theta_n^*\right)\theta_n,\\ \Lambda&=\frac{\partial\Lambda}{\partial\theta_n}\left(\theta_n^*,c^*\right)\theta_n+\frac{\partial\Lambda}{\partial c}\left(\theta_n^*,c^*\right)c_T,\end{aligned} \tag{5.3.9}$$

In Ω_I:

$$\boldsymbol{\nabla}\cdot\boldsymbol{v}_I=0, \tag{5.3.10}$$

$$\boldsymbol{\nabla}p_I-\varepsilon\mu\nabla^2\boldsymbol{v}_I=\mathbf{0}, \tag{5.3.11}$$

$$\varepsilon\frac{\partial c_I}{\partial t}+\boldsymbol{\nabla}\cdot\left(c^*\boldsymbol{v}_I\right)=\frac{1}{Pe_I}\boldsymbol{\nabla}^2c_I. \tag{5.3.12}$$

Boundary conditions on the scaffold surface, $\partial\Omega_S$:

$$\boldsymbol{v}_n=\boldsymbol{v}_w=\mathbf{0}, \quad \boldsymbol{\nabla}c_T\cdot\boldsymbol{n}_S=0, \tag{5.3.13}$$

and on the tissue boundary Γ:

$$\varepsilon\frac{\partial F}{\partial t}+\boldsymbol{\nabla}F^*\cdot\boldsymbol{v}_\Gamma=0, \tag{5.3.14}$$

$$\theta_n^*\left(\boldsymbol{v}_n-\boldsymbol{v}_\Gamma\right)\cdot\boldsymbol{n}=0, \tag{5.3.15}$$

$$\theta_w^*\left(\boldsymbol{v}_w-\boldsymbol{v}_\Gamma\right)\cdot\boldsymbol{n}=\left(\boldsymbol{v}_I-\boldsymbol{v}_\Gamma\right)\cdot\boldsymbol{n}, \tag{5.3.16}$$

$$
\begin{aligned}
-\left(p_w+\theta_n^*\phi_n\right)\boldsymbol{I}+\varepsilon\theta_n^*\left(\boldsymbol{\nabla}\boldsymbol{v}_n+\left(\boldsymbol{\nabla}\boldsymbol{v}_n\right)^{\mathsf{T}}-\frac{2}{3}\left(\boldsymbol{\nabla}\cdot\boldsymbol{v}_n\right)\boldsymbol{I}\right)& \\
+\varepsilon\mu\theta_w^*\left(\boldsymbol{\nabla}\boldsymbol{v}_w+\left(\boldsymbol{\nabla}\boldsymbol{v}_w\right)^{\mathsf{T}}-\frac{2}{3}\left(\boldsymbol{\nabla}\cdot\boldsymbol{v}_w\right)\boldsymbol{I}\right)& \\
=-p_I\boldsymbol{I}+\varepsilon\mu\left(\boldsymbol{\nabla}\boldsymbol{v}_I+\boldsymbol{\nabla}\boldsymbol{v}_I^{\mathsf{T}}\right),& \quad (5.3.17)
\end{aligned}
$$

$$
\left[\boldsymbol{v}_i\cdot\boldsymbol{t}\right]_-^+=0, \quad (5.3.18)
$$

$$
\left[c^*\left(\boldsymbol{v}_i-\boldsymbol{v}_T\right)\cdot\boldsymbol{n}-\frac{1}{Pe_i}\boldsymbol{\nabla}c_i\cdot\boldsymbol{n}\right]_-^+=0, \quad (5.3.19)
$$

$$
\left[c_i\right]_-^+=0, \quad (5.3.20)
$$

where $i=T,\ I$, and the linearised weighted mixture velocity is given by

$$
\boldsymbol{v}_T=\theta_n^*\boldsymbol{v}_n+\theta_w^*\boldsymbol{v}_w. \quad (5.3.21)
$$

Assuming $1\gg\varepsilon\gg\delta$, we expand variables and differential operators in terms of $\boldsymbol{x}$ and $\boldsymbol{X}$ as before:

$$
\psi\left(\boldsymbol{x},\boldsymbol{X},t;\varepsilon\right)=\psi^{(0)}\left(\boldsymbol{x},\boldsymbol{X},t\right)+\varepsilon\psi^{(1)}\left(\boldsymbol{x},\boldsymbol{X},t\right)+... \quad (5.3.22)
$$

$$
\boldsymbol{\nabla}=\boldsymbol{\nabla}_{\boldsymbol{x}}+\varepsilon\boldsymbol{\nabla}_{\boldsymbol{X}},\quad \nabla^2=\nabla_{\boldsymbol{x}}^2+2\varepsilon\boldsymbol{\nabla}_{\boldsymbol{x}}\cdot\boldsymbol{\nabla}_{\boldsymbol{X}}+\varepsilon^2\nabla_{\boldsymbol{X}}^2. \quad (5.3.23)
$$

5.3.2 *At leading order*

The equations and boundary conditions at leading order are given below. In the tissue domain, Ω_T:

$$
\theta_n^*\boldsymbol{\nabla}_{\boldsymbol{x}}\cdot\boldsymbol{v}_n^{(0)}=S_n^{(0)}, \quad (5.3.24)
$$

$$
\theta_w^*\boldsymbol{\nabla}_{\boldsymbol{x}}\cdot\boldsymbol{v}_w^{(0)}=-\bar{\rho}S_n^{(0)}, \quad (5.3.25)
$$

$$
\theta_n^{(0)}+\theta_w^{(0)}=0, \quad (5.3.26)
$$

$$
\boldsymbol{\nabla}_{\boldsymbol{x}}\cdot\boldsymbol{v}_T^{(0)}=\left(1-\bar{\rho}\right)S_n^{(0)}, \quad (5.3.27)
$$

$$
\theta_n^*\boldsymbol{\nabla}_{\boldsymbol{x}}\left(p_w^{(0)}+\phi_n^{(0)}\right)=\boldsymbol{0}, \quad (5.3.28)
$$

$$
\theta_w^*\boldsymbol{\nabla}_{\boldsymbol{x}}p_w^{(0)}=\boldsymbol{0}, \quad (5.3.29)
$$

$$
\boldsymbol{\nabla}_{\boldsymbol{x}}\cdot\left(c^*\boldsymbol{v}_T^{(0)}\right)=\frac{1}{Pe_T}\nabla_{\boldsymbol{x}}^2c_T^{(0)}-\Lambda^{(0)}. \quad (5.3.30)
$$

In the interstitial domain, Ω_I:

$$\boldsymbol{\nabla}_{\boldsymbol{x}} \cdot \boldsymbol{v}_I^{(0)} = 0, \tag{5.3.31}$$

$$\boldsymbol{\nabla}_{\boldsymbol{x}} p_I^{(0)} = \mathbf{0}, \tag{5.3.32}$$

$$\boldsymbol{\nabla}_{\boldsymbol{x}} \cdot \left(c^* \boldsymbol{v}_I^{(0)} \right) = \frac{1}{Pe_I} \nabla_{\boldsymbol{x}}^2 c_I^{(0)}. \tag{5.3.33}$$

Boundary conditions on Γ:

$$\theta_n^* \left(\boldsymbol{v}_n^{(0)} - \boldsymbol{v}_\Gamma^{(0)} \right) \cdot \boldsymbol{n} = 0, \tag{5.3.34}$$

$$\theta_w^* \left(\boldsymbol{v}_w^{(0)} - \boldsymbol{v}_\Gamma^{(0)} \right) \cdot \boldsymbol{n} = \left(\boldsymbol{v}_I^{(0)} - \boldsymbol{v}_\Gamma^{(0)} \right) \cdot \boldsymbol{n}, \tag{5.3.35}$$

$$\boldsymbol{v}_T^{(0)} \cdot \boldsymbol{t} = \boldsymbol{v}_I^{(0)} \cdot \boldsymbol{t}, \tag{5.3.36}$$

$$- \left(p_w^{(0)} + \theta_n^* \phi_n^{(0)} \right) \boldsymbol{I} = -p_I^{(0)} \boldsymbol{I}, \tag{5.3.37}$$

$$\boldsymbol{\nabla}_{\boldsymbol{x}} F^* \cdot \boldsymbol{v}_\Gamma^{(0)} = 0, \tag{5.3.38}$$

$$c^* \left(\boldsymbol{v}_T^{(0)} - \boldsymbol{v}_\Gamma^{(0)} \right) \cdot \boldsymbol{n} - \frac{1}{Pe_T} \boldsymbol{\nabla}_{\boldsymbol{x}} c_T^{(0)} \cdot \boldsymbol{n} = c^* \left(\boldsymbol{v}_I^{(0)} - \boldsymbol{v}_\Gamma^{(0)} \right) \cdot \boldsymbol{n} - \frac{1}{Pe_I} \boldsymbol{\nabla}_{\boldsymbol{x}} c_I^{(0)} \cdot \boldsymbol{n}, \tag{5.3.39}$$

$$c_T^{(0)} = c_I^{(0)}, \tag{5.3.40}$$

where

$$\boldsymbol{v}_T^{(0)} = \theta_n^* \boldsymbol{v}_n^{(0)} + \theta_w^* \boldsymbol{v}_w^{(0)}. \tag{5.3.41}$$

Boundary conditions on $\partial\Omega_S$:

$$\boldsymbol{v}_n^{(0)} = \boldsymbol{v}_w^{(0)} = \mathbf{0}, \quad \boldsymbol{\nabla}_{\boldsymbol{x}} c_T^{(0)} \cdot \boldsymbol{n}_S = 0. \tag{5.3.42}$$

Lastly, we note that, in view of (5.3.9), the phase transfer, intraphase pressure and nutrient uptake functions depend only on $\theta_n^{(0)}$, $c_T^{(0)}$ (and the relevant steady states), so that

$$S_n^{(0)} = S_{n,1} \left(\theta_n^{(0)}, c_T^{(0)} \right), \quad \phi_n^{(0)} = \phi_{n,1} \left(\theta_n^{(0)} \right), \quad \Lambda^{(0)} = \Lambda_1 \left(\theta_n^{(0)}, c_T^{(0)} \right). \tag{5.3.43}$$

Equation (5.3.38) tells us that $\boldsymbol{\nabla}_{\boldsymbol{x}} F^* = \mathbf{0}$ or $\boldsymbol{v}_\Gamma^{(0)} \cdot \boldsymbol{n} = 0$, but the latter holds most generally. So we take the boundary to be stationary at this order

which implies no growth of Ω_T so, as in section 4.3.2, we rescale $S_n^{(0)}$ and $\Lambda^{(0)}$ to $O(\varepsilon)$ for consistency. Of course if the two phases are of equal density, phase transfer (increase in volume fraction θ_n) may occur without affecting the size of the domain Ω_T but any change in θ_n at the boundary is likely to induce a flux and associated growth of Ω_T.

Following similar arguments to section 4.3.2 we find that pressures, nutrient concentrations and cell volume fraction are independent of the microscale variable $\boldsymbol{x}$, i.e.

$$p^{(0)}(\boldsymbol{X},t) = p_I^{(0)}(\boldsymbol{X},t) = p_w^{(0)}(\boldsymbol{X},t) + \theta_n^* \phi_n^{(0)}(\boldsymbol{X},t), \tag{5.3.44}$$

$$c^{(0)}(\boldsymbol{X},t) = c_T^{(0)}(\boldsymbol{X},t) = c_I^{(0)}(\boldsymbol{X},t), \tag{5.3.45}$$

$$\theta_n^{(0)} = \theta_n^{(0)}(\boldsymbol{X},t). \tag{5.3.46}$$

5.3.3 *At O(ε)*

The equations and boundary conditions at $O(\varepsilon)$ are given below. In Ω_T:

$$\frac{\partial \theta_n^{(0)}}{\partial t} + \theta_n^* \left(\boldsymbol{\nabla}_{\boldsymbol{x}} \cdot \boldsymbol{v}_n^{(1)} + \boldsymbol{\nabla}_{\boldsymbol{X}} \cdot \boldsymbol{v}_n^{(0)} \right) = S_n^{(0)}, \tag{5.3.47}$$

$$\boldsymbol{\nabla}_{\boldsymbol{x}} \cdot \boldsymbol{v}_T^{(1)} + \boldsymbol{\nabla}_{\boldsymbol{X}} \cdot \boldsymbol{v}_T^{(0)} = (1-\bar{\rho})\, S_n^{(0)}, \tag{5.3.48}$$

$$\theta_n^* \left[\boldsymbol{\nabla}_{\boldsymbol{x}} \left(p_w^{(1)} + \phi_n^{(1)} \right) + \boldsymbol{\nabla}_{\boldsymbol{X}} \left(p_w^{(0)} + \phi_n^{(0)} \right) + \beta \theta_w^* \left(\boldsymbol{v}_n^{(0)} - \boldsymbol{v}_w^{(0)} \right) - \nabla_{\boldsymbol{x}}^2 \boldsymbol{v}_n^{(0)} \right] = \boldsymbol{0}, \tag{5.3.49}$$

$$\theta_w^* \left[\boldsymbol{\nabla}_{\boldsymbol{x}} p_w^{(1)} + \boldsymbol{\nabla}_{\boldsymbol{X}} p_w^{(0)} + \beta \theta_n^* \left(\boldsymbol{v}_w^{(0)} - \boldsymbol{v}_n^{(0)} \right) - \mu \nabla_{\boldsymbol{x}}^2 \boldsymbol{v}_w^{(0)} \right] = \boldsymbol{0}, \tag{5.3.50}$$

$$\frac{\partial c^{(0)}}{\partial t} + c^* \left(\boldsymbol{\nabla}_{\boldsymbol{x}} \cdot \boldsymbol{v}_T^{(1)} + \boldsymbol{\nabla}_{\boldsymbol{X}} \cdot \boldsymbol{v}_T^{(0)} \right) = \frac{1}{Pe_T} \nabla_{\boldsymbol{x}}^2 c_T^{(1)} - \Lambda^{(0)}, \tag{5.3.51}$$

where $\boldsymbol{v}_T^{(1)} = \theta_n^* \boldsymbol{v}_n^{(1)} + \theta_w^* \boldsymbol{v}_w^{(1)}$. In Ω_I:

$$\boldsymbol{\nabla}_{\boldsymbol{x}} \cdot \boldsymbol{v}_I^{(1)} + \boldsymbol{\nabla}_{\boldsymbol{X}} \cdot \boldsymbol{v}_I^{(0)} = 0, \tag{5.3.52}$$

$$\boldsymbol{\nabla}_{\boldsymbol{x}} p_I^{(1)} + \boldsymbol{\nabla}_{\boldsymbol{X}} p^{(0)} - \mu \nabla_{\boldsymbol{x}}^2 \boldsymbol{v}_I^{(0)} = \boldsymbol{0}, \tag{5.3.53}$$

$$\frac{\partial c^{(0)}}{\partial t} + c^* \left(\boldsymbol{\nabla}_{\boldsymbol{x}} \cdot \boldsymbol{v}_I^{(1)} + \boldsymbol{\nabla}_{\boldsymbol{X}} \cdot \boldsymbol{v}_I^{(0)} \right) = \frac{1}{Pe_I} \nabla_{\boldsymbol{x}}^2 c_I^{(1)}. \tag{5.3.54}$$

On Γ:

$$\theta_n^* \left(\boldsymbol{v}_n^{(1)} - \boldsymbol{v}_\Gamma^{(1)} \right) \cdot \boldsymbol{n} = 0, \tag{5.3.55}$$

$$\theta_w^* \left(\boldsymbol{v}_w^{(1)} - \boldsymbol{v}_\Gamma^{(1)} \right) \cdot \boldsymbol{n} = \left(\boldsymbol{v}_I^{(1)} - \boldsymbol{v}_\Gamma^{(1)} \right) \cdot \boldsymbol{n}, \tag{5.3.56}$$

$$\boldsymbol{v}_T^{(1)} \cdot \boldsymbol{t} = \boldsymbol{v}_I^{(1)} \cdot \boldsymbol{t}, \tag{5.3.57}$$

$$\begin{aligned} &- \left(p_w^{(1)} + \theta_n^* \phi_n^{(1)} \right) \boldsymbol{I} + \theta_n^* \left(\boldsymbol{\nabla}_{\boldsymbol{x}} \boldsymbol{v}_n^{(0)} + \left(\boldsymbol{\nabla}_{\boldsymbol{x}} \boldsymbol{v}_n^{(0)} \right)^{\mathsf{T}} \right) \\ &\quad + \mu \theta_w^* \left(\boldsymbol{\nabla}_{\boldsymbol{x}} \boldsymbol{v}_w^{(0)} + \left(\boldsymbol{\nabla}_{\boldsymbol{x}} \boldsymbol{v}_w^{(0)} \right)^{\mathsf{T}} \right) = -p_I^{(1)} \boldsymbol{I} + \mu \left(\boldsymbol{\nabla}_{\boldsymbol{x}} \boldsymbol{v}_I^{(0)} + \left(\boldsymbol{\nabla} \boldsymbol{v}_I^{(0)} \right)^{\mathsf{T}} \right), \end{aligned} \tag{5.3.58}$$

$$\frac{\partial F^{(0)}}{\partial t} + \boldsymbol{\nabla}_{\boldsymbol{x}} F^* \cdot \boldsymbol{v}_\Gamma^{(1)} = 0, \tag{5.3.59}$$

$$\begin{aligned} c^* \left(\boldsymbol{v}_T^{(1)} - \boldsymbol{v}_\Gamma^{(1)} \right) \cdot \boldsymbol{n} - \frac{1}{Pe_T} \left(\boldsymbol{\nabla}_{\boldsymbol{x}} c_T^{(1)} + \boldsymbol{\nabla}_{\boldsymbol{X}} c^{(0)} \right) \cdot \boldsymbol{n} \\ = c^* \left(\boldsymbol{v}_I^{(1)} - \boldsymbol{v}_\Gamma^{(1)} \right) \cdot \boldsymbol{n} - \frac{1}{Pe_I} \left(\boldsymbol{\nabla}_{\boldsymbol{x}} c_I^{(1)} + \boldsymbol{\nabla}_{\boldsymbol{X}} c^{(0)} \right) \cdot \boldsymbol{n}, \end{aligned} \tag{5.3.60}$$

$$c_T^{(1)} = c_I^{(1)}. \tag{5.3.61}$$

On $\partial\Omega_s$:

$$\boldsymbol{v}_n^{(1)} = \boldsymbol{v}_w^{(1)} = \boldsymbol{0}, \quad \boldsymbol{\nabla}_{\boldsymbol{x}} c_T^{(1)} \cdot \boldsymbol{n} + \boldsymbol{\nabla}_{\boldsymbol{X}} c_T^{(0)} \cdot \boldsymbol{n}_s = 0. \tag{5.3.62}$$

5.3.4 *Appropriate form for macroscale velocities and microscale pressures*

In the following sections we use the integral average, defined by (4.3.60), and, due to the similar form of the momentum equations, we again take the appropriate form for the macroscale velocities and microscale pressures to be given by (4.3.61).

5.3.5 *Microscale cell problem*

Substituting these into (5.3.31) and (5.3.53) we find that in Ω_I the following hold, (where μ is assumed constant),

$$\boldsymbol{\nabla}_{\boldsymbol{x}} \cdot \boldsymbol{K}_I^{\mathsf{T}} = \boldsymbol{0}, \tag{5.3.63}$$

$$\boldsymbol{\nabla}_{\boldsymbol{x}} \boldsymbol{a}_I^{\mathsf{T}} - \boldsymbol{I} - \mu \nabla_{\boldsymbol{x}}^2 \boldsymbol{K}_I = \boldsymbol{0}, \tag{5.3.64}$$

with (5.3.35) giving that on Γ,

$$\boldsymbol{K}_I^{\mathsf{T}} \boldsymbol{n} = \boldsymbol{0}. \tag{5.3.65}$$

In Ω_T, the phase velocities and pressures are given by

$$\boldsymbol{v}_n^{(0)} = -\boldsymbol{K}_n \boldsymbol{\nabla}_{\boldsymbol{X}} p^{(0)} \quad \boldsymbol{v}_w^{(0)} = -\boldsymbol{K}_w \boldsymbol{\nabla}_{\boldsymbol{X}} p^{(0)} \tag{5.3.66}$$

$$p_w^{(1)} = -\boldsymbol{a}_w \boldsymbol{\nabla}_{\boldsymbol{X}} p^{(0)} - \bar{p}_w \quad p_n^{(1)} = p_w^{(1)} + \phi_n^{(1)} = -\boldsymbol{a}_n \boldsymbol{\nabla}_{\boldsymbol{X}} p^{(0)} - \bar{p}_n. \tag{5.3.67}$$

From equations (5.3.24, 5.3.25) we then have that

$$\boldsymbol{\nabla}_{\boldsymbol{x}} \cdot \boldsymbol{K}_n^{\mathsf{T}} = \boldsymbol{0}, \quad \boldsymbol{\nabla}_{\boldsymbol{x}} \cdot \boldsymbol{K}_w^{\mathsf{T}} = \boldsymbol{0}, \tag{5.3.68}$$

in Ω_T. The two momentum equations (5.3.49) and (5.3.50) provide:

$$\left[\boldsymbol{\nabla}_{\boldsymbol{x}} \boldsymbol{a}_n^{\mathsf{T}} - \boldsymbol{I} - \nabla_{\boldsymbol{x}}^2 \boldsymbol{K}_n - \beta \theta_w^* \left(\boldsymbol{K}_w - \boldsymbol{K}_n\right)\right] \boldsymbol{\nabla}_{\boldsymbol{X}} p^{(0)} - \theta_w^* \boldsymbol{\nabla}_{\boldsymbol{X}} \phi_n^{(0)} = \boldsymbol{0}, \tag{5.3.69}$$

$$\left[\boldsymbol{\nabla}_{\boldsymbol{x}} \boldsymbol{a}_w^{\mathsf{T}} - \boldsymbol{I} - \mu \nabla_{\boldsymbol{x}}^2 \boldsymbol{K}_w - \beta \theta_n^* \left(\boldsymbol{K}_n - \boldsymbol{K}_w\right)\right] \boldsymbol{\nabla}_{\boldsymbol{X}} p^{(0)} + \theta_n^* \boldsymbol{\nabla}_{\boldsymbol{X}} \phi_n^{(0)} = \boldsymbol{0}, \tag{5.3.70}$$

in Ω_T whilst (5.3.34,5.3.35) and (5.3.42) give

$$\boldsymbol{K}_n^{\mathsf{T}} \boldsymbol{n} = \boldsymbol{0}, \quad \boldsymbol{K}_w^{\mathsf{T}} \boldsymbol{n} = \boldsymbol{0} \text{ on } \Gamma, \tag{5.3.71}$$

$$\boldsymbol{K}_n = \boldsymbol{0}, \quad \boldsymbol{K}_w = \boldsymbol{0} \text{ on } \partial\Omega_S. \tag{5.3.72}$$

Using the continuity of stress condition (5.3.58) we find that, as the microscale invariant contributions to stress are continuous, i.e. $\bar{p}_I = \theta_n^* \bar{p}_n + \theta_w^* \bar{p}_w$, on the boundary, Γ, we have

$$-\boldsymbol{a}_T \otimes \boldsymbol{I} + \left(\boldsymbol{\nabla} \boldsymbol{K}_T + \left(\boldsymbol{\nabla} \boldsymbol{K}_T\right)^{\mathsf{T}}\right) = -\boldsymbol{a}_I \otimes \boldsymbol{I} + \mu \left(\boldsymbol{\nabla} \boldsymbol{K}_I + \left(\boldsymbol{\nabla} \boldsymbol{K}_I\right)^{\mathsf{T}}\right), \tag{5.3.73}$$

where $i = T,\ f$ and

$$\boldsymbol{K}_T = \theta_n^* \boldsymbol{K}_n + \mu \theta_w^* \boldsymbol{K}_w \quad \text{and} \quad \boldsymbol{a}_T = \theta_n^* \boldsymbol{a}_n + \theta_w^* \boldsymbol{a}_w. \tag{5.3.74}$$

We note that although a standard Stokes-type cell problem (as seen in the large drag model, section 4.3.5) is obtained in Ω_I, the multiphase dynamics in Ω_T leads to significantly increased complexity. In particular, we obtain a pair of coupled modified Stokes problems, determining the permeability tensors $\boldsymbol{K}_i$ and extra pressures $\boldsymbol{a}_i$ for each phase, which are further coupled to the flow in Ω_I via the stress continuity boundary conditions. Moreover, and in contrast to other simplified analyses of this type, the microscale cell problems and corresponding macroscale dynamics are coupled through the macroscale pressure and active cell behaviour terms. Such a multiscale cell problem poses significant computational challenges. See chapter 7 for more details. Despite the complexity due to the coupling, the cell problem is quasi-static and hence much simpler than that of [44].

Additionally we note that the coupling of the microscale cell problems and corresponding macroscale dynamics can be avoided by use of an alternative ansatz for the macroscale velocities and microscale pressures. This is explored further in chapter 6.

5.3.6 *Averaging over the microscale*

Averaging equations (5.3.48) and (5.3.52), using the average defined in (4.3.60), then using the divergence theorem we find

$$\boldsymbol{\nabla}_{\boldsymbol{X}} \cdot \langle \boldsymbol{v}_I^{(0)} \rangle_I = \frac{1}{|\Omega|} \int_\Gamma \boldsymbol{v}_I^{(1)} \cdot \boldsymbol{n} \, \mathrm{d}S, \tag{5.3.75}$$

$$\boldsymbol{\nabla}_{\boldsymbol{X}} \cdot \langle \boldsymbol{v}_T^{(0)} \rangle_T = -\frac{1}{|\Omega|} \int_\Gamma \boldsymbol{v}_T^{(1)} \cdot \boldsymbol{n} \, \mathrm{d}S + \langle (1 - \bar{\rho}) \, S_n^{(0)} \rangle_T, \tag{5.3.76}$$

where

$$\boldsymbol{v}_T^{(0)} = \theta_n^* \boldsymbol{v}_n^{(0)} + \theta_w^* \boldsymbol{v}_w^{(0)}. \tag{5.3.77}$$

Note that the contribution from the scaffold-tissue boundary, arising from application of the divergence theorem to the average of (5.3.48), is zero since

all phase velocities normal to the scaffold are zero there. Using boundary conditions (5.3.55) and (5.3.56), and defining the average macroscale velocity by

$$\bar{\boldsymbol{v}}_T^{(0)} = \langle \boldsymbol{v}_T^{(0)} \rangle_T + \langle \boldsymbol{v}_I^{(0)} \rangle_I, \tag{5.3.78}$$

we obtain

$$\boldsymbol{\nabla}_{\boldsymbol{X}} \cdot \bar{\boldsymbol{v}}_T^{(0)} = \langle (1-\bar{\rho})\, S_n^{(0)} \rangle_T. \tag{5.3.79}$$

As in the large drag model, if $\rho_n = \rho_w$ then the right hand side is equal to zero and the flow is incompressible. If $\rho_n \neq \rho_w$ then this describes the change in volume due to the change in density as phase transfer occurs. Alternatively, using (5.3.66) we have an equation for the macroscale pressure,

$$\boldsymbol{\nabla}_{\boldsymbol{X}} \cdot \left(\bar{\boldsymbol{K}} \boldsymbol{\nabla}_{\boldsymbol{X}} p^{(0)} \right) = -\langle (1-\bar{\rho})\, S_n^{(0)} \rangle_T, \tag{5.3.80}$$

where

$$\bar{\boldsymbol{K}} = \langle \boldsymbol{K}_T \rangle_T + \langle \boldsymbol{K}_I \rangle_I. \tag{5.3.81}$$

Averaging the nutrient equations (5.3.51) and (5.3.54) over their respective domains gives

$$\Phi_T \frac{\partial c^{(0)}}{\partial t} + c^* (1-\bar{\rho}) \langle S_n^{(0)} \rangle_T = \frac{1}{Pe_T} \langle \nabla_{\boldsymbol{x}}^2 c_T^{(1)} \rangle_T - \langle \Lambda^{(0)} \rangle_T, \tag{5.3.82}$$

$$\Phi_I \frac{\partial c^{(0)}}{\partial t} = \frac{1}{Pe} \langle \nabla_{\boldsymbol{x}}^2 c_I^{(1)} \rangle_I, \tag{5.3.83}$$

where $\Phi_i = |\Omega_i|/|\Omega|$. Summing (5.3.82) and (5.3.83), and applying the divergence theorem, boundary condition (5.3.60) and periodicity yields the macroscale nutrient concentration,

$$\Phi_{T\cup I} \frac{\partial c^{(0)}}{\partial t} + c^* (1-\bar{\rho}) \langle S_n^{(0)} \rangle_T = -\langle \Lambda^{(0)} \rangle_T, \tag{5.3.84}$$

where $\Phi_{T\cup I} = |\Omega_T \cup \Omega_I|/|\Omega|$. This is similar to the model of chapter 4 as, in addition to the nutrient uptake by mitosis, we have an apparent source/sink term caused by the density change related to phase transfer. For example, if the cell phase is denser than the water phase then as water becomes cells some of the nutrient it contains is given up, creating a source. Of course, if phase densities are identical then this term is zero.

Finally, averaging the equation for the cell volume fraction (5.3.47) and applying the divergence theorem and boundary condition (5.3.55) we find

$$\frac{\partial}{\partial t}\langle\theta_n^{(0)}\rangle_T + \theta_n^*\left(\boldsymbol{\nabla}_{\boldsymbol{X}}\cdot\langle\boldsymbol{v}_n^{(0)}\rangle_T + \langle\boldsymbol{v}_\Gamma^{(1)}\cdot\boldsymbol{n}\rangle_\Gamma\right) = \langle S_n^{(0)}\rangle_T. \tag{5.3.85}$$

As in the macroscale model of the previous chapter, which in some cases requires the surface production term to be prescribed, here a constitutive model assumption or closure constraint is needed to fix $\boldsymbol{v}_\Gamma^{(1)}\cdot\boldsymbol{n}$. This is explored in the following chapter.

In this section, using a multiple scales analysis we have derived a macroscale description of the flow, nutrient concentration and cell volume fraction. The resulting model includes detail from the microscale geometry via $\boldsymbol{K}_i$, obtained by solution of the cell problem of 5.3.5, and contributions from the microscale growth through $S_n^{(0)}$ and $\boldsymbol{v}_\Gamma^{(1)}\cdot\boldsymbol{n}$. In the following section we investigate subcases of the linearised model, specifically that of inviscid water and linearisation about the trivial steady state, as well as alternative boundary conditions, as discussed in section 3.6, to see what consequence these variations have on the resulting cell problem and macroscale description.

5.4 SUBCASES OF THE MODEL AND ALTERNATIVE BOUNDARY CONDITIONS

We now consider a couple of subcases of the model which provide simpler Stokes problems on the periodic cell, as well as the impact of different choices of boundary conditions on the scaffold and with respect to nutrient concentration.

5.4.1 *Inviscid water*

In some cases it may be preferable to model the water phase as inviscid as, for example, in [89]. We set $\mu = 0$ to remove the viscous terms associated with the water phase but retain the interphase drag β.

Since the water is inviscid, in the interstitial domain (5.2.18) reduces to

$$\boldsymbol{\nabla} p_I = \mathbf{0} \tag{5.4.1}$$

and so p_I is spatially uniform. A sensible choice is to set $p_I = 0$, though in general of course $p_I = p_I(t)$. With no pressure gradients to drive a flow, we must also choose $\boldsymbol{v}_I = \mathbf{0}$.

Due to the overall pressure $p^{(0)}$ being equal to zero in this case, the appropriate forms for the macroscale velocities and microscale pressures are written in terms of $p_w^{(0)}$. Our Stokes problem in the tissue domain in this case is given by equations (5.3.68)–(5.3.72) and

$$\boldsymbol{\nabla}_{\boldsymbol{x}} \boldsymbol{a}_w^{\mathsf{T}} - \boldsymbol{I} - \beta\theta_n^* \left(\boldsymbol{K}_n - \boldsymbol{K}_w\right) = \mathbf{0} \tag{5.4.2}$$

$$\boldsymbol{\nabla}_{\boldsymbol{x}} \boldsymbol{a}_n^{\mathsf{T}} - \left(1 - \frac{1}{\theta_n^*}\right) \boldsymbol{I} - \nabla_{\boldsymbol{x}}^2 \boldsymbol{K}_n - \beta\theta_w^* \left(\boldsymbol{K}_w - \boldsymbol{K}_n\right) = \mathbf{0} \tag{5.4.3}$$

This simplification of the cell problem, (i.e the removal of the $\boldsymbol{\nabla}_{\boldsymbol{X}} p_w^{(0)}$ and $\boldsymbol{\nabla}_{\boldsymbol{X}} \phi_n^{(0)}$ terms) is due to the fact that the continuity of pressures at leading order (5.3.44) becomes

$$0 = p_w^{(0)} + \theta_n^* \phi_n^{(0)}, \tag{5.4.4}$$

as we have zero pressure in Ω_I. This allows the elimination of $\phi_n^{(0)}$ terms. This model is also simpler in that there is no Stokes problem in the interstitial domain coupled to that in the tissue. The macroscale equations remain the same.

5.4.2 *Trivial steady state for cell volume fraction*

In the case that we take the steady state to be the trivial one, $\theta_n^* = 0$, our equations simplify significantly, with the Stokes problem reduced to

$$\boldsymbol{\nabla}_{\boldsymbol{x}} \cdot \boldsymbol{K}_i^{\mathsf{T}} = \boldsymbol{0} \qquad \boldsymbol{\nabla}_{\boldsymbol{x}} \boldsymbol{a}_i^{\mathsf{T}} - \boldsymbol{I} - \mu \nabla_{\boldsymbol{x}}^2 \boldsymbol{K}_i = \boldsymbol{0}, \tag{5.4.5}$$

for $i = f$ in Ω_I and $i = w$ in Ω_T, whilst on the boundary, Γ,

$$\boldsymbol{K}_i^{\mathsf{T}} \boldsymbol{n} = \boldsymbol{0}, \qquad \left[-\boldsymbol{a}_i \otimes \boldsymbol{I} + \left(\boldsymbol{\nabla} \boldsymbol{K}_i + \mu \left(\boldsymbol{\nabla} \boldsymbol{K}_i \right)^{\mathsf{T}} \right) \right]_-^+ = \boldsymbol{0}. \tag{5.4.6}$$

The macroscale equations for velocity, pressure and nutrient remain unchanged, except that in this case

$$\bar{\boldsymbol{K}} = \langle \boldsymbol{K}_w \rangle_T + \langle \boldsymbol{K}_I \rangle_I \quad \text{and} \quad \bar{\boldsymbol{v}}^{(0)} = \langle \boldsymbol{v}_w^{(0)} \rangle_T + \langle \boldsymbol{v}_I^{(0)} \rangle_I, \tag{5.4.7}$$

in equations (5.3.79) and (5.3.80), whilst the equation for cell volume fraction is reduced to

$$\frac{\partial \langle \theta_n^{(0)} \rangle_T}{\partial t} = \langle S_n^{(0)} \rangle_T, \tag{5.4.8}$$

so it is no longer necessary to define or compute numerically the velocity of the tissue boundary, Γ. Note that when we use the equations linearised about the trivial steady state we do not find that the cell volume fraction, $\theta_n^{(0)}$, is independent of the microscale variable $\boldsymbol{x}$. Whilst the equations can be solved to determine the averaged cell volume fraction, we can not get microscale variation detail. Although linearising about the trivial steady state removes the requirement to solve for or define a boundary velocity or flux in order to solve the macroscale equations (compare (5.4.8) and (5.3.85)), the resulting model is much less interesting.

5.4.3 *Alternative scaffold boundary conditions*

In the model described above, for simplicity, we imposed a no slip condition on the tissue-scaffold boundary. It may, however, be appropriate to consider

less restrictive choices of scaffold boundary conditions as cells can move in response to chemical or physical signals by changes in their shape driven by the cytoskeleton. Reasons for this 'cell crawl' vary, from forming new tissue during embryonic development to repairing damage to skin, bone and nerves [84].

Alternative choices of boundary condition, as discussed in section 3.6, include a slip condition such as

$$\boldsymbol{v}_n = b\frac{\partial \boldsymbol{v}_n}{\partial n} \tag{5.4.9}$$

where b is a constant of proportionality and $\partial/\partial n$ denotes the normal derivative, or free slip

$$\frac{\partial \boldsymbol{v}_n}{\partial n} = 0. \tag{5.4.10}$$

In both cases we retain the no penetration condition,

$$\boldsymbol{v}_n \cdot \boldsymbol{n} = 0, \tag{5.4.11}$$

since the scaffold is a rigid solid. The effective macroscale equations remain the same in each case and the only change to the Stokes problem is in the tissue-scaffold boundary conditions. The above equations give

$$\boldsymbol{K}_n = b\frac{\partial \boldsymbol{K}_n}{\partial n}, \quad \frac{\partial \boldsymbol{K}_n}{\partial n} = \boldsymbol{0}, \quad \boldsymbol{K}_n^{\mathsf{T}}\boldsymbol{n} = \boldsymbol{0} \tag{5.4.12}$$

as the choice of boundary conditions to be applied at $\partial\Omega_s$ in the Stokes problem. (Note that the slip condition is of similar form to that obtained by Irons *et al.* [75] in a similar cell problem, for a porous medium growth model.)

5.4.4 *Alternative nutrient concentration boundary conditions*

We consider alternatives for the nutrient concentration boundary condition on the tissue-interstitium interface, Γ, and their effect on the multiscale model. As discussed in section 3.6, in [139] three different options are suggested:

OPTION 1 - CONTINUITY OF CONCENTRATION

$$c_T = c_I. \tag{5.4.13}$$

We used this simple boundary condition in the original model presented above.

OPTION 2 - FLUX CONDITION The flux of nutrient concentration across the boundary is proportional to the difference in concentrations on either side,

$$(c_I \boldsymbol{v}_I - D_I \boldsymbol{\nabla} c_I) \cdot \boldsymbol{n} = (c_T \boldsymbol{v}_T - D_T \boldsymbol{\nabla} c_T) \cdot \boldsymbol{n} = r\,(c_T - c_I)\,, \tag{5.4.14}$$

where r is a constant.

OPTION 3 - CONSEQUENCE OF SPECIES SOLUBILITY

$$\alpha c_I = c_T, \tag{5.4.15}$$

where α is a constant.

We investigate the choice of boundary condition, and scaling of associated constant, on the effective macroscale description. Note that the choice of condition has no direct impact on the Stokes problem on the periodic cell.

Option 2 - Flux condition

First the boundary condition is linearised, and we assume at steady state the nutrient concentration is equal and uniform across both domains, Ω_I and Ω_T, and that $r = O(1)$ here. The linearised boundary condition is given by:

$$c^* \left(\boldsymbol{v}_I - \boldsymbol{v}_\Gamma - \frac{1}{Pe_I} \boldsymbol{\nabla} c_I \right) \cdot \boldsymbol{n} = c^* \left(\boldsymbol{v}_T - \boldsymbol{v}_\Gamma - \frac{1}{Pe_T} \boldsymbol{\nabla} c_T \right) \cdot \boldsymbol{n} = r\,(c_T - c_I)\,. \tag{5.4.16}$$

For the multiple scales analysis we choose that

$$r = \begin{cases} r & \text{or} \\ \varepsilon \bar{r} \end{cases} \tag{5.4.17}$$

where r, $\bar{r} = O(1)$. At leading order

$$-\frac{1}{Pe_I}\boldsymbol{\nabla}_{\boldsymbol{x}} c_I^{(0)} \cdot \boldsymbol{n} = -\frac{1}{Pe_T}\boldsymbol{\nabla}_{\boldsymbol{x}} c_T^{(0)} \cdot \boldsymbol{n} = \begin{cases} r\left(c_T^{(0)} - c_I^{(0)}\right) \\ 0 \end{cases} \tag{5.4.18}$$

We recall that the leading order problem is quasi-steady so there is no growth of Ω_T, flux of fluid across Γ or nutrient uptake. Corrrespondingly, and in line with the linearised model setup, it is sensible to assume that there is no induced diffusive transport of nutrient across Γ either. In the first sub-case this implies that, since $r \neq 0$, $c_T^{(0)} = c_I^{(0)}$, whilst in the second sub-case there is already no diffusion across the interface.

In both cases, the leading order concentration in each domain is independent of $\boldsymbol{x}$, and in the first only we require $c_T^{(0)} = c_I^{(0)}$. Following through the rest of the analysis for the first case we find that the effective macroscale equation is unchanged,

$$\Phi_{T\cup I}\frac{\partial c^{(0)}}{\partial t} + c^*\left(1-\bar{\rho}\right)\langle S_n^{(0)}\rangle_T = -\langle \Lambda^{(0)}\rangle_T. \tag{5.4.19}$$

In the second case, as leading order concentrations in each domain may be different, the equations are changed slightly as we do not have the same simplifications. The averaged equations in each domain are given by

$$\Phi_T\frac{\partial c_T^{(0)}}{\partial t} + c^*\left(1-\bar{\rho}\right)\langle S_n^{(0)}\rangle_T = -\langle \bar{r}\left(c_T^{(0)} - c_I^{(0)}\right)\rangle_\Gamma - \langle \Lambda^{(0)}\rangle_T \tag{5.4.20}$$

$$\Phi_I\frac{\partial c_I^{(0)}}{\partial t} = \langle \bar{r}\left(c_T^{(0)} - c_I^{(0)}\right)\rangle_\Gamma, \tag{5.4.21}$$

which are the same as in [139] except that the advection term has been linearised. Macroscale nutrient concentration in this case is given by two coupled equations, one for each of $c_T^{(0)}$ and $c_I^{(0)}$. We do, however, still see an apparent nutrient source/sink due to difference in phase density and the uptake term remains the same.

Option 3 - Consequence of species solubility

Here the boundary condition on the tissue-interstitium interface is given by

$$\alpha c_I = c_T, \tag{5.4.22}$$

where α is a constant. We assume that α is a known value, although in reality it is likely to be a function of the cell volume fraction. When linearising the model equations we can no longer assume that at steady state nutrient concentration is uniform across the entire unit cell unless $\alpha = 1$ which returns us to option 1 – continuity of concentration. We instead suppose that nutrient concentration is uniform in each domain, connected by the boundary condition, i.e.

$$c_T = c_T^* + \delta c_{T1} + ... \tag{5.4.23}$$

$$c_I = c_I^* + \delta c_{I1} + ... \tag{5.4.24}$$

where

$$\alpha c_I^* = c_T^*. \tag{5.4.25}$$

As previously, c_T^* is determined by choosing the value of nutrient concentration at which both the cell proliferation term, S_n, and nutrient uptake, λ, are zero. (In the example in [139] the constant linking the two concentrations, here α, is taken to be of O(ε) as solubility is assumed to be much less in one domain than the other. We choose it to be O(1) instead.)

The linearised and rescaled equations for the nutrient concentration are given by:

$$\varepsilon\frac{\partial c_{T,1}}{\partial t} + \boldsymbol{\nabla}\cdot\left(c_T^*\left(\theta_n^*\boldsymbol{v}_{n,1} + \theta_w^*\boldsymbol{v}_{w,1}\right)\right) = \frac{1}{Pe_T}\nabla^2 c_{T,1} - \Lambda_1 \text{ in } \Omega_T, \tag{5.4.26}$$

$$\varepsilon\frac{\partial c_{I,1}}{\partial t} + \boldsymbol{\nabla}\cdot\left(c_I^*\boldsymbol{v}_{I,1}\right) = \frac{1}{Pe_I}\boldsymbol{\nabla}^2 c_{I,1} \text{ in } \Omega_I, \tag{5.4.27}$$

$$\left[c_i^*\left(\boldsymbol{v}_{i,1} - \boldsymbol{v}_{\Gamma,1}\right)\cdot\boldsymbol{n} - \frac{1}{Pe_i}\boldsymbol{\nabla}c_{i,1}\cdot\boldsymbol{n}\right]_-^+ = 0, \tag{5.4.28}$$

$$\alpha c_{I,1} = c_{T,1} \text{ on } \Gamma. \tag{5.4.29}$$

All other equations remain unchanged from the original analysis, except that in cell proliferation and nutrient uptake terms c^* is replaced by c_T^*.

At leading order, after simplifications are made due to no nutrient uptake or growth, and dropping the subscripts associated with the linearisation,

$$0 = \frac{1}{Pe_T}\nabla_{\boldsymbol{x}}^2 c_T^{(0)} \text{ on } \Omega_T, \tag{5.4.30}$$

$$0 = \frac{1}{Pe_I}\boldsymbol{\nabla}_{\boldsymbol{x}}^2 c_I^{(0)} \text{ on } \Omega_I, \tag{5.4.31}$$

$$\left[\frac{1}{Pe_i}\boldsymbol{\nabla}_{\boldsymbol{x}} c_i^{(0)} \cdot \boldsymbol{n}\right]_-^+ = 0, \tag{5.4.32}$$

$$\alpha c_I^{(0)} = c_T^{(0)} \text{ on } \Gamma. \tag{5.4.33}$$

From this we conclude that both $c_I^{(0)}$ and $c_T^{(0)}$ are independent of the microscale and related by (5.4.33).

At next order the relevant equations are:

$$\begin{aligned}&\frac{\partial c_T^{(0)}}{\partial t} + c_T^*\left(\boldsymbol{\nabla}_{\boldsymbol{x}} \cdot \left(\theta_n^* \boldsymbol{v}_n^{(1)} + \theta_w^* \boldsymbol{v}_w^{(1)}\right) + \boldsymbol{\nabla}_{\boldsymbol{X}} \cdot \left(\theta_n^* \boldsymbol{v}_n^{(0)} + \theta_w^* \boldsymbol{v}_w^{(0)}\right)\right)\\ &= \frac{1}{Pe_T}\nabla_{\boldsymbol{x}}^2 c_T^{(1)} - \Lambda^{(0)} \text{ on } \Omega_T,\end{aligned} \tag{5.4.34}$$

$$\frac{\partial c_I^{(0)}}{\partial t} + c_I^*\left(\boldsymbol{\nabla}_{\boldsymbol{x}} \cdot \boldsymbol{v}_I^{(1)} + \boldsymbol{\nabla}_{\boldsymbol{X}} \cdot \boldsymbol{v}_I^{(0)}\right) = \frac{1}{Pe_I}\boldsymbol{\nabla}_{\boldsymbol{x}}^2 c_I^{(1)} \text{ on } \Omega_I, \tag{5.4.35}$$

$$\left[c_i^*\left(\boldsymbol{v}_i^{(1)} - \boldsymbol{v}_\Gamma^{(1)}\right) \cdot \boldsymbol{n} - \frac{1}{Pe_i}\left(\boldsymbol{\nabla}_{\boldsymbol{x}} c_i^{(1)} + \boldsymbol{\nabla}_{\boldsymbol{X}} c_i^{(0)}\right) \cdot \boldsymbol{n}\right]_-^+ = 0, \tag{5.4.36}$$

$$\alpha c_I^{(1)} = c_T^{(1)} \text{ on } \Gamma. \tag{5.4.37}$$

On averaging (5.4.34) and (5.4.35) over their domains, we obtain:

$$\Phi_T \frac{\partial c_T^{(0)}}{\partial t} + c_T^*\left(1 - \bar{\rho}\right)\langle S_n^{(0)}\rangle_T = \langle \frac{1}{Pe_T}\boldsymbol{\nabla}_{\boldsymbol{x}} c_T^{(1)} \cdot \boldsymbol{n}\rangle_\Gamma - \langle \Lambda^{(0)}\rangle_T, \tag{5.4.38}$$

$$\Phi_I \frac{\partial c_I^{(0)}}{\partial t} = -\langle \frac{1}{Pe_I}\boldsymbol{\nabla}_{\boldsymbol{x}} c_I^{(1)} \cdot \boldsymbol{n}\rangle_\Gamma. \tag{5.4.39}$$

Averaging boundary condition (5.4.36) over Γ and rearranging, we find that

$$\langle \frac{1}{Pe_T}\boldsymbol{\nabla}_{\boldsymbol{x}} c_T^{(1)} \cdot \boldsymbol{n}\rangle_\Gamma - \langle \frac{1}{Pe_I}\boldsymbol{\nabla}_{\boldsymbol{x}} c_I^{(1)} \cdot \boldsymbol{n}\rangle_\Gamma = \left(c_T^* - c_I^*\right)\langle Q^{(0)}\rangle_\Gamma \tag{5.4.40}$$

where

$$Q^{(0)} = \left(\boldsymbol{v}_I^{(1)} - \boldsymbol{v}_\Gamma^{(1)}\right) \cdot \boldsymbol{n} = \left(\boldsymbol{v}_T^{(1)} - \boldsymbol{v}_\Gamma^{(1)}\right) \cdot \boldsymbol{n} = \theta_w^*\left(\boldsymbol{v}_w^{(1)} - \boldsymbol{v}_\Gamma^{(1)}\right) \cdot \boldsymbol{n} \tag{5.4.41}$$

The overall equation, by summing (5.4.38) and (5.4.39) is

$$\Phi_T \frac{\partial c_T^{(0)}}{\partial t} + \Phi_I \frac{\partial c_I^{(0)}}{\partial t} + c_T^* (1-\bar{\rho}) \langle S_n^{(0)} \rangle_T = (c_T^* - c_I^*) \langle Q^{(0)} \rangle_\Gamma - \langle \Lambda^{(0)} \rangle_T, \quad (5.4.42)$$

where c_I^* and $c_I^{(0)}$ can be removed by (5.4.25) and (5.4.33) to give

$$\left(\Phi_T + \frac{1}{\alpha} \Phi_I \right) \frac{\partial c_T^{(0)}}{\partial t} + c_T^* (1-\bar{\rho}) \langle S_n^{(0)} \rangle_T = c_T^* \left(1 - \frac{1}{\alpha} \right) \langle Q^{(0)} \rangle_\Gamma - \langle \Lambda^{(0)} \rangle_T, \quad (5.4.43)$$

and $Q^{(0)}$ must be determined. Note that when $\alpha = 1$, i.e. we have continuity of concentration on the boundary, we obtain (5.3.84) as in the original model, and $Q^{(0)}$ no longer appears.

The term $Q^{(0)}$ describes the leading order flux of material across the boundary of the tissue domain. Given the velocity of the boundary, v_Γ, one can track its position using the level set equation. In the case where the phase densities are equal, the increase in the volume of the tissue domain is due only to the influx of material and hence gives $Q^{(0)}$.

5.5 SUMMARY

In this chapter we derived an effective macroscale description of nutrient limited tissue growth, from the underlying microscale multiphase model of chapter 3. In chapter 4, we assumed the drag between the cell and water phases of the tissue was large to give a problem more amenable to a multiscale analysis. Here, to permit active cell motion and therefore allow a more complex description of tissue growth, we relaxed this assumption. As a fully nonlinear analysis of the type considered in [44] is complicated by the interphase transfer that we accommodate and since we seek a tractable description, here we considered a linearisation of the model to permit a more straightforward multiscale analysis. This different approach allows material to cross the tissue-interstitium boundary, removing the need for a surface production term, as well as allowing cell motility via cell-cell interaction.

Via a a two scale analysis, we obtain an effective macroscale description of tissue growth that consists of Darcy flow, with compressibility dependent on the difference in density between the tissue phases, and differential equations for the nutrient concentration and cell volume fraction. These are similar to those derived in the large drag limit case, in that microscale growth appears in the leading order macroscale description and there is an apparent nutrient source/sink due to phase density differences. There are differences due to the linearisation about a steady state with zero velocities and the lack of surface production term in this case.

The macroscale formulation is parameterised by permeability tensors, with multiscale dependence, provided by a set of modified Stokes-type cell problems. The Stokes problems are more complex than those of chapter 4, due to the additional coupling to the macroscale pressures. They can be solved numerically to find the permeabilities for each phase in each domain, as functions of the cell volume fraction and the gradient of the macroscale pressures (see chapter 7 for more detail). We also note that this additional complexity can in fact be avoided by using an alternative choice of appropriate form for the macroscale velocities and microscale pressures. This is explored further in chapter 6.

The effect of a number of subcases and alternate boundary conditions on the macroscale description are investigated. The case where the water is modelled as inviscid provides significant simplifications to the Stokes problems, decoupling them from the macroscale pressures, whilst linearisation about the trivial steady state value for the cell volume fraction removes the need to determine the tissue boundary velocity. Different scaffold boundary conditions can be easily incorporated by minor changes to the Stokes problems and alternative nutrient concentration boundary conditions impact the macroscale differential equation.

The macroscale equation for the cell volume fraction includes the term $\boldsymbol{v}_\Gamma \cdot \boldsymbol{n}$, the $O(\varepsilon)$ tissue-interstitium boundary velocity. This is unknown but must be determined to close the model. The boundary velocity should arise

naturally from the movement of the cells in response to intraphase pressure gradients, and in principle can be obtained via a suitable free boundary problem. Alternatively, for simplicity, one could define it constitutively and to provide a rationale for this choice we investigate numerically the full non-linear model (see section 3.8), in one spatial dimension, in chapter 7.

There are of course limitations to the model, including that the linearised equations are only strictly valid close to the steady state. Other limitations such as the constraint on the length scales and local periodicity can be met more easily by some scaffolds than others, whilst creating a periodic tissue layer over the entire scaffold may be challenging in all cases.

There are many possible extensions to this work such as finding a way to derive a macroscale description without linearisation, or considering timescales on which the scaffold degrades. The multiphase mixture model is interesting in itself and its travelling-wave behaviour is studied further in the chapter 7, in particular, in order to determine the tissue-interstitium boundary velocity and provide closure to the model.

6

AN ALTERNATIVE ANSATZ FOR THE LINEARISED MULTISCALE MODEL

6.1 INTRODUCTION

In chapter 5 we derived an effective macroscale description of nutrient-limited tissue growth. This consists of coupled microscale cell problems, see section 5.3.5, and a macroscale equations for Darcy flow, nutrient concentration and cell volume fraction (5.3.79,5.3.80,5.3.84,5.3.85). The cell problems are coupled to the macroscale description through the macroscale pressure and active cell behaviour terms, leading to significant computational challenges. In particular, they must be solved multiple times to determine the permeabilities as functions of the macroscale variables. By use of an alternative ansatz for the macroscale velocities and microscale pressures, proposed by Jon Chapman, it is possible to avoid this complexity, deriving cell problems without macroscale dependence. In this chapter we give the more suitable ansatz form and derive the resulting cells problems.

6.2 APPROPRIATE FORM FOR THE MACROSCALE VELOCITIES AND MICROSCALE PRESSURES

Due to the linearity of the momentum equations, see (4.3.47,4.3.50) and (5.3.495.3.50), it is typical [52, 100, 115, 140] to take an appropriate form

for the macroscale velocities and microscale pressures to be given by the following ansatz:

$$\boldsymbol{v}_i^{(0)} = -\boldsymbol{K}_i \boldsymbol{\nabla}_X p^{(0)} \text{ and } p_i^{(1)} = -\boldsymbol{a}_i \boldsymbol{\nabla}_X p^{(0)} - \bar{p}_i, \tag{6.2.1}$$

where $p^{(0)}$ is the overall macroscale pressure, $\boldsymbol{K}_i$ are tensors describing the permeability, $\boldsymbol{a}_i$ are first order tensors imparting microscale variation, and $\bar{p}_i$ are the mean values of the first order pressures in Ω_i, hence microscale invariant. In the linearised model of chapter 5, this choice of ansatz results in coupling of the cell problems to the macroscale pressure and active cell behaviour terms in the tissue domain. We seek to remove this complexity, and as both the macroscale pressure and active cell behaviour terms appear linearly in the momentum equations (5.3.49,5.3.50) a more appropriate for the macroscale velocities and microscale pressures takes the following form:

$$\begin{aligned} \boldsymbol{v}_i^{(0)} &= -\boldsymbol{K}_i \boldsymbol{\nabla}_X p_w^{(0)} - \boldsymbol{M}_i \boldsymbol{\nabla}_X \phi_n^{(0)}, \\ p_i^{(1)} &= -\boldsymbol{a}_i \boldsymbol{\nabla}_X p_w^{(0)} - \boldsymbol{b}_i \boldsymbol{\nabla}_X \phi_n^{(0)} - \bar{p}_i. \end{aligned} \tag{6.2.2}$$

Note that rather than an ansatz in terms the overall macroscale pressure $p^{(0)}$, in (6.2.2) the macroscale velocities and microscale pressures are given as linear functions of the macroscale common mixture pressure $p_w^{(0)}$ and extra pressure due to cell aggregation $\phi_n^{(0)}$. (Recall, from the leading order analysis of chapter 5 we obtained (5.3.44), i.e.

$$p^{(0)}(\boldsymbol{X}, t) = p_{\scriptscriptstyle I}^{(0)}(\boldsymbol{X}, t) = p_w^{(0)}(\boldsymbol{X}, t) + \theta_n^* \phi_n^{(0)}(\boldsymbol{X}, t).) \tag{6.2.3}$$

In the limit of large drag (chapter 4) and the interstitial domain in the linearised model (chapter 5), where pressure caused by cell aggregation is not a feature, the original ansatz (4.3.61) remains suitable.

6.3 MICROSCALE CELL PROBLEM

Substituting (6.2.2) into equation (5.3.24) we have

$$\left[\boldsymbol{\nabla}_{\boldsymbol{x}} \cdot \boldsymbol{K}_n^{\mathsf{T}}\right] \boldsymbol{\nabla}_X p_w^{(0)} + \left[\boldsymbol{\nabla}_{\boldsymbol{x}} \cdot \boldsymbol{M}_n^{\mathsf{T}}\right] \boldsymbol{\nabla}_X \phi_n^{(0)} = 0, \tag{6.3.1}$$

as both $p_w^{(0)}$ and $\phi_n^{(0)}$ are independent of $\boldsymbol{x}$. Assuming that $\boldsymbol{\nabla}_X p_w^{(0)}$, $\boldsymbol{\nabla}_X \phi_n^{(0)} \neq \mathbf{0}$ and the $\boldsymbol{\nabla}_X p_w^{(0)}$, $\boldsymbol{\nabla}_X \phi_n^{(0)}$ terms are not equal and opposite, (6.3.1) implies that

$$\boldsymbol{\nabla}_{\boldsymbol{x}} \cdot \boldsymbol{K}_n^{\mathsf{T}} = \mathbf{0}, \quad \boldsymbol{\nabla}_{\boldsymbol{x}} \cdot \boldsymbol{M}_n^{\mathsf{T}} = \mathbf{0}, \tag{6.3.2}$$

in Ω_T. Similarly from equation (5.3.25) we have

$$\boldsymbol{\nabla}_{\boldsymbol{x}} \cdot \boldsymbol{K}_w^{\mathsf{T}} = \mathbf{0}, \quad \boldsymbol{\nabla}_{\boldsymbol{x}} \cdot \boldsymbol{M}_w^{\mathsf{T}} = \mathbf{0}, \tag{6.3.3}$$

in Ω_T. The two momentum equations (5.3.49) and (5.3.50) provide:

$$\boldsymbol{\nabla}_{\boldsymbol{x}} \boldsymbol{a}_n^{\mathsf{T}} - \boldsymbol{I} - \nabla_{\boldsymbol{x}}^2 \boldsymbol{K}_n - \beta \theta_w^* \left(\boldsymbol{K}_w - \boldsymbol{K}_n \right) = \mathbf{0}, \tag{6.3.4}$$

$$\boldsymbol{\nabla}_{\boldsymbol{x}} \boldsymbol{a}_w^{\mathsf{T}} - \boldsymbol{I} - \mu \nabla_{\boldsymbol{x}}^2 \boldsymbol{K}_w - \beta \theta_n^* \left(\boldsymbol{K}_n - \boldsymbol{K}_w \right) = \mathbf{0}, \tag{6.3.5}$$

$$\boldsymbol{\nabla}_{\boldsymbol{x}} \boldsymbol{b}_n^{\mathsf{T}} - \boldsymbol{I} - \nabla_{\boldsymbol{x}}^2 \boldsymbol{M}_n - \beta \theta_w^* \left(\boldsymbol{M}_w - \boldsymbol{M}_n \right) = \mathbf{0}, \tag{6.3.6}$$

$$\boldsymbol{\nabla}_{\boldsymbol{x}} \boldsymbol{b}_w^{\mathsf{T}} - \mu \nabla_{\boldsymbol{x}}^2 \boldsymbol{M}_w - \beta \theta_n^* \left(\boldsymbol{M}_n - \boldsymbol{M}_w \right) = \mathbf{0}, \tag{6.3.7}$$

in Ω_T. Note that the last equation contains no forcing via $\boldsymbol{I}$, but it does have dependence on $\boldsymbol{M}_n$, which is subject to forcing, through the interphase drag term. Boundary conditions (5.3.34,5.3.35) and (5.3.42) give

$$\boldsymbol{K}_n^{\mathsf{T}} \boldsymbol{n} = \mathbf{0}, \quad \boldsymbol{K}_w^{\mathsf{T}} \boldsymbol{n} = \mathbf{0}, \quad \boldsymbol{M}_n^{\mathsf{T}} \boldsymbol{n} = \mathbf{0}, \quad \boldsymbol{M}_w^{\mathsf{T}} \boldsymbol{n} = \mathbf{0} \text{ on } \Gamma, \tag{6.3.8}$$

$$\boldsymbol{K}_n = \mathbf{0}, \quad \boldsymbol{K}_w = \mathbf{0}, \quad \boldsymbol{M}_n = \mathbf{0}, \quad \boldsymbol{M}_w = \mathbf{0} \text{ on } \partial\Omega_S. \tag{6.3.9}$$

Using the continuity of stress condition (5.3.58) we find that, as the microscale invariant contributions to stress are continuous, i.e. $\bar{p}_I = \theta_n^* \bar{p}_n + \theta_w^* \bar{p}_w$, on the boundary, Γ, we have

$$\begin{aligned} &\left[-\boldsymbol{a}_T \otimes \boldsymbol{I} + \left(\boldsymbol{\nabla} \boldsymbol{K}_T + (\boldsymbol{\nabla} \boldsymbol{K}_T)^{\mathsf{T}} \right) \right] \boldsymbol{\nabla}_X p_w^{(0)} \\ &+ \left[-\boldsymbol{b}_T \otimes \boldsymbol{I} + \left(\boldsymbol{\nabla} \boldsymbol{M}_T + (\boldsymbol{\nabla} \boldsymbol{M}_T)^{\mathsf{T}} \right) \right] \boldsymbol{\nabla}_X \phi_n^{(0)} \\ &= \left[-\boldsymbol{a}_I \otimes \boldsymbol{I} + \mu \left(\boldsymbol{\nabla} \boldsymbol{K}_I + (\boldsymbol{\nabla} \boldsymbol{K}_I)^{\mathsf{T}} \right) \right] \boldsymbol{\nabla}_X p_I^{(0)}, \end{aligned} \tag{6.3.10}$$

where

$$\boldsymbol{K}_T = \theta_n^* \boldsymbol{K}_n + \mu \theta_w^* \boldsymbol{K}_w, \qquad \boldsymbol{a}_T = \theta_n^* \boldsymbol{a}_n + \theta_w^* \boldsymbol{a}_w, \tag{6.3.11}$$

$$\boldsymbol{M}_T = \theta_n^* \boldsymbol{M}_n + \mu \theta_w^* \boldsymbol{M}_w, \qquad \boldsymbol{b}_T = \theta_n^* \boldsymbol{b}_n + \theta_w^* \boldsymbol{b}_w. \tag{6.3.12}$$

Using (5.3.44) to replace $p^{(0)}$, (6.3.10) becomes

$$-\boldsymbol{a}_T \otimes \boldsymbol{I} + \left(\boldsymbol{\nabla} \boldsymbol{K}_T + (\boldsymbol{\nabla} \boldsymbol{K}_T)^{\mathsf{T}}\right) = -\boldsymbol{a}_I \otimes \boldsymbol{I} + \mu \left(\boldsymbol{\nabla} \boldsymbol{K}_I + (\boldsymbol{\nabla} \boldsymbol{K}_I)^{\mathsf{T}}\right), \tag{6.3.13}$$

$$-\boldsymbol{b}_T \otimes \boldsymbol{I} + \left(\boldsymbol{\nabla} \boldsymbol{M}_T + (\boldsymbol{\nabla} \boldsymbol{M}_T)^{\mathsf{T}}\right) = \theta_n^* \left[-\boldsymbol{a}_I \otimes \boldsymbol{I} + \mu \left(\boldsymbol{\nabla} \boldsymbol{K}_I + (\boldsymbol{\nabla} \boldsymbol{K}_I)^{\mathsf{T}}\right)\right]. \tag{6.3.14}$$

Whilst the number of cell problems has increased as a result of the change in ansatz we find that the permeability tensors are no longer dependent on macroscale pressures. Previously, as a consequence of this dependency, the cell problems required solving multiple times to determine the permeabilities as functions of the macroscale pressures. Now decoupled, only one solution to the cell problems is necessary for a given microscale geometry, providing significant simplification to the model.

6.4 IMPACT ON THE MACROSCALE DESCRIPTION

The impact on the macroscale level description of this alternative form for the macroscale velocities and microscale pressures is minimal. Equation (5.3.79) for the average macroscale velocity and (5.3.84) for nutrient concentration remain unchanged. In the equation for cell volume fraction (5.3.85), $\boldsymbol{v}_n^{(0)}$ is given by the new ansatz (6.2.2). Finally, in the equation for macroscale pressure, (5.3.80), becomes

$$\boldsymbol{\nabla}_{\boldsymbol{X}} \cdot \left(\tilde{\boldsymbol{K}} \boldsymbol{\nabla}_{\boldsymbol{X}} p_w^{(0)} + \tilde{\boldsymbol{M}} \boldsymbol{\nabla}_{\boldsymbol{X}} \phi_n^{(0)}\right) = -\langle (1-\bar{\rho})\, S_n^{(0)} \rangle_T, \tag{6.4.1}$$

where

$$\tilde{\boldsymbol{K}} = \langle \theta_n^* \boldsymbol{K}_n + \theta_w^* \boldsymbol{K}_w \rangle_T + \langle \boldsymbol{K}_I \rangle_I, \quad \tilde{\boldsymbol{M}} = \langle \theta_n^* \boldsymbol{M}_n + \theta_w^* \boldsymbol{M}_w \rangle_T + \langle \theta_n^* \boldsymbol{K}_I \rangle_I. \tag{6.4.2}$$

Recall that $\phi_n^{(0)}$ is not an additional unknown variable but is a known linearised function of $\theta_n^{(0)}$ given by (5.3.43).

6.5 IN THE INVISCID WATER SUBCASE

As previously, when the water phase is modelled as inviscid, the overall pressure $p^{(0)}$ is zero and consequently so is $p_w^{(0)} + \theta_n^* \phi_n^{(0)}$. This means that the new ansatz (6.2.2) can be rewritten as

$$\begin{aligned} \boldsymbol{v}_i^{(0)} &= \left[-\boldsymbol{K}_i + \frac{1}{\theta_n^*} \boldsymbol{M}_i \right] \boldsymbol{\nabla}_X p_w^{(0)}, \\ p_i^{(1)} &= \left[-\boldsymbol{a}_i + \frac{1}{\theta_n^*} \boldsymbol{b}_i \right] \boldsymbol{\nabla}_X p_w^{(0)} - \bar{p}_i, \end{aligned} \tag{6.5.1}$$

which is essentially the form used in section 5.4.1 where the terms in square brackets are given by single tensors.

6.6 SUMMARY

The alternative ansatz for the macroscale velocities and microscale pressures described in this chapter, suggested by Jon Chapman, gives considerable simplification to the model of chapter 5. Whilst the number of problems on the periodic cell is increased, there is no coupling to the macroscale pressures. This reduction in complexity means that the Stokes-type cell problems can be solved once for a given geometry and does not require an exploration of parameter space to determine the permeability tensor as a function of the macroscale pressure.

Whilst cell problems have been simplified, the macroscale equation for cell volume fraction (5.3.85) remains unchanged, hence the model is still subject to the issue of closure regarding the tissue-interstitium boundary velocity. This is addressed in the following chapter.

7

MODEL CLOSURE AND NUMERICAL SOLUTIONS

7.1 INTRODUCTION

In chapters 4 and 5, we began with a pore-scale multiphase mixture model for tissue growth on a scaffold, and derived suitable effective equations for the dynamics at the macro-scale via multiscale homogenisation. The resulting macroscale models are not closed; the first requires specification of surface production and the second the microscale motion of the free tissue boundary. In principle these can be obtained directly by considering a suitable free boundary problem but here, for simplicity, we seek to specify the boundary velocity constitutively.

To rationalise a suitable constitutive statement for the interface velocity, and hence provide closure to the macroscale description, we investigate in this chapter the travelling wave behaviour of the underlying microscale multiphase model. Considering a $1D$ reduction for simplicity, here we find solutions in the form of travelling waves, as observed in a similar formulation described in [89]. We investigate the dependence of the interface velocity on the various model parameters, concentrating in particular on those associated with the cells' motile properties, to inform a suitable constitutive choice for the interface velocity. Using this form for the velocity, we present illustrative numerical simulations of the microscopic cell problems and corresponding effective macroscale description, for the inviscid water case.

Beginning with the full equations in section 7.2, we reduce them following the method of [89] in section 7.3 to a pair of coupled partial differential equations describing the volume fraction of cells and their velocity. In section 7.4 we introduce the method of finite volumes, with which we obtain numerical solutions to the model in section 7.5. In section 7.6 we present the illustrative numerical simulations for the microscopic cell problems and corresponding effective macroscale description. Conclusions for this chapter are given in section 7.7

7.2 MODEL EQUATIONS

We consider, for simplicity, the multiphase mixture model of chapter 3 in a semi-infinite one dimensional domain, $0 \leqslant x < \infty$, with the scaffold-tissue boundary located at $x = 0$. The scaffold is unreactive and hence not involved in the calculations except to stop any material moving past this point. The tissue domain exists from the scaffold to the free boundary at $x = \Gamma(t)$. Beyond this is the interstitial domain, containing only water. This is illustrated in figure 13.

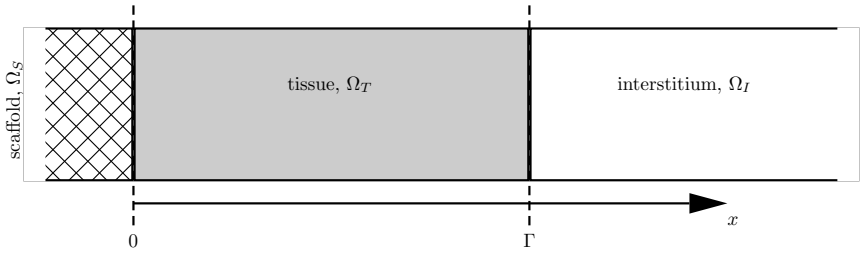


Figure 13: Illustration to show the three domains for the 1D model.

In the tissue domain, Ω_T, we have the two phase mixture of cells and water, with volume fractions θ_n and θ_w respectively. In one dimension the conservation and momentum equations (3.8.2,3.8.4–3.8.7) are given by:

$$\frac{\partial \theta_n}{\partial t} + \frac{\partial}{\partial x}(\theta_n v_n) = S_n, \tag{7.2.1}$$

$$\frac{\partial}{\partial x}(\theta_n v_n + \theta_w v_w) = 0, \tag{7.2.2}$$

$$\theta_n + \theta_w = 1, \tag{7.2.3}$$

$$-\theta_n \frac{\partial p_w}{\partial x} - \frac{\partial}{\partial x}\left(\theta_n^2\left(-\nu + \frac{\kappa\theta_n}{1-\theta_n}\right)\right) + \frac{\partial}{\partial x}\left(\frac{4}{3}\theta_n \frac{\partial v_n}{\partial x}\right) + \beta\theta_n\theta_w(v_w - v_n) = 0, \tag{7.2.4}$$

$$-\theta_w \frac{\partial p_w}{\partial x} + \frac{\partial}{\partial x}\left(\frac{4}{3}\mu\theta_w \frac{\partial v_w}{\partial x}\right) + \beta\theta_n\theta_w(v_n - v_w) = 0. \tag{7.2.5}$$

Note that here we have assumed that the two phases are of equal density, which aids the simplification which follows in the next section. In the interstitial domain, Ω_I, where we have the water phase only present, the governing equations (3.8.9–3.8.11) are:

$$\frac{\partial v_I}{\partial x} = 0, \tag{7.2.6}$$

$$\theta_w = 1, \tag{7.2.7}$$

$$\frac{\partial p_I}{\partial x} + \frac{\partial}{\partial x}\left(\frac{4}{3}\mu\frac{\partial v_I}{\partial x}\right) = 0. \tag{7.2.8}$$

The concentration of nutrient, on which the growth function S_n depends, in each domain is described by advection-diffusion equations (3.8.8, 3.8.12):

$$\frac{\partial c_T}{\partial t} + \frac{\partial}{\partial x}(c_T(\theta_n v_n + \theta_w v_w)) = \frac{\partial}{\partial x}\left(\frac{1}{Pe_T}\frac{\partial c_T}{\partial x}\right) - \lambda, \tag{7.2.9}$$

$$\frac{\partial c_I}{\partial t} + \frac{\partial}{\partial x}(c_I v_I) = \frac{\partial}{\partial x}\left(\frac{1}{Pe_I}\frac{\partial c_I}{\partial x}\right). \tag{7.2.10}$$

At the boundary with the scaffold, $x = 0$, we have the following conditions, from (3.8.13–3.8.15):

$$\frac{\partial \theta_n}{\partial x} = 0, \quad v_n = v_w = 0, \quad \frac{\partial c_T}{\partial x} = 0, \tag{7.2.11}$$

guaranteeing no penetration of cells, water or nutrient into the scaffold. The position of the free interface, Γ, is located where the cell density

vanishes[1]. The boundary conditions, continuity of mass flux (3.8.17,3.8.18), stress (3.8.20), nutrient concentration and flux (3.8.21,3.8.22), on the interface $x = \Gamma$ are given by

$$(v_I - v_\Gamma) = \theta_w (v_w - v_\Gamma), \tag{7.2.12}$$

$$\theta_n (v_n - v_\Gamma) = 0 \tag{7.2.13}$$

$$-p_I + \frac{4}{3}\mu\frac{\partial v_I}{\partial x} = -p_w - \theta_n^2\left(-\nu + \frac{\kappa\theta_n}{1-\theta_n}\right) + \frac{4}{3}\theta_n\frac{\partial v_n}{\partial x} + \frac{4}{3}\mu\theta_w\frac{\partial v_w}{\partial x}, \tag{7.2.14}$$

$$c_T = c_I, \tag{7.2.15}$$

$$\frac{1}{Pe_T}\frac{\partial c_T}{\partial x} = \frac{1}{Pe_I}\frac{\partial c_I}{\partial x}. \tag{7.2.16}$$

This model has strong similarities to that of [89] where tissue growth within a scaffold is studied. The main difference is that the model in [89] is posed on the macroscale, with the scaffold, tissue and interstitium represented as phases of a mixture. Scaffold interaction is given similarly to the tissue phase, with cells affinity for the scaffold described by a similar functional form as the cell-cell attraction, ϕ_n, and interphase drag between scaffold and cells. Our model describes microscale dynamics, with a two phase mixture representing the tissue and two further domains for the scaffold and interstitium. Whilst the tissue description used here does not include the scaffold related terms of [89], we do include viscosity of the water phase and cell-water drag which are neglected therein.

7.3 REDUCTION

Following [89], the model (7.2.1–7.2.8) can be expressed as a pair of differential equations in two variables. This provides a convenient form for numerical solution. To aid this we also simplify the equations (7.2.9,7.2.9) relating to nutrient concentration.

1 In the numerical analysis that follows, we see that cell density may vanish at multiple points when the steady state is unstable. However, we do not focus on this case.

7.3.1 *Interstitial domain, Ω_I*

Considering first the interstitial domain, we see that equations (7.2.6) and (7.2.8) imply that v_I and p_I are independent of x. Following [89] we assume that

$$v_I,\ p_I \to 0 \text{ as } x \to \infty, \tag{7.3.1}$$

which reduces the interstitial variables to

$$v_I = 0 \text{ and } p_I = 0. \tag{7.3.2}$$

7.3.2 *Tissue domain, Ω_T*

We begin by integrating (7.2.2) with respect to x, which gives $\theta_n v_n + \theta_w v_w = k$, for some function of time $k(t)$. Applying the boundary conditions (7.2.11) we find that $k = 0$. This, in addition to equation (7.2.3), allows us to eliminate both θ_w and v_w by

$$\theta_w = 1 - \theta_n, \tag{7.3.3}$$

$$v_w = -\frac{\theta_n}{1-\theta_n} v_n. \tag{7.3.4}$$

Next we eliminate p_w from our equations by subtracting the product of θ_n and (7.2.5) from that of θ_w and (7.2.4) to give

$$\begin{aligned} -\theta_w \frac{\partial}{\partial x}\left(\theta_n^2\left(-\nu + \frac{\kappa\theta_n}{1-\theta_n}\right)\right) + \theta_w \frac{\partial}{\partial x}\left(\frac{4}{3}\theta_n \frac{\partial v_n}{\partial x}\right) \\ - \theta_n \frac{\partial}{\partial x}\left(\frac{4}{3}\mu\theta_w \frac{\partial v_w}{\partial x}\right) + \beta\theta_n\theta_w\left(v_w - v_n\right) = 0. \end{aligned} \tag{7.3.5}$$

After elimination of θ_w and v_w, and rearranging, the behaviour in the tissue domain is given by two equations, in terms of θ_n and v_n:

$$\frac{\partial \theta_n}{\partial t} + \frac{\partial}{\partial x}\left(\theta_n v_n\right) = S_n, \tag{7.3.6}$$

$$A\frac{\partial^2 v_n}{\partial x^2} + B\frac{\partial v_n}{\partial x} + C v_n = D, \tag{7.3.7}$$

where

$$S_n = k_m\theta_n\left(1-\theta_n\right) - k_n\theta_n, \tag{7.3.8}$$

$$A = \frac{4}{3}\theta_n\left(1+\left(\mu-1\right)\theta_n\right), \tag{7.3.9}$$

$$B = \frac{4}{3}\frac{\partial\theta_n}{\partial x}\frac{1}{1-\theta_n}\left((1-\mu)\theta_n^2 + 2(\mu-1)\theta_n + 1\right), \tag{7.3.10}$$

$$C = -\beta\theta_n + \frac{4}{3}\frac{\mu\theta_n}{1-\theta_n}\left(\frac{\partial^2\theta_n}{\partial x^2} + \frac{1}{1-\theta_n}\left(\frac{\partial\theta_n}{\partial x}\right)^2\right), \tag{7.3.11}$$

$$D = \left(1-\theta_n\right)\left(-2\nu\theta_n + \frac{\kappa\theta_n^2\left(3-2\theta_n\right)}{\left(1-\theta_n\right)^2}\right)\frac{\partial\theta_n}{\partial x}. \tag{7.3.12}$$

$$\tag{7.3.13}$$

Of course, the behaviour is also dependent on the nutrient concentration, through k_m and possibly k_n as functions of c. The appropriate reduction of the remaining equations is discussed in the next section.

7.3.3 *Nutrient concentration*

In order to include nutrient dependent growth, we consider the generic nutrient, concentration c_T described by the following equation,

$$\frac{\partial c_T}{\partial t} = \frac{\partial}{\partial x}\left(\frac{1}{Pe_T}\frac{\partial c_T}{\partial x}\right) - \lambda(c_T,\theta_n), \tag{7.3.14}$$

in the tissue domain. (The absence of the advection term is due to the aggregate velocity being zero, see section 7.3.2.) For simplicity, we make the assumption that diffusion in both domains is much faster than growth and uptake, reducing (7.3.14) to

$$\frac{\partial}{\partial x}\left(\frac{1}{Pe_T}\frac{\partial c_T i}{\partial x}\right) = 0, \tag{7.3.15}$$

and similarly for (7.2.10). Along with boundary conditions (7.2.15,7.2.16), these give uniform nutrient concentration, c^*, across the tissue. Whilst this may be seen as an oversimplification, it is of relevance to the multiscale model where at leading order nutrient concentration is independent of the micro scale (i.e. x). We choose to consider this option in the numerics that follow.

7.3.4 *Boundary conditions*

Boundary condition (7.2.13) simply means that the interface velocity is given by the velocity of the cells at the interface, and used in (7.2.12) reduces it to

$$v_w = -\frac{\theta_n}{1-\theta_n} v_n, \tag{7.3.16}$$

which we had already determined to hold in the tissue from (7.3.4). The final boundary condition (7.2.14) is the continuity of stress across the interface. We have already established that the stress on the interstitial side is equal to zero so are left with

$$0 = -p_w - \theta_n^2 \left(-\nu + \frac{\kappa \theta_n}{1-\theta_n} \right) + \frac{4}{3}\theta_n \frac{\partial v_n}{\partial x} + \frac{4}{3}\mu\theta_w \frac{\partial v_w}{\partial x}. \tag{7.3.17}$$

Instead, for simplicity, we choose to impose $\partial v_n / \partial x = 0$ as in [89]. In summary, the boundary conditions that we use in the following numerics are given by

$$\text{at } x = 0: \quad \frac{\partial \theta_n}{\partial x} = 0, \quad v_n = 0, \quad \frac{\partial c_I}{\partial x} = 0, \tag{7.3.18}$$

$$\text{at } x = \Gamma: \quad \theta_n = 0, \quad \frac{\partial v_n}{\partial x} = 0, \quad c_T = c_I. \tag{7.3.19}$$

Now that we have reduced our model to two differential equations, and accompanying boundary conditions, following the approach of [89], we next discuss the numerical methods used to seek solutions.

7.4 FINITE VOLUME NUMERICAL SCHEME

7.4.1 *Overview*

Finite volume schemes are commonly used for problems involving the shallow water equations, such as dam break [65] and coastal wave problems [73]. They are particularly useful for simulating hyperbolic conservation

laws [91], such as our equation for θ_n, (7.3.6). To utilise this method the equation(s) should first be rearranged into the general conservative form

$$\frac{\partial U}{\partial t} + \frac{\partial F}{\partial x} + S = 0, \tag{7.4.1}$$

where U is the variable of interest, F are the fluxes (advective or diffusive) and S are the source terms. The domain is then divided into a number of computational cells in which we have given 'volumes' of U. To evolve the solution from the initial conditions the flux F across each cell boundary is calculated and, since the flux across a cell boundary is equal to the flux into its neighbour, the total volume of U is conserved.

There are many different methods that may be used to calculate these fluxes such as upwind and Lax-Wendroff, in addition to associated flux- or slope-limiters that help to avoid spurious numerical oscillations. Here we use a semidiscrete MUSCL (Monotonic Upstream-Centred Scheme for Conservation Laws) scheme [149]. It consists of the following stages:

- Begin with a piecewise **constant** approximation for U, with the value of U uniform across each cell. See figure 14.
- Use a slope limiter to construct a piecewise **linear** approximation for U in each cell. See figure 15.
- Calculate the flux F of U across each cell boundary, using the values to the left and right of the boundary given by the piecewise linear approximations.
- Calculate the source term S for each cell using the central U value in each cell.
- Integrate numerically with respect to time, using for example Runge-Kutta, to update the solution for U.
- Repeat.

7.4.2 *Method*

We begin with our equation for the cell volume fraction (7.3.6) written in the conservative form

$$\frac{\partial \theta_n}{\partial t} + \frac{\partial}{\partial x}\left(\theta_n v_n\right) - S_n = 0, \tag{7.4.2}$$

and note that $U = \theta_n$, $F = \theta_n v_n$ and $S = -S_n$. We divide x into N cells of equal length, Δx, for simplicity, with uniform cell volume fraction across each cell, see figure 14.

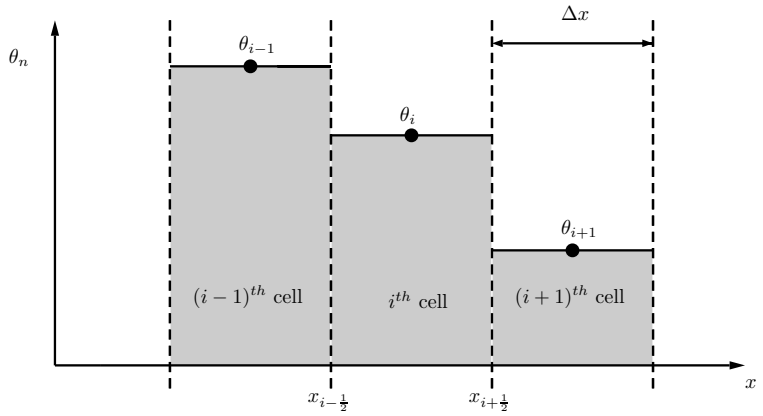


Figure 14: Illustration to show numbering of cells and edges, and piecewise constant approximation for θ_n.

Next we construct the piecewise linear approximation to increase the spatial accuracy of the method. To do this we can choose from a wide range of total variation diminishing (TVD) slope limiters, see [91], constructed to avoid introducing nonphysical oscillations. We choose the monotonized central (MC) slope limiter, which gives the gradient of the linear approximation in the i^{th} cell by

$$\sigma_i = \text{minmod}\left(\left(\frac{\theta_{i+1} - \theta_{i-1}}{2\Delta x}\right), 2\left(\frac{\theta_i - \theta_{i-1}}{\Delta x}\right), 2\left(\frac{\theta_{i+1} - \theta_i}{\Delta x}\right)\right), \tag{7.4.3}$$

where the *minmod* function is given by

$$\text{minmod}(a,b,c) = \begin{cases} \min(a,b,c) & \text{if } a,b,c > 0 \\ \max(a,b,c) & \text{if } a,b,c < 0 \\ 0 & \text{otherwise.} \end{cases} \tag{7.4.4}$$

This limiter gives first order accuracy at local extrema, where $\sigma_i = 0$ and the piecewise approximation is constant across the cell, but second order accuracy over smooth sections.

The cell volume fraction θ_n across the computational cells now looks like the illustration shown in figure 15, with the values on the left and the right boundaries of each computational cell denoted by θ_i^L and θ_i^R respectively. These can easily be found by:

$$\theta_i^L = \theta_i - \frac{\Delta x}{2}\sigma_i, \tag{7.4.5}$$

$$\theta_i^R = \theta_i + \frac{\Delta x}{2}\sigma_i. \tag{7.4.6}$$

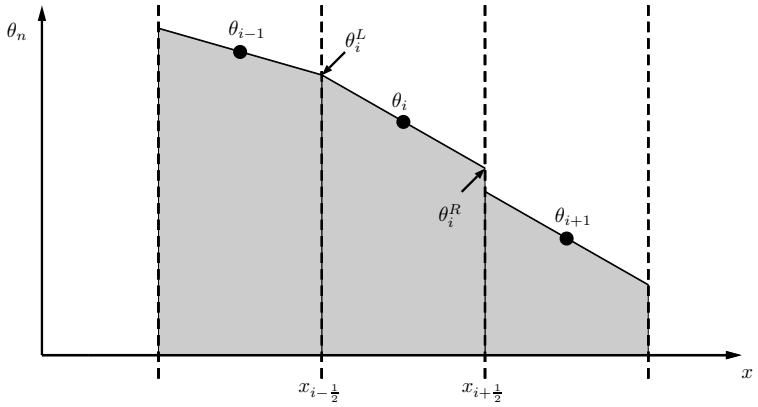


Figure 15: Illustration to show the piecewise linear approximation for θ_n.

Next we determine the flux across each interface using an upwind flux. For hyperbolic problems upwinding is required for stability. The direction of flux across a cell boundary is dependent on the sign of λ, where

$$\lambda = \frac{\partial F}{\partial U} = \frac{\partial}{\partial \theta}\left(\theta_n v_n\right), \tag{7.4.7}$$

and is approximated by

$$\lambda_{i+\frac{1}{2}} = \frac{\theta_{i+1}^L v_{i+1} - \theta_i^R v_i}{\theta_{i+1}^L - \theta_i^R}. \tag{7.4.8}$$

The flux is then given by:

$$F_{i+\frac{1}{2}} = \begin{cases} \theta_i^R v_i & \text{if } \lambda_{i+\frac{1}{2}} \geqslant 0 \\ \theta_i^L v_{i+1} & \text{if } \lambda_{i+\frac{1}{2}} < 0. \end{cases} \tag{7.4.9}$$

Note that equation (7.3.6) can be rewritten as

$$\frac{\partial \theta_n}{\partial t} + \lambda \frac{\partial \theta_n}{\partial x} = S_n \text{ where } \lambda = \frac{\partial}{\partial \theta_n}\left(\theta_n v_n\right), \tag{7.4.10}$$

showing its similarity to Burgers equation, for which the direction (forward or backward) of finite differencing that results in a stable numerical scheme is determined by the sign of λ.

The semi-discrete form of the cell volume fraction equation (7.4.2) is given by

$$\frac{d\theta_i}{dt} = -\frac{1}{\Delta x}\left[F_{i+\frac{1}{2}} - F_{i-\frac{1}{2}}\right] + S_n\left(\theta_i\right), \tag{7.4.11}$$

which states that the change in volume fraction in a computational cell is given by the fluxes F across the cell boundaries and growth through source term S_n. Note that the source term is a function of the cell volume fraction at the centre of the computational cell. For the time stepping we use MATLAB's built in solver ode23.m, a Runge-Kutta method with adaptive step size.

7.4.3 *Velocity*

Recall that the complete model consists of the conservation equation (7.4.2) for the cell volume fraction θ_n, as well as the boundary value problem (7.3.7) for the cell velocities, v_n. These can be found for a given cell volume fraction distribution by solving the finite difference form of (7.3.7). The velocity is recalculated at each time step for the current value of θ_n.

7.4.4 *The boundary region*

Whilst slope limiters help avoid the introduction of nonphysical oscillations, they can act to reduce the slope at discontinuities, smearing solutions. See, for example, chapter 6 of [91] which illustrates the effect on slopes of a number of limiters. Here, the small amount of diffusion introduced by

the numerical method causes the sharp edge of the tissue to be smoothed slightly. This can be improved by increasing the number of grid points, sharpening the interface. There remains, however, a leading edge with very small values of θ_n which spreads across to an additional cell at each time step. Due to the very small magnitudes, this causes problems for the velocity solver which finds the cell velocities for given θ_n profiles. In order to avoid this, we use an approach from the study of the shallow water equations, in particular where there is a dam break problem onto a dry bed. We follow the method, described in [73], as follows:

- A small tolerance value θ_{tol} is chosen for θ_n.
- At an interface where the cell volume fraction is such that $\theta_n < \theta_{tol}$ on both sides, no flux is permitted.
- All other fluxes between all other neighbouring cells are calculated as before.

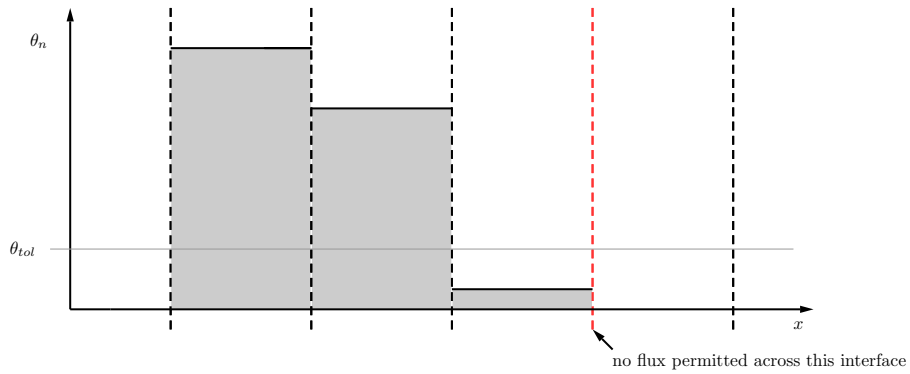


Figure 16: Illustration to show where flux of material is not permitted due to θ_n being below some chosen tolerance level.

The cutoff value for θ_n is chosen such that the cell volume fraction, θ_n, and cell velocities, v_n, are impacted as little as possible but retain accuracy in the velocity solver. Equation (7.3.7) is solved for v_n from $x = 0$ to the first cell for which $\theta_n < \theta_{tol}$. All other computational cells are assigned $v_n = 0$. See figure 16.

Having simplified our model and discussed the numerical approach taken, we next explore the behaviour of the tissue for different parameter values via both numerical and analytical approaches.

7.5 RESULTS

We consider separately the results obtained for two sub cases of the model:

- viscous cell phase, inviscid water phase
- viscous cell and water phases

7.5.1 *Sub case 1: Viscous cells - inviscid water*

We note that, as described in section 7.2, a very similar case is considered in [89] where the behaviour of travelling wave solutions is investigated. We closely follow the methods and analysis given therein.

In the following numerics we use the parameter values given in Table 3 unless otherwise indicated.

Table 3.: Parameter values employed in the microscale numerical experiment unless stated otherwise, for equations (7.3.6–7.3.7). Values for k_m and k_n taken from [89].

Parameter	Value
k_m	1.8×10^{-4}
k_n	3.4×10^{-5}
ν	1.2×10^{-2}
κ	8.0×10^{-3}
β	1.0×10^{4}
c	1

The initial behaviour of the wave depends on the choice of initial cell volume fraction profile. On a short timescale, where cell proliferation, S_n, is negligible, movement of the cells is driven by the intraphase pressure to obtain the wave's 'preferred profile'. In the core region of the tissue the cell volume fraction tends to the non-trivial steady state value, θ^*, where

$$\theta^* = \frac{k_m - k_n}{k_m}, \tag{7.5.1}$$

whilst at the leading edge, just inside the moving boundary, takes the value $\theta^\dagger$ termed the aggregate density, to be determined below. See figure 17 for numerical examples of adjustment to the preferred profile from two different initial conditions.

The aggregate density is determined by the boundary layer analysis of [89] as follows. Results (see figures 17, 18 and 21) indicate that after the initial relaxation behaviour, described above, solutions are of travelling wave form, propagating with constant speed. Transforming equations (7.3.6) and (7.3.7) using $z = x - v_\Gamma t$, where v_Γ is a constant wave speed and $z = 0$ is the position of the interface, gives

$$(v_n - v_\Gamma)\frac{d\theta_n}{dz} + \theta_n \frac{dv_n}{dz} = S_n, \tag{7.5.2}$$

$$F\frac{d\theta_n}{dz} + \frac{d}{dz}\left(\frac{4}{3}\theta_n \frac{dv_n}{dz}\right) - \beta\frac{\theta_n}{1-\theta_n}v_n = 0, \tag{7.5.3}$$

where

$$F(\theta_n) = \theta_n\left(2\nu - \frac{\kappa\theta_n(3-2\theta_n)}{(1-\theta_n)^2}\right). \tag{7.5.4}$$

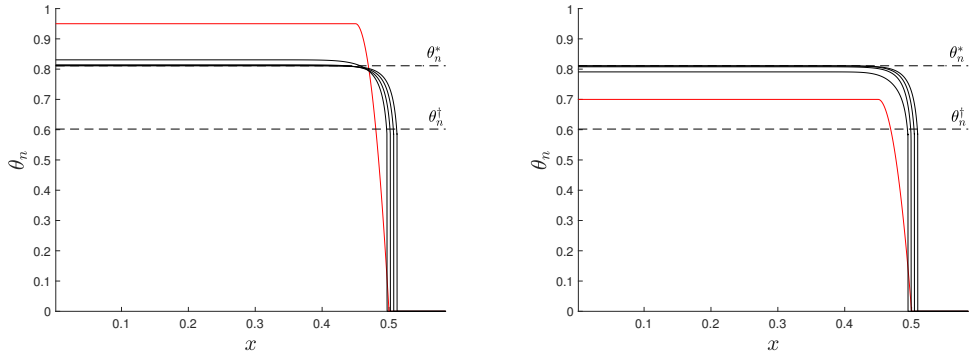
Close to the interface,

$$\theta_n^\dagger \frac{dv_n}{dz} \sim S_n(\theta_n^\dagger), \tag{7.5.5}$$

$$F\frac{d\theta_n}{dz} \sim -\frac{d}{dz}\left(\frac{4}{3}\theta_n\frac{dv_n}{dz}\right), \tag{7.5.6}$$

where $\theta_n \sim \theta_n^\dagger$, $v_n \sim v_\Gamma$ and the drag term is negligible. Integrating (7.5.6) with respect to z and using (7.5.5) gives

$$\int_0^{\theta_n^\dagger} F(\theta_n)\,\mathrm{d}\theta_n + \frac{4}{3}S_n\left(\theta_n^\dagger\right) = 0. \tag{7.5.7}$$



(a) (b)

Figure 17: Initial wave behaviour. Initial cell volume fraction shown in red. Cell volume fraction in the core region tends to the steady state θ_n^*. A steep edge to the tissue develops, with the cell volume fraction value just inside the moving boundary taking the value of the aggregate density, $\theta^\dagger$. Parameters: $\nu = 0.012$, $\kappa = 0.008$, $\beta = 1000000$, $t = 0, 12500, 25000, 37500, 50000$.

On evaluating the integral, we obtain

$$\nu\theta_n^{\dagger 2} - \frac{\kappa\theta_n^{\dagger 3}}{1-\theta_n^\dagger} + \frac{4}{3}\theta_n^\dagger\left(k_m\left(1-\theta_n^\dagger\right) - k_n\right) = 0, \tag{7.5.8}$$

which can be solved numerically to obtain the aggregate density, $\theta^\dagger$.

The relationship between these two values, the steady state θ^* and the aggregate density $\theta^\dagger$, governs the long time behaviour of the wave. For fixed rates k_m and k_n, the wave behaviour is determined by the strength of the cell-cell attraction and repulsion, and their relative magnitude.

Numerical solutions show three wave behaviours, as illustrated by figure 18. If $\theta^* > \theta^\dagger$ then forward travelling waves are observed, whilst for $\theta^* < \theta^\dagger$ the direction is reversed[2]. A third behaviour, break up of the tissue into aggregates, occurs when parameters are chosen such that θ^* becomes unstable. (See the stability analysis of section 5.2.3, in particular equation (5.2.34).) These three regions of parameter space are illustrated by figure 19.

2 The leading edge of the tissue moves back as it steepens with time, before this leads to numerical issues

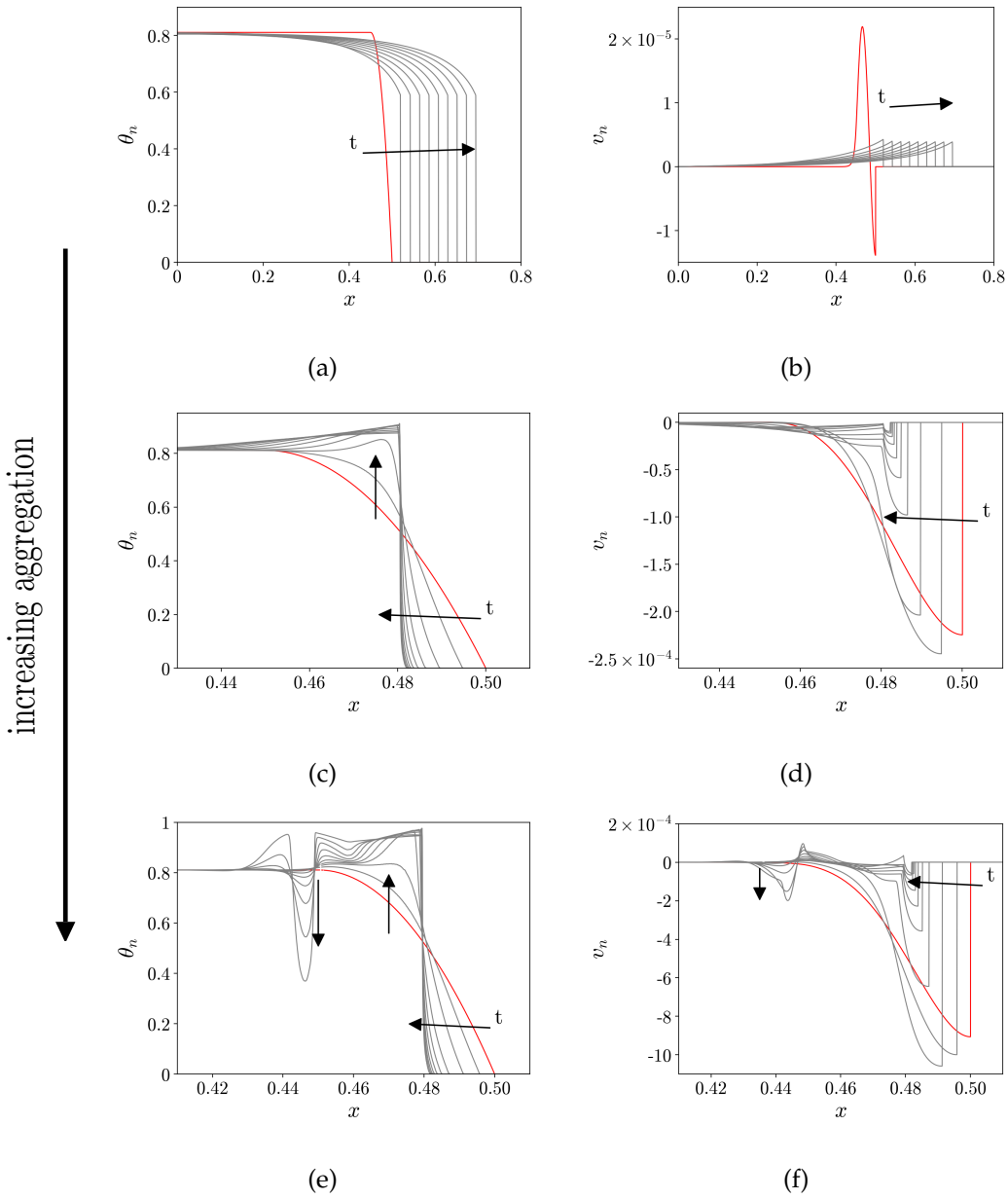


Figure 18: Cell volume fraction distribution and cell velocity obtained from numerical simulations of equations (7.3.6–7.3.7) for increasing time, showing the changing behaviour of the tissue as the aggregation parameter is increased. Initial profiles in red. For low values, forward-travelling waves occur, while for increased aggregation the waves travel backwards and even higher values cause the break up of the tissue. Parameter values: (a), (b) $\nu = 0.012$, $t = 50000$, (c), (d) $\nu = 0.08$, $t = 200$, (e), (f) $\nu = 0.3$, $t = 40$. All other parameters as given in Table 3.

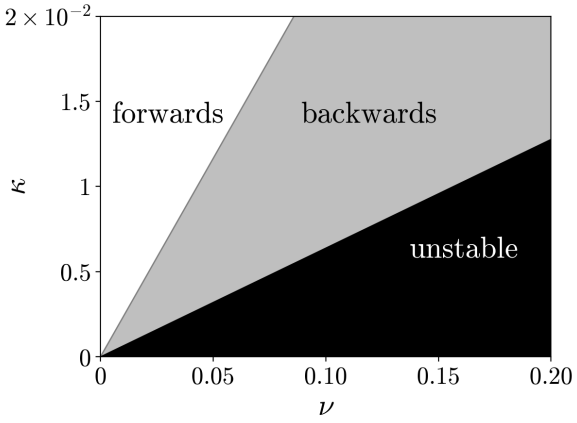


Figure 19: Regions of (ν, κ) space where forward travelling, backwards travelling and unstable waves occur. Lines for stationary waves (separating white and grey region) and stability (separating grey and black region) are plotted using (7.5.8) (with $\theta^\dagger = \theta^*$) and (5.2.34).

FORWARD WAVE After adjusting from the initial profile the wave takes the steady state value 0.811 at $x = 0$ and the aggregate density followed by a steep drop at the leading edge. The velocity of the cells towards the centre is low due the effects of interphase drag, keeping the cell volume fraction at approximately the steady state value despite cell repulsion. Closer to the edge the drag has less impact, as the viscous and extra pressure terms of (7.3.7) dominate, so as the cells proliferate they move apart in response to the cell-cell repulsion, pushing the wave forward. For a given parameter set, the boundary velocity tends to a constant value, as the width of the boundary region of cells contributing to repulsion tends to a constant.

BACKWARD WAVE Here, the cells towards the centre remain at the steady state value as previously, but behaviour at the edge is reversed. The cells pull together, due to stronger cell-cell aggregation, to achieve the higher aggregate density, as shown in figure 18c. This is greater than the steady state value so results in the death of cells which are then replaced by

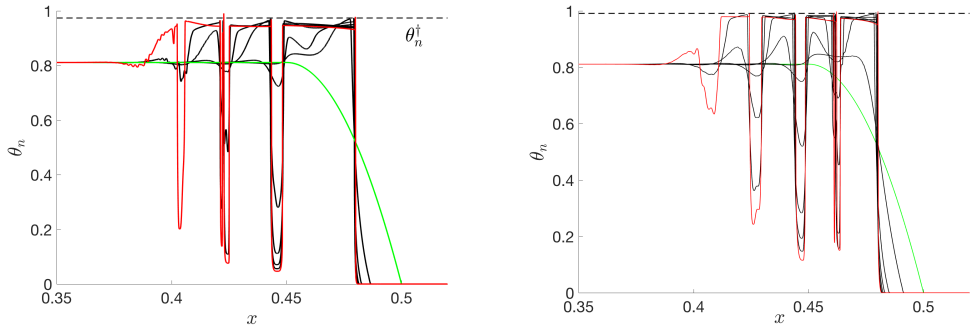
others which are pulled in by the intraphase pressure. For longer times, the steepening edge leads to numerical issues.

BREAK-UP This occurs when aggregation is much larger than repulsion. As in the backward wave case, although somewhat faster, the leading edge steepens and the cell volume fraction increases. In addition the tissue starts to break up as cells are pulled from the left as well as the right, and another peak of cell density begins to form further back from the wave front. If the simulation is run for longer we see (despite numerical issues at points of sharp gradient) that the tissue splits into a number of blocks along its length. See figure 20. Higher aggregation strength leads to quicker break up of the tissue.

We also highlight that the results summarised here are in agreement with those presented by Lemon King [89] (obtained via a different numerical method), including those associated with unstable break-up. Moreover, these are consistent with travelling wave and stability analyses. Together with relevant numerical convergence tests, we are therefore confident in our numerical results for the timeframes considered here.

Whilst this behaviour is interesting, we wish to find a suitable expression for the boundary velocity, particularly in the case where the tissue is growing.

In [89], estimates are found for the wave speed in the case of zero drag and for 'slow' waves. Here, in order to validate the numerics and inform our general wave speed expression, we find wave speed estimates for our model following the analysis of [89]. In the case of zero drag forces, intraphase pressures dominate across the whole tissue rather than only the leading region and the cell volume fraction is equal to the aggregate density throughout. All the cells proliferate (or die) at the same rate and act to push (or pull) the wave, so the velocity is a function of the width of the tissue. This can be seen by observing that both cell volume fraction and $\partial v_n/\partial x$



(a) (b)

Figure 20: Graphs illustrating break up of tissue at high aggregation, including numerical issues. Green – initial cell volume fraction profile; black – intermediate profiles; red – final profile. (a) $\nu = 0.3$, final time $t = 100$. (b) $\nu = 0.9$, final time $t = 20$. Other parameters as given in Table 3.

are uniform across the tissue, see figure 21, which reduces the equation for the conservation of mass (7.3.6) to $\partial v/\partial x = S_n(\theta_n)/\theta_n$. By integrating with respect to x and applying boundary conditions (7.3.18) and $\theta_n = \theta_n^\dagger$ at $x = \Gamma$, we find that the boundary velocity is given by

$$v_\Gamma \approx \frac{S_n\left(\theta_n^\dagger\right)}{\theta_n^\dagger}\Gamma(t), \tag{7.5.9}$$

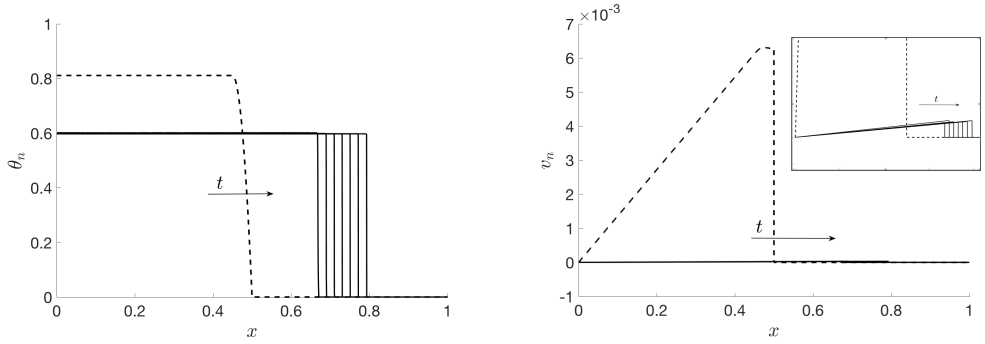
hence the tissue grows, and the boundary velocity increases, exponentially.

The second estimate is achieved for 'slow waves', when the steady state is approximately equal to the aggregate density, i.e. $\theta_n^* \approx \theta_n^\dagger$. To obtain the estimate, first we switch to travelling wave coordinates via the transformation $z = x - v_\Gamma t$ where v_Γ is a constant, obtaining (7.5.2) and (7.5.4). These can be rewritten as

$$(v_n - v_\Gamma)\frac{d\theta_n}{dz} = S_n(\theta_n) - \theta_n u_n, \tag{7.5.10}$$

$$\frac{dv_n}{dz} = u_n, \tag{7.5.11}$$

$$\frac{du_n}{dz} = \frac{3}{4}\beta(1-\theta_n)^{-1}v_n - (\theta_n)^{-1}\left(u_n + \frac{3}{4}F(\theta_n)\right)\frac{d\theta_n}{dz}. \tag{7.5.12}$$



(a) (b)

Figure 21: Graphs to show the evolution of the cell volume fraction and cell velocity when there is no interphase drag. The cell volume fraction (figure (a)) adjusts to take the value of the aggregate density, $\theta_n^\dagger$, throughout the tissue, whilst the gradient of the velocity tends to a constant, see (b). Parameters: $\beta = 0$, final time $t = 5000$. Other parameters as given in Table 3.

By linearising the equations about the steady state, such that

$$\theta_n = \theta_n^* + \delta\theta_1 + ... \tag{7.5.13}$$

$$v_n = \delta v_1 + ... \tag{7.5.14}$$

$$u_n = \delta u_1 + ... \tag{7.5.15}$$

$$v_\Gamma = \delta v_{\Gamma 1} + ... \tag{7.5.16}$$

where $\delta = \theta_n^\dagger - \theta_n^*$, at $O(\delta)$ we obtain

$$S_n'(\theta_n^*)\,\theta_1 = \theta_n^* u_1, \tag{7.5.17}$$

$$\frac{dv_1}{dz} = u_1, \tag{7.5.18}$$

$$\frac{du_1}{dz} = \frac{3}{4}\beta(1-\theta_n^*)^{-1} v_1 - (\theta_n^*)^{-1}\left(\frac{3}{4}F(\theta_n^*)\right)\frac{d\theta_1}{dz}. \tag{7.5.19}$$

Elimination of θ_1 and v_1 yields

$$\frac{d^2u_1}{dz^2} = \gamma^2 u_1, \tag{7.5.20}$$

with

$$\gamma = \sqrt{\left(\frac{3\beta(1-\theta_n^*)^{-1}}{4 + 3F(\theta_n^*)/S_n'(\theta_n^*)}\right)}. \tag{7.5.21}$$

Solving (7.5.20), and seeking solutions for θ_1 and v_1, according to boundary conditions

$$\theta_n = \theta_n^\dagger, \quad v_n = v_\Gamma, \quad u_n = S_n\left(\theta_n^\dagger\right)/\theta_n^\dagger \quad \text{at } z = 0, \tag{7.5.22}$$

gives

$$\theta_1 = \mathrm{e}^{\gamma z}, \quad v_1 = v_\Gamma \mathrm{e}^{\gamma z}, \quad u_1 = S_n\left(\theta_n^\dagger\right)/\theta_n^\dagger \mathrm{e}^{\gamma z}, \tag{7.5.23}$$

and hence, via (7.5.18), the approximate wave speed for slow waves is,

$$v_\Gamma \approx \frac{S_n\left(\theta_n^\dagger\right)}{\theta_n^\dagger}\sqrt{\frac{4 + 3F\left(\theta_n^*\right)/S_n'\left(\theta_n^*\right)}{3\beta\left(1-\theta_n^*\right)^{-1}}}. \tag{7.5.24}$$

Having found wave speed approximations for zero drag and 'slow' waves we now use these results to help inform the choice of an equation for the boundary velocity in a wider range of cases. In particular, we focus on forward travelling waves with nonzero interphase drag, taking the wave velocity to be that of long time behaviour, when it converges to some uniform value. The wave velocity is taken to be the cell phase velocity v_n for a value of θ_n just below $\theta_n^\dagger$, i.e. on the sharp leading edge. This corresponds to the maximum cell velocity for a given wave profile, for forward travelling waves as considered here. The results are shown in figure 22 where crosses denote data points and curves are the velocity function. Points of zero velocity are determined by solving (7.5.8) with $\theta_n^\dagger = \theta_n^*$.

First we see that increasing the strength of cell repulsion increases wave speed whilst increasing aggregation decreases it. Increasing the level of nutrient concentration (uniform across the tissue) increases the cell proliferation rate and hence the wave velocity.

Whilst zero interphase drag resulted in exponentially increasing velocity, introducing drag results in a constant wave velocity, given sufficient time. The strength of the drag determines the width of tissue where interphase pressures can dominate, the stronger the drag, the smaller the width. So we find that increasing drag decreases wave speed and $1/\sqrt{\beta}$, as appears in the slow wave estimate, is a good fit here.

By observing the relationship between the various parameters and the boundary velocity, and using MATLAB's curve fitting tool, we find that a good fit to the data is given by

$$v_\Gamma = \frac{1}{\sqrt{\beta}} \left(\frac{c - c^*}{1 - c^*} \right) \left[\gamma_1 \kappa^{\alpha_1} \nu^3 + \gamma_2 \kappa^{\alpha_2} \nu^2 + \gamma_3 \kappa^{\alpha_3} \nu + \gamma_4 \kappa^{\alpha_4} \right], \tag{7.5.25}$$

where

$$c^* = \frac{k_n (\nu + \kappa)}{k_m \kappa}, \tag{7.5.26}$$

and values of parameters α_i and γ_i are given in Table 4. This particular form for v_Γ is chosen as it provides a good qualitative fit to the results obtained. In particular the cubic form for aggregation is suitable, since it maintains a negative wave speed after aggregation passes the critical value for a stationary wave. The dependence on interphase drag is taken from the approximate wave speed solution (7.5.24) that is obtained analytically. Whilst our focus here is on the qualitative nature of the fit, we note that the R^2 values obtained for the numerical fits shown in figure 22 are all above 0.983.

Table 4.: Parameter values for boundary velocity estimate (7.5.25).

Parameter	Value	Parameter	Value
α_1	-2.6	γ_1	-2.8×10^{-5}
α_2	-1.6	γ_2	5.1×10^{-4}
α_3	-0.45	γ_3	-4.1×10^{-3}
α_4	0.53	γ_4	1.0×10^{-2}

The boundary velocity given by (7.5.25) is also compared to that found by using the shooting method set up as described in [89]. This alternative method allows the boundary velocity to be determined without solving the time dependent problem until long time behaviour is reached. A solution trajectory of the model equations in travelling wave coordinates, equations

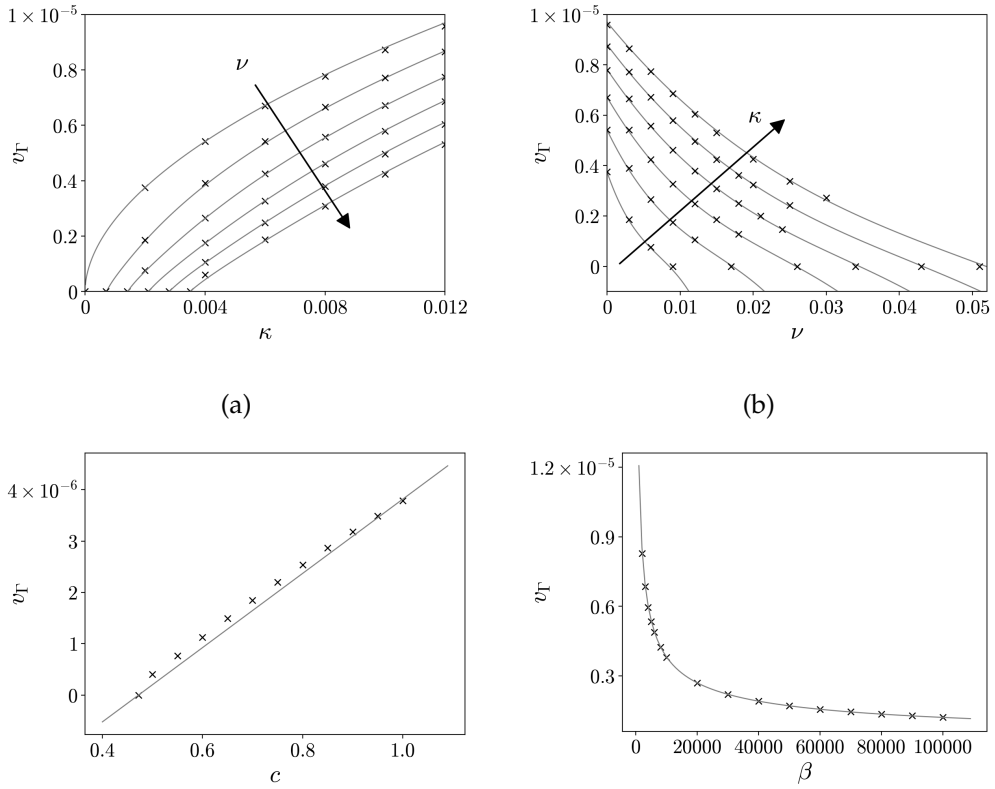


Figure 22: Graphs showing the relationship between boundary velocity of a forward travelling wave and (a) aggregation ν, (b) repulsion κ, (c) nutrient concentration c and (d) interphase drag β. Crosses denote values obtained from the numerical solution (via the finite volumes method) of (7.3.6) and (7.3.7), whilst solid lines are suggested fits to the data by (7.5.25). Parameters (a) $\kappa = 2\times10^{-3} - 1.2\times10^{-2}$, (b) $\nu = 0 - 1.2\times10^{-2}$. All other parameters as given in Table 3.

(7.5.10–7.5.12), that connects values at the free boundary (7.5.22) to the steady state,

$$\theta_n = \theta_n^*, \quad v_n = 0, \quad u_n = 0 \tag{7.5.27}$$

within the tissue, i.e. at $z = -\infty$, is sought. The boundary velocity v_Γ is used as the shooting parameter, and is varied until the two points are connected.

In figure 23, the boundary velocities obtained by equation (7.5.25), the shooting method and the linear 'slow wave' approximation (7.5.24) are compared. We see that (7.5.24) provides a good approximation only for slow-moving waves, as expected, whilst (7.5.25) and results obtained via the shooting method show good agreement for both fast and slow moving waves.

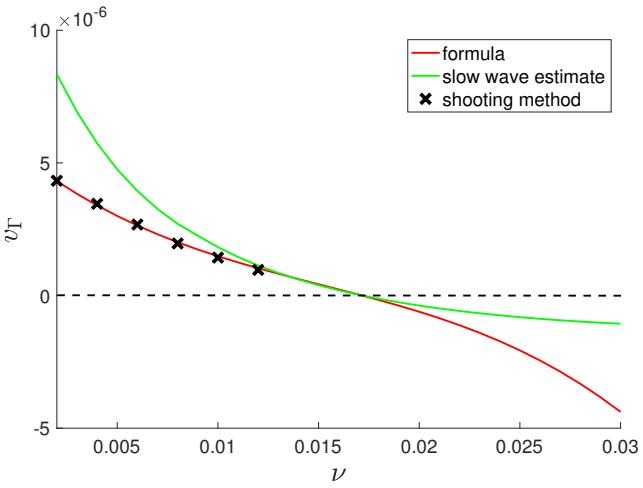


Figure 23: A comparison of boundary velocity estimates obtained from (7.5.25), the slow wave approximation (7.5.24) and the shooting method. The 'slow wave' approximation (green) only provides a good velocity estimate for slow moving waves, whilst the shooting method (crosses) shows good agreement with (7.5.25) (red) for both fast and slow moving waves. Parameter values: $\kappa = 0.004$. All other parameters as given in Table 3.

We have investigated the behaviour of the tissue for a range of parameter values, in the case where the water phase is inviscid. Approximations for the boundary velocity were found for 'slow waves', in the absence of

interphase drag, and for forward travelling waves. The analysis and results of this section closely followed those of the similar model found in [89]. Next we look at the behaviour of the tissue when both the cell and water phases are modelled as viscous fluids.

7.5.2 *Sub case 2: Viscous cells - viscous water*

We now consider the case where both phases are viscous, initially of equal viscosity. In contrast to the case where the water phase is inviscid, we find that the leading edge of the tissue is pinned.

Using the same numerical methods described in section 7.4 we appear to obtain travelling wave solutions but on refinement of the spatial mesh the wave speed reduces and the leading edge becomes progressively steeper, and we appear to see convergence to a stationary tissue domain. See figure 24.

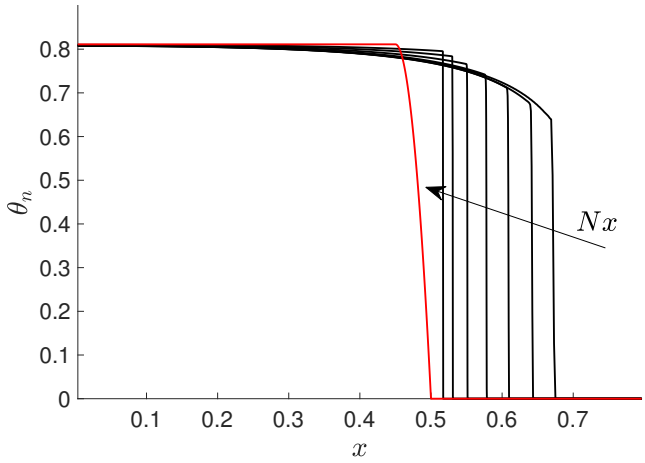


Figure 24: Graph to show the effect of increasing the number of computational cells, Nx, on the wave behaviour. Red line shows the initial profile, and black curves are for time $T = 50000$, and increasing $Nx = 1000, 2000, 4000, 8000, 16000, 32000$. All parameters fixed at values in Table 3.

For other values of aggregation and repulsion, including when aggregation is set to zero, the same behaviour occurs. The edge of the tissue steepens and the wave speed decreases to zero as the number of computational cells increases (i.e they decrease in width).

Our results indicate that the sharp drop in cell volume fraction at the edge of the tissue occurs over the same number of cells ($> 1 cells$), but now over a shorter distance, causing an increase in magnitude of $\partial\theta_n/\partial x$. When the velocity solver calculates the cell velocity, given the cell volume fraction profile, the prefactor C of v_n, in equation (7.3.11), becomes comparatively much larger than the rest of the terms in (7.3.7) at the tissue edge, for increasing Nx. (Note that C has no dependence on the gradient of θ_n when the water phase is modelled as inviscid, due to the prefactor μ, so this problem does not occur there.) As $\partial\theta_n/\partial x \to \infty$ the velocity equation (7.3.7) tends to $Cv_n = 0$ at leading order, and since C is non zero we must have $v_n = 0$. The steepness of the edge effectively causes it to be pinned in position whilst the cells in the rest of the tissue move and grow until the steady state value is achieved throughout.

The sharp edge to the tissue, which causes issues when both phases, as opposed to just the cell phase, are viscous, occurs due to the form of the intraphase pressure chosen. In [43], a two phase gel model, which is conceptually similar to our tissue model but with different application, is derived and analysed. The gel consists of a solvent and a polymer phase, with the inclusion of osmotic pressure due to the chemically active nature of the polymers. Gradients in osmotic pressure induce a force on the polymers, similar to gradients in intraphase pressure for the cell phase. In order for the gel to hold an edge (a distinct separation between gel and surrounding solvent which may move), it is shown that the osmotic pressure must be of the form $\theta_p^2 f(\theta_p)$ where θ_p is the volume fraction of polymer and f is a function such that $f(\theta_{p,ref}) = 0$ and $f(\theta_p) \leqslant 0$ for $0 < \theta_p < \theta_{p,ref}$.

In our model the intraphase pressure appears in the cell phase momentum equation as

$$\theta_n \phi_n = \theta_n^2 \left(-\nu + \frac{\kappa \theta_n}{(1-\theta_n)} \right), \tag{7.5.28}$$

which is of the appropriate form to 'hold an edge', maintaining a distinct interface between the tissue and the surroundings. It is this steep edge which causes the tissue to be pinned when both phases are modelled as viscous fluids.

Whilst we could investigate alternative forms for the intracellular pressure, we choose to reduce the steepness of the leading edge through the introduction of diffusion. We add diffusion of the cell phase so that (7.3.6) becomes

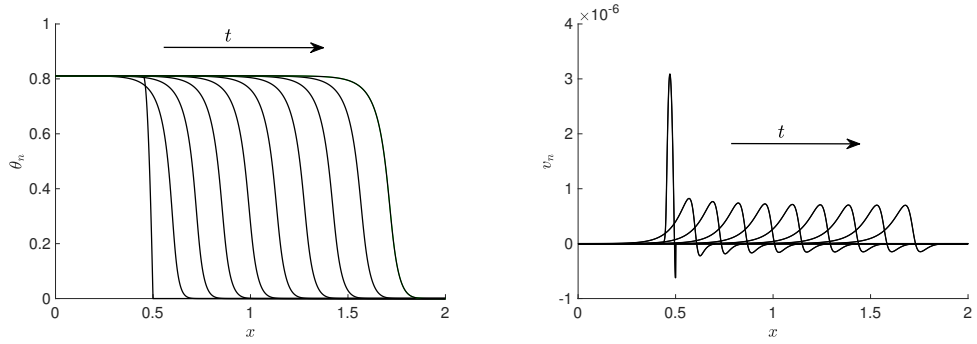
$$\frac{\partial \theta_n}{\partial t} + \frac{\partial}{\partial x}\left(\theta_n v_n\right) = S_n + D_n \frac{\partial^2 \theta_n}{\partial x^2}, \tag{7.5.29}$$

where D_n is small. The additional term could be accommodated through the inclusion of diffusive fluxes in the finite volume solver, but as the mass conservation equation is no longer hyperbolic, we choose instead to use a finite difference solver to obtain the results that follow.

Adding diffusion results in a more diffuse tissue boundary, (see figure 25), and travelling wave behaviour is observed. To determine the boundary velocity we find the time taken for a point on the front, e.g. $\theta = 0.4$, to cover a known distance. As previously, after initial dynamics, v_Γ tends to a constant value.

The movement of the travelling wave can now be driven solely by diffusion, so we seek to find a balance, where there is enough diffusion to allow the wave to move, but cell aggregation and repulsion retain an effect, thereby allowing an approximation for the boundary velocity such as (7.5.25) to reasonably apply.

By varying the parameter values for aggregation, diffusion and repulsion we investigate the impact on the wave velocity. As one can see from figure 26 it is possible to see some similarities with the viscous-inviscid case:



(a) (b)

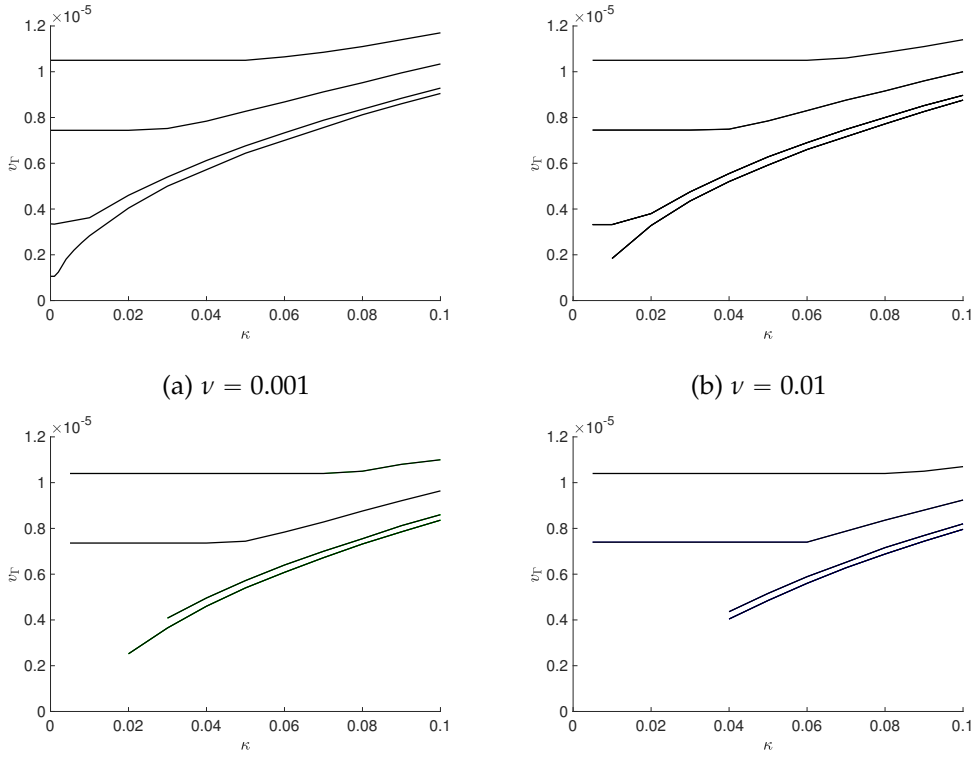
Figure 25: Graph to show the travelling wave behaviour on the introduction of diffusion. Evolution of (a) cell volume fraction and (b) cell velocity with time. Parameters: $D_n = 5\times10^{-8}$, $\beta = 1\times10^{5}$, $\nu = 0.004$, $\kappa = 0.008$. Other parameters fixed at values in Table 3.

as repulsion increases speed increases, and as aggregation increases wave speed decreases.

Figures 26(a)-(d) show how the boundary velocity varies with repulsion for a range of diffusion and aggregation values. The black lines on figure 26 are for increasing diffusion (bottom to top). For low diffusion we see the relationship between velocity and repulsion is of qualitatively similar form to the inviscid water case except, for very low repulsion where it becomes insensitive to κ and the wave speed is determined by diffusive effects alone. For increased diffusion, the range of values of κ for which the edge motion is diffusion-driven is increased.

Figure 27 allows us to view the data in a different way. The dotted line shows the boundary velocity for diffusion-driven waves, with no aggregation or repulsion. The coloured lines represent different aggregation and repulsion strength combinations.

As diffusion is increased, we see that whatever the strength of the cell-cell interactions, the boundary velocity tends to that of a purely diffusion driven wave. For lower values of diffusion the velocity depends strongly



(a) $\nu = 0.001$

(b) $\nu = 0.01$

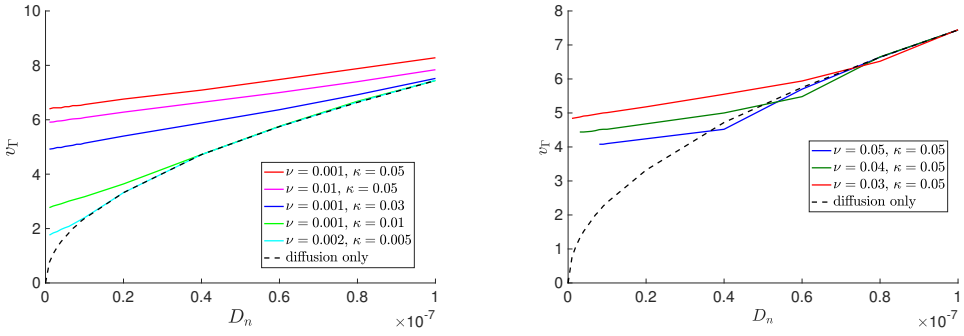
(c) $\nu = 0.02$

(d) $\nu = 0.03$

Figure 26: Effect of diffusion, repulsion κ and aggregation ν on boundary velocity. High diffusion dominates the velocity, especially at lower repulsion values. For lower diffusion, the relationship between repulsion and boundary velocity has a similar form to that found for the case of inviscid water. Lines on (a)–(d) for $D = 2 \times 10^{-9}, 2 \times 10^{-8}, 1 \times 10^{-7}, 2 \times 10^{-7}$, bottom to top. Sensible results are not obtainable for low repulsion and low diffusion.

on the magnitude of the aggregation and repulsion parameters, with lower aggregation and higher repulsion giving faster waves.

In figure 27(b) we see that values of the boundary velocity dip below that expected for a wave driven only by diffusion. This is due to the 'anti-diffusion' effect of the attractive cell-cell forces, as observed in [113]. In [113], a similar two phase model, it was shown that diffusion is reduced by cells' tendency to aggregate and increased by their tendency to repel.



(a) (b)

Figure 27: Graph to show the relationship between boundary velocity and diffusion for different combinations of aggregation and repulsion. Other parameters as given in Table 3.

Here we have explored the behaviour of the tissue when both phases are modelled as viscous, and on the addition of diffusion of the cell phase, have observed results that are qualitatively similar to when the water phase is inviscid. We consider that a function of a similar form to (7.5.25) would be reasonable in this case, but as this is computationally intensive it is not sought here.

Using the results obtained in the inviscid water case to provide closure, next we show how the corresponding macroscale model, and accompanying Stokes problem, may be solved numerically.

7.6 NUMERICAL EXPERIMENTS

We now present a series of illustrative numerical simulations of the microscopic cell problems and the corresponding effective macroscale description. We consider, in particular, the case for which the water phase is inviscid. To enable closure of our multiscale description, we use the representation (7.5.25) for $\boldsymbol{v}_\Gamma^{(1)} \cdot \boldsymbol{n}$ in (5.3.85). As (7.5.25) was obtained from analysis in 1D, there is not a direct correspondence between the two models;

the representation nevertheless provides a useful approximation. First we recapitulate the relevant equations.

7.6.1 *Microscopic cell problem*

In this particular sub-case, as described in section 5.4.1, we set $\mu = 0$ (but retain the interphase viscous drag term). In this case, an appropriate ansatz[3] is:

$$\boldsymbol{v}_i^{(0)} = -\boldsymbol{K}_i \boldsymbol{\nabla}_X p_w^{(0)} \text{ and } p_i^{(1)} = -\boldsymbol{a}_i \boldsymbol{\nabla}_X p_w^{(0)} - \bar{p}_i \text{ for } i = n, w, \tag{7.6.1}$$

where pressures $p_w^{(0)}$, $\bar{p}_i$ are microscale invariant and $\boldsymbol{K}_i$, $\boldsymbol{a}_i$ are tensors as described in section 5.3.4, with $\langle \boldsymbol{a}_i \rangle_T = \boldsymbol{0}$. In the tissue domain, Ω_T, the Stokes problem is given by:

$$\boldsymbol{\nabla}_{\boldsymbol{x}} \cdot \boldsymbol{K}_n^\mathsf{T} = \boldsymbol{0}, \quad \boldsymbol{\nabla}_{\boldsymbol{x}} \cdot \boldsymbol{K}_w^\mathsf{T} = \boldsymbol{0}, \tag{7.6.2}$$

$$\boldsymbol{\nabla}_{\boldsymbol{x}} \boldsymbol{a}_w^\mathsf{T} - \boldsymbol{I} - \beta\theta_n^* \left(\boldsymbol{K}_n - \boldsymbol{K}_w\right) = \boldsymbol{0}, \tag{7.6.3}$$

$$\boldsymbol{\nabla}_{\boldsymbol{x}} \boldsymbol{a}_n^\mathsf{T} - \left(1 - \frac{1}{\theta_n^*}\right) \boldsymbol{I} - \nabla_{\boldsymbol{x}}^2 \boldsymbol{K}_n - \beta\theta_w^* \left(\boldsymbol{K}_w - \boldsymbol{K}_n\right) = \boldsymbol{0}. \tag{7.6.4}$$

On Γ:

$$\boldsymbol{K}_n^\mathsf{T} \boldsymbol{n} = \boldsymbol{0}, \quad \boldsymbol{K}_w^\mathsf{T} \boldsymbol{n} = \boldsymbol{0}, \quad \left(\theta_n^* \boldsymbol{K}_n^\mathsf{T} + \theta_w^* \boldsymbol{K}_w^\mathsf{T}\right) \boldsymbol{t} = \boldsymbol{0}. \tag{7.6.5}$$

On $\partial\Omega_S$:

$$\boldsymbol{K}_n = \boldsymbol{0}, \quad \boldsymbol{K}_w = \boldsymbol{0}. \tag{7.6.6}$$

Finally solutions must be periodic on the boundaries of the periodic cell. The equations in this case have been simplified by the use of the continuity of pressures (5.3.44) which becomes $0 = p_w^{(0)} + \theta_n^* \phi_n^{(0)}$.

In Ω_I we have $p_I^{(0)} = 0$ and, thereby, $\boldsymbol{v}_I = \boldsymbol{0}$. We note that despite the simplifications outlined above, the cell problem comprises a non-trivial coupled Darcy-Stokes problem. Together with its dependence on θ^* and the boundary conditions relevant to the microscale set-up it is therefore similar

3 While an alternative ansatz was proposed in chapter 6, here, where the water phase is inviscid it reduces to the original form used in chapter 5

to, but distinct from, the cell problems encountered in other related studies, such as [46, 115, 126].

7.6.2 *Macroscale description*

The macroscale description is given by (5.3.79,5.3.80,5.3.84,5.3.85) where

$$\bar{\boldsymbol{v}}^{(0)} = \langle \theta_n^* \boldsymbol{v}_n^{(0)} + \theta_w^* \boldsymbol{v}_w^{(0)} \rangle_\tau, \tag{7.6.7}$$

$$\bar{\boldsymbol{K}} = \langle \theta_n^* \boldsymbol{K}_n + \theta_w^* \boldsymbol{K}_w \rangle_\tau \tag{7.6.8}$$

Additionally, we are required to specify the linearised growth and nutrient uptake functions for (5.3.84) and (5.3.85). For generality we choose $S_n^{(0)}$ and $\Lambda^{(0)}$ that support non-trivial steady states θ_n^*, c^* as follows:

$$S_n^{(0)} = \begin{cases} k_m \theta_n^* (1 - \theta_n^*) c^{(0)} & \text{if } c^{(0)} > 0, \\ k_n \theta_n^* c^{(0)} & \text{if } c^{(0)} < 0, \end{cases} \tag{7.6.9}$$

$$\Lambda^{(0)} = \begin{cases} \lambda k_m \theta_n^* c^{(0)} & \text{if } c^{(0)} > 0, \\ 0 & \text{if } c^{(0)} < 0. \end{cases} \tag{7.6.10}$$

Such a choice corresponds to a threshold (steady state) nutrient concentration, c^*, below which cell growth is negligible whilst above it we neglect cell death. Finally, we take $\boldsymbol{v}_\Gamma^{(1)} \cdot \boldsymbol{n}$ to be some constant multiple of (7.5.25), with this additional parameter denoted Y.

7.6.3 *Microscale Problem*

We now present representative numerical experiments, carried out by Joseph Collis, demonstrating the numerical approximation to the solution of the microscale system described in section 7.6.1. Our focus here is to parameterize the dependence of macroscopic model on the underlying microscopic geometry. For computational simplicity, we consider only two-dimensional calculations; however, we note that the methods employed here translate naturally to three dimensions.

In the following computations we consider the microscale geometry $\Omega = (0,1)^2$, decomposed into disjoint subsets Ω_I, Ω_T and Ω_S. For simplicity, we choose a symmetric geometry that may be parameterized by five parameters (r_E, r_I, r_C, ℓ_1 and ℓ_2). A schematic diagram of the microscale geometry is provided in Figure 28.

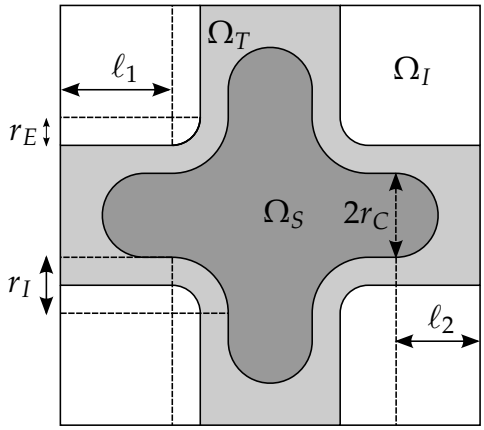


Figure 28: Schematic diagram of the microscale domain, Ω, employed in the example numerical solution of equations (7.6.2–7.6.4).

It is beyond the scope of this work to provide a full description of the discretizations applied to the microscale PDEs; here we provide only details of the finite element spaces and application of boundary conditions and appropriate references. We employ standard finite element methods for the coupled microscale system, approximating $(\boldsymbol{K}_w, \boldsymbol{a}_w)$ with mixed Raviart-Thomas/discontinuous Galerkin elements [30, 127], and $(\boldsymbol{K}_n, \boldsymbol{a}_n)$ with Taylor-Hood elements [145]. The periodic boundary conditions on $\partial\Omega_T \cap \partial\Omega$ are strongly imposed on the approximation of $\boldsymbol{K}_w$ and $\boldsymbol{K}_n$. Similarly, the boundary conditions for $\boldsymbol{K}_w$ on Γ given by (7.6.5), and both $\boldsymbol{K}_n$ and $\boldsymbol{K}_w$ on $\partial\Omega_s$ given by (7.6.6) are strongly imposed. Finally, the condition on $\boldsymbol{K}_n$ on Γ given by (7.6.5) is weakly imposed, see [21, 110]. Figure 29 shows representative numerical solutions of the microscale system obtained using the parameter values provided in Table 5. Further, we note that under the assumptions on the geometrical parameters, the sizes of the respective

domains are given by $|\Omega_I| = 0.36$, $|\Omega_T| = 0.48$ and $|\Omega_S| = 0.16$ (i.e. the porosity is 84%, in line with [67]).

Table 5.: Parameter values employed in the microscale numerical experiment.

Parameter	Value
β	1.0×10^4
θ_n^*	0.8111
θ_w^*	0.1889
r_E	0.05
r_I	0.2
r_C	0.05
ℓ_1	0.25
ℓ_2	0.2

Due to the symmetries of Ω_I, Ω_T and Ω_S, the computation of $\left(\boldsymbol{K}_{n/w}\right)_{11}$ and $\left(\boldsymbol{K}_{n/w}\right)_{12}$ is sufficient to specify $\boldsymbol{K}_{n/w}$ in Ω_T. Given this observation, we may use the numerical approximations shown in Figure 29 to calculate the spatially averaged permeabilities as

$$\left\langle \boldsymbol{K}_w \right\rangle_T = \begin{pmatrix} 3.01 \times 10^{-4} & -5.81 \times 10^{-11} \\ -5.81 \times 10^{-11} & 3.01 \times 10^{-4} \end{pmatrix} \tag{7.6.11}$$

and

$$\left\langle \boldsymbol{K}_n \right\rangle_T = \begin{pmatrix} -5.16 \times 10^{-6} & -2.90 \times 10^{-11} \\ -2.90 \times 10^{-11} & -5.16 \times 10^{-6} \end{pmatrix}. \tag{7.6.12}$$

We note that the off-diagonal entries of $\left\langle \boldsymbol{K}_w \right\rangle_T$ and $\left\langle \boldsymbol{K}_n \right\rangle_T$ are, effectively, zero: under the choice of geometry shown in Figure 28, we would expect $\left\langle \boldsymbol{K}_w \right\rangle_T$ and $\left\langle \boldsymbol{K}_n \right\rangle_T$ to be isotropic, to within the discretization error in numerical scheme, and the results (7.6.11) and (7.6.12) are consistent with this.

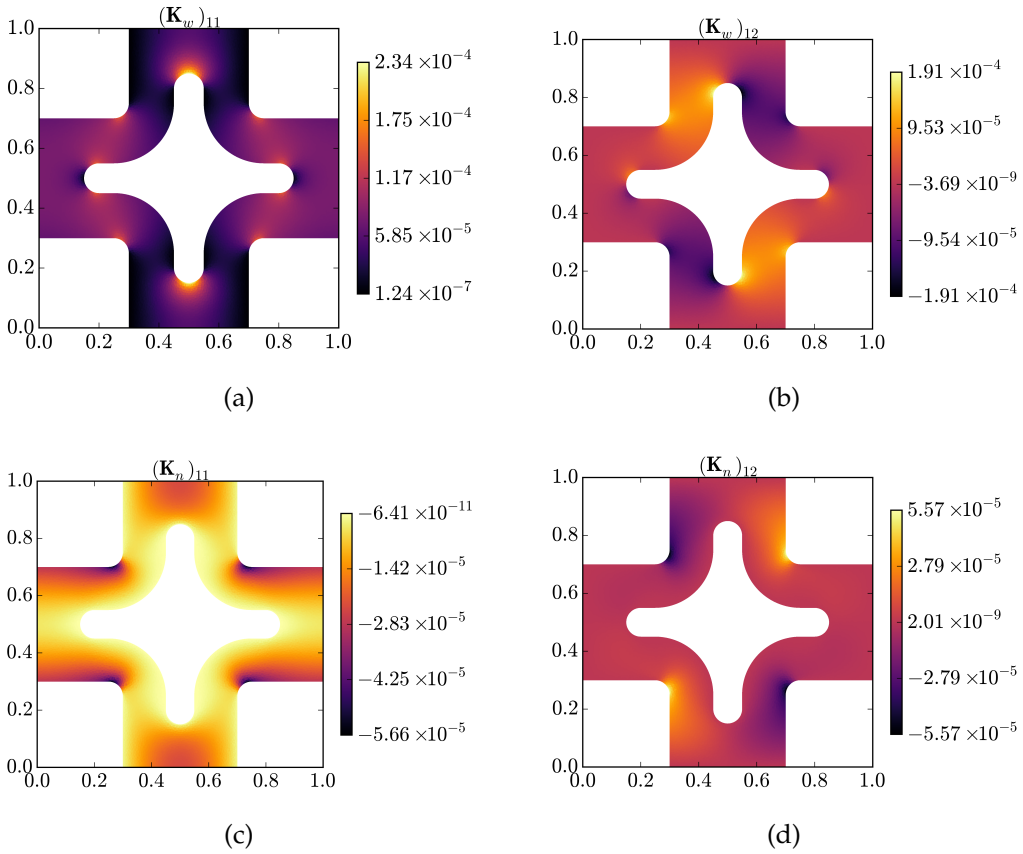


Figure 29: Numerical approximation of $\boldsymbol{K}_n$ and $\boldsymbol{K}_w$, from the solution of the microscale problem given by equations (7.6.2–7.6.4).

7.6.4 *Macroscale Problem*

We now consider numerical experiments, carried out by Joseph Collis, demonstrating the corresponding macroscopic behaviour of the system described in section 7.6.2. We highlight that our focus here is to highlight the macroscale model dynamics that arise from a suitable consideration of the multiscale growth processes together with appropriate numerical methods to facilitate their calculation. Representative parameter values, boundary and initial data, and geometry are considered, in conjunction with microscale data obtained from the numerical experiments discussed in section 7.6.3. For computational simplicity, we once more restrict out

attention to two-dimensional calculations, though we again note that the methods employed here generalise naturally.

Denoting the macroscale domain and its boundary, by Ω_L and $\partial\Omega_L$, respectively, we specify the pressure boundary condition as

$$p_w^{(0)} = 0 \qquad \text{on } \partial\Omega_L, \tag{7.6.13}$$

and initial conditions, at $t = 0$,

$$c^{(0)} = 1 \qquad \text{in } \Omega_L \tag{7.6.14}$$

and

$$\theta_n^{(0)} = 0.6 \qquad \text{in } \Omega_L, \tag{7.6.15}$$

on the nutrient and cell volume fractions, respectively. Further, we define our macroscale domain to be $\Omega_L = \left\{X : \sqrt{X_1^2 + X_2^2} < 1\right\}$.

To compute the numerical approximation of the macroscale flow system we employ a mixed Raviart-Thomas/discontinuous Galerkin finite element [30, 127]. As there is no spatial component to the evolution of the cell volume fraction and nutrient concentration, we simply employ an explicit Euler time-stepping scheme in the discretization of (5.3.85) and (5.3.84).

Figure 30 shows the dependence of $\theta_n^{(0)}$ on a range of parameters in the macroscale model. The effect of cell-cell aggregation and repulsion on the cell volume fraction is illustrated by Figures 30(a) and (b), showing that increased repulsion or decreased aggregation results in lower $\theta_n^{(0)}$. Figures 30(c) and (d) show the dependence of $\theta_n^{(0)}$ and $c^{(0)}$ on λ, with increasing uptake depleting nutrient faster and hence leading to slower increase in $\theta_n^{(0)}$. Figure 30(e) depicts the effect of varying Y on $\theta_n^{(0)}$. We note that $c^{(0)}$ does not vary strongly with other parameters in the model, and hence forgo the inclusion of those plots here. In the numerical results presented in this figure we consider only the case $\bar{\rho} = 1$. As there is no density difference, however, the forcing in the flow equations reduces to zero and the pressure $p_w^{(0)}$ is identically zero throughout Ω_L.

In the case where there is a moderate density difference between the viscous and inviscid fluids we obtain a non-trivial pressure $p_w^{(0)}$, the

evolution of which is shown in Figure 31. Over the course of the simulation we are able to observe an initial increase in the pressure inside the domain, as the cell volume fraction decreases (cf. Figure 30(e)), followed by a decrease in pressure as the cell volume fraction increases. At this level of density difference, however, (and for the other parameter values chosen) the differences in evolution of both $\theta_n^{(0)}$ and $c^{(0)}$ are small and, therefore, we do not include those figures here.

7.7 SUMMARY

In this chapter we have investigated the behaviour of the microscale multiphase tissue model with the aim of proposing a method for the closure of the multiscale model of chapter 5. We then employ this in a specific limiting case to illustrate how the coupled macroscale description and cell problem can be solved. The work in this chapter, other than section 7.5.2, has been published in [71].

Beginning by considering the multiphase tissue description in one dimension and reducing the number of variables, we obtain a pair of coupled equations describing the volume fraction of cells and their velocity. Here, for simplicity, we assume that nutrient diffusion is much faster than uptake and hence take nutrient concentration to be uniform across the tissue.

First we considered the case where the water phase is taken to be inviscid, resulting in a very similar model to that of [89]. Using the method of finite volumes the coupled equations are solved numerically for a range of parameter values. After an initial transient, dependent on the initial condition, the cell volume fraction distribution takes the form of a travelling wave. Closely following the analysis of [89], we determine that the type of behaviour observed is characterised by the relationship between the aggregate density (the cell volume fraction just inside the

moving boundary), the steady state cell fraction and its stability, resulting in forward, backward or unstable waves.

In view of our focus on growing tissues, and due to numerical issues, we concentrate on forward-travelling waves and obtain a suitable expression for the wave speed by fitting to wave speeds obtained numerically for a wide range of parameters. This work is validated against approximate wave speeds found analytically for slow waves and in the absence of drag, following [89], and those found by use of the shooting method.

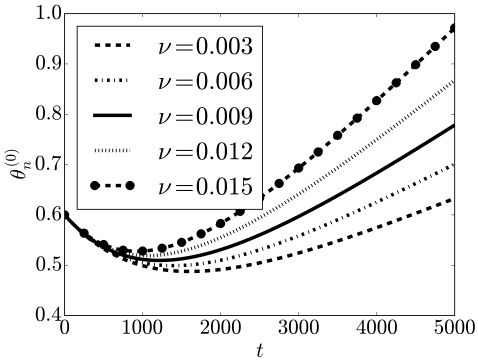
Next we considered the case where both phases of the tissue are viscous. This leads to some difficulties with the numerics, so we introduced diffusion of the cell phase. Qualitatively similar behaviour to the previous case is observed, so with small cell phase diffusion a formula for the wave speed of comparable form may be reasonable. Obtaining this is computationally intensive, however, so it is not sought here.

As a result of studying the multiscale model, we have an estimate of the tissue boundary velocity which we use to provide closure to the coupled macroscale description and cell problem of chapter 5, when the water phase is inviscid. With the model now closed, we show how it can be solved numerically in this limit case.

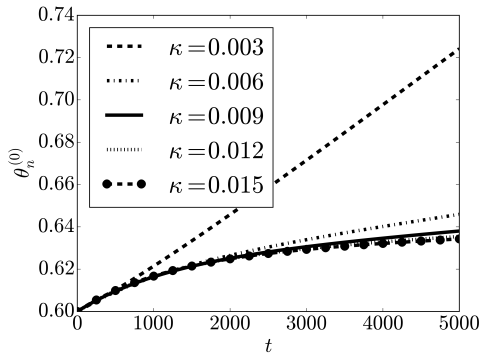
The cell problem is solved, for computational simplicity, in two dimensions on a sample geometry. The solutions of this microscale problem, the permeabilities, are used to parameterise the macroscale model. Again in two dimensions, we solve for the macroscopic behaviour, investigating its dependence on a range of parameters: cell aggregation, repulsion, boundary velocity and nutrient uptake. For moderately different phase densities the behaviour of macroscale pressure is shown, whilst a lack of density difference results in trivial pressure.

Having derived a macroscale description for tissue growth in chapter 5, and provided closure and illustrative numeric results here, in the next chapter we use similar techniques for a different problem. Multiscale homogenisation, as used in chapters 4 and 5 to derive macroscale tissue

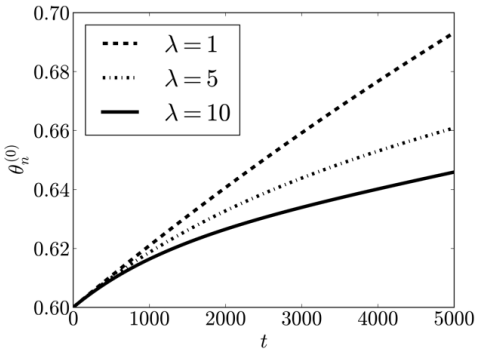
growth models, is utilised to investigate experimental data concerned with drug uptake by cells.



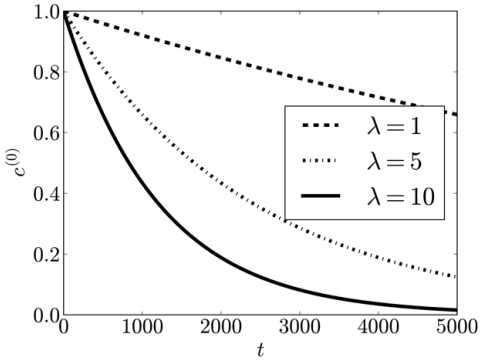
(a) Dependence of $\theta_n^{(0)}$ on ν with $\Upsilon = 0.05$, $\lambda = 10$, $\kappa = 0.012$.



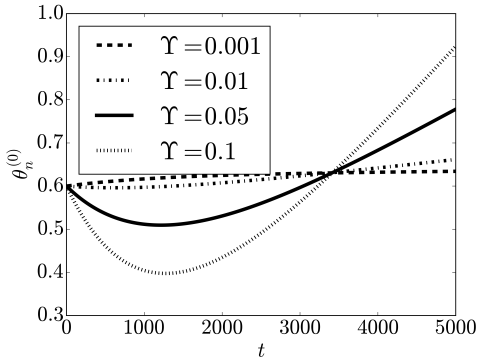
(b) Dependence of $\theta_n^{(0)}$ on κ with $\Upsilon = 0.001$, $\nu = 0.009$, $\lambda = 10$.



(c) Dependence of $\theta_n^{(0)}$ on λ with $\Upsilon = 0.001$, $\nu = 0.009$, $\kappa = 0.006$.

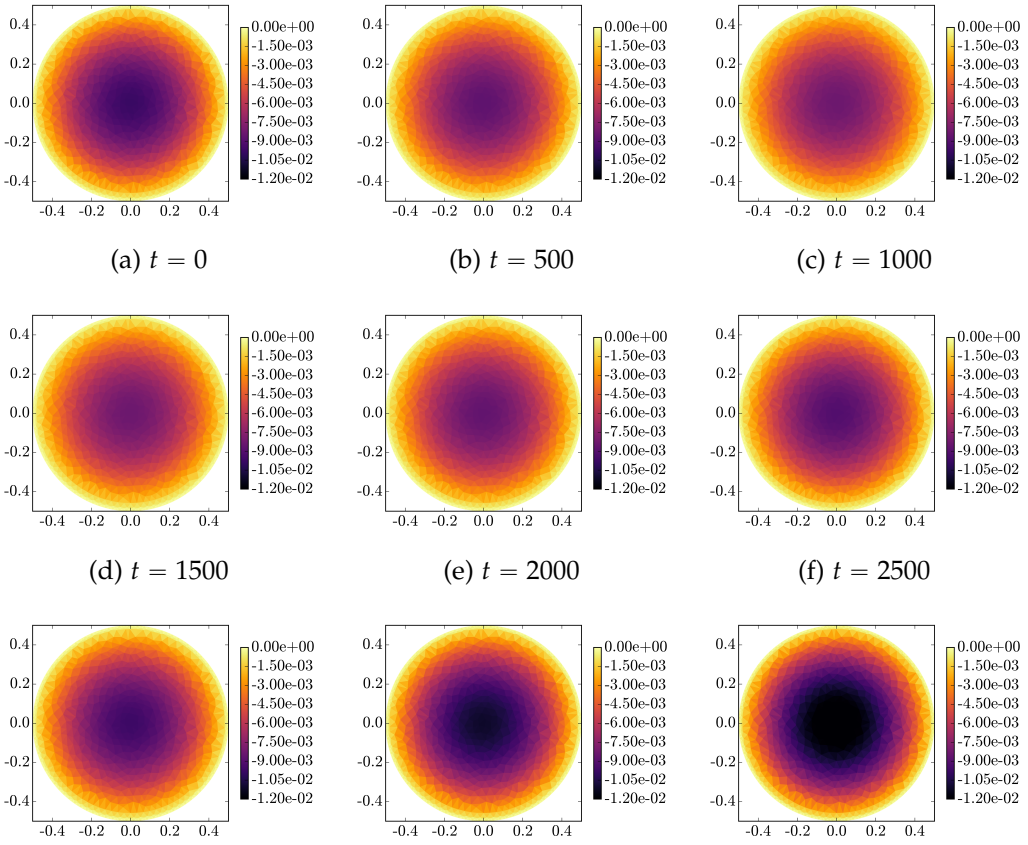


(d) Dependence of $c^{(0)}$ on λ with $\Upsilon = 0.001$, $\nu = 0.009$, $\kappa = 0.006$.



(e) Dependence of $\theta_n^{(0)}$ on Υ with $\kappa = 0.006$, $\nu = 0.009$, $\lambda = 10$.

Figure 30: Plots demonstrating the dependence of the evolution of nutrient concentration and cell volume fraction on parameters in the macroscale model, described by equations (5.3.79,5.3.80,5.3.84,5.3.85) and boundary conditions (7.6.13–7.6.15) with $\bar{\rho} = 1$.



(a) $t = 0$ (b) $t = 500$ (c) $t = 1000$

(d) $t = 1500$ (e) $t = 2000$ (f) $t = 2500$

(g) $t = 3000$ (h) $t = 4000$ (i) $t = 5000$

Figure 31: Plots showing the leading order pressure for $\mathrm{Y} = 0.05$, $\nu = 0.009$, $\kappa = 0.012$, $\bar{\rho} = 1.5$, and $\lambda = 10$, from the solution of the macroscale problem described by equations (5.3.79,5.3.80,5.3.84,5.3.85) and boundary conditions (7.6.13–7.6.15).

8

DRUG DELIVERY TO TUMOUR SPHEROIDS

8.1 INTRODUCTION

With 1 in 2 people in the UK expected to be diagnosed with cancer in their lifetime [12] a significant amount of research is focussed on the detection and successful treatment of the disease, characterised by the uncontrolled growth and spread of abnormal cells. One treatment for breast cancer is the drug Palbociclib, which works by blocking the binding of adenosine triphosphate (ATP) to CDK4/6 proteins within cells thereby arresting them in the Gap 1 (G1) phase of the cell cycle and stopping their growth. It can be used in combination with endocrine therapy, where it improves outcomes [42]. To work effectively the drug must reach the cancerous cells and be taken up by them.

Recent experimental work has been undertaken by collaborators (University of Bradford) to improve understanding of the drug penetration and distribution in a tumour, with the aim of informing the development of the best treatment regimes. It involves human breast cancer cells (MCF-7) and human colorectal adenocarcinoma cells (DLD-1) being placed into a Palbociclib solution and the uptake of the drug from the solution measured, as well as the efflux of the drug into drug-free medium from cells pre-exposed to the drug. In addition to comparing the behaviour of the two cell lines, the difference between individual cells and spheroids (model tumours) is also investigated.

In the uptake experiments, summarised by figure 34, cells in solution take up the drug much quicker than the spheroids, with MCF-7 cells and spheroids having a greater uptake than DLD-1. These results are illustrated by figure 32.

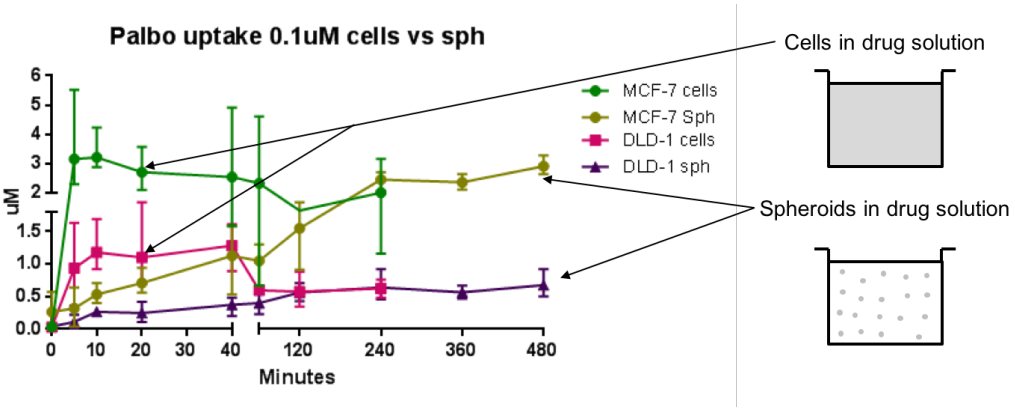


Figure 32: Experimental results for drug uptake for cells (green and magenta curves) and spheroids (olive and purple curves) at different time points. (Courtesy of Jade Spencer)

In the efflux experiments (summarised by figure 35) once a steady state had been achieved, the cells/spheroids were removed from the drug solution and placed into a drug-free one. The efflux of drug into the solution was measured. The results (see figure 33) are much more similar for the cells and spheroid cases than those observed in the uptake experiment.

We wish to construct a model to capture and explain the different uptake functions (and efflux) for cells and spheroids. As the cells and spheroids are well mixed in the medium, we may assume that they are evenly distributed, so enabling analysis via homogenisation. We begin with a brief description of the experimental procedure in section 8.2 and a possible binding model for the drug in section 8.3. In section 8.4 we set up the model and nondimensionalise the equations. Based on two possible scaling choices, we derive, via homogenisation, two effective descriptions in section 8.5 for the uptake of drug by the spheroids in solution. These are solved numerically in section 8.6 to illustrate model behaviour and then fitting to the experimental

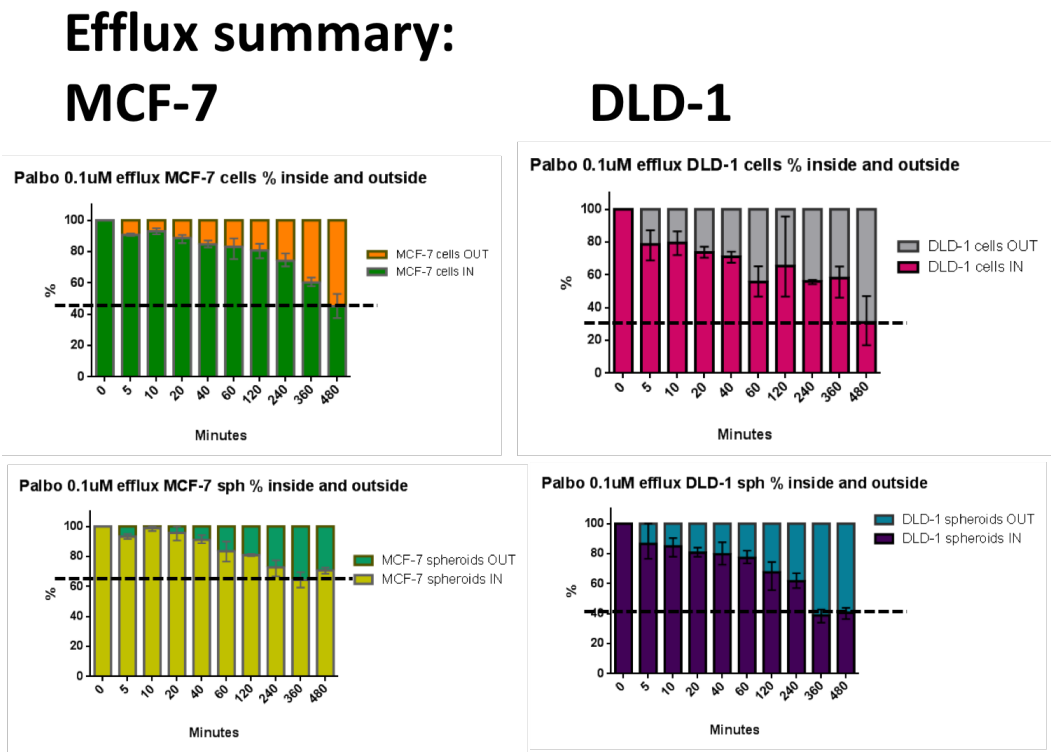


Figure 33: Experimental results for drug efflux for MCF-7 cells and spheroids (left) and DLD-1 cells and spheroids (right). Bars show the percentage of drug inside and outside the cells/spheroids at different time points.

data is attempted. In 8.7 we discuss determination of the effective diffusion coefficient, and show numerical solutions for a number of spheriods. Finally the chapter is summarised in 8.8.

8.2 EXPERIMENTAL SETUP

In this section we describe the experimental methods used to determine the uptake and efflux of drug by the cancer cells and spheroids. Each experiment is repeated three times for each time point, for MCF-7 and DLD-1 cells and spheroids

8.2.1 *Uptake experiment*

To determine the uptake of drug by the cells the following experimental procedure is followed, as illustrated in figure 34.

1. 1×10^6 cells or 30 spheroids (of approximate volume $1.5\mu L$) are placed in an Eppendorf (laboratory tubes, see figure 34) and $1ml$ $100nM$ Palbociclib in media is added.

2. The Eppendorf is incubated for 0 to 240min and 0 to 480min for cells and spheroids respectively (a separate Eppendorf is used for each time point) and then the drug containing media is removed. The cells are washed three times in order to remove any residual drug.

3. An organic solvent is added to the washed cells which are then subject to ultrasonic vibration to fragment the cells, releasing the drug into the solvent.

4. The solvent is removed and evaporated, leaving the drug which is then reconstituted and a sample analysed by liquid chromatography mass spectrometry (LCMS).

5. The resulting concentration is used to calculate the actual concentration that was within the cells.

8.2.2 *Efflux experiment*

To determine the efflux of drug from the cells into the surrounding media the following experimental procedure is followed, as illustrated in figure 35.

1. 1×10^6 cells or 30 spheroids (of approximate volume $1.5\mu L$) are placed in an Eppendorf and $1ml$ $100nM$ Palbociclib in media is added

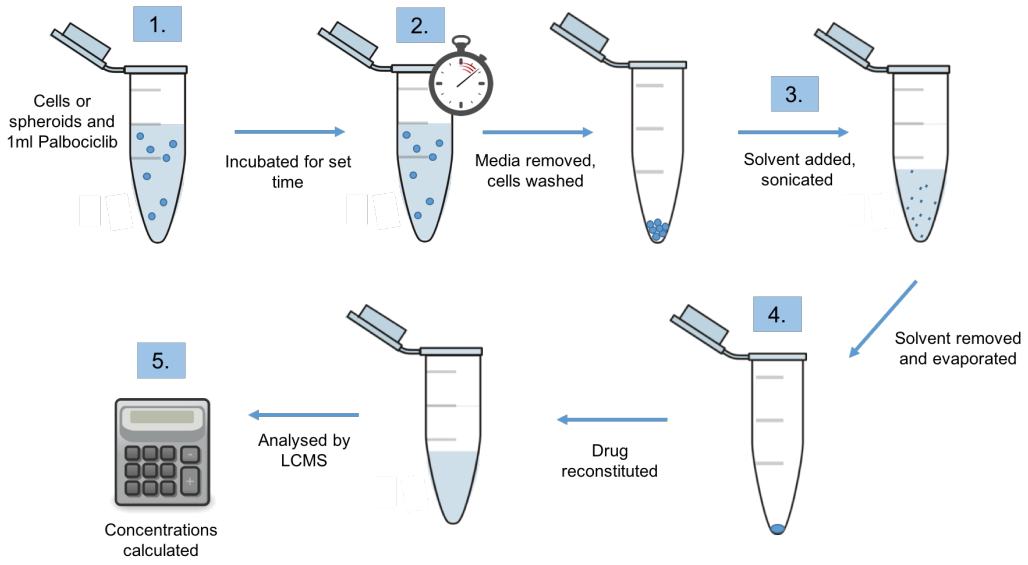


Figure 34: Diagram for drug uptake experiment.

2. The Eppendorf is incubated for 60 minutes and then the drug containing media is removed. The cells are washed three times in order to remove any residual drug.

3. $50\mu L$ of fresh media is added to the cells which are then incubated for 5 to 240min and 5 to 480 min for cells and spheroids respectively.

4. The cells and media are separated and the cells washed. Then stage 3 and 4 of the uptake experiment are followed, with solvent additionally added then evaporated from the media.

5. The resulting concentrations are used to calculate the actual concentration that was within and outside the cells.

8.3 BINDING MODEL FOR DRUG UPTAKE

To describe the uptake of drug by the cells and spheroids we use the binding model of [68], a simple kinetic model in which the drug binds reversibly to sites within the cell.

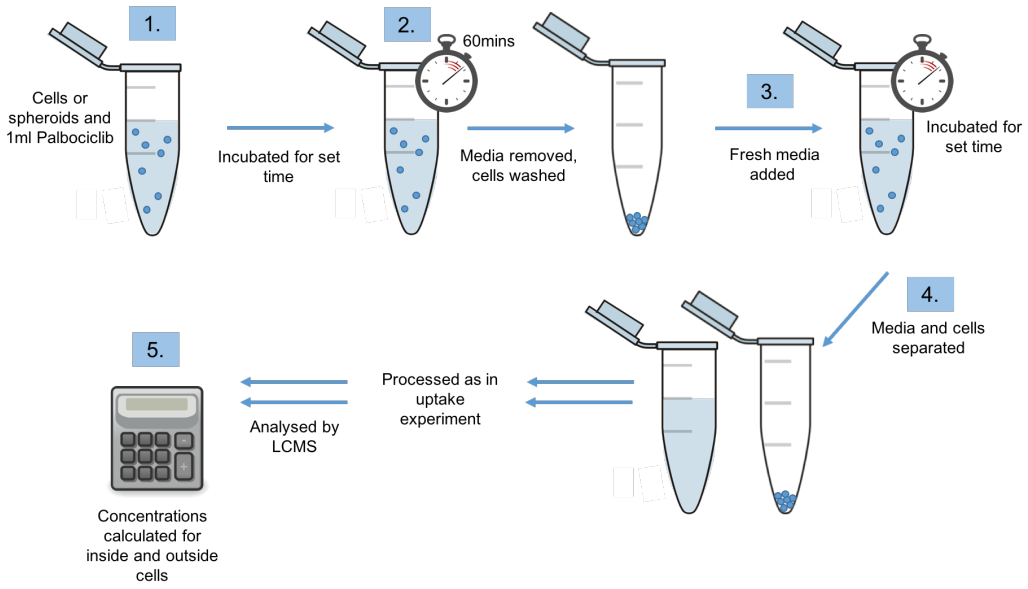


Figure 35: Diagram for drug efflux experiment.

The spheroids are taken to be composed of cellular and extracellular space, of volume fractions δ_2 and δ_1 respectively. In the extracellular space the drug, with concentration c_{1s}, is free to diffuse and be taken up by the cells. Within the cells, there is both a free and a bound concentration of drug, c_2 and c_3, see figure 36, with movement between these states dependent on drug association and disassociation rates as well as the concentration of binding sites, c_0. The binding model is given by:

$$\delta_1 \frac{\partial c_{1s}}{\partial t} = D_s \nabla^2 c_{1s} + \alpha k_1 \left(c_2 - c_{1s}\right), \tag{8.3.1}$$

$$\delta_2 \frac{\partial c_2}{\partial t} = \alpha k_1 \left(c_{1s} - c_2\right) - \delta_2 k_2 c_2 \left(c_0 - c_3\right) + \delta_2 k_{-2} c_3, \tag{8.3.2}$$

$$\delta_2 \frac{\partial c_3}{\partial t} = \delta_2 k_2 c_2 \left(c_0 - c_3\right) - \delta_2 k_{-2} c_3, \tag{8.3.3}$$

where model parameters are described in table 6.

Note that in the case of single cells (as opposed to spheroids), there is no extracellular space so we use the reduced model,

$$\frac{\partial c_2}{\partial t} = -k_2 c_2 \left(c_0 - c_3\right) + k_{-2} c_3, \tag{8.3.4}$$

$$\frac{\partial c_3}{\partial t} = k_2 c_2 \left(c_0 - c_3\right) - k_{-2} c_3. \tag{8.3.5}$$

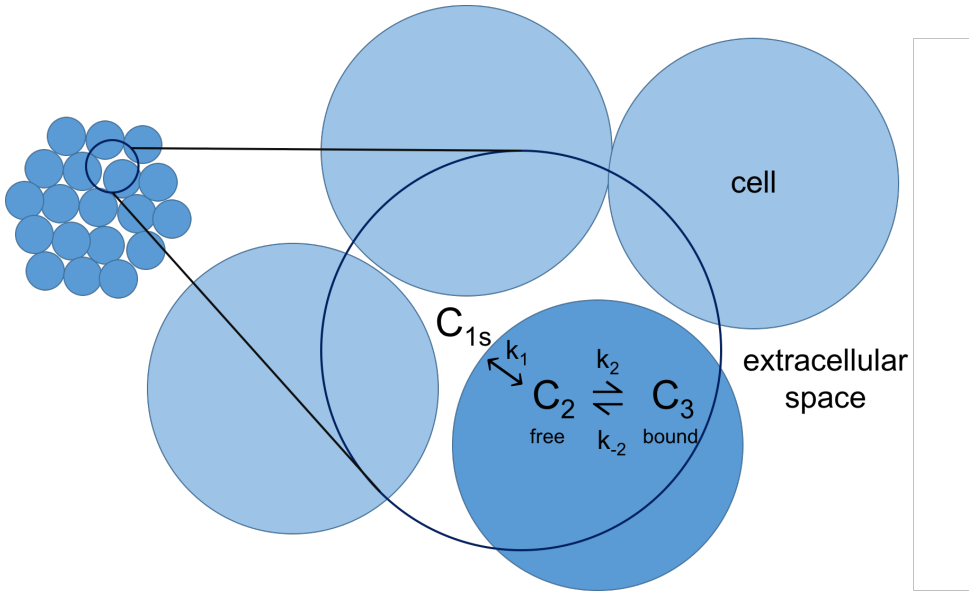


Figure 36: Illustration showing the extracellular, c_{1s}, intracellular free, c_2, and intracellular bound, c_3, drug concentrations.

Table 6.: Description of binding model parameters values

Parameter	Description
α	ratio of cellular surface area to volume
c_0	concentration of binding sites
D_s	diffusivity in spheroid
δ_1	volume fraction of extracellular space in spheroid
δ_2	volume fraction of cellular space in spheroid
k_1	transmembrane rate of drug transport
k_2	drug association rate
k_{-2}	drug disassociation rate

In the model setup and analysis which follows we use the full spheroid version of the binding model, but this can easily be reduced to that for single cells.

8.4 MODEL SETUP

As the cells/spheroids are assumed to be fully mixed in the medium, we take them to be evenly distributed, making it possible to take a homogenisation approach to the problem. A periodic cell may be taken to be a single spheroid and the region of neighbouring fluid, as illustrated by figure 37.

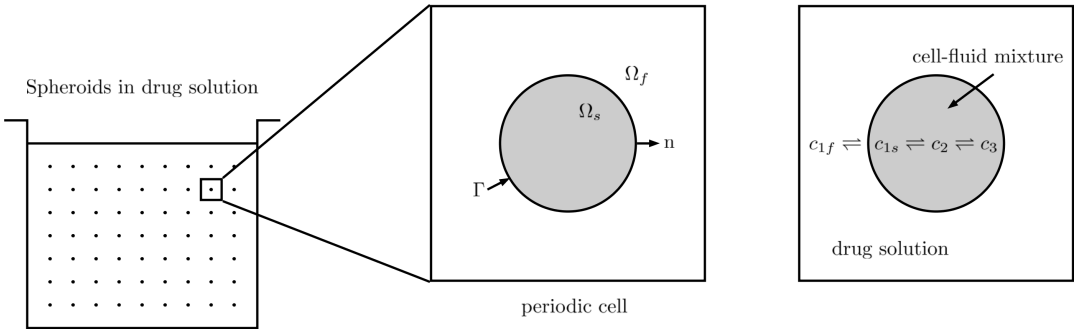


Figure 37: A periodic cell, comprising drug solution, Ω_f, and a single spheroid Ω_s. The spheroid is described by a mixture model of cell and fluid phases.

The fluid region, Ω_f, contains the drug solution, assumed stationary, whilst Ω_s represents a spheroid, comprised of extracellular space, volume fraction δ_1, and cells, volume fraction δ_2.

The drug in the solution, concentration c_{1f}, is free to diffuse throughout the fluid with diffusivity D_f

$$\frac{\partial c_{1f}}{\partial t} = D_f \nabla^2 c_{1f}. \tag{8.4.1}$$

To describe the drug concentration in Ω_s we use the binding model (8.3.1–8.3.3).

On the solution spheroid boundary, Γ, we propose two possible sets of conditions. The first, and simplest choice, consists of continuity of diffusive flux and of drug concentration,

$$D_s \boldsymbol{\nabla} c_{1s} \cdot \boldsymbol{n} = D_f \boldsymbol{\nabla} c_{1f} \cdot \boldsymbol{n} \quad \text{and} \quad c_{1s} = c_{1f}. \tag{8.4.2}$$

Alternatively, the diffusive flux across the boundary may be both continuous and proportional to the concentration drop across it,

$$D_s \boldsymbol{\nabla} c_{1s} \cdot \boldsymbol{n} = D_f \boldsymbol{\nabla} c_{1f} \cdot \boldsymbol{n} = \gamma \left(c_{1f} - c_{1s} \right) \tag{8.4.3}$$

where γ is the coefficient of permeability for the boundary. This membrane law introduces an additional parameter but may be more appropriate as it has been used to describe transport of molecules across tumour vasculature [76].

8.4.1 *Steady state*

We note that a homogeneous steady state exists, given by

$$c_{1f} = c_{1s} = c_2 = K, \quad c_3 = \frac{k_2 c_0 K}{k_2 K + k_{-2}} \tag{8.4.4}$$

where the constant K can be determined, given initial conditions and parameter values, by considering global conservation of the drug. We see in the numerical experiments later in this chapter that concentration of drug tends to this steady state. Additionally the relationship between binding and unbinding rates may help to determine these parameters from the experimental data.

8.4.2 *Non dimensionalisation*

We nondimensionalise the microscale equations with characteristic values for nutrient concentration, C, and length, l,

$$c_i = C c_i^*, \quad \boldsymbol{x} = l \boldsymbol{x}^*, \quad t = \frac{l}{\gamma} t^*, \tag{8.4.5}$$

where asterisk denotes dimensionless variables and choose to consider the timescale of nutrient uptake (via the permeable spheroid boundary) into the spheroid. Dropping the asterisks for convenience, the dimensionless form of the model equations is given below. In the fluid domain, Ω_f:

$$\frac{\partial c_{1f}}{\partial t} = D_F \nabla^2 c_{1f}. \tag{8.4.6}$$

In the spheroid domain, Ω_s:

$$\delta_1 \frac{\partial c_{1s}}{\partial t} = D_S \nabla^2 c_{1s} + K_1 \left(c_2 - c_{1s}\right), \tag{8.4.7}$$

$$\delta_2 \frac{\partial c_2}{\partial t} = K_1 \left(c_{1s} - c_2\right) - \delta_2 K_2 c_2 \left(c_0 - c_3\right) + \delta_2 K_{-2} c_3, \tag{8.4.8}$$

$$\delta_2 \frac{\partial c_3}{\partial t} = \delta_2 K_2 c_2 \left(c_0 - c_3\right) - \delta_2 K_{-2} c_3. \tag{8.4.9}$$

As above, on the boundary, $\Gamma = \Omega_s \cap \Omega_f$, we impose either

$$D_S \boldsymbol{\nabla} c_{1s} \cdot \boldsymbol{n} = D_F \boldsymbol{\nabla} c_{1f} \cdot \boldsymbol{n} \quad \text{and} \quad c_{1s} = c_{1f}, \tag{8.4.10}$$

or

$$D_S \boldsymbol{\nabla} c_{1s} \cdot \boldsymbol{n} = D_F \boldsymbol{\nabla} c_{1f} \cdot \boldsymbol{n} = \left(c_{1f} - c_{1s}\right). \tag{8.4.11}$$

The dimensionless parameters are defined by

$$D_F = \frac{D_f}{\gamma l}, \quad D_S = \frac{D_s}{\gamma l}, \quad K_1 = \frac{\alpha k_1 l}{\gamma}, \quad K_2 = \frac{C k_2 l}{\gamma}, \quad K_{-2} = \frac{k_{-2} l}{\gamma}. \tag{8.4.12}$$

D_F and D_S represent the ratio of diffusive transport rate to uptake rate whilst the K_i are the ratios of rates of transmembrane transport, drug association and disassociation, to the uptake rate.

In the next section we consider the impact of different scalings and boundary conditions on the effective equations obtained from (8.4.6–8.4.11) via homogenisation.

8.5 HOMOGENISATION

The choice of scalings (and boundary conditions) applied to the problem impacts the homogenised equations achieved (and whether valid macroscale equations can be obtained). We look at a number of possibilities below. Note that, as in previous chapters, we use the following volume average,

$$\langle g \rangle_i = \frac{1}{|\Omega|} \int_{\Omega_i} g \, \mathrm{d}V. \tag{8.5.1}$$

8.5.1 *Similar drug diffusivities in both domains*

We begin by supposing that diffusion is of similar magnitude in both the fluid and the spheroid, and much faster than uptake, i.e.

$$D_F = \frac{1}{\varepsilon^2}\tilde{D}_F, \quad D_S = \frac{1}{\varepsilon^2}\tilde{D}_S, \tag{8.5.2}$$

where tildes denote rescaled parameters and $\varepsilon \ll 1$. Dropping tilde notation for convenience, our rescaled equations are given below.

In the fluid domain, Ω_f:

$$\frac{\partial c_{1f}}{\partial t} = \frac{1}{\varepsilon^2} D_F \nabla^2 c_{1f}. \tag{8.5.3}$$

In the spheroid domain, Ω_s:

$$\delta_1 \frac{\partial c_{1s}}{\partial t} = \frac{1}{\varepsilon^2} D_S \nabla^2 c_{1s} + K_1 \left(c_2 - c_{1s}\right), \tag{8.5.4}$$

$$\delta_2 \frac{\partial c_2}{\partial t} = K_1 \left(c_{1s} - c_2\right) - \delta_2 K_2 c_2 \left(c_0 - c_3\right) + \delta_2 K_{-2} c_3, \tag{8.5.5}$$

$$\delta_2 \frac{\partial c_3}{\partial t} = \delta_2 K_2 c_2 \left(c_0 - c_3\right) - \delta_2 K_{-2} c_3. \tag{8.5.6}$$

On the boundary, $\Gamma = \Omega_s \cap \Omega_f$, either

$$\frac{1}{\varepsilon^2} D_S \boldsymbol{\nabla} c_{1s} \cdot \boldsymbol{n} = \frac{1}{\varepsilon^2} D_F \boldsymbol{\nabla} c_{1f} \cdot \boldsymbol{n} \quad \text{and} \quad c_{1s} = c_{1f}, \tag{8.5.7}$$

or

$$\frac{1}{\varepsilon^2} D_S \boldsymbol{\nabla} c_{1s} \cdot \boldsymbol{n} = \frac{1}{\varepsilon^2} D_F \boldsymbol{\nabla} c_{1f} \cdot \boldsymbol{n} = \left(c_{1f} - c_{1s}\right). \tag{8.5.8}$$

As in previous multiscale analyses, we introduce the macroscale coordinate $\boldsymbol{X}$ where $\boldsymbol{X} = \varepsilon \boldsymbol{x}$ ($\boldsymbol{x}$ being the microscale coordinate). Since the two length scales are well-separated we treat $\boldsymbol{x}$ and $\boldsymbol{X}$ as independent and expand variables and differential operators in multiple-scales form as follows:

$$c_i\left(\boldsymbol{x}, \boldsymbol{X}, t; \varepsilon\right) = c_i^{(0)}\left(\boldsymbol{x}, \boldsymbol{X}, t\right) + \varepsilon c_i^{(1)}\left(\boldsymbol{x}, \boldsymbol{X}, t\right) + \ldots \tag{8.5.9}$$

$$\boldsymbol{\nabla} = \boldsymbol{\nabla}_{\boldsymbol{x}} + \varepsilon \boldsymbol{\nabla}_{\boldsymbol{X}}, \quad \nabla^2 = \nabla_{\boldsymbol{x}}^2 + 2\varepsilon \boldsymbol{\nabla}_{\boldsymbol{x}} \cdot \boldsymbol{\nabla}_{\boldsymbol{X}} + \varepsilon^2 \nabla_{\boldsymbol{X}}^2, \tag{8.5.10}$$

where $i = 1f, 1s, 2, 3$. Recall that c_0 is the concentration of binding sites, assumed to be constant, and so is not expanded. In addition to the boundary conditions on Γ, we assume that $c_i^{(j)}$ for $j = 0, 1, ...$ are periodic in $\boldsymbol{x}$. We now analyse the equations at each order in ε, with the aim of obtaining a description of the macroscale drug uptake.

At leading order, $O(1/\varepsilon^2)$,:

$$0 = D_F \nabla_{\boldsymbol{x}}^2 c_{1f}^{(0)}, \tag{8.5.11}$$

$$0 = D_S \nabla_{\boldsymbol{x}}^2 c_{1s}^{(0)}, \tag{8.5.12}$$

with boundary conditions

$$D_S \boldsymbol{\nabla}_{\boldsymbol{x}} c_{1s}^{(0)} \cdot \boldsymbol{n} = D_F \boldsymbol{\nabla}_{\boldsymbol{x}} c_{1f}^{(0)} \cdot \boldsymbol{n} \quad \text{and} \quad c_{1s}^{(0)} = c_{1f}^{(0)}, \tag{8.5.13}$$

or

$$D_S \boldsymbol{\nabla}_{\boldsymbol{x}} c_{1s}^{(0)} \cdot \boldsymbol{n}_{\boldsymbol{x}} = D_F \boldsymbol{\nabla}_{\boldsymbol{x}} c_{1f}^{(0)} \cdot \boldsymbol{n} = 0. \tag{8.5.14}$$

In the case of continuity of concentration on the boundary (8.5.13), we conclude that

$$c_{1s}^{(0)} = c_{1f}^{(0)} = c^{(0)}(\boldsymbol{X}, t), \tag{8.5.15}$$

i.e. that drug concentration is independent of the microscale and uniform across the entire periodic cell. This occurs at steady state, when the uptake dynamics of interest have already occurred. This suggests that continuity of concentration is not an appropriate boundary condition here.

From the alternative set of boundary conditions (8.5.14), we conclude that

$$c_{1s}^{(0)} = c_{1s}^{(0)}(\boldsymbol{X}, t), \quad c_{1f}^{(0)} = c_{1f}^{(0)}(\boldsymbol{X}, t), \tag{8.5.16}$$

i.e. that drug concentration is independent of the microscale but can be different in each domain.

At next order, $O(1/\varepsilon)$,:

$$0 = D_F \nabla_{\boldsymbol{x}}^2 c_{1f}^{(1)}, \tag{8.5.17}$$

$$0 = D_S \nabla_{\boldsymbol{x}}^2 c_{1s}^{(1)}, \tag{8.5.18}$$

$$0 = D_S \left(\boldsymbol{\nabla}_{\boldsymbol{X}} c_{1s}^{(0)} + \boldsymbol{\nabla}_{\boldsymbol{x}} c_{1s}^{(1)} \right) \cdot \boldsymbol{n} = D_F \left(\boldsymbol{\nabla}_{\boldsymbol{X}} c_{1f}^{(0)} + \boldsymbol{\nabla}_{\boldsymbol{x}} c_{1f}^{(1)} \right) \cdot \boldsymbol{n}. \tag{8.5.19}$$

Suitable forms for $c_{1i}^{(1)}$ for $i = f, s$ are given by

$$c_{1i}^{(1)} = \boldsymbol{\chi}_i(\boldsymbol{x}) \boldsymbol{\nabla}_{\boldsymbol{X}} c_{1i}^{(0)} + \bar{c}_i(\boldsymbol{X}, t), \tag{8.5.20}$$

where $\boldsymbol{\chi}_i$ are $\boldsymbol{x}$-periodic, imparting microscale variation, with $\langle \boldsymbol{\chi}_i \rangle_i = 0$, and where $\bar{c}_i$ are the mean values of the first order concentrations. Substituting (8.5.20) into equations (8.5.17–8.5.19) we have the following cell problems to solve, in order to obtain $\boldsymbol{\chi}_i$,

$$0 = \nabla_{\boldsymbol{x}}^2 \boldsymbol{\chi}_i \quad \text{in } \Omega_i, \tag{8.5.21}$$

$$0 = D_i (\boldsymbol{\nabla}_{\boldsymbol{x}} \boldsymbol{\chi}_i + \boldsymbol{I}) \cdot \boldsymbol{n} \quad \text{on } \Gamma. \tag{8.5.22}$$

The model equations at $O(1)$ are given by:

$$\frac{\partial c_{1f}^{(0)}}{\partial t} = D_F \left(\nabla_{\boldsymbol{x}}^2 c_{1f}^{(2)} + 2\boldsymbol{\nabla}_{\boldsymbol{x}} \cdot \boldsymbol{\nabla}_{\boldsymbol{X}} c_{1f}^{(1)} + \nabla_{\boldsymbol{X}}^2 c_{1f}^{(0)} \right), \tag{8.5.23}$$

$$\delta_1 \frac{\partial c_{1s}^{(0)}}{\partial t} = D_S \left(\nabla_{\boldsymbol{x}}^2 c_{1s}^{(2)} + 2\boldsymbol{\nabla}_{\boldsymbol{x}} \cdot \boldsymbol{\nabla}_{\boldsymbol{X}} c_{1s}^{(1)} + \nabla_{\boldsymbol{X}}^2 c_{1s}^{(0)} \right) + K_1 \left(c_2^{(0)} - c_{1s}^{(0)} \right), \tag{8.5.24}$$

$$\delta_2 \frac{\partial c_2^{(0)}}{\partial t} = K_1 \left(c_{1s}^{(0)} - c_2^{(0)} \right) - \delta_2 K_2 c_2^{(0)} \left(c_0 - c_3^{(0)} \right) + \delta_2 K_{-2} c_3^{(0)}, \tag{8.5.25}$$

$$\delta_2 \frac{\partial c_3^{(0)}}{\partial t} = \delta_2 K_2 c_2^{(0)} \left(c_0 - c_3^{(0)} \right) - \delta_2 K_{-2} c_3^{(0)}, \tag{8.5.26}$$

with boundary condition, on Γ,

$$D_S \left(\boldsymbol{\nabla}_{\boldsymbol{x}} c_{1s}^{(2)} + \boldsymbol{\nabla}_{\boldsymbol{X}} c_{1s}^{(1)} \right) \cdot \boldsymbol{n} = D_F \left(\boldsymbol{\nabla}_{\boldsymbol{x}} c_{1f}^{(2)} + \boldsymbol{\nabla}_{\boldsymbol{X}} c_{1f}^{(1)} \right) \cdot \boldsymbol{n} = \left(c_{1f}^{(0)} - c_{1s}^{(0)} \right). \tag{8.5.27}$$

Averaging over the relevant domains using (8.5.1) and applying the boundary condition (8.5.27), we obtain the following macroscale equations:

$$\frac{|\Omega_f|}{|\Omega|} \frac{\partial c_{1f}^{(0)}}{\partial t} = \bar{D}_F \nabla_{\boldsymbol{X}}^2 c_{1f}^{(0)} + \frac{S}{|\Omega|} \left(c_{1f}^{(0)} - c_{1s}^{(0)} \right), \tag{8.5.28}$$

$$\frac{\delta_1 |\Omega_s|}{|\Omega|} \frac{\partial c_{1s}^{(0)}}{\partial t} = \bar{D}_S \nabla_{\boldsymbol{X}}^2 c_{1s}^{(0)} - \frac{S}{|\Omega|} \left(c_{1f}^{(0)} - c_{1s}^{(0)} \right) + \frac{K_1 |\Omega_s|}{|\Omega|} \left(c_2^{(0)} - c_{1s}^{(0)} \right), \tag{8.5.29}$$

$$\frac{\delta_2 |\Omega_s|}{|\Omega|} \frac{\partial c_2^{(0)}}{\partial t} = \frac{K_1 |\Omega_s|}{|\Omega|} \left(c_{1s}^{(0)} - c_2^{(0)} \right) - \frac{\delta_2 K_2 |\Omega_s|}{|\Omega|} c_2^{(0)} \left(c_0 - c_3^{(0)} \right) + \frac{\delta_2 |\Omega_s|}{|\Omega|} K_{-2} c_3^{(0)}, \tag{8.5.30}$$

$$\frac{\delta_2 |\Omega_s|}{|\Omega|} \frac{\partial c_3^{(0)}}{\partial t} = \frac{\delta_2 |\Omega_s|}{|\Omega|} K_2 c_2^{(0)} \left(c_0 - c_3^{(0)} \right) - \frac{\delta_2 |\Omega_s|}{|\Omega|} K_{-2} c_3^{(0)}. \tag{8.5.31}$$

The effective diffusivities, $\bar{D}_f$ and $\bar{D}_s$, are given by

$$\bar{D}_F = \frac{1}{|\Omega|}\int_{\Omega_f} D_F\left(\boldsymbol{\nabla}_{\boldsymbol{x}}\boldsymbol{\chi}_f + \boldsymbol{I}\right)\mathrm{d}V, \tag{8.5.32}$$

$$\bar{D}_S = \frac{1}{|\Omega|}\int_{\Omega_s} D_S\left(\boldsymbol{\nabla}_{\boldsymbol{x}}\boldsymbol{\chi}_s + \boldsymbol{I}\right)\mathrm{d}V, \tag{8.5.33}$$

and

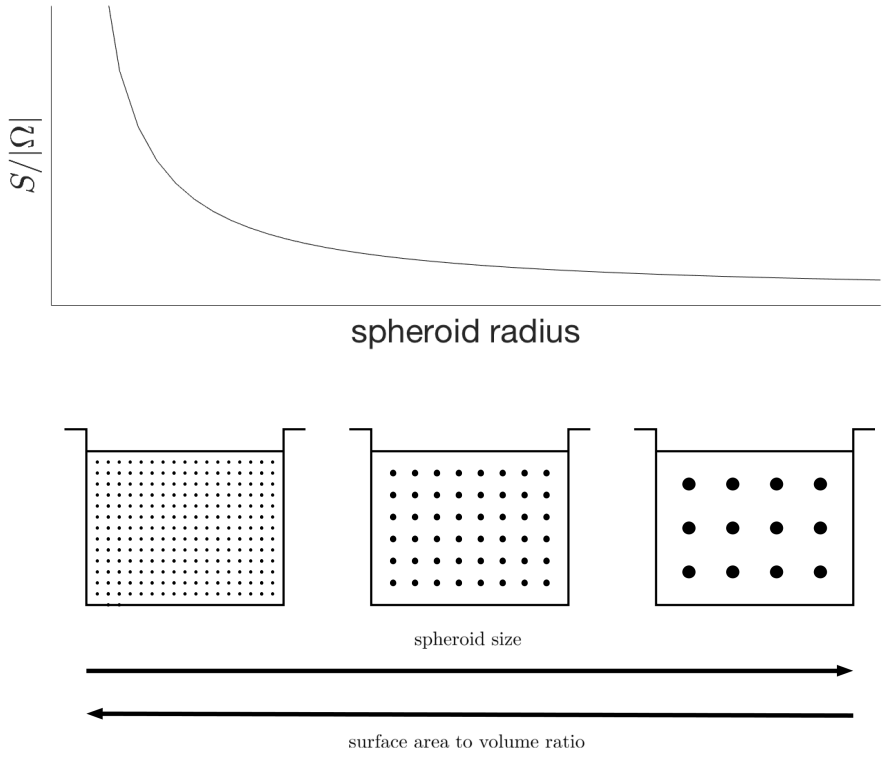
$$\mathrm{S} = \int_{\Gamma}\mathrm{d}S. \tag{8.5.34}$$

Note that in general $c_2^{(0)}$ and $c_3^{(0)}$ are not independent of the microscale, but here, where we consider uniform initial conditions for both uptake and efflux experiments, the assumption is valid.

SUMMARY The above macroscale description has been derived without specification of the exact periodic cell geometry, so we apply it to some particular simple examples below to see the effect on drug uptake.

Consider a number of identical drug solutions, each containing a different size of spheroid. The total volume of cells in each is the same, so larger spheroids implies fewer of them (figure 38). Consider a periodic cell from each, containing a single spheroid, as illustrated in figure 37. In each case the volume fractions $|\Omega_f|/|\Omega|$ and $|\Omega_s|/|\Omega|$ are the same, and, as the geometry of the periodic cell is the same (varying only in overall size), the effective diffusivities are too. The only change in the macroscale description due to spheroid size is $\mathrm{S}/|\Omega|$, the prefactor to the uptake term. More specifically, $\mathrm{S}/|\Omega| \propto 1/r$, as shown in figure 38, so smaller spheroids results in a faster drug uptake. This is intuitive, having a larger overall surface area, by using smaller spheroids and more of them, one would expect faster uptake.

Next we consider a different rescaling of the diffusivities, allowing diffusion within the spheroid to play a role in uptake rate.



.

Figure 38: Sketch illustrating the relationship between spheroid size and the surface area to volume ratio.

8.5.2 *Highly contrasting diffusivities, membrane law*

Here we suppose that diffusion is fast in the fluid but comparable with uptake within the spheroid, i.e.

$$D_F = \frac{1}{\varepsilon^2}\tilde{D}_F, \quad D_S = \tilde{D}_S, \tag{8.5.35}$$

and that on the boundary the flux of drug is proportional to the concentration jump. The rescaled model equations are given below. In the fluid domain, Ω_f:

$$\frac{\partial c_{1f}}{\partial t} = \frac{1}{\varepsilon^2} D_F \nabla^2 c_{1f}. \tag{8.5.36}$$

In the spheroid domain, Ω_s:

$$\delta_1 \frac{\partial c_{1s}}{\partial t} = D_S \nabla^2 c_{1s} + K_1 \left(c_2 - c_{1s} \right), \tag{8.5.37}$$

$$\delta_2 \frac{\partial c_2}{\partial t} = K_1 \left(c_{1s} - c_2 \right) - \delta_2 K_2 c_2 \left(c_0 - c_3 \right) + \delta_2 K_{-2} c_3, \tag{8.5.38}$$

$$\delta_2 \frac{\partial c_3}{\partial t} = \delta_2 K_2 c_2 \left(c_0 - c_3 \right) - \delta_2 K_{-2} c_3. \tag{8.5.39}$$

On the boundary, $\Gamma = \Omega_s \cap \Omega_f$,

$$D_S \boldsymbol{\nabla} c_{1s} \cdot \boldsymbol{n} = \frac{1}{\varepsilon^2} D_F \boldsymbol{\nabla} c_{1f} \cdot \boldsymbol{n} = \left(c_{1f} - c_{1s} \right). \tag{8.5.40}$$

Next the variables and differential operators are expanded in multiple scales form, as given by () and (), and the equations at each order in ε analysed.

At leading order, $O(1/\varepsilon^2)$:

$$0 = D_F \nabla_{\boldsymbol{x}}^2 c_{1f}^{(0)}, \tag{8.5.41}$$

$$0 = D_F \boldsymbol{\nabla}_{\boldsymbol{x}} c_{1f}^{(0)} \cdot \boldsymbol{n}, \tag{8.5.42}$$

from which we conclude that

$$c_{1f}^{(0)} = c_{1f}^{(0)} \left(\boldsymbol{X}, t \right), \tag{8.5.43}$$

i.e. that drug concentration in the fluid is independent of the microscale.

At next order, $O(1/\varepsilon)$:

$$0 = D_F \nabla_{\boldsymbol{x}}^2 c_{1f}^{(1)}, \tag{8.5.44}$$

$$0 = D_F \left(\boldsymbol{\nabla}_{\boldsymbol{X}} c_{1f}^{(0)} + \boldsymbol{\nabla}_{\boldsymbol{x}} c_{1f}^{(1)} \right) \cdot \boldsymbol{n}. \tag{8.5.45}$$

As previously, a suitable form for $c_{1f}^{(1)}$ is given by

$$c_{1f}^{(1)} = \boldsymbol{\chi}_f \left(\boldsymbol{x} \right) \boldsymbol{\nabla}_{\boldsymbol{X}} c_{1f}^{(0)} + \bar{c}_f \left(\boldsymbol{X}, t \right), \tag{8.5.46}$$

where $\boldsymbol{\chi}_f$ is $\boldsymbol{x}$-periodic and $\langle \boldsymbol{\chi}_f \rangle_f = 0$. Substituting into equations (8.5.44–8.5.45) we have the following cell problem to solve, in order to obtain $\boldsymbol{\chi}_f$.

$$0 = \nabla_{\boldsymbol{x}}^2 \boldsymbol{\chi}_f \quad \text{in } \Omega_f, \tag{8.5.47}$$

$$0 = D_F \left(\boldsymbol{\nabla}_{\boldsymbol{x}} \boldsymbol{\chi}_f + \boldsymbol{I} \right) \cdot \boldsymbol{n} \quad \text{on } \Gamma. \tag{8.5.48}$$

Note that whilst this analysis follows that of section 8.5.1 for drug concentration in the fluid, due to the slower diffusion within the spheroid we obtain no information on $c_{1s}^{(0)}$ until we consider terms at the next order of the expansion.

At $O(\varepsilon^2)$ the equations are given by:

$$\frac{\partial c_{1f}^{(0)}}{\partial t} = D_F\left(\nabla_{\boldsymbol{x}}^2 c_{1f}^{(2)} + 2\boldsymbol{\nabla}_{\boldsymbol{x}}\cdot\boldsymbol{\nabla}_{\boldsymbol{X}} c_{1f}^{(1)} + \nabla_{\boldsymbol{X}}^2 c_{1f}^{(0)}\right), \tag{8.5.49}$$

$$\delta_1\frac{\partial c_{1s}^{(0)}}{\partial t} = D_S\nabla_{\boldsymbol{x}}^2 c_{1s}^{(0)} + K_1\left(c_2^{(0)} - c_{1s}^{(0)}\right), \tag{8.5.50}$$

$$\delta_2\frac{\partial c_2^{(0)}}{\partial t} = K_1\left(c_{1s}^{(0)} - c_2^{(0)}\right) - \delta_2 K_2 c_2^{(0)}\left(c_0 - c_3^{(0)}\right) + \delta_2 K_{-2} c_3^{(0)}, \tag{8.5.51}$$

$$\delta_2\frac{\partial c_3^{(0)}}{\partial t} = \delta_2 K_2 c_2^{(0)}\left(c_0 - c_3^{(0)}\right) - \delta_2 K_{-2} c_3^{(0)}. \tag{8.5.52}$$

On the boundary, Γ,

$$D_S\boldsymbol{\nabla}_{\boldsymbol{x}} c_{1s}^{(0)}\cdot\boldsymbol{n} = D_F\left(\boldsymbol{\nabla}_{\boldsymbol{x}} c_{1f}^{(2)} + \boldsymbol{\nabla}_{\boldsymbol{X}} c_{1f}^{(1)}\right)\cdot\boldsymbol{n} = \left(c_{1f}^{(0)} - c_{1s}^{(0)}\right). \tag{8.5.53}$$

Averaging (8.5.49), and applying the boundary condition (8.5.53), we obtain

$$\frac{|\Omega_f|}{|\Omega|}\frac{\partial c_{1f}^{(0)}}{\partial t} = \bar{D}_F\nabla_{\boldsymbol{X}}^2 c_{1f}^{(0)} + \langle c_{1f}^{(0)}\rangle_\Gamma - \langle c_{1s}^{(0)}\rangle_\Gamma, \tag{8.5.54}$$

for the fluid domain, with effective diffusivity,

$$\bar{D}_F = \frac{1}{|\Omega|}\int_{\Omega_f} D_F\left(\boldsymbol{\nabla}_{\boldsymbol{x}}\boldsymbol{\chi}_f + \boldsymbol{I}\right)\mathrm{d}V. \tag{8.5.55}$$

In the spheroid, we have the micrscale problem

$$\delta_1\frac{\partial c_{1s}^{(0)}}{\partial t} = D_S\nabla_{\boldsymbol{x}}^2 c_{1s}^{(0)} + K_1\left(c_2^{(0)} - c_{1s}^{(0)}\right), \tag{8.5.56}$$

$$\delta_2\frac{\partial c_2^{(0)}}{\partial t} = K_1\left(c_{1s}^{(0)} - c_2^{(0)}\right) - \delta_2 K_2 c_2^{(0)}\left(c_0 - c_3^{(0)}\right) + \delta_2 K_{-2} c_3^{(0)}, \tag{8.5.57}$$

$$\delta_2\frac{\partial c_3^{(0)}}{\partial t} = \delta_2 K_2 c_2^{(0)}\left(c_0 - c_3^{(0)}\right) - \delta_2 K_{-2} c_3^{(0)}, \tag{8.5.58}$$

with

$$D_S\boldsymbol{\nabla}_{\boldsymbol{x}} c_{1s}^{(0)}\cdot\boldsymbol{n} = \left(c_{1f}^{(0)} - c_{1s}^{(0)}\right) \text{ on } \Gamma. \tag{8.5.59}$$

SUMMARY If diffusion is slow in the spheroid compared to that in the fluid, then we see microscale variation in the spheroid drug concentrations. Keeping this complexity, on which the drug uptake may have significant dependence on the microscale, results in a microscale problem to solve in Ω_s.

Whilst it may not be immediately obvious, homogenisation does achieve simplifications to the model. As the drug concentration in the fluid on the boundary, Γ, is independent of the microscale, it is uniform for a given spheroid. If the spheroids are spheres, this results in the cell problem being radially symmetric and hence simplified.

8.5.3 *Model simulations and comparison*

The nondimensionalisation of the model in section 8.4.2 helped to indicate which scalings to use in the multiscale analysis. Here, however, we return to dimensional equations in order to obtain numerical results comparable with both those obtained experimentally and the parameter fitting carried out by Matthew Hubbard (University of Nottingham).

We begin with the model where diffusion is fast in both the medium and intercellular fluid. Equations (8.5.28–8.5.31) in dimensional form are given by:

$$\frac{|\Omega_f|}{|\Omega|}\frac{\partial c_{1f}^{(0)}}{\partial t} = \bar{D}_f \nabla_{\mathbf{X}}^2 c_{1f}^{(0)} + \frac{\gamma \mathrm{S}}{|\Omega|}\left(c_{1f}^{(0)} - c_{1s}^{(0)}\right), \tag{8.5.60}$$

$$\frac{\delta_1|\Omega_s|}{|\Omega|}\frac{\partial c_{1s}^{(0)}}{\partial t} = \bar{D}_s \nabla_{\mathbf{X}}^2 c_{1s}^{(0)} - \frac{\gamma \mathrm{S}}{|\Omega|}\left(c_{1f}^{(0)} - c_{1s}^{(0)}\right) + \frac{\alpha k_1|\Omega_s|}{|\Omega|}\left(c_2^{(0)} - c_{1s}^{(0)}\right), \tag{8.5.61}$$

$$\frac{\delta_2|\Omega_s|}{|\Omega|}\frac{\partial c_2^{(0)}}{\partial t} = \frac{\alpha k_1|\Omega_s|}{|\Omega|}\left(c_{1s}^{(0)} - c_2^{(0)}\right) - \frac{\delta_2 k_2|\Omega_s|}{|\Omega|}c_2^{(0)}\left(c_0 - c_3^{(0)}\right) + \frac{\delta_2|\Omega_s|}{|\Omega|}k_{-2}c_3^{(0)}, \tag{8.5.62}$$

$$\frac{\delta_2|\Omega_s|}{|\Omega|}\frac{\partial c_3^{(0)}}{\partial t} = \frac{\delta_2|\Omega_s|}{|\Omega|}k_2 c_2^{(0)}\left(c_0 - c_3^{(0)}\right) - \frac{\delta_2|\Omega_s|}{|\Omega|}k_{-2}c_3^{(0)}. \tag{8.5.63}$$

These can be solved numerically to find drug uptake by the spheroids. By considering uniform initial conditions:

$$c_{1f}^{(0)} = 1\times10^{-7}M, \quad c_{1s}^{(0)} = c_2^{(0)} = c_3^{(0)} = 0M, \tag{8.5.64}$$

which are reasonable given that the drug solution is well mixed and spheroids are initially drug free, then concentrations remain uniform with time. In this case diffusive terms and spatial variation can be ignored, reducing (8.5.60–8.5.63) to a set of ODEs. Two solutions, for spheroids of radius 1.65×10^{-4}m and 7.66×10^{-6}m, are illustrated by figure 39, showing the drug concentrations for uptake from the solution.

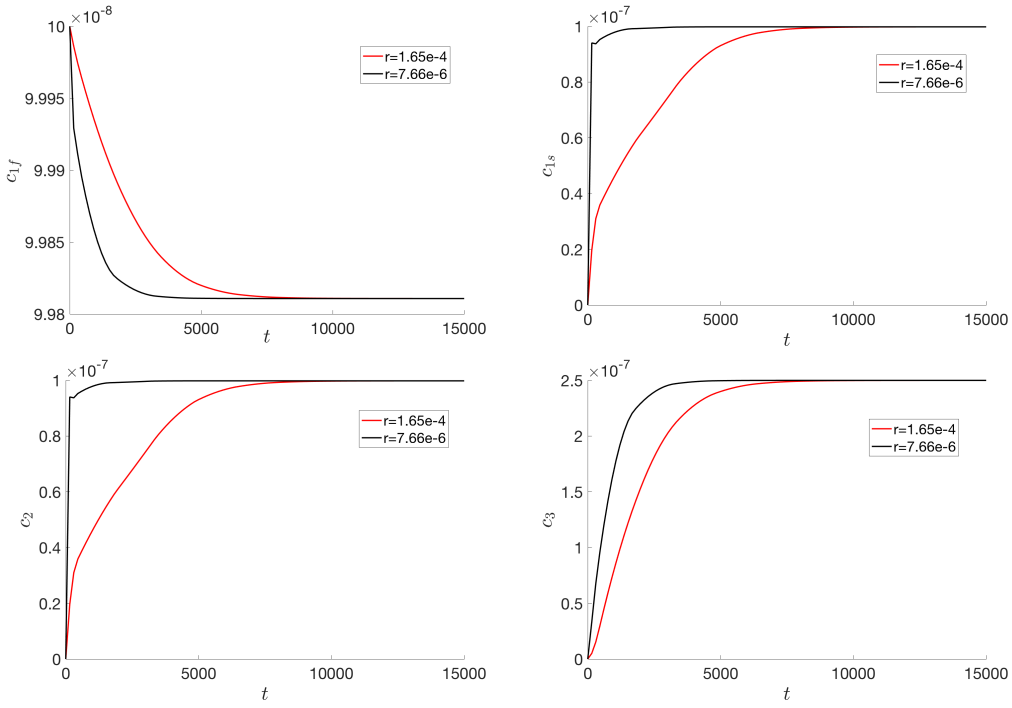


Figure 39: Solving the macroscale equations for drug uptake when diffusivities are fast in both the medium and intercellular space, (8.5.60–8.5.63), for spheres of radius 1.65×10^{-4}m (red) and 7.66×10^{-6}m (black).

Initially, there is a sharp decrease in c_{1f} and corresponding increase in c_{1s} as drug is taken up from the medium into the intercellular fluid. The increase in free drug concentration within the cells, c_2, matches that of

c_{1s} due to the fast transmembrane rate of drug transport. Note that for the smaller spheroids this initial behaviour is much faster as they have a larger total surface area over which to take up the drug. The decrease in c_{1f} and increase in c_{1s} and c_2 then slows as drug binding becomes more dominant and c_3 tends to the steady state value. Note that the bound concentration is higher than the free concentration as the binding rate is faster than unbinding here.

Next we consider the model where diffusion is fast in the medium only, i.e. $D_F \gg D_S$. Equations (8.5.54–8.5.59) in dimensional form are given by:

$$\frac{|\Omega_f|}{|\Omega|}\frac{\partial c_{1f}^{(0)}}{\partial t} = \bar{D}_f \nabla_{\boldsymbol{X}}^2 c_{1f}^{(0)} + \gamma\left(\langle c_{1f}^{(0)}\rangle_\Gamma - \langle c_{1s}^{(0)}\rangle_\Gamma\right), \tag{8.5.65}$$

in Ω_f, whilst in the spheroid, Ω_s, we have the cell problem

$$\delta_1\frac{\partial c_{1s}^{(0)}}{\partial t} = D_s\nabla_{\boldsymbol{x}}^2 c_{1s}^{(0)} + \alpha k_1\left(c_2^{(0)} - c_{1s}^{(0)}\right), \tag{8.5.66}$$

$$\delta_2\frac{\partial c_2^{(0)}}{\partial t} = \alpha k_1\left(c_{1s}^{(0)} - c_2^{(0)}\right) - \delta_2 k_2 c_2^{(0)}\left(c_0 - c_3^{(0)}\right) + \delta_2 k_{-2} c_3^{(0)}, \tag{8.5.67}$$

$$\delta_2\frac{\partial c_3^{(0)}}{\partial t} = \delta_2 k_2 c_2^{(0)}\left(c_0 - c_3^{(0)}\right) - \delta_2 k_{-2} c_3^{(0)}, \tag{8.5.68}$$

with

$$D_s\boldsymbol{\nabla}_{\boldsymbol{x}} c_{1s}^{(0)}\cdot\boldsymbol{n} = \gamma\left(c_{1f}^{(0)} - c_{1s}^{(0)}\right) \text{ on } \Gamma. \tag{8.5.69}$$

Equation (8.5.65–8.5.69) can be solved numerically to find drug uptake by the spheroids. We again consider uniform initial conditions:

$$c_{1f}^{(0)} = 1\times10^{-7}M, \quad c_{1s}^{(0)} = c_2^{(0)} = c_3^{(0)} = 0M. \tag{8.5.70}$$

As before the diffusive term in the macroscale fluid equation can be ignored, and hence spatial variation removed, reducing (8.5.65) to an ODE. Here, where diffusion is slow within the intercellular space, however, spatial variation remains in the microscale spheroid cell problem.

Two solutions are given in figure 40 and 41, showing the concentrations of drug, in the fluid and spheroid, during uptake from the solution, for spheres of radius 1.65×10^{-4}m and 7.66×10^{-6}m respectively, for a fixed value of diffusion, D_s.

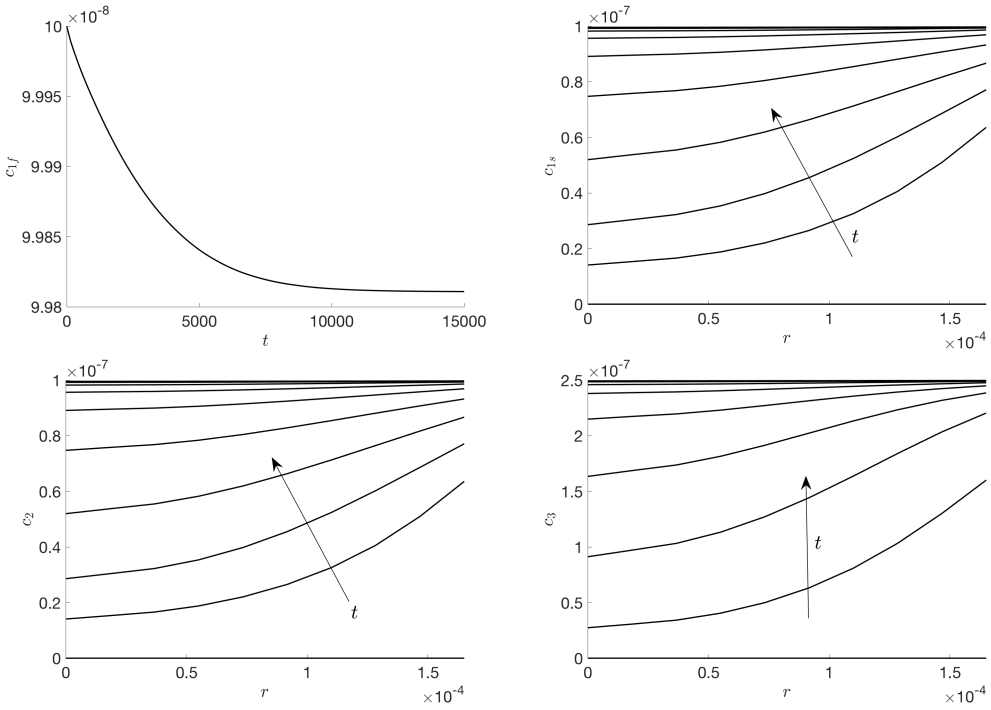


Figure 40: Solving the macroscale equation in the solution (8.5.65) and microscale equations in the spheroid (8.5.66–8.5.69) for the highly contrasting diffusivities case ($D_F \gg D_S$) for spheres of radius 1.65×10^{-4}m.

For spheres of radius 1.65×10^{-4}m (figure 40), we see a smooth decrease in c_{1f} as drug is taken up by the spheroids which levels off as the steady state is reached. Within the spheroid we see high concentrations towards the edge with the drug diffusing towards the centre for increasing time. For c_{1s} and c_2 there is similar variation in concentration due to the fast transmembrane rate of drug transport. Concentrations within the spheroid level to the steady state values, high for the bound concentration due to the relatively fast binding to unbinding rates.

For spheres of radius 7.66×10^{-6}m (figure 41,), we see a sharper initial decrease in c_{1f} than for larger spheres (figure 40). This occurs due to the higher surface area to volume ratio provided by the smaller spheres (as also observed in figure 39), with the intercellular and free cellular concentrations increasing quickly as a consequence. The concentration in the fluid, c_{1f},

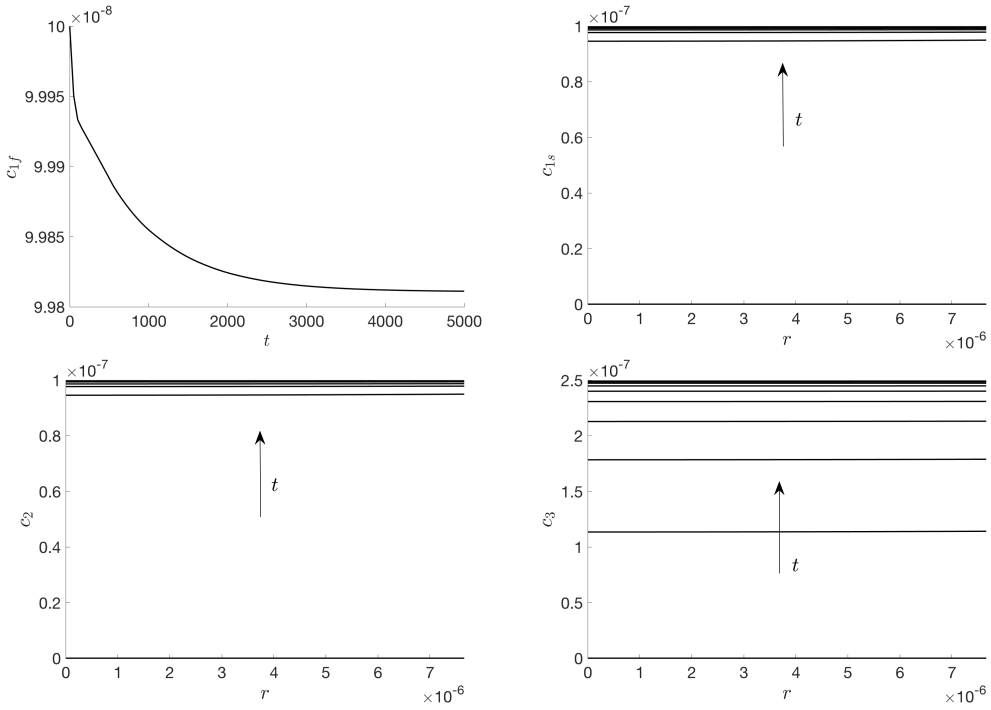
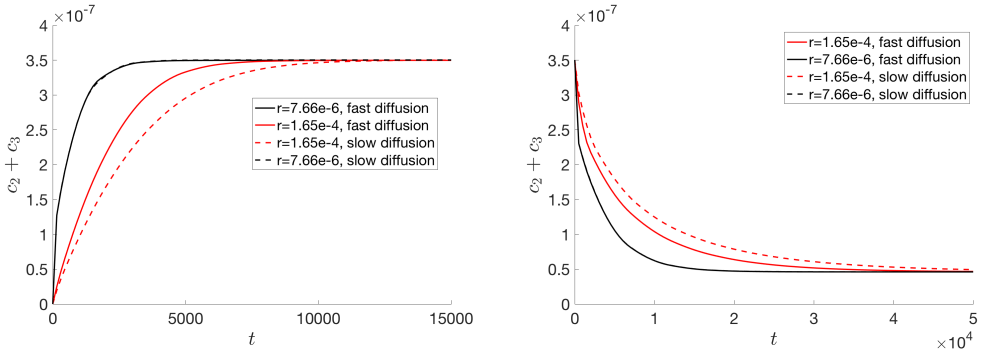


Figure 41: Solving the macroscale equation in the solution (8.5.65) and microscale equations in the spheroid (8.5.66–8.5.69) for the highly contrasting diffusivities case ($D_F \gg D_S$) for spheres of radius 7.66×10^{-6}m.

then decreases more slowly until the bound drug reaches its steady state concentration. Timescales associated with diffusion across a spheroid with radius R are given by R^2/D, i.e. the relative sizes of R and D. Here, due to the much smaller size of spheroid, diffusion results in uniform concentrations.

Having shown illustrative solutions to both models, for two sizes of spheroid, we now compare their results for drug uptake and efflux in figure 42. For the smaller spheroids, where diffusion is large relative to spheroid radius, the concentration is close to uniform across them (see figure 41), there is little difference between the methods. For larger spheroids, the time taken for the drug to diffuse across the extracellular fluid slows down the rate of uptake by the cells.

Drug concentrations for the efflux setup show similar behaviour to the uptake, smaller spheroids reach the steady state faster and slow diffusion within the extracellular fluid slows the efflux. Note, however, that efflux occurs over a longer timescale than uptake due to the relatively slow unbinding rate.



(a) (b)

Figure 42: (a) Drug uptake and (b) efflux for the similar (–) and highly contrasting diffusivities (- -), for spheres of radius 1.65×10^{-4}m (red) and 7.66×10^{-6}m (black). Note that results for smaller spheroids are very similar in both cases and hence difficult to distinguish.

8.6 DATA FITTING

Here we discuss fitting of the models derived in the previous section to the experimental data shown in figures 32 and 33. Parameter fitting, and associated figure 43, were carried out and created by Matthew Hubbard (University of Nottingham). Table 7 shows the known parameter values, whilst rates k_1, k_2, k_{-2}, concentration of binding sites c_0 and diffusion in the spheroid D_s are to be determined by fitting to the experimental data.

Initial conditions for the uptake numerical simulations are given by

$$c_{1f}^{(0)} = 0.1\mu M, \quad c_{1s}^{(0)} = c_2^{(0)} = c_3^{(0)} = 0. \tag{8.6.1}$$

Table 7.: Binding model parameters values used in parameter fitting. Values courtesy of collaborators. Surface areas and volumes are estimated from the radii, assuming spherical cells.

Parameter	DLD-1 Value	MCF-7 Value
cell radius	7.33×10^{-6}m	9.23×10^{-6}m
spheroid radius	1.65×10^{-4}m	
volume of cells	$1.65\mu l$	$3.28\mu l$
total cellular surface area	6.75×10^{-4}m^2	1.07×10^{-3}m^2

Parameter	Value
δ_1	$1/17$
δ_2	$16/17$
media volume	1ml (uptake), $50\mu l$ (efflux)

For the efflux, the uptake simulation is run for 60 minutes (see section 8.2), to determine the concentration within the cells/spheroid, and then $c_{1f}^{(0)}$ is set to zero.

For the drug uptake by cells the fast diffusion model is used, neglecting the concentration c_{1s}, which is not present in this case. A fit to experimental data for DLD-1 cells using this model is shown in figure 43(a,c,e).

To obtain numerical solutions for spheroids (assumed spherical), a radially symmetric compartment model is used, i.e. a finite volume discretisation of the continuous equations (8.5.54–8.5.59). Each compartment is approximately the width of a single layer of cells, with diffusion coded as permeability through the compartment interfaces, see [68]. A fit to experimental data for DLD-1 spheroids using this model is shown in figure 43(b,d,f).

Data fitting was carried out by using standard least squares and χ^2, which scales each point by its variance, weakening the influence of points with

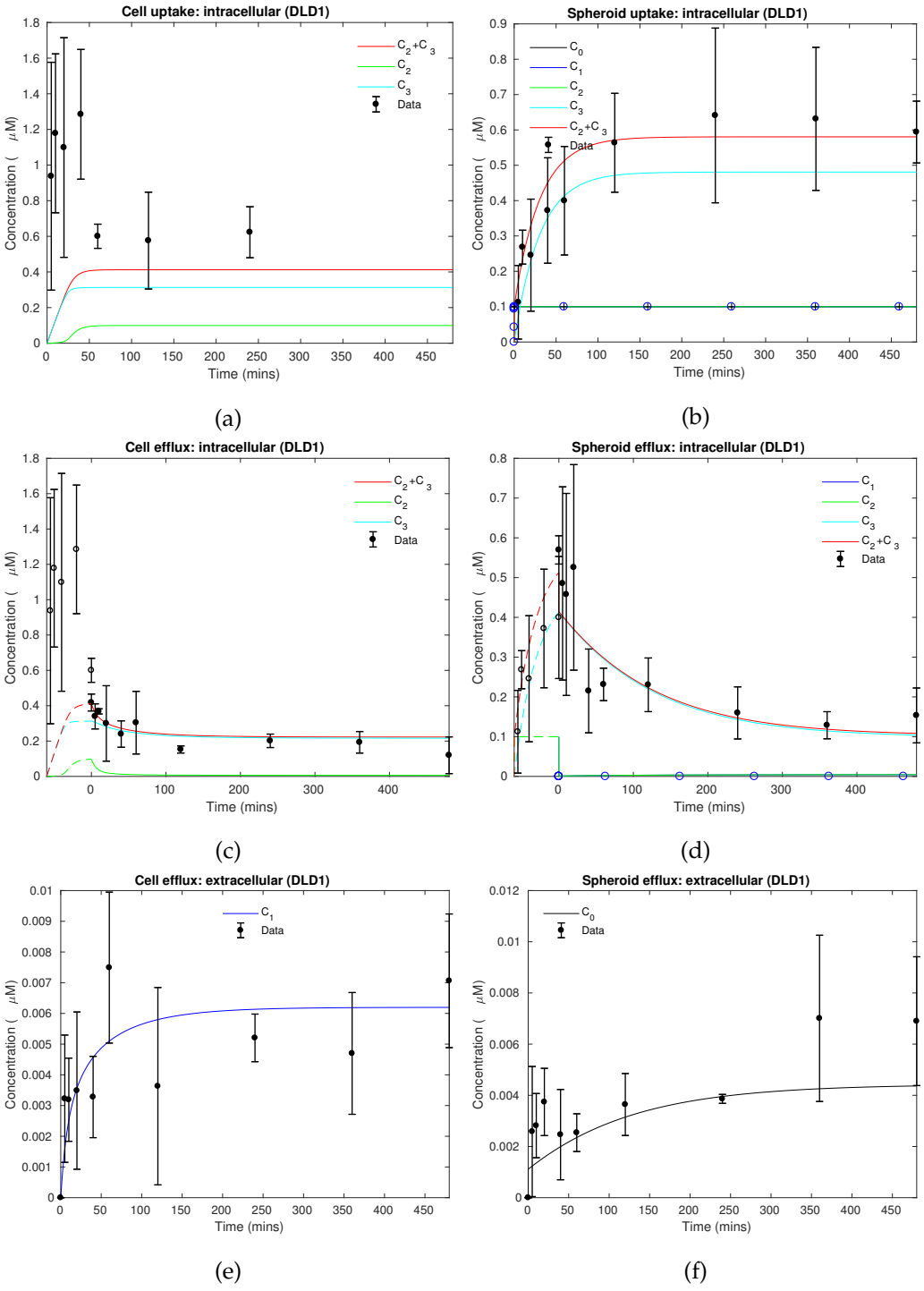


Figure 43: Fitting to the experimental data for uptake and efflux, for DLD1 cells and spheroids. χ^2 fitting. Parameter values obtained from this fit to the data are given in table 8.

large variance. There was difficulty in fitting the model to the data and it was not possible to get a qualitative fit to the MCF-7 data. In particular,

Table 8.: Binding model parameters values obtaining by fit shown in figure 43.

Parameter	Cell fit value	Spheroid fit value
c_0	3.23×10^{-7}M	5.87×10^{-7}M
D_s	–	$8.60\times10^{-8}\mathrm{m}^2s^{-1}$
k_1	$5.34\times10^{-9}\mathrm{ms}^{-1}$	$4.38\times10^{-6}\mathrm{ms}^{-1}$
k_2	$2.54\times10^{10}\mathrm{M}^{-1}s^{-1}$	$4.48\times10^{3}\mathrm{M}^{-1}s^{-1}$
k_{-2}	$7.72\times10^{1}\mathrm{s}^{-1}$	$9.90\times10^{-5}\mathrm{s}^{-1}$

there was difficulty in obtaining unique sets of parameters and the results are sensitive to the initialisation of parameter fitting and weighting of data sets. One of the problems is that the total mass of drug in the system (media and cells) varies in the experimental data. Whilst it is possible that drug could be lost during the procedure, for example during the washing of cells/spheroids, it is difficult to see how it could increase. The model chosen is mass conservative and so unable to accommodate this variation in total drug. Additionally, it can not capture the initial rise and fall exhibited in figure 43.

A general conclusion that may be drawn is that binding of drug within the cells must be faster than unbinding because uptake occurs quicker than efflux, and because binding needs to be quick to maintain a high drug concentration within the cells.

In summary, while homogenisation resulted in simplified models, and can capture different uptake and efflux rates, the data was not sufficient for successful parametisation. The inconsistencies in the total amount of drug within the system suggest that there were differences in the procedures and repeat experiments may be needed. Additional features to the drug binding model, such as active transport of drug out of the cells, should then be investigated.

8.7 EFFECTIVE DIFFUSION

In our numerical experiments we assumed uniform initial conditions, thereby removing the need to include or calculate the effective diffusion of drug in the medium surrounding the spheroids. Should this not be the case, the cell problem (8.5.47–8.5.48), where χ_f is x periodic and $\langle \chi_f \rangle_f = 0$, must be solved. This boundary value problem consists of an independent problem for each of the components of the vector χ, with its solution dependent on the geometry of the periodic cell. Diffusion of the drug are restricted by the presence of the cells and spheroids, reducing the diffusivity on macroscopic lengthscales.

Effective diffusivities for various geometries have previously been investigated including, for example, circles [81, 128] and squares [131] in $2D$ and in 3D, spheres [150] and ellipsoids [59, 112]. Using a result derived by Maxwell [99] the effective diffusivity, $\bar{D}_F$, for a substance of diffusivity D_F, arising from a dilute suspension of spheres is given by

$$\bar{D}_F = \frac{D_F}{1 + \frac{1}{2}\phi}, \tag{8.7.1}$$

where ϕ is the volume fraction of spheres. Classical approaches were used to investigate not just the effect of the shape and volume fraction of obstacles on the effective diffusion but also the arrangement of the obstacles. For example Rayleigh's multipole method provides an approximation for discs on a square lattice arrangement as a function of volume fraction ϕ at low to moderate volume fractions [128]:

$$D_{eff}(\phi) = \frac{1}{1-\phi}\left[1 - \frac{2\phi}{1 + \phi - 0.3058\phi^4}\right] \quad \text{for } \phi < 0.7. \tag{8.7.2}$$

Using the same method [81] derived the equivalent for discs arranged on a 2D hexagonal lattice:

$$D_{eff}(\phi) = \frac{1}{1-\phi}\left[1 - \frac{2\phi}{1 + \phi - 0.07542\phi^6}\right] \quad \text{for } \phi < 0.8. \tag{8.7.3}$$

In 3D, Rayleigh additionally obtained the effective diffusion for spheres arranged on a cubic lattice,

$$D_{eff}(\phi) = \frac{1}{1-\phi}\left[1 - \frac{3\phi}{2+\phi-0.3914\phi^{\frac{10}{3}}}\right] \quad \text{for } \phi < 0.25, \tag{8.7.4}$$

which gives similar results to Maxwell's equation (8.7.1) for small volume fractions.

Ellipsoidal particles are considered in [81, 112], where diffusivity no longer independent of direction. The greater the difference in relative dimension (major and minor axis length), the more variance in the effective diffusion around spheres.

Using COMSOL, χ can be determined numerically for a given periodic cell. Figure 44 shows the graphical representation of χ for discs of increasing radius. The results obtained for the effective diffusion, calculated from χ via (8.5.55), are compared with those obtained using (8.7.2) in figure 45. As the size of the discs increase the available area for diffusion is reduced, and the distance between two points is increased, causing a reduction in the effective diffusion. For a volume fraction greater than approximately 0.7 the effective diffusion starts to drop off more steeply as the edges of the discs get closer to those of the periodic cell and eventually cut the fluid domain into disjoint sections.

Figures 48 and 46 show graphical representations of the vector χ for a sphere and ellipses of different major minor axis ratios. The effective diffusion coefficient can then be determined via (8.5.55). In contrast to the case of discs and spheres, where diffusion is isotropic, for ellipses diffusion is anisotropic. This is illustrated by figure 47 which shows how D_{11} and D_{22} (where D_{ij}, $i, j = 1, 2$, is the diffusion coefficient matrix) vary as the ratio of the axis of an ellipse is changed, whilst keeping volume fraction constant. For approximately equal major minor axis ratios the components of χ look similar, up to rotation through 90 degrees. As the ellipse becomes increasingly oblate χ_x decreases in magnitude as there is less of an obstruction in the x-direction whilst the converse arises for χ_y.

8.8 SUMMARY

In this chapter we derived models describing the uptake (and efflux) of the drug Palbociclib by cells and spheroids, in order to quantify the role of key factors governing the penetration and distribution of the drug in tumours. We began by describing the experimental procedure, whereby cancer cells or spheroids are placed in drug (Palbociclib) containing media for a set time and their drug uptake measured. In additional experiments, after 60 minutes taking up the drug, the cells or spheroids were removed and placed in fresh media. the concentration of drug in both the cells and the media was measured after a set time.

A simple binding model for the drug, due to [68], was described and the model set up in such a way as to be amenable to homogenisation, then nondimensionalised. Using two different scalings, two macroscale models for concentration of drug were derived. In the first it was assumed that diffusion, both in the medium and the spheroid, is much faster than uptake. This resulted in a full macroscale description, with all concentrations being independent of the microscale. In this case, uptake varies due to difference in surface area to volume ratio.

In the second model, where only diffusion in the drug medium is much faster than uptake, i.e. $D_F \gg D_S$, the same macroscale description for transport in the fluid as in the first scaling is achieved. Within the spheroid, however, a microscale problem must be solved to describe the transport and binding of the drug. This allows for microscale variation in concentration within the spheroid as the drug diffuses across it. Example numerical solutions were given to illustrate how uptake and efflux can vary with spheroid size, for both models.

The models are then fitted to the experimental data in order to determine various parameters, including binding rates and the concentration of binding sites. Unfortunately, there was difficulty in fitting to the data and obtaining a unique set of parameters. The mass conservative model chosen

can not properly describe a system where total mass of drug varies, or when there is a rise and subsequent fall in uptake by DLD-1 cells.

Palbociclib has high intracellular binding properties, as demonstrated by the comparatively higher concentration achieved in the cells than the surrounding fluid. It is possible that this is the cause of slower uptake for spheroids if high binding rates are slowing the distribution of drug towards the interior. This variation in concentration across a spheroid (hence on the microscale) is only permitted in the model for $D_F \gg D_S$, where diffusion in the intercellular space is slower than the surrounding fluid and impacted by the binding rates. It would be interesting to fit the model to experimental data obtained for 5-fluorouracil, a drug which has lower intracellular binding properties. No difference in the uptake between cells and spheroids was observed in this case, so it would be instructive to see if the slow intercellular diffusion model can provide a good description when binding rates are greatly reduced.

The effective diffusivity of the drug in the medium was then discussed as this would become important when non-uniform initial conditions are used. Factors such as the relative volume fraction of spheroid to media and their geometry are related to the effective diffusion coefficient.

Further work should begin with repetition of the experiments in case of procedural errors, followed by modifications to the model description to accommodate more of the features observed. For example, introduction of the active transport of drug out of the DLD-1 cells may be able to explain the difference between the maximum uptake between the cell lines. It would, however, introduce additional parameters that need to be determined.

The experiments described in this chapter and the accompanying mathematical model are currently in preparation for publication [39].

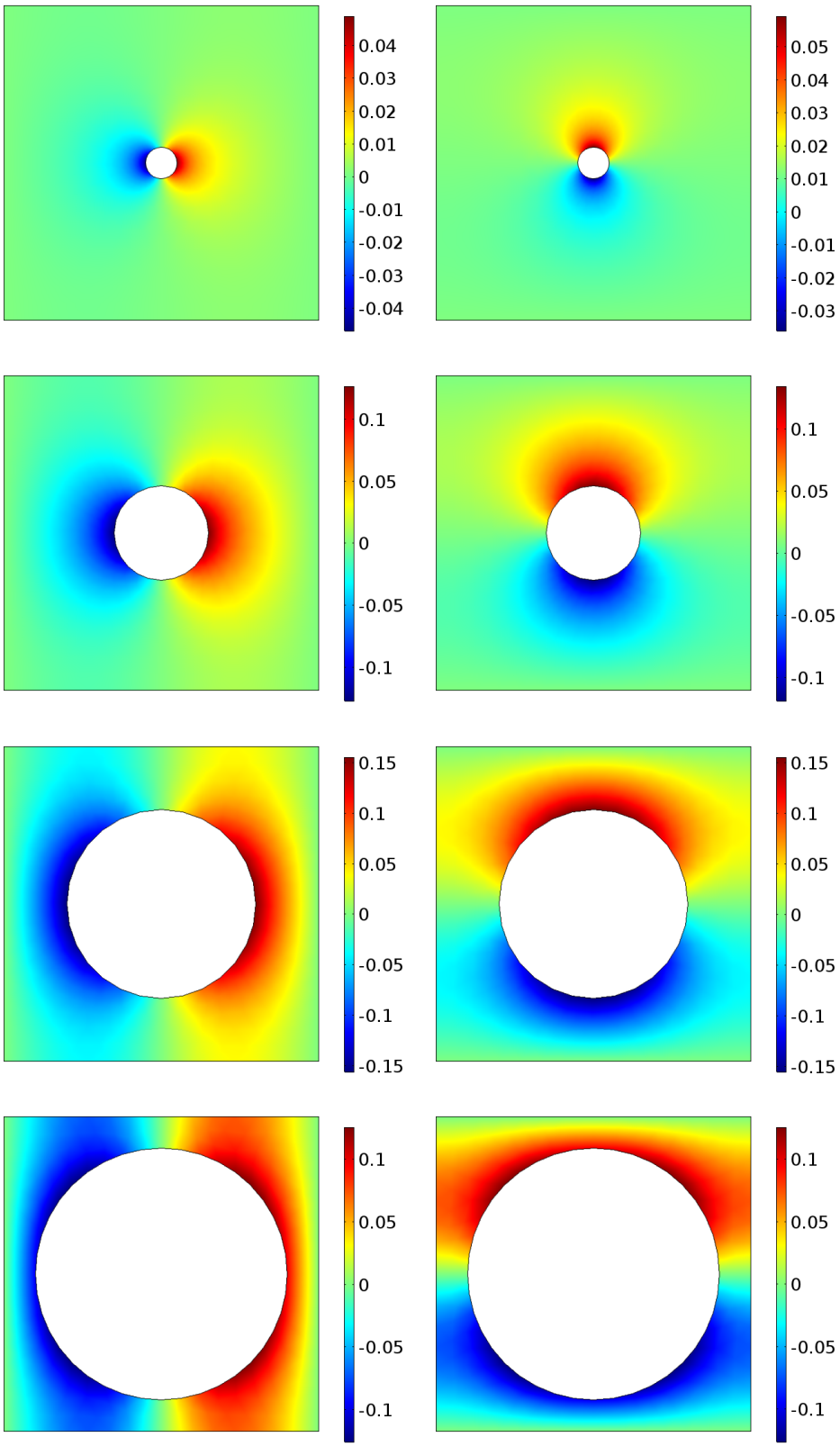


Figure 44: Graphical representation of the solution $\chi = (\chi_x, \chi_y)$ to (8.5.47,8.5.48) for discs of increasing volume fraction. The first column shows χ_x, and the second χ_y.

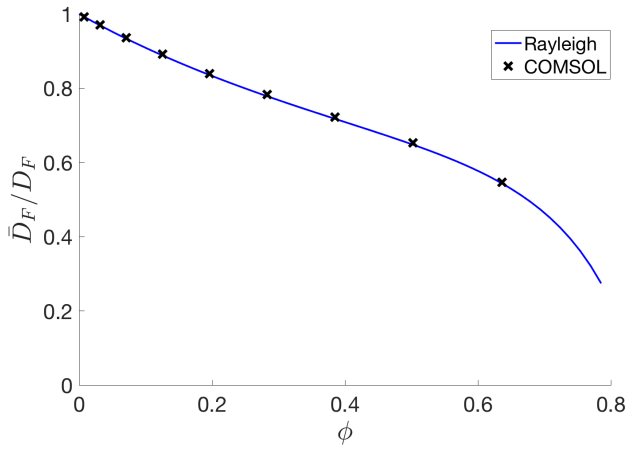


Figure 45: Comparison of effective diffusion for discs of increasing radius obtained by COMSOL solutions to (8.5.47,8.5.48) and Rayleigh's approximation (8.7.2).

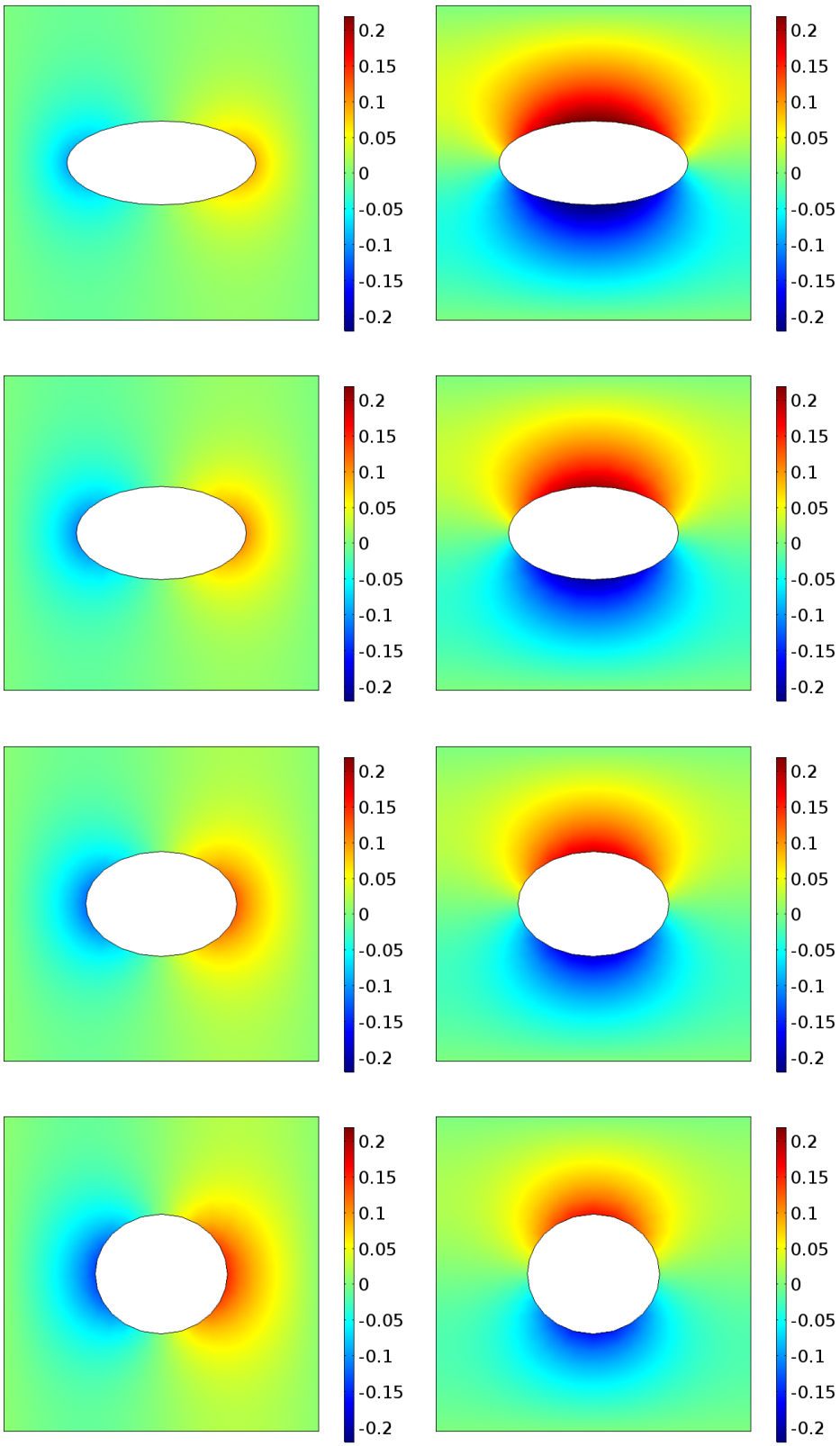


Figure 46: Graphical representation of the solution $\chi = (\chi_x, \chi_y)$ to (8.5.47,8.5.48) for ellipses of the same volume fraction. The first column shows χ_x, and the second χ_y.

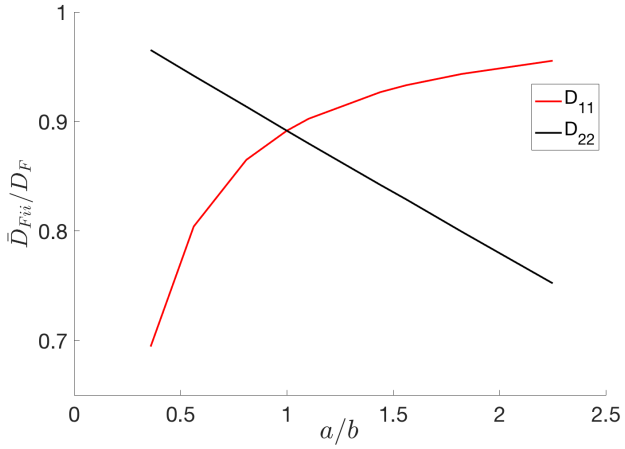


Figure 47: Graph to show how D_{11} and D_{22} vary as the ratio of the axis of an ellipse is changed.

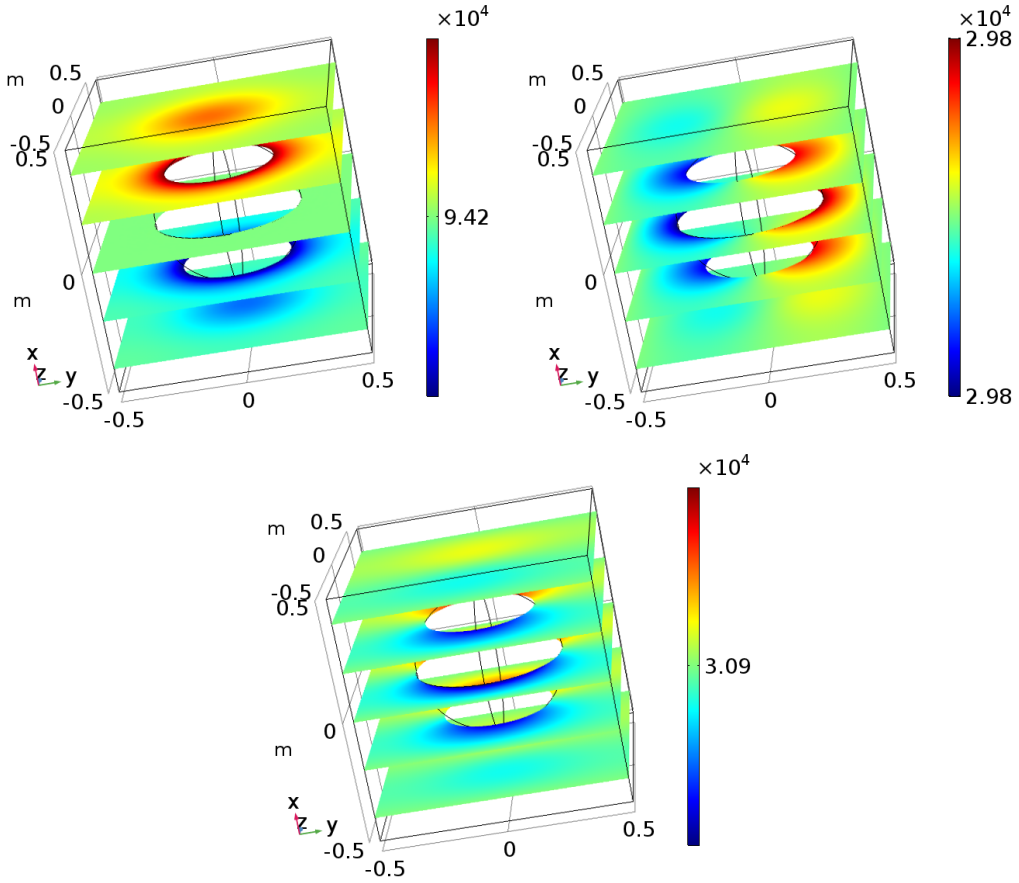


Figure 48: Graphical representation of $\chi = (\chi_x, \chi_y, \chi_z)$ to (8.5.47,8.5.48) for a sphere of radius 0.3 in a unit cube. χ_x – top left; χ_y – top right; χ_z – bottom centre.

9

CONCLUSIONS AND FURTHER WORK

9.1 CONCLUDING DISCUSSION

The aim of this thesis was to derive new effective descriptions of deformable, adaptively remodelling biological tissue by combining multiphase mixture models and multiscale homogenisation. In particular, we focus on a tissue engineering context where computational models can be used to test out potential experimental setups and scaffolds, allowing the most promising possibilities to be identified, thereby saving time and money. Through aiding the design of more successful methods for growing tissue we can better produce rejection-proof tissues for transplant, more representative tissues for toxicological research, as well as meat with a smaller environmental impact than that reared in the traditional way.

We extended the work of O'Dea *et al.* [115], in which effective macroscale equations, incorporating explicitly the influence of microscale structure and dynamics, are derived to describe tissue growth on a scaffold. In this model, [115], the tissue is considered to be a solid layer on a solid (indistinguishable) scaffold with cell proliferation and extracellular matrix deposition represented by accretion or surface growth at a rate dependent on uptake of some generic nutrient. In a similar work [126], the growing media, again undergoing growth by accretion, is instead taken to behave as a linear elastic solid.

In this thesis, we addressed the simplistic description of growth as a solid accretion process. We employed a multiphase description (as used in [72, 90] for example) to represent tissue growth dynamics. This accommodates both volumetric growth and active cell motion, thereby giving a more realistic representation of the tissue. Multiscale homogenisation, as used in [115, 126], is then utilised to obtain effective macroscale descriptions of the growing tissue. These provide a description for a more complex growing tissue than in [115] yet, by considering slow (quasi-static) growth, retain the simplicity of the model.

We began chapter 2 by summarising the biology of tissue, how it grows and remodels through a range of interacting factors across multiple spatial and temporal scales, and summarised its importance in the study of tissue engineering, morphogenesis, wound healing and cancer. The various mathematical methods, including discrete and continuous models, that have been employed to describe tissue and aspects of its behaviour were then compared.

In chapter 3 we set up our model for tissue growth on a scaffold, including a detailed description of the mixture model of Lemon *et al.* [90] which we use to describe the tissue. We took the tissue to be composed of two viscous fluid phases, cells and intercellular fluid. In contrast to simple growth by solid accretion, this mixture model allows more complex behaviour, accommodating cell-cell interactions and volumetric growth. The tissue grows on the surface of a scaffold, with remaining space filled with culture medium rich in nutrient on which growth depends.

In chapter 4 we assume that the drag between the two phases which comprise the tissue is very large. In this limit the two phases are subject to the same velocity, except in a narrow boundary layer where distinct phase velocities are permitted. A multiple scales analysis was then carried out to derive a macroscale model from the underlying microscale description of chapter 3. The effective macroscale description is given by differential equations for the cell volume fraction and nutrient concentration, Darcy

flow of culture medium and tissue, whose permeability is determined by the solution of a pair of coupled Stokes cell problems. In addition to dependence on the microstructure through the permeability tensors, the macroscale description also includes contributions from the microscale growth despite the choice of quasi-steady scalings.

Whilst the model derived in chapter 4 allowed the cell volume fraction to vary throughout the tissue, the constrained mixture assumption did not permit cell motility via cell-cell interaction. As a consequence of this, growth of the tissue domain must be specified constitutively rather than arising as a consequence of cell motility, essentially occurring as accretion.

To retain individual phase motion and therefore accommodate the movement of cells, and permit growth through the movement of material into the tissue domain, we relaxed the large drag assumption in chapter 5. As an alternative method to reduce the degree of non-linearity of the microscale model, enabling a more straightforward multiscale analysis, we linearised the microscale equations about a steady state. After a brief discussion on the stability of the steady state, the multiscale analysis was carried out on the linearised equations. Again we derived an effective macroscale description comprising Darcy flow of culture medium and tissue, and differential equations for the cell volume fraction and nutrient concentration.

In this case, however, the cell problem for determining permeabilities is more complex. It consists of a standard Stokes-type cell problem in the culture medium domain, as previously, coupled to a pair of coupled modified Stokes problems in the tissue, one for each phase. Moreover, and in contrast to other simplified analyses of this type, the microscale cell problems and corresponding macroscale dynamics are coupled through the macroscale pressure and active cell behaviour terms. This multiscale cell problem therefore poses significant computational challenges as the permeabilities for a given microscale geometry must be solved not once but multiple times to determine them as functions of the macroscale

pressures. We also derived the model for different choices of scaffold and nutrient boundary conditions to permit movement of cells on the scaffold surface and alternatives to continuity of nutrient concentration on the tissue-interstitium interface. Due to the challenges introduced to the cell problem, we also considered the simplified case where the water phase is inviscid as this removes the problematic coupling.

In chapter 6, we show how the complex coupling of the cell problems to the macroscale pressures in the model of chapter 5 can be removed, along with associated computational challenges, by use of an alternative ansatz for the microscale pressures and macroscale velocities. This results in an increased number of cell problems to solve, but these are free from macroscale dependence and hence only require solving once.

Whilst the models of chapter 5 allowed cell-cell interaction and flow into the tissue, they are not closed. The microscale velocity of the tissue-interstitium boundary appears in the macroscale equation for cell volume fraction, and is required to achieve closure. This is unknown but must be determined to close the model. The boundary velocity should arise naturally from the movement of the cells in response to intraphase pressure gradients, and in principle be obtainable via a suitable free boundary problem. Alternatively, for simplicity, one could define it constitutively, motivating some of the numerical work in the following chapter.

In chapter 7 we investigated the behaviour of the tissue mixture model, both analytically and numerically, in order to provide insight on closure of the macroscale models. For simplicity we considered a 1D reduction of the full multiphase model, initially for the case where the water phase is inviscid. As in the similar formulation of [89], we observed solutions in the form of travelling waves, dependent on the relationship between the relative strengths of cell-cell aggregation and repulsion which characterise the intraphase pressure for the cells. Analytical approximations of the wave speed are obtained for when there is no interphase drag and for 'slow waves'. By taking a numerical approach, we then investigated the

relationship between various parameters and the boundary velocity, finding a more general equation that provides a good fit to the wave speeds obtained. This is used to motivate the constitutive choice for the boundary velocity in subsequent numerical work.

When both phases of the tissue are viscous, similar travelling wave behaviour was observed on the addition of diffusion of the cell phase to the model. Diffusion reduces the steepness of the leading edge, preventing it from being pinned to a fixed position and hence stopping growth of the tissue domain. We conclude that a function of a similar form to that in the inviscid water case would be reasonable in this case, but as this is computationally intensive it is not sought.

Using the form for the interface velocity obtained from the numerical investigation, a simple case of the macroscale model, when the water phase is inviscid, is illustrated numerically. This includes solution of the accompanying microscale 'cell' problem, of chapter 5, for a sample 2D geometry. Note that when the water phase is inviscid both the original and alternative ansatz forms are equivalent.

In chapter 8 we constructed models for the uptake of drug by cancer spheroids in solution. Experimental data supplied by collaborators (University of Bradford) showed that uptake was much quicker for cells than for spheroids, detail that we wished to capture with our model. Using an existing drug binding model [68] we set up the model so that a single spheroid and neighbouring region of drug solution constitutes a periodic cell. Homogenisation was then used to derive two different models, depending on the relative rates of diffusivity, in the drug solution and extracellular fluid, to uptake.

The first, when diffusivities within both the solution and extracellular fluid are fast, resulted in a macroscale model where uptake rate is dependent on the surface area to volume ratio of the spheroid. With fast diffusion of the drug, the concentrations can be considered independent of the microscale, i.e. constant across the cell or spheroid. The second,

when diffusion is fast in the drug solution only, consisted of a macroscale description outside the spheroids and a cell problem inside. This allows variation in concentration across the spheroid, as diffusion within it is slow, and the rate of uptake decreases as the radius, and hence distance to diffuse, is increased. This scaling, with its microscale problem for the drug concentrations within the spheroid, allows a more complex description as concentrations are no longer uniform at the microscale. These models were illustrated with sample numerical solutions before attempting to fit them to the numerical data. Whilst some of the behaviour seen in the experiments was shown by the models, there were problems accommodating all features and obtaining unique sets of parameters. Ways of obtaining the effective diffusion coefficient, required if drug distribution in the fluid is not initially uniform, were discussed and some numerical solutions shown.

9.2 FURTHER WORK

Whilst the effect of varying some model parameters, such as nutrient uptake rate and strength of cell-cell attraction, was investigated in chapter 7, it would be interesting to carry out sensitivity analyses to perturbations in model parameters, such as those governing the cell problem geometries. With the improved ansatz of chapter 6 the resulting cell problems can be solved more efficiently when the fluid is modelled as viscous, allowing for wider exploration of parameter space.

In our models for tissue growth we made a number of simplifying assumptions which, if relaxed, may prove to be more applicable to *in vitro* tissue engineering. For example, the scaffold itself was taken to be a rigid unreactive solid, but for transplants and other applications it is often degradable, breaking down as it is replaced by extracellular material laid down by the cells. Investigating the behaviour and interactions of tissue and scaffold on these timescales may provide additional guidance in the design of scaffolds and the experimental setup. A consequence of these longer

timescales is that the microscale geometry can no longer be considered quasi-steady, resulting in the need to evolve the tissue boundaries with both the scaffold and interstitium and, consequently, solving the cell problem to determine permeabilities multiple times. Evolving the boundaries brings complexity, see [44], where growth of and flow through a porous medium are considered equally important.

Simplification of the multiphase model used for the tissue description occurred through the assumption of large interphase drag (chapter 4) and linearisation about a uniform steady state (chapter 5). The large drag assumption enforced equal leading order velocities for the two phases, not permitting the movement of cells in response to intraphase pressures. Whilst the use of linearisation did accommodate this model feature, it was itself restrictive in that the model is then only strictly valid close to the steady state. Both methods limit the applicability of the model, but were deemed necessary to simplify the microscale description for the multiscale analysis compared to the challenging analysis of Collis *et al.* [44], which does not reduce the degree of nonlinearity in the underlying model. It would be interesting to see if it is possible to retain the full microscale description and still derive an effective macroscale one without applying simplifications to remove the nonlinear terms from the mass conservation and continuity equations. Inclusion of non-linear coupled processes at the microscale, however, results in a mathematically challenging, if not impossible, homogenisation.

An additional problem with the growth models is that of closure; in both models we do not know the movement of the tissue-interstitium boundary. In the case of the large drag limit this was resolved by introducing a surface production term or phase transfer rate, constitutively specified, and preferably dependent on the concentration of available nutrient. This additionally dealt with the problem with the boundary conditions, where no material was able to cross the tissue-interstitium interface, and hence supply growth. For the linearised model, closure was

provided by investigation of the full multiphase model in one dimension, which informed the constituitive choice for the boundary velocity. It would be preferable if the tissue-interstitium interface velocity could be acquired via an analytical method, especially as an averaged or macroscale description to complement the other model equations. In [137] an effective model for biofilm growth is derived via homogenisation. It consists of Darcy's law and upscaled transport equations with effective coefficients, given by the evolving microstructure at the pore scale. The level set equation, describing the position of the biofilm, is reduced to an ODE for porosity given in terms of averaged macroscopic rates. To obtain this useful form, however, it was necessary to make the simplifying assumption that the microstructure evolves uniformly (i.e. the normal velocity is uniform along the microscale boundary). It may be worth investigating alternative scaling choices, recall in the analysis presented time and pressure were rescaled with ε, in order to see if it is possible to obtain a closed macroscale description, avoiding the need to supply an extra condition at the tissue-interstitium boundary.

It would be interesting to obtain relevant parameter values and use the tissue growth models to compare scaffold designs or investigate behaviour in experimentally comparable 3D setups. Although these models are simplified it would be useful to see if they can provide any practical insight.

Regarding the drug uptake model of chapter 8, this work would possibly benefit from further experimental data to determine reliability and check for procedural errors, in particular the measured gain in overall drug within the system. On collection of further data, the choice of binding model could be reviewed or additional processes incorporated, such as inclusion of an efflux transporter (actively removing the drug from within the cells), in order to provide a better fit.

A

BOUNDARY LAYER ANALYSIS IN THE LARGE DRAG LIMIT

In the limit of large interphase drag ($\beta \gg 1$), as used in chapter 4, the velocities of the two tissue phases are equal at leading order. As discussed therein, a consequence of this is that no material can cross the tissue-interstitium boundary. In order to permit growth of the tissue, not driven by density difference or instantaneous mass creation, we introduced phase transfer occurring on the boundary. This effectively reduces growth to accretion, defined or prescribed by the choice of surface production term.

In the boundary layer, of thickness $O(1/\sqrt{\beta})$, the large drag model breaks down and distinct phase velocities arise, hence allowing a flux of water into the tissue and providing material for growth. In this appendix we seek to understand the behaviour in this boundary layer, with the aim of informing an appropriate surface production term with which to provide closure for the macroscale model.

A.1 INITIAL BOUNDARY LAYER ANALYSIS

We begin with a simplified boundary layer analysis following the method used in [113], and ignore the nutrient concentration. We consider a two dimensional boundary layer where the tissue-interstitium boundary, $\Gamma(t)$, is flat and move to a travelling frame of reference, such that $\hat{y} = y - \Gamma(t)$ and the boundary position is given by $\hat{y} = 0$. Additionally, we introduce

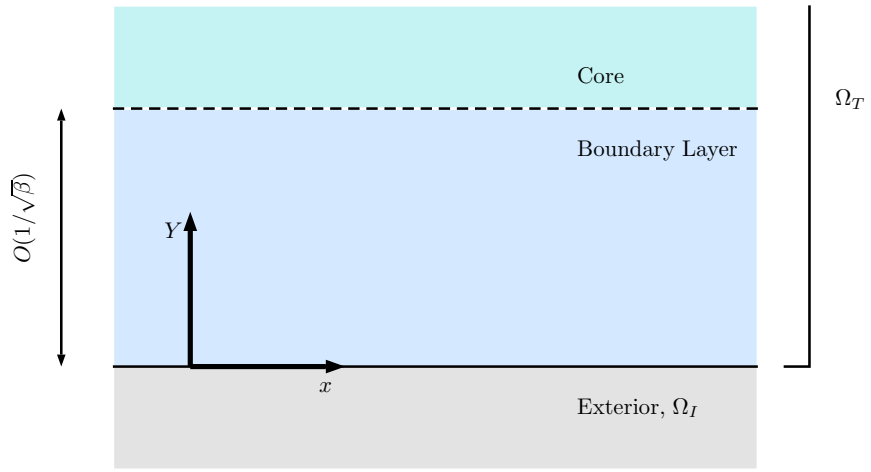


Figure 49: Illustration to show the boundary layer coordinates

a boundary layer coordinate $Y = \sqrt{\beta}\hat{y}$. The boundary layer and the new coordinates are illustrated by figure 49.

We denote the boundary layer variables by upper case letters: Θ_n, P, P_w and $\boldsymbol{V}_i = (U_i, V_i/\sqrt{k})$, where $i = n, w$; the scaling on V_i is suggested by equation (3.8.5). P is the combined pressure given by $\theta_N P_n + (1-\theta_N)P_w$. Equations (3.8.2), (3.8.5)–(3.8.7) then give:

$$\frac{\partial \Theta_n}{\partial t} + \frac{\partial}{\partial x}\left(\Theta_n U_n\right) + \frac{\partial}{\partial Y}\left(\Theta_n V_n\right) = S_n\left(\Theta_n\right), \tag{A.1.1}$$

$$\frac{\partial}{\partial x}\left(\Theta_n U_n + \left(1-\Theta_n\right)U_w\right) + \frac{\partial}{\partial Y}\left(\Theta_n V_n + \left(1-\Theta_n\right)V_w\right) = S_n\left(\Theta_n\right) + \bar{\rho} S_w\left(\Theta_n\right), \tag{A.1.2}$$

$$\begin{aligned}\frac{1}{\beta}\left(1-\Theta_n\right)\frac{\partial P_w}{\partial x} + \left(U_w - U_n\right) - \left(1-\Theta_n\right)\left(\frac{4}{3\beta}\frac{\partial^2 U_w}{\partial x^2} + \frac{\partial^2 U_w}{\partial Y^2} + \frac{1}{3\beta}\frac{\partial^2 V_w}{\partial x \partial Y}\right) \\ + \frac{1}{\beta}\frac{\partial \Theta_n}{\partial x}\left(\frac{4}{3}\frac{\partial U_w}{\partial x} - \frac{2}{3}\frac{\partial V_w}{\partial Y}\right) + \frac{\partial \Theta_n}{\partial Y}\left(\frac{\partial U_w}{\partial Y} + \frac{1}{\beta}\frac{\partial V_w}{\partial x}\right) = 0,\end{aligned} \tag{A.1.3}$$

$$\begin{aligned}\left(1-\Theta_n\right)\frac{\partial P_w}{\partial Y} + \left(V_w - V_n\right) - \left(1-\Theta_n\right)\left(\frac{4}{3}\frac{\partial^2 V_w}{\partial Y^2} + \frac{1}{\beta}\frac{\partial^2 V_w}{\partial x^2} + \frac{1}{3}\frac{\partial^2 U_w}{\partial x \partial Y}\right) \\ + \frac{\partial \Theta_n}{\partial x}\left(\frac{\partial U_w}{\partial Y} + \frac{1}{\beta}\frac{\partial V_w}{\partial x}\right) + \frac{\partial \Theta_n}{\partial Y}\left(\frac{4}{3}\frac{\partial V_w}{\partial Y} - \frac{2}{3}\frac{\partial U_w}{\partial x}\right) = 0,\end{aligned} \tag{A.1.4}$$

$$-\frac{1}{\beta}\frac{\partial P}{\partial x}+\mu\Theta_n\left(\frac{4}{3\beta}\frac{\partial^2 U_n}{\partial x^2}+\frac{\partial^2 U_n}{\partial Y^2}+\frac{1}{3\beta}\frac{\partial^2 V_n}{\partial x\partial Y}\right)+\mu\frac{\partial\Theta_n}{\partial x}\left(\frac{4}{3\beta}\frac{\partial U_n}{\partial x}-\frac{2}{3\beta}\frac{\partial V_n}{\partial Y}\right)+\mu\frac{\partial\Theta_n}{\partial Y}\left(\frac{\partial U_n}{\partial Y}+\frac{1}{\beta}\frac{\partial V_n}{\partial x}\right)+(1-\Theta_n)\left(\frac{4}{3\beta}\frac{\partial^2 U_w}{\partial x^2}+\frac{\partial^2 U_w}{\partial Y^2}+\frac{1}{3\beta}\frac{\partial^2 V_w}{\partial x\partial Y}\right)-\frac{\partial\Theta_n}{\partial x}\left(\frac{4}{3\beta}\frac{\partial U_w}{\partial x}-\frac{2}{3\beta}\frac{\partial V_w}{\partial Y}\right)-\frac{\partial\Theta_n}{\partial Y}\left(\frac{\partial U_w}{\partial Y}+\frac{1}{\beta}\frac{\partial V_w}{\partial x}\right)=0, \tag{A.1.5}$$

$$-\frac{\partial P}{\partial Y}+\mu\Theta_n\left(\frac{4}{3}\frac{\partial^2 V_n}{\partial Y^2}+\frac{1}{\beta}\frac{\partial^2 V_n}{\partial x^2}+\frac{1}{3}\frac{\partial^2 U_n}{\partial x\partial Y}\right)+\mu\frac{\partial\Theta_n}{\partial x}\left(\frac{\partial U_n}{\partial Y}+\frac{1}{\beta}\frac{\partial V_n}{\partial x}\right)+\mu\frac{\partial N}{\partial Y}\left(\frac{4}{3}\frac{\partial V_n}{\partial Y}-\frac{2}{3}\frac{\partial U_n}{\partial x}\right)+(1-\Theta_n)\left(\frac{4}{3}\frac{\partial^2 V_w}{\partial Y^2}+\frac{1}{\beta}\frac{\partial^2 V_w}{\partial x^2}+\frac{1}{3}\frac{\partial^2 U_w}{\partial x\partial Y}\right)-\frac{\partial\Theta_n}{\partial x}\left(\frac{\partial U_w}{\partial Y}+\frac{1}{\beta}\frac{\partial V_w}{\partial x}\right)-\frac{\partial\Theta_n}{\partial Y}\left(\frac{4}{3}\frac{\partial V_w}{\partial Y}-\frac{2}{3}\frac{\partial U_w}{\partial x}\right)=0. \tag{A.1.6}$$

A.1.1 *Multiple scales analysis*

Expanding the boundary layer variables in the following form

$$\Psi=\Psi_0+\frac{1}{\sqrt{\beta}}\Psi_1+... \tag{A.1.7}$$

gives at leading order, the equations below.

$$\frac{\partial\Theta_{n0}}{\partial t}+\frac{\partial}{\partial x}\left(\Theta_{n0}U_{n0}\right)+\frac{\partial}{\partial Y}\left(\Theta_{n0}V_{n0}\right)=S_n\left(\Theta_{n0}\right) \tag{A.1.8}$$

$$\frac{\partial}{\partial x}\left(\Theta_{n0}U_{n0}+\left(1-\Theta_{n0}\right)U_{w0}\right)+\frac{\partial}{\partial Y}\left(\Theta_{n0}V_{n0}+\left(1-\Theta_{n0}\right)V_{w0}\right)=S_n\left(\Theta_{n0}\right)+\bar{\rho}S_w\left(\Theta_{n0}\right), \tag{A.1.9}$$

$$U_{w0}-U_{n0}=\left(1-\Theta_{n0}\right)\frac{\partial^2 U_{w0}}{\partial Y^2}-\frac{\partial\Theta_{n0}}{\partial Y}\frac{\partial U_{w0}}{\partial Y}, \tag{A.1.10}$$

$$V_{w0}-V_{n0}=\left(1-\Theta_{n0}\right)\left(-\frac{\partial P_{w0}}{\partial Y}+\frac{4}{3}\frac{\partial^2 V_{w0}}{\partial Y^2}+\frac{1}{3}\frac{\partial^2 U_{w0}}{\partial x\partial Y}\right)-\frac{\partial\Theta_{n0}}{\partial x}\frac{\partial U_{w0}}{\partial Y}-\frac{\partial\Theta_{n0}}{\partial Y}\left(\frac{4}{3}\frac{\partial V_{w0}}{\partial Y}-\frac{2}{3}\frac{\partial U_{w0}}{\partial x}\right), \tag{A.1.11}$$

$$\mu\frac{\partial^2 U_{n0}}{\partial Y^2} = \frac{\Theta_{n0}-1}{\Theta_{n0}}\frac{\partial^2 U_{w0}}{\partial Y^2} + \frac{1}{\Theta_{n0}}\frac{\partial \Theta_{n0}}{\partial Y}\left(\frac{\partial U_{w0}}{\partial Y} - \mu\frac{\partial U_{n0}}{\partial Y}\right), \tag{A.1.12}$$

$$\begin{aligned}\frac{\partial P_0}{\partial Y} &= \mu\Theta_{n0}\left(\frac{4}{3}\frac{\partial^2 V_{n0}}{\partial Y^2} + \frac{1}{3}\frac{\partial^2 U_{n0}}{\partial x \partial Y}\right) + (1-\Theta_{n0})\left(\frac{4}{3}\frac{\partial^2 V_{w0}}{\partial Y^2} + \frac{1}{3}\frac{\partial^2 U_{w0}}{\partial x \partial Y}\right)\\ &+ \frac{\partial \Theta_{n0}}{\partial x}\left(\mu\frac{\partial U_{n0}}{\partial Y} - \frac{\partial U_{w0}}{\partial Y}\right)\\ &+ \frac{\partial \Theta_{n0}}{\partial Y}\left(\frac{4}{3}\left(\mu\frac{\partial V_{n0}}{\partial Y} - \frac{\partial V_{w0}}{\partial Y}\right) - \frac{2}{3}\left(\mu\frac{\partial U_{n0}}{\partial x} - \frac{\partial U_{w0}}{\partial x}\right)\right).\end{aligned} \tag{A.1.13}$$

As $Y \to \infty$ we require the velocities of each phase to be equal, as they are the same in the core flow. Guided by this requirement we take the leading order velocities to be

$$U_{i0} = \widetilde{U}, \quad V_{i0} = \widetilde{V}, \quad i = n, w. \tag{A.1.14}$$

Using this equations (A.1.10) and (A.1.12) become

$$0 = \frac{\partial}{\partial Y}\left((1-\Theta_{n0})\frac{\partial \widetilde{U}}{\partial Y}\right), \tag{A.1.15}$$

$$0 = \frac{\partial}{\partial Y}\left(((\mu-1)\Theta_{n0}+1)\frac{\partial \widetilde{U}}{\partial Y}\right). \tag{A.1.16}$$

Together these imply that $\Theta_{n0} = \Theta_{n0}(x,t)$. Also $\widetilde{U}$ must be of the following form,

$$\widetilde{U} = a(x,t)\,Y + b(x,t), \tag{A.1.17}$$

for some functions a and b.

A.1.2 *Matching to the core flow*

We want the variables in the boundary layer to match up to the core equations, (4.2.3), (4.2.7) and (4.2.8), as $Y \to \infty$, so we require the matching condition:

$$\lim_{Y\to\infty}\left\{\Psi_0 + \frac{1}{\sqrt{\beta}}\Psi_1 + \ldots\right\} = \left\{\psi_0 + \frac{Y}{\sqrt{\beta}}\frac{\partial \psi_0}{\partial y} + \frac{1}{\sqrt{\beta}}\psi_1 + \ldots\right\}\Bigg|_{y=0}. \tag{A.1.18}$$

Matching (A.1.17) to the core flow we find:

$$\lim_{Y\to\infty}\left\{a\left(x,t\right)Y+b\left(x,t\right)+\frac{1}{\sqrt{\beta}}U_1+...\right\}=\left\{u_0+\frac{Y}{\sqrt{\beta}}\frac{\partial u_0}{\partial y}+\frac{1}{\sqrt{\beta}}u_1+...\right\}\Bigg|_{y=0}. \tag{A.1.19}$$

so that $a\left(x,t\right)=O\left(1/\sqrt{\beta}\right)$. Hence, at leading order,

$$\widetilde{U}=\widetilde{U}\left(x,t\right)=u_0|_{y=0}. \tag{A.1.20}$$

Via (A.1.9) we then conclude, since $S_n+\bar{\rho}S_w$ is a function of $\Theta_{n0}\left(x,t\right)$, that $\widetilde{V}$ takes the form

$$\widetilde{V}=c\left(x,t\right)Y+d\left(x,t\right), \tag{A.1.21}$$

for some functions c and d. Matching (A.1.21) to the core flow,

$$\lim_{Y\to\infty}\left\{\frac{1}{\sqrt{\beta}}\left(c\left(x,t\right)Y+d\left(x,t\right)+\frac{1}{\sqrt{\beta}}V_1+...\right)\right\}= \left\{v_0+\frac{Y}{\sqrt{\beta}}\frac{\partial v_0}{\partial y}+\frac{1}{\sqrt{\beta}}v_1+...\right\}\Bigg|_{y=0}, \tag{A.1.22}$$

we see that at leading order $v_0|_{y=0}=0$. Also,

$$c\left(x,t\right)=\left.\frac{\partial v_0}{\partial y}\right|_{y=0},\quad d\left(x,t\right)=v_1|_{y=0}. \tag{A.1.23}$$

Equation (A.1.13) and the matching condition (A.1.18), implies

$$P_0=P_0\left(x,t\right)=p_0|_{y=0}. \tag{A.1.24}$$

From equation (A.1.11) we similarly find that $P_{w0}=P_{w0}\left(x,t\right)$. Lastly, we conclude $\Theta_{n0}\left(x,t\right)=\theta_{n0}|_{y=0}$.

A.1.3 *Matching to the exterior flow*

The boundary layer flow at $Y=0$ (i.e. on the interface, Γ) must be related to the exterior flow through the boundary conditions. Here our boundary conditions are mass conservation across the boundary and continuity of tangential velocity and the stress vector.

Considering first mass flux across Γ we have

$$\Theta_n V_n = 0 \tag{A.1.25}$$

$$(\Theta_n)\, V_w = v_i. \tag{A.1.26}$$

At leading order these become

$$\Theta_{n0} \widetilde{V} = 0 \tag{A.1.27}$$

$$(1 - \Theta_{n0})\, \widetilde{V} = v_{i1}, \tag{A.1.28}$$

as v_{i0} must be zero as V is $O(1/\sqrt{\beta})$. Substituting in the form for $\widetilde{V}$ from (A.1.21) gives the appropriate boundary conditions for the core flow equations as

$$\theta_{n0} v_1 = 0 \tag{A.1.29}$$

$$(1 - \theta_{n0})\, v_1 = v_{i1}. \tag{A.1.30}$$

This analysis has provided a rationale for appropriate boundary conditions to be applied to the core flow, as employed in [113]. However, this is not sufficient to address the aim of this section, which is to understand the boundary layer dynamics in the case for which material is able to cross the interface. In particular we see that both v_1 and v_{i1}, i.e. the leading order non-zero velocities in the core and exterior regions, are equal to the boundary velocity. Considering higher order terms does not seem to provide further insight.

The problem with this method is that within the boundary layer it is assumed, at leading order, that the phase velocities are equal, thereby supplying no new knowledge. Additionally the behaviour of the nutrient concentration, on which growth depends, is not included in the above analysis. We incorporate this in our second boundary layer analysis below.

A.2 SECOND BOUNDARY LAYER ANALYSIS

We next consider a second boundary layer analysis, which includes nutrient concentration, following the method used in [83]. As the boundary layer is

thin, it is sufficient to consider the dynamics in one dimension. We choose to look at the fast consumption or thin rim limit for growth, which is valid for large tissue domains or where nutrient is consumed quickly. We choose to scale the nutrient consumption by cells such that nutrient, and therefore growth only occurs in a thin rim of thickness $O(1/\sqrt{\beta})$, (i.e. within the boundary layer considered above, where the large drag limit breaks down).

We make two further simplifications, that the phase densities are equal, and that the nutrient equation can be approximated by its quasi-steady limit, as diffusion is quicker than advection.

After rescaling, as in the previous analysis, our boundary layer equations are given by

$$\frac{\partial \Theta_n}{\partial t} + \frac{\partial}{\partial Y}\left(\Theta_n V_n\right) = S_n\left(\Theta_n, C\right), \tag{A.2.1}$$

$$\frac{\partial}{\partial Y}\left(\Theta_n V_n + \left(1-\Theta_n\right) V_w\right) = S_n\left(\Theta_n, C\right) + \bar{\rho} S_w\left(\Theta_n, C\right), \tag{A.2.2}$$

$$\left(1-\Theta_n\right)\frac{\partial P_w}{\partial Y} + \left(V_w - V_n\right) - \frac{4}{3}\frac{\partial}{\partial Y}\left(\left(1-\Theta_n\right)\frac{\partial V_w}{\partial Y}\right) = 0, \tag{A.2.3}$$

$$\Theta_n \frac{\partial P_w}{\partial Y} + \frac{\partial}{\partial Y}\left(\Theta_n \phi_n\left(\Theta_n\right)\right) + \left(V_n - V_w\right) - \frac{4}{3}\frac{\partial}{\partial Y}\left(\Theta_n \frac{\partial V_n}{\partial Y}\right) = 0, \tag{A.2.4}$$

$$\frac{\partial}{\partial Y}\left(\frac{1}{Pe}\frac{\partial C}{\partial Y}\right) = \lambda\left(\Theta_n, C\right), \tag{A.2.5}$$

where ϕ_n is the function describing the cell-cell interactions.

These equations require numerical solution, subject to the appropriate boundary conditions. In chapter 7 we discuss the full model in one dimension, where these equations hold across the whole tissue domain, and seek numerical solutions.

A.3 SUMMARY

We have sought understanding of the boundary layer behaviour by following two different methods of analysis. The aim was to provide closure to the multiscale model of chapter 4, via guidance in the choice of Q in boundary condition (4.2.21). Within the boundary layer the interphase drag term is of comparable order to the rest of the momentum contributions allowing distinct phase velocities and hence a flow across the tissue-interstitium interface. This flow of material permits the tissue to grow without the need for instantaneous or surface growth.

The first method, although providing a rationale for appropriate boundary conditions to be applied to the core flow, is not sufficient to understand the dynamics of interest. This is due to the assumption that within the boundary layer the leading order phase velocities are equal. The second method results in a series of differential equations which need to be solved numerically.

As we encounter the problem of closure in the linearised model (chapter 5) also, we investigate the multiphase model further in chapter 7, in particular by solving numerically, equations similar to those obtained in the second boundary layer analysis.

BIBLIOGRAPHY

[1] Farlex Partner Medical Dictionary. https://medical-dictionary.thefreedictionary.com/cells.

[2] *Mosby's Medical Dictionary*. Elsevier, 9th edition, 2009.

[3] World's first lab-grown burger is eaten in London. http://www.bbc.co.uk/news/science-environment-23576143, August 2013.

[4] How long do the different stages of the cell cycle take? http://book.bionumbers.org/how-long-do-the-different-stages-of-the-cell-cycle-take/, September 2015.

[5] The American Heritage Stedman's Medical Dictionary. http://dictionary.reference.com/browse/tissue, Sep 2015.

[6] Organ donation and transplantation - NHS Blood and Transplant. http://www.nhsbt.nhs.uk/what-we-do/organ-donation-transplantation/, 2016.

[7] Tissue engineering and regenerative medicine - National Institute of Biomedicel Imaging and Bioengineering. https://www.nibib.nih.gov/science-education/science-topics/tissue-engineering-and-regenerative-medicine, 2016.

[8] Connective tissues: Loose, fibrous, and cartilage. Boundless Biology. https://www.boundless.com/biology/textbooks/boundless-biology-textbook/the-animal-body-basic-form-and-function-33/

animal-primary-tissues-193/
connective-tissues-loose-fibrous-and-cartilage-738-11968/, June 2017.

[9] Epithethial tissue, anatomy and physiology, Openstax CNX. http://cnx.org/contents/FPtK1zmh@6.27:oWqVExrJ@3/Epithelial-Tissue, June 2017.

[10] Organization of living things. https://www.ck12.org/biology/Organization-of-Living-Things/lesson/Organization-of-Living-Things-BIO/, June 2017.

[11] T. H. Adair and J.-P. Montani. Angiogenesis. In *Colloquium Series on Integrated Systems Physiology: From Molecule to Function*, volume 2, pages 1–84. Morgan & Claypool Life Sciences, 2010.

[12] A. Ahmad, N. Ormiston-Smith, and P. Sasieni. Trends in the lifetime risk of developing cancer in great britain: comparison of risk for those born from 1930 to 1960. *British Journal of Cancer*, 112(5):943–947, 2015.

[13] R. Akhtar, M. J. Sherratt, J. K. Cruickshank, and B. Derby. Characterizing the elastic properties of tissues. *Materials Today*, 14(3):96–105, 2011.

[14] K. R. Albe, M. H. Butler, and B. E. Wright. Cellular concentrations of enzymes and their substrates. *Journal of Theoretical Biology*, 143(2):163–195, 1990.

[15] D. Ambrosi and L. Preziosi. On the closure of mass balance models for tumor growth. *Mathematical Models and Methods in Applied Sciences*, 12(05):737–754, 2002.

[16] A. R. Anderson. A hybrid mathematical model of solid tumour invasion: the importance of cell adhesion. *Mathematical Medicine and Biology*, 22(2):163–186, 2005.

[17] G. Ateshian and J. Humphrey. Continuum mixture models of biological growth and remodeling: past successes and future opportunities. *Annual review of biomedical engineering*, 14:97–111, 2012.

[18] E. Baas, J. H. Kuiper, Y. Yang, M. A. Wood, and A. J. El Haj. In vitro bone growth responds to local mechanical strain in three-dimensional polymer scaffolds. *Journal of Biomechanics*, 43(4):733–739, 2010.

[19] I. Babuska. Homogenization approach in engineering. Technical report, Maryland Univ., College Park (USA). Inst. for Fluid Dynamics and Applied Mathematics, 1975.

[20] L. Band and J. King. Multiscale modelling of auxin transport in the plant-root elongation zone. *Journal of Mathematical Biology*, 65(4):743–785, 2012.

[21] Y. Bazilevs and T. J. R. Hughes. Weak imposition of Dirichlet boundary conditions in fluid mechanics. *Computers & Fluids*, 36(1):12–26, 2007. Challenges and Advances in Flow Simulation and Modeling.

[22] A. Bensoussan, J.-L. Lions, and G. Papanicolaou. *Asymptotic analysis for periodic structures*, volume 5. North-Holland Publishing Company Amsterdam, 1978.

[23] N. Bhardwaj and S. C. Kundu. Electrospinning: a fascinating fiber fabrication technique. *Biotechnology Advances*, 28(3):325–347, 2010.

[24] J. Blazek. *Computational Fluid Dynamics: Principles and Applications*. Elsevier, 2005.

[25] J. T. Bonner. A way of following individual cells in the migrating slugs of dictyostelium discoideum. *Proceedings of the National Academy of Sciences*, 95(16):9355–9359, 1998.

[26] L. G. Bowden. *Mathematical approaches to modelling healing of full thickness circular skin wounds*. PhD thesis, University of Oxford, 2015.

[27] M. B. Bracken. Why animal studies are often poor predictors of human reactions to exposure. *Journal of the Royal Society of Medicine*, 102(3):120–122, 2009.

[28] C. Breward, H. Byrne, and C. Lewis. Modelling the interactions between tumour cells and a blood vessel in a microenvironment within a vascular tumour. *European Journal of Applied Mathematics*, 12(05):529–556, 2001.

[29] C. Breward, H. Byrne, and C. Lewis. The role of cell-cell interactions in a two-phase model for avascular tumour growth. *Journal of Mathematical Biology*, 45(2):125–152, 2002.

[30] F. Brezzi and M. Fortin. *Mixed and Hybrid Finite Element Methods*. Springer-Verlag, New York, 1991.

[31] D. L. Brown, P. Popov, and Y. Efendiev. Effective equations for fluid-structure interaction with applications to poroelasticity. *Applicable Analysis*, 93(4):771–790, 2014.

[32] A. K. Bryan, A. Goranov, A. Amon, and S. R. Manalis. Measurement of mass, density, and volume during the cell cycle of yeast. *Proceedings of the National Academy of Sciences*, 107(3):999–1004, 2010.

[33] K. Burg, W. Holder Jr, C. Culberson, R. Beiler, K. Greene, A. Loebsack, W. Roland, P. Eiselt, D. Mooney, and C. Halberstadt. Comparative study of seeding methods for three-dimensional polymeric scaffolds. *Journal of biomedical materials research*, 51(4):642–649, 2000.

[34] R. Burridge and J. B. Keller. Poroelasticity equations derived from microstructure. *The Journal of the Acoustical Society of America*, 70(4):1140–1146, 1981.

[35] H. Byrne and M. A. Chaplain. Free boundary value problems associated with the growth and development of multicellular spheroids. *European Journal of Applied Mathematics*, 8(06):639–658, 1997.

[36] H. Byrne and L. Preziosi. Modelling solid tumour growth using the theory of mixtures. *Mathematical Medicine and Biology*, 20(4):341–366, 2003.

[37] H. M. Byrne, J. R. King, D. S. McElwain, and L. Preziosi. A two-phase model of solid tumour growth. *Applied Mathematics Letters*, 16(4):567–573, 2003.

[38] S. Cartmell and A. El Haj. Mechanical bioreactors for bone tissue engineering. In *Bioreactors for tissue engineering*, pages 193–208. Springer, 2005.

[39] M. J. Casulleras, M. Hubbard, P. Loadman, and J. Spencer. Palbociclib cellular uptake and efflux in in vitro models of disaggregated cells and spheroids. in preparation.

[40] C.-T. Chen, D. S. Malkus, and R. Vanderby. A fiber matrix model for interstitial fluid flow and permeability in ligaments and tendons. *Biorheology*, 35(2):103–118, 1998.

[41] H.-C. Chen and Y.-C. Hu. Bioreactors for tissue engineering. *Biotechnology letters*, 28(18):1415–1423, 2006.

[42] A. S. Clark, T. B. Karasic, A. DeMichele, D. J. Vaughn, M. O'Hara, R. Perini, P. Zhang, P. Lal, M. Feldman, M. Gallagher, et al. Palbociclib (pd0332991)—a selective and potent cyclin-dependent kinase inhibitor: a review of pharmacodynamics and clinical development. *JAMA oncology*, 2(2):253–260, 2016.

[43] N. Cogan and J. Keener. Channel formation in gels. *SIAM Journal on Applied Mathematics*, 65(6):1839–1854, 2005.

[44] J. Collis, D. Brown, M. E. Hubbard, and R. O'Dea. Effective equations governing an active poroelastic medium. In *Proceedings of the Royal Society A.*, volume 473. The Royal Society, 2017.

[45] J. Collis, M. E. Hubbard, and R. D. O'Dea. Computational modelling of multiscale, multiphase fluid mixtures with application to tumour growth. *Computer Methods in Applied Mechanics and Engineering*, 309:554–578, 2016.

[46] J. Collis, M. E. Hubbard, and R. D. O'Dea. A multi-scale analysis of drug transport and response for a multi-phase tumour model. *European Journal of Applied Mathematics*, pages 1–36, 2016.

[47] F. Concha. *Solid-Liquid Separation in the Mining Industry*. Springer, 2014.

[48] V. Cristini, X. Li, J. S. Lowengrub, and S. M. Wise. Nonlinear simulations of solid tumor growth using a mixture model: invasion and branching. *Journal of Mathematical Biology*, 58(4):723–763, 2009.

[49] J. Currey and G. Butler. The mechanical properties of bone tissue in children. *The Journal of bone and joint surgery. American volume*, 57(6):810–814, 1975.

[50] J. H. Cushman, L. S. Bennethum, and B. X. Hu. A primer on upscaling tools for porous media. *Advances in Water Resources*, 25(8):1043–1067, 2002.

[51] H. Darcy. *Les fontaines publiques de la ville de Dijon: exposition et application...* Victor Dalmont, 1856.

[52] Y. Davit, C. G. Bell, H. Byrne, L. A. Chapman, L. S. Kimpton, G. E. Lang, K. H. Leonard, J. M. Oliver, N. Pearson, R. Shipley, et al. Homogenization via formal multiscale asymptotics and volume averaging: How do the two techniques compare? *Advances in Water Resources*, 62:178–206, 2013.

[53] E. Donà, J. D. Barry, G. Valentin, C. Quirin, A. Khmelinskii, A. Kunze, S. Durdu, L. R. Newton, A. Fernandez-Minan, W. Huber, et al. Directional tissue migration through a self-generated chemokine gradient. *Nature*, 503(7475):285–289, 2013.

[54] D. Drasdo. Center-based single-cell models: An approach to multi-cellular organization based on a conceptual analogy to colloidal particles. In *Single-Cell-Based Models in Biology and Medicine*, pages 171–196. Springer, 2007.

[55] D. A. Drew and S. L. Passman. *Theory of multicomponent fluids*, volume 135. Springer Science & Business Media, 2006.

[56] M. G. Dunn and F. H. Silver. Viscoelastic behavior of human connective tissues: relative contribution of viscous and elastic components. *Connective tissue research*, 12(1):59–70, 1983.

[57] E. Farahani, H. K. Patra, J. R. Jangamreddy, I. Rashedi, M. Kawalec, R. K. R. Pariti, P. Batakis, and E. Wiechec. Cell adhesion molecules and their relation to (cancer) cell stemness. *Carcinogenesis*, 35(4):747–759, 2014.

[58] G. Forgacs, R. A. Foty, Y. Shafrir, and M. S. Steinberg. Viscoelastic properties of living embryonic tissues: a quantitative study. *Biophysical Journal*, 74(5):2227–2234, 1998.

[59] H. Fricke. The electric permittivity of a dilute suspension of membrane-covered ellipsoids. *Journal of Applied Physics*, 24(5):644–646, 1953.

[60] P. Friedl and D. Gilmour. Collective cell migration in morphogenesis, regeneration and cancer. *Nature Reviews Molecular Cell Biologyell biology*, 10(7):445–457, 2009.

[61] M. Gad-el Hak and P. R. Bandyopadhyay. Questions in fluid mechanics. *Journal of Fluids Engineering*, 117:3–5, 1995.

[62] B. S. Gardiner, K. K. Wong, G. R. Joldes, A. J. Rich, C. W. Tan, A. W. Burgess, and D. W. Smith. Discrete element framework for modelling extracellular matrix, deformable cells and subcellular components. *PLoS Comput Biol*, 11(10):e1004544, 2015.

[63] J.-L. Gennisson, T. Deffieux, E. Macé, G. Montaldo, M. Fink, and M. Tanter. Viscoelastic and anisotropic mechanical properties of in vivo muscle tissue assessed by supersonic shear imaging. *Ultrasound in medicine and biology*, 36(5):789–801, 2010.

[64] M. Geoffrey, H. Cooper, and E. Robert. *Cell: A Molecular Approach*. Sinauer Associates Incorporated, 2015.

[65] D. George. Adaptive finite volume methods with well-balanced Riemann solvers for modeling floods in rugged terrain: Application to the Malpasset dam-break flood (France, 1959). *International Journal for Numerical Methods in Fluids*, 66(8):1000–1018, 2011.

[66] J. R. Gershlak, S. Hernandez, G. Fontana, L. R. Perreault, K. J. Hansen, S. A. Larson, B. Y. Binder, D. M. Dolivo, T. Yang, T. Dominko, et al. Crossing kingdoms: Using decellularized plants as perfusable tissue engineering scaffolds. *Biomaterials*, 125:13–22, 2017.

[67] S. Grenier, M. Sandig, D. W. Holdsworth, and K. Mequanint. Interactions of coronary artery smooth muscle cells with 3d porous polyurethane scaffolds. *Journal of Biomedical Materials Research Part A*, 89(2):293–303, 2009.

[68] C. M. Groh, M. E. Hubbard, P. F. Jones, P. M. Loadman, N. Periasamy, B. D. Sleeman, S. W. Smye, C. J. Twelves, and R. M. Phillips. Mathematical and computational models of drug transport in tumours. *Journal of The Royal Society Interface*, 11(94):20131173, 2014.

[69] W. H. Grover, A. K. Bryan, M. Diez-Silva, S. Suresh, J. M. Higgins, and S. R. Manalis. Measuring single-cell density. *Proceedings of the National Academy of Sciences*, 108(27):10992–10996, 2011.

[70] D. Guidolin, P. Rebuffat, and G. Albertin. Cell-oriented modeling of angiogenesis. *The Scientific World Journal*, 11:1735–1748, 2011.

[71] E. Holden, J. Collis, B. Brook, and R. O'Dea. A multiphase multiscale model for nutrient limited tissue growth. *ANZIAM Special Edition*, in press.

[72] M. Hubbard and H. Byrne. Multiphase modelling of vascular tumour growth in two spatial dimensions. *Journal of Theoretical Biology*, 316:70–89, 2013.

[73] M. E. Hubbard and N. Dodd. A 2D numerical model of wave run-up and overtopping. *Coastal Engineering*, 47(1):1–26, 2002.

[74] L. Hufnagel, A. A. Teleman, H. Rouault, S. M. Cohen, and B. I. Shraiman. On the mechanism of wing size determination in fly development. *Proceedings of the National Academy of Sciences*, 104(10):3835–3840, 2007.

[75] L. Irons, J. Collis, and R. D. O'Dea. Microstructural influences on growth and transport in biological tissue—a multiscale description. In *Modeling of microscale transport in biological processes*, pages 311–334. Elsevier, 2017.

[76] R. K. Jain. Transport of molecules across tumor vasculature. *Cancer and Metastasis Reviews*, 6(4):559–593, 1987.

[77] R. K. Jain. Delivery of molecular and cellular medicine to solid tumors. *Advanced Drug Delivery Reviews*, 46(1):149–168, 2001.

[78] R. K. Jain, P. Au, J. Tam, D. G. Duda, and D. Fukumura. Engineering vascularized tissue. *Nature Biotechnology*, 23(7):821–824, 2005.

[79] A. E. Jakus, E. B. Secor, A. L. Rutz, S. W. Jordan, M. C. Hersam, and R. N. Shah. Three-dimensional printing of high-content graphene scaffolds for electronic and biomedical applications. *ACS Nano*, 9(4):4636–4648, 2015.

[80] P. A. Janmey. Mechanical properties of cytoskeletal polymers. *Current opinion in cell biology*, 3(1):4–11, 1991.

[81] H. Jóhannesson and B. Halle. Solvent diffusion in ordered macrofluids: a stochastic simulation study of the obstruction effect. *The Journal of Chemical Physics*, 104(17):6807–6817, 1996.

[82] J. B. Keller. Darcy's law for flow in porous media and the two-space method. *Nonlinear Partial Differential Equations in Engineering and Applied Sciences*, 31:429–443, 1980.

[83] J. King and S. Franks. Mathematical modelling of nutrient-limited tissue growth. In *Free Boundary Problems*, pages 273–282. Springer, 2007.

[84] A. J. Kuszak. How cells crawl the dynamics of cell motility. `https://irp.nih.gov/sites/default/files/catalyst/catalyst_v21i5.pdf`, September 2013.

[85] R. Langer. Biodegradable polymer scaffolds for tissue engineering. *Bio/technology*, 12, 1994.

[86] E. W. Larsen. Neutron transport and diffusion in inhomogeneous media. I. *Journal of Mathematical Physics*, 16(7):1421–1427, 1975.

[87] E. W. Larsen. Neutron transport and diffusion in inhomogeneous media. II. *Nuclear Science and Engineering*, 60(4):357–368, 1976.

[88] G. Lemon and J. King. Multiphase modelling of cell behaviour on artificial scaffolds: effects of nutrient depletion and spatially

nonuniform porosity. *Mathematical Medicine and Biology*, 24(1):57–83, 2007.

[89] G. Lemon and J. King. Travelling-wave behaviour in a multiphase model of a population of cells in an artificial scaffold. *Journal of Mathematical Biology*, 55(4):449–480, 2007.

[90] G. Lemon, J. King, H. Byrne, O. Jensen, and K. Shakesheff. Mathematical modelling of engineered tissue growth using a multiphase porous flow mixture theory. *Journal of Mathematical Biology*, 52(5):571–594, 2006.

[91] R. J. LeVeque. *Finite volume methods for hyperbolic problems*, volume 31. Cambridge university press, 2002.

[92] C. Y. Lin, N. Kikuchi, and S. J. Hollister. A novel method for biomaterial scaffold internal architecture design to match bone elastic properties with desired porosity. *Journal of Biomechanics*, 37(5):623–636, 2004.

[93] Z. Liu and L. Bilston. On the viscoelastic character of liver tissue: experiments and modelling of the linear behaviour. *Biorheology*, 37(3):191–201, 2000.

[94] H. Lodish, A. Berk, and S. Zipursky. *Molecular Cell Biology*. W. H. Freeman, New York, 4th edition edition, 2000.

[95] H. Lodish, A. Berk, and S. Zipursky. *Molecular Cell Biology*, chapter Tumor Cells and the Onset of Cancer. W. H. Freeman, New York, 4th edition edition, 2000.

[96] S. Lubkin and T. Jackson. Multiphase mechanics of capsule formation in tumors. *Transactions-American Society of Mechanical Engineers Journal of Biomechanical Engineering*, 124(2):237–243, 2002.

[97] R. Luciano and E. Sacco. Homogenization technique and damage model for old masonry material. *International Journal of Solids and Structures*, 34(24):3191–3208, 1997.

[98] A. Matzavinos and M. Ptashnyk. Homogenization of oxygen transport in biological tissues. *Applicable Analysis*, 95(5):1013–1049, 2016.

[99] J. C. Maxwell. *A treatise on electricity and magnetism*, volume 1. Clarendon press, 1881.

[100] C. Mei and J.-L. Auriault. The effect of weak inertia on flow through a porous medium. *Journal of Fluid Mechanics*, 222:647–663, 1991.

[101] C. C. Mei and B. Vernescu. *Homogenization methods for multiscale mechanics*. World scientific, 2010.

[102] U. Meyer. The history of tissue engineering and regenerative medicine in perspective. In *Fundamentals of Tissue Engineering and Regenerative Medicine*, pages 5–12. Springer, 2009.

[103] J. S. Miller, K. R. Stevens, M. T. Yang, B. M. Baker, D.-H. T. Nguyen, D. M. Cohen, E. Toro, A. A. Chen, P. A. Galie, X. Yu, et al. Rapid casting of patterned vascular networks for perfusable engineered three-dimensional tissues. *Nature Materials*, 11(9):768–774, 2012.

[104] L. Morland and S. Sellers. Multiphase mixtures and singular surfaces. *International Journal of Non-linear Mechanics*, 36(1):131–146, 2001.

[105] G. Morris, J. Bridge, L. Brace, A. Knox, J. Aylott, C. Brightling, A. Ghaemmaghami, and F. Rose. A novel electrospun biphasic scaffold provides optimal three-dimensional topography for in vitro co-culture of airway epithelial and fibroblast cells. *Biofabrication*, 6(3):035014, 2014.

[106] F. T. Moutos, K. A. Glass, S. A. Compton, A. K. Ross, C. A. Gersbach, F. Guilak, and B. T. Estes. Anatomically shaped tissue-engineered cartilage with tunable and inducible anticytokine delivery for biological joint resurfacing. *Proceedings of the National Academy of Sciences*, 113(31):E4513–E4522, 2016.

[107] N. Murisic, V. Hakim, I. G. Kevrekidis, S. Y. Shvartsman, and B. Audoly. From discrete to continuum models of three-dimensional deformations in epithelial sheets. *Biophysical journal*, 109(1):154–163, 2015.

[108] P. J. Murray, A. Walter, A. G. Fletcher, C. M. Edwards, M. J. Tindall, and P. K. Maini. Comparing a discrete and continuum model of the intestinal crypt. *Physical biology*, 8(2):026011, 2011.

[109] T. J. Newman. Modeling multi-cellular systems using sub-cellular elements. *arXiv preprint q-bio/0504028*, 2005.

[110] J. A. Nitsche. Über ein variationsprinzip zur lösung dirichlet-problemen bei verwendung von teilräumen die keinen randbedingungen unteworfen sind. *Abh. Math. Sem. Univ. Hamburg*, 36:9 – 15, 1971.

[111] F. J. O'Brien. Biomaterials & scaffolds for tissue engineering. *Materials Today*, 14(3):88–95, 2011.

[112] J. A. Ochoa-Tapia, P. Stroeve, and S. Whitaker. Diffusive transport in two-phase media: Spatially periodic models and maxwell's theory for isotropic and anisotropic systems. *Chemical Engineering Science*, 49(5):709–726, 1994.

[113] R. O'Dea. *Multiphase modelling of tissue growth in dynamic culture conditions*. PhD thesis, University of Nottingham, 2008.

[114] R. O'Dea and J. King. Multiscale analysis of pattern formation via intercellular signalling. *Mathematical Biosciences*, 231(2):172–185, 2011.

[115] R. O'Dea, M. Nelson, A. El Haj, S. Waters, and H. Byrne. A multiscale analysis of nutrient transport and biological tissue growth in vitro. *Mathematical Medicine and Biology*, 32(3):345–366, 2014.

[116] R. O'Dea, J. Osborne, A. El Haj, H. Byrne, and S. Waters. The interplay between tissue growth and scaffold degradation in engineered tissue constructs. *Journal of Mathematical Biology*, 67(5):1199–1225, 2013.

[117] R. O'Dea, S. Waters, and H. Byrne. A multiphase model for tissue construct growth in a perfusion bioreactor. *Mathematical Medicine and Biology*, 27(2):95–127, 2010.

[118] R. D. O'Dea and J. R. King. Continuum limits of pattern formation in hexagonal-cell monolayers. *Journal of Mathematical Biology*, 64(3):579–610, 2012.

[119] P. Olczyk, Ł. Mencner, and K. Komosinska-Vassev. The role of the extracellular matrix components in cutaneous wound healing. *BioMed Research International*, 2014.

[120] J. M. Osborne. Multiscale model of colorectal cancer using the cellular potts framework. *Cancer Informatics*, 14(Suppl 4):83, 2015.

[121] H. C. Ott, T. S. Matthiesen, S.-K. Goh, L. D. Black, S. M. Kren, T. I. Netoff, and D. A. Taylor. Perfusion-decellularized matrix: using nature's platform to engineer a bioartificial heart. *Nature Medicine*, 14(2):213–221, 2008.

[122] E. Palsson and H. G. Othmer. A model for individual and collective cell movement in dictyostelium discoideum. *Proceedings of the National Academy of Sciences*, 97(19):10448–10453, 2000.

[123] F. Pampaloni, E. G. Reynaud, and E. H. Stelzer. The third dimension bridges the gap between cell culture and live tissue. *Nature Reviews Molecular Cell Biology*, 8(10):839–845, 2007.

[124] N. Pearson, R. Shipley, S. Waters, and J. Oliver. Multiphase modelling of the influence of fluid flow and chemical concentration on tissue growth in a hollow fibre membrane bioreactor. *Mathematical Medicine and Biology*, 31(4):393–430, 2014.

[125] R. Penta, D. Ambrosi, and A. Quarteroni. Multiscale homogenization for fluid and drug transport in vascularized malignant tissues. *Mathematical Models and Methods in Applied Sciences*, 25(01):79–108, 2015.

[126] R. Penta, D. Ambrosi, and R. Shipley. Effective governing equations for poroelastic growing media. *The Quarterly Journal of Mechanics and Applied Mathematics*, 67(1):69–91, 2014.

[127] P. A. Raviart and J. M. Thomas. A mixed finite element method for second order elliptic problems. In I. Galligani and E. Magenes, editors, *Mathematical Aspects of the Finite Element Method*, Lectures Notes in Math. 606. Springer-Verlag, New York, 1977.

[128] L. Rayleigh. LVI. on the influence of obstacles arranged in rectangular order upon the properties of a medium. *The London, Edinburgh, and Dublin Philosophical Magazine and Journal of Science*, 34(211):481–502, 1892.

[129] K. A. Rejniak. An immersed boundary framework for modelling the growth of individual cells: an application to the early tumour development. *Journal of Theoretical Biology*, 247(1):186–204, 2007.

[130] C. Rosenberg. Wound healing in the patient with diabetes mellitus. *The Nursing clinics of North America*, 25(1):247–261, 1990.

[131] D. Ryan, R. Carbonell, and S. Whitaker. A theory of diffusion and reaction in porous media. In *AIChE Symposium Series*, volume 202, pages 46–62, 1981.

[132] K. S. Saladin and L. Miller. *Anatomy & Physiology*. WCB/McGraw-Hill New York, 1998.

[133] E. Sanchez-Palencia. Solutions périodiques par rapport aux variables d'espace et applications. *CR Acad. Sc. Paris*, 271(A):1129–1132, 1970.

[134] E. Sanchez-Palencia. Comportements local et macroscopique d'un type de milieux physiques heterogenes. *International Journal of Engineering Science*, 12(4):331–351, 1974.

[135] S. Sandersius, C. J. Weijer, and T. J. Newman. Emergent cell and tissue dynamics from subcellular modeling of active biomechanical processes. *Physical Biology*, 8(4):045007, 2011.

[136] A. Sarvazyan, T. J. Hall, M. W. Urban, M. Fatemi, S. R. Aglyamov, and B. S. Garra. An overview of elastography–an emerging branch of medical imaging. *Current Medical Imaging Reviews*, 7(4):255, 2011.

[137] R. Schulz and P. Knabner. An effective model for biofilm growth made by chemotactical bacteria in evolving porous media. *SIAM Journal on Applied Mathematics*, 77(5):1653–1677, 2017.

[138] N. Shanks, R. Greek, and J. Greek. Are animal models predictive for humans? *Philosophy, Ethics, and Humanities in Medicine*, 4(1):2, 2009.

[139] R. Shipley. *Multiscale Modelling of Fluid and Drug Transport in Vascular Tumours*. PhD thesis, St. Hugh's College University of Oxford, 2008.

[140] R. Shipley and S. Chapman. Multiscale modelling of fluid and drug transport in vascular tumours. *Bulletin of Mathematical Biology*, 72(6):1464–1491, 2010.

[141] R. Shipley, G. Jones, R. Dyson, B. Sengers, C. Bailey, C. Catt, C. Please, and J. Malda. Design criteria for a printed tissue engineering construct: a mathematical homogenization approach. *Journal of Theoretical Biology*, 259(3):489–502, 2009.

[142] J. J. Song, J. P. Guyette, S. E. Gilpin, G. Gonzalez, J. P. Vacanti, and H. C. Ott. Regeneration and experimental orthotopic transplantation of a bioengineered kidney. *Nature Medicine*, 19(5):646–651, 2013.

[143] G. Stokes. G.(1845), on the theories of internal friction of fluids in motion. *Transactions of the Cambridge Philosophical Society*, 8:287.

[144] S. Tanaka. Simulation frameworks for morphogenetic problems. *Computation*, 3(2):197–221, 2015.

[145] C. Taylor and P. Hood. A numerical solution of the Navier-Stokes equations using the finite element technique. *Computers & Fluids*, 1(1):73 – 100, 1973.

[146] C. Truesdell. *Rational thermodynamics*. Springer Science & Business Media, 2012.

[147] H. L. Tuomisto and M. J. Teixeira de Mattos. Environmental impacts of cultured meat production. *Environmental Science & Technology*, 45(14):6117–6123, 2011.

[148] S. Turner and J. A. Sherratt. Intercellular adhesion and cancer invasion: a discrete simulation using the extended potts model. *Journal of Theoretical Biology*, 216(1):85–100, 2002.

[149] B. Van Leer. Towards the ultimate conservative difference scheme. V. A second-order sequel to Godunov's method. *Journal of Computational Physics*, 32(1):101–136, 1979.

[150] P. Venema, R. Struis, J. Leyte, and D. Bedeaux. The effective self-diffusion coefficient of solvent molecules in colloidal crystals. *Journal of Colloid and Interface Science*, 141(2):360–373, 1991.

[151] J. P. Ward and J. King. Mathematical modelling of avascular-tumour growth. *Mathematical Medicine and Biology*, 14(1):39–69, 1997.

[152] S. Waters, L. Cummings, K. Shakesheff, and F. Rose. Tissue growth in a rotating bioreactor. part i: mechanical stability. *Mathematical Medicine and Biology*, 23(4):311–337, 2006.

[153] C. Wei and J. Dong. Direct fabrication of high-resolution three-dimensional polymeric scaffolds using electrohydrodynamic hot jet plotting. *Journal of Micromechanics and Microengineering*, 23(2):025017, 2013.